Redox Evolution of the Early Earth's Mantle

DISSERTATION

zur Erlangung des akademischen Grades eines
Doktors der Naturwissenschaften (Dr. rer. nat.)
in der Bayreuther Graduiertenschule für Mathematik und
Naturwissenschaften (BayNAT) der Universität Bayreuth

vorgelegt von

Katherine Armstrong

geboren in Monterey, California

Bayreuth, 2018

Redox Evolution of the Early Earth's Mantle

———————————————

DISSERTATION

zur Erlangung des akademischen Grades eines
Doktors der Naturwissenschaften (Dr. rer. nat.)
in der Bayreuther Graduiertenschule für Mathematik und
Naturwissenschaften (BayNAT) der Universität Bayreuth

vorgelegt von

Katherine Armstrong

geboren in Monterey, California

Bayreuth, 2018

Die vorliegende Arbeit wurde in der Zeit von Februar 2015 bis November 2018 in Bayreuth am Bayerischen Geoinstitut unter Betreuung von Herrn Dr. Dan Frost angefertigt.

Vollständiger Abdruck der von der Bayreuther Graduiertenschule für Mathematik und Naturwissenschaften (BayNAT) der Universität Bayreuth genehmigten

Dissertation eingereicht am:	31 Oktober 2018
Zulassung durch das Leitungsgremium:	02 November 2018
Wissenschaftliches Kolloquium:	28 November 2018

Amtierender Direktor: Prof. Dr. Dirk Schüler

Prüfungsausschuss:

Prof. Dr. Daniel Frost	(Gutachter)
PD Dr. Catherine McCammon	(Gutachterin)
Prof Dr. David Rubie	(Vorsitz)
PD Dr. Gerd Steinle-Neumann	

Abstract

The redox state of the Earth's upper mantle controls the nature of volatile phases degassing from the interior and has, therefore, influenced the development of habitable surface conditions. An important event in the creation of these conditions was the rapid oxidation of the upper mantle after core formation. During accretion, mantle silicates equilibrated with core-forming metallic iron. This would have imposed a low mantle oxygen fugacity ($f\mathrm{O}_2$), where H_2O, CH_4 and H_2 would be the dominant degassing species. Throughout the geological record, however, $f\mathrm{O}_2$ of the upper mantle has been 4-5 orders of magnitude higher, such that H_2O and CO_2 are the dominant volcanic gasses. The mechanism by which the mantle oxidised has implications for volatile delivery and fractionation in the early Earth and for the evolution of an oxygen-rich atmosphere.

In this experimental study, mantle oxidation mechanisms have been investigated. Pressure has been found to stabilise ferric iron components in some mantle minerals, such that they contain a significant fraction of Fe^{3+} even in equilibrium with iron metal. If a ferric component in silicate magmas undergoes similar stabilisation, melt at the base of a deep magma ocean could have precipitated iron metal via the reaction $3FeO = Fe^0 + 2FeO_{1.5}$. Separation of this iron metal to the core could then have raised the redox state of the mantle. In order to test this scenario, the proportions of Fe^{3+} and Fe^{2+} silicate melt components have been measured as a function of pressure at buffered oxygen fugacities.

First, an oxygen buffering assemblage for use at pressures at the top of Earth's lower mantle was calibrated. Phase relations, compressibility and thermal expansivity of Ru and RuO_2 were investigated in a multianvil device using *in-situ* X-ray diffraction at the Advanced Photon Source in Chicago. Rutile-structured RuO_2 was found to undergo two phase transformations, first at $\sim$7 GPa to an orthorhombic structure and then above $\sim$12 GPa to a cubic structure. The phase boundary of the cubic phase was constrained for the first time at high pressure and temperature. A thermodynamic description of the phase transformations along with equation of state data allows the oxygen fugacity

buffered by the Ru + O_2 = RuO_2 equilibrium to be accurately determined to lower mantle conditions.

Secondly, an andesitic melt was equilibrated with the Ru-RuO_2 buffer in a multianvil press between 5 and 24 GPa, and further experiments were performed on the same melt in equilibrium with iron metal. The recovered sample were analysed using Mössbauer spectroscopy to determine the $Fe^{3+}/\sum Fe$ ratio. This ratio was found to decrease with pressure up to 8 GPa, but above 15 GPa this trend reverses. Based on the equation of state properties of the iron melt components, we develop a model that describes this behaviour. The predictions of this model at conditions of iron-metal saturation are in good agreement with further experiments. This indicates that the $Fe^{3+}/\sum Fe$ ratio of a magma ocean extending into the lower mantle would have approached $\sim$0.2, which means that the melt-metal equilibrium, $3FeO = Fe + 2FeO_{1.5}$, must shift to the right with pressure. A magma ocean initially poor in $FeO_{1.5}$ would, therefore, precipitate metallic iron at depth. Separation of this iron to the core would raise the redox state of the mantle. Such a magma ocean would develop a gradient in oxygen fugacity with depth, from conditions of metallic iron saturation at lower mantle pressures to that of the present day mantle at the surface. This magma ocean redox stratification ensured that H_2O and CO_2 were the dominant atmosphere-forming gases throughout the later stages of accretion. There are a number of further important implications for the distribution of volatiles within the Earth and differences in the redox states between planetary interiors.

Another frequently proposed scenario is mantle oxidation by H_2O. One mechanism for this to operate is if the resulting hydrogen is sequestered into the core rather than reducing the surrounding mantle back to the initial level. At upper mantle conditions the oxygen fugacity of the mantle could only be raised above iron metal equilibrium if this core-forming phase were a sulfide liquid. A slightly hydrous mid ocean ridge basaltic melt was equilibrated with an FeS melt at 3 GPa, to test the effect of an exsolving sulfide melt on the redox state of the remaining silicate. Hydrogen contents of quenched sulphide liquids were measured for the first time using Elastic Recoil Detection Analysis and found to be the equivalent of up to 1300 weight ppm H_2O. A lack of

consistency in H partitioning between silicate melt and sulfide, however, suggests that the entire H content of the initial sulphide may not be preserved in the crystallised liquid. The partitioning of H and O into a separating sulfide melt is examined based on the available data and found to have insignificant effects on the oxidation state of the remaining mantle.

Zusammenfassung

Der Oxidationszustand des oberen Erdmantels bestimmt, welche flüchtigen Verbindungen aus dem Erdinneren entgasen und beeinflusst damit die Entwicklung der Bewohnbarkeit der Erdoberfläche stark. Ein wichtiges Ereignis im Entstehen der Habitabilität war die schnelle Oxidation des oberen Erdmantels nach der Segregation des Erdkerns. Während der Planetenbildung befanden sich die Mantelsilikate im Gleichgewicht mit Eisen, und damit in einem Zustand mit niedriger Sauerstofffugazität (fO_2): H_2O, CH_4 und H_2 sind in so einem Zustand die volatilen Verbindungen, die aus dem Erdmantel entgasen. Über den ganzen Verlauf der Erdgeschichte war der fO_2-Wert im oberen Erdmantel jedoch 4-5 Größenordnungen höher, sodass H_2O und CO_2 als vulkanische Gase an die Oberfläche kamen. Der Oxidationsprozess, der im Mantel stattgefunden hat, ist deshalb von großer Wichtigkeit für den Transport und die Fraktionierung von Volatilen in der jungen Erde, sowie für die Entwicklung einer sauerstoffreichen Atmosphäre.

Dieser Oxidationsmechanismus wurde mit Hilfe von Experimenten in dieser Dissertation untersucht. Druck spielt bei der Stabilisierung des Fe^{3+}-Gehalts in einigen Mantelmineralien eine große Rolle, so dass diese Mineralien, sogar in Gleichgewicht mit metallischem Eisen (Fe^0), einen großen Anteil an Fe^{3+} enthalten. Falls Fe^{3+} in Silikatschmelzen eine ähnliche Stabilisierung erfährt, können Schmelzen am Grund des Magmaozeans durch die Reaktion $3FeO$ = Fe_2O_3+ Fe^0 metallisches Eisen ausgefällen, und durch die Separation des metallischen Eisen den Oxidationszustand des Erdmantels erhöhen. Um diese Hypothese zu untersuchen, wurde in der vorliegenden Arbeit die Anteile von Fe^{3+} und Fe^{2+} in Silikatschmelzen als Funktion des Drucks unter Anwendung

eines Sauerstofffugazität-Puffers untersucht.

Zuerst wurde ein Sauerstoff-Puffer kalibriert, der bei Bedingungen des tiefen Erdmantels angewendet werden kann. Die Phasenbeziehungen, Kompressibilität und den thermischen Ausdehnungskoeffizienten von Ru und RuO_2 wurden mit Hilfe von Röntgenbeugung in der Vielstempelpresse an der Advanced Photon Source in Chicago untersucht. Für RuO_2 wurden zwei Phasenübergänge beobachtet: bei ~7 GPa von einer tetragonalen (Rutil-Typ) zu einer orthorhombischen Phase und bei ~12 GPa zu einer kubischen Struktur. Die Phasengrenze der kubischen Phase wurde in der vorliegenden Arbeit zum ersten Mal bei hohem Druck und hoher Temperatur bestimmt. Eine thermodynamische Beschreibung der Phasenübergänge sowie die bestimmte Zustandsgleichung ermöglichen es, die Suaerstofffugazität der Pufferreaktion $Ru + O_2 = RuO_2$ bei Bedingungen des tiefen Erdmantels zu bestimmen.

In einem zweiten Experiment wurde andesitische Schmelze unter Anwendung des Ru-RuO_2-Puffers in der Vielstempelpresse im Druckbereich 5-24 GPa in ein Gleichgewicht, und weitere Experimente wurden in Gegenwart von metallischem Eisen durchgeführt. Die bei diesen Versuchen gewonnenen Proben wurden mit Hilfe von Mössbauer-Spektroskopie untersucht um das $Fe^{3+}/\sum Fe$-Verhältnis zu bestimmen. Dieses Verhältnis nimmt mit Druck bis 8 GPa ab, und bei Drücken über 15 GPa steigt es wieder an, ein Verhalten, das mit Hilfe der Zustandsgleichung der Eisenkomponenten modelliert werden kann. Vorhersagen dieses Modells stimmen mit weiteren Experimenten bei Eisen-Sättigung gut überein. Das beschrieben Verhalten und dazugehörige Modell weisen darauf hin, dass das Verhätnis $Fe^{3+}/\sum Fe$ im Magmaozean bei Druckbedingungen des tiefen Erdmantels einen Wert von ~0.2 erreicht, womit das Schmelzen-Metall Gleichgewicht, $3FeO = Fe_2O_3 + Fe^0$, sich bei hohem Druck auf die rechte Seite der Reaktion verschiebt. Ein Magmaozean, der ursprünglich an Fe^{3+} arm ist, würde folglich in der Tiefe metallisches Eisen ausfällen, und das Abscheiden dieses Eisen in den Erdkern würde den Oxidationszustand des Mantels erhöhen. Ein solcher Magmaozean würde dann einen Sauerstofffugazitätsgradienten mit Tiefe aufweisen, von Bedingungen der Metallsättigung im tiefen Erdmantel zu modernen Werten an der Erdoberfläche. Diese Schichtung im Oxidationszustand des Magmaozeans bewirkt,

dass bereits während der späten Phase der Planetenbildung H_2O und CO_2 die Atmosphärenbildung bestimmt haben. Aus den Ergebnissen ergeben sich weitere wichtige Folgerungen für die Verteilung von volatilen Komponenten in der Erde und Unterschiede im Redoxzustand im Innern verschiedener Planeten.

Oxidation des Mantels durch Eintrag von H_2O ist eine beliebte Alternativhypothese. Dies wäre unter anderem dann möglich, wenn Wasserstoff in den Erdkern transportiert wird und damit nicht zur Reduktion des Erdmantels auf das Ausgangsniveau zur Verfügung steht. Bei Bedingungen des oberen Erdmantels wäre dies nur möglich, wenn die Sauerstofffugazität über das Eisen-Metall-Gleichgewicht erhöht wird, was ein Sulfid als kernbildende Schmelze erfordert. Um diese Hypothese zu untersuchen, wurde ein leicht wasserhaltiger Ozeankamm-Basalt mit FeS bei 3 GPa ins Gleichgewicht gebracht. Dieses Experiment erlaubt es, den Einfluss einer sich bildenden Sulfidschmelze auf den Redoxzustand des zurückbleibenden Silikats zu untersuchen. Der Wasserstoffgehalt der abgeschreckten Sulfidschmelze wurde zum ersten Mal mit Hilfe der elastischen Rückstreudetektionsanalyse bestimmt, und ein Wasserstoffgehalt von bis zu 1300 ppm (Gewicht) wurde gemessen. Die fehlende Konsistenz in der Bestimmung der Verteilung von H zwischen der Silikatschmelze und des Sulfids weist darauf hin, dass nicht der vollständige H-Gehalt des Sulfids beim Abschrecken erhalten bleibt. Auf Basis der untersuchten Partitionierung von Wasserstoff und Sauerstoff in die sich bildende Sulfidschmelze ergibt sich ein vernachlässigbarer Einfluss auf den Oxidationszustand des zurückbleibenden Mantels.

Contents

Contents

Contents

1 Introduction

Central to understanding the origins of life on Earth and assessing the possible past habitability of other terrestrial planets, satellites, or exoplanets is understanding the processes by which the early Earth became habitable. The nature of the upper mantle during the Hadean would have been consequential to the habitability of the young Earth, as the composition and oxidation state of the mantle would have controlled the composition of any degassing volatiles, thus exerting a major influence on the composition of the earliest atmosphere (e.g., Kump et al., 2001).

A reduced mantle, which likely existed during the formation of the core as discussed below, would have produced a reduced atmosphere, dominated by species such as CO, CH_4, and H_2 (e.g., Hirschmann, 2012; Kasting et al., 1993). Today, however, the upper mantle is several orders of magnitude more oxidised than metal saturation implies. Futher, evidence from redox-sensitive elements in ancient rocks imply that the oxidation state of the mantle increased dramatically very quickly after the end of core formation (e.g., Delano, 2001; Trail et al., 2011). Thus the the dominant degassing volatile species, and therefore earliest atmosphere, would have comprised largely H_2O and CO_2.

In addition to influencing early habitability, the oxidation state of the mantle regulates the compostion of volatile-rich fluids and melts in the interior of the Earth, affecting magma genesis and metasomatism (e.g. Frost and McCammon, 2008). Further, mantle redox state, quantified as the oxygen fugacity, or fO_2, controls the partitioning of many species and elements, including H_2O, between fractionating reservoirs. In particular, the siderophile tendency of many elements is strongly dependent on the prevailing fO_2 (O'Neill, 1991;

Wade and Wood, 2005; Mann et al., 2009). Understanding the redox evolution of the mantle could therefore allow for better constraints on the nature of the light element(s) in the core. Mantle fO_2 also defines the stability of most carbon-bearing phases, and determines the Fe^{3+} and OH contents of minerals, which in turn affects rheology and other transport properties (Frost and McCammon, 2008).

The mantle's oxidation state has therefore been an important parameter throughout Earth's history. Today the Earth's upper mantle is uniformly about 5 orders of magnitude more oxidised than it would have been during differentiation, indicating that one or more processes increased the fO_2 of the mantle after core formation ceased (O'Neill, 1991). The nature and timing of this oxidation mechanism has implications for the proportion and distribution of volatile elements accreted and retained within the Earth, as well as the composition of the earliest atmosphere (Hirschmann, 2012). Understanding this oxidation process may therefore be instrumental to understanding the Earth's evolution into a habitable planet, and this work attempts to place constraints on plausible processes that may have worked to oxidise the mantle.

1.1 Differentiation and metal-silicate equilibrium

Many of the details of the differentiation process remain uncertain, but it is clear that during core formation the silicate material that would later become the mantle and crust was in chemical equilibrium with iron metal. The evidence for this is found in the measured abundances of elements present in the Earth's mantle and crust (bulk silicate Earth, or BSE), compared to chondritic meteorites, which are our best estimate for the bulk composition of the solar system.

1.1.1 Chondritic Earth

The Earth is, as a whole, believed to be chemically similar to chondritic meteorites, which, collectively, are fragments of undifferentiated planetesimals

that appear to have remained largely unprocessed from the very beginning of the solar system (e.g. Brearley and Jones, 1998; Wood, 1988). Though the chondritic meteorite groups vary somewhat in composition, they have in common identical ratios of refractory lithophile elements, i.e., elements that would not fractionate due to their volatility or preference for a metallic or sulfide phase (e.g., Rubin, 2011). These abundance ratios are also the same as those measured in the solar photosphere (e.g., Palme and O'Neill, 2003). It has therefore long been assumed that the suite of chondritic metorities represents the bulk composition of the solar system, and that the variations between the groups reflect different accretion histories of the parent asteroids and/or local compositional variability within the solar nebula (Allègre et al., 1995). CI carbonaceous chondrites, specifically, have elemental abundances that most closely match the solar composition, and so are commonly used as a proxy for the primitive bulk composition of the solar system (e.g., Anders and Grevesse, 1989).

Measurements of the relative abundances of elements in the bulk silicate Earth show that refractory lithophile elements are also present at the same relative abundances (figure 1.1) as chondrites. This is generally accepted as strong evidence that the bulk Earth is, at least to a first order approximation, chondritic in composition and that depleted elements reflect fractionation processes during or after accretion (e.g. Ringwood, 1979; Wänke et al., 1984; McDonough and Sun, 1995). Indeed, most of the constraints on fractionation processes that occurred throughout Earth's history derive from comparing the Earth's mantle composition to that of chondrites (e.g., Palme and O'Neill, 2003).
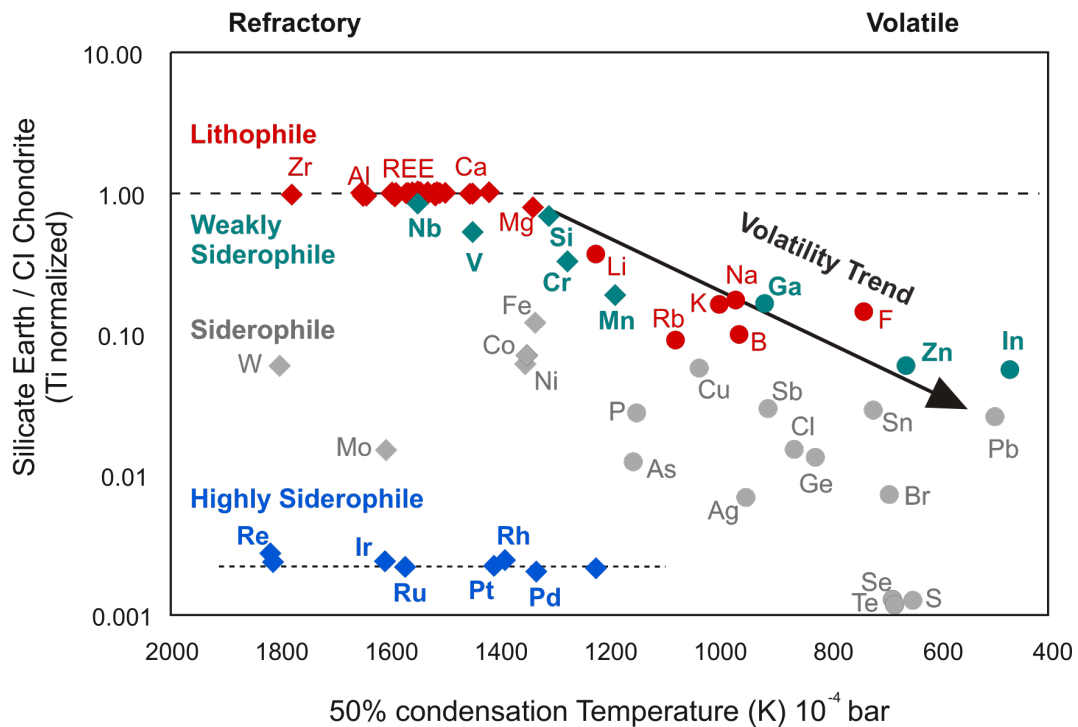
Figure 1.1: Relative abundances of elements in the bulk silicate Earth. Lithophile elements that would not be expected to fractionate due to volatility, i.e. those more refractory than Mg, are present in the same ratios as CI chondrites, indicating that the bulk Earth is chondritic. Refractory siderophile elements are therefore depleated from the mantle due to core formation. The highly siderophile elements (blue symbols) have a flat (chondritic relative) abundance pattern, despite having vastly different metal/silicate partition coefficients. They were therefore probably completely stripped from the mantle and then added back after the end of core formation. Figure is modified from Frost et al. (2008).

1.1.2 Differentiation

The most consequential post-accretion process on the Earth was the physical separation of the metallic iron-nickel material that is now the core from the silicates that comprise the mantle. There is substantial evidence from achondritic meteorites, which are remnants of differentiated planetesimals that were collisionally disrupted and broken apart, that this occurred very rapidly after the beginning of the solar system (e.g., Weiss and Elkins-Tanton, 2013). Iron meteorites are pieces of metallic cores, while stony achondrites represent the mantles. Isotopes of hafnium and tungsten in these planetesimal fragments provide a strong constraint on the timing of differentiation. ^{182}W is a decay

product of ^{182}Hf, and the two elements have different geochemical behaviour: tungsten is siderophile (i.e. prefers a metallic phase) and hafnium is lithophile (i.e. prefers a silicate phase). If metal-silicate differentiation happens before ^{182}Hf has fully decayed (<45 Ma after the beginning of the solar system), the Hf would remain in the silicate, and later decay to W. This tunsten would then be stranded in the silicate and visible as a positive ^{182}W anomaly in the silicate with a corresponding negative anomaly in the metal compared to chondrite (e.g., Kleine and Walker, 2017).

Studies of achondrites using this method have determined that small planetesimals had grown to large enough size to retain sufficient heat (supplied primarily by gravitational release and the decay of short-lived radionuclides) to melt throughout, allowing the heavier metallic iron alloy to sink and form a core by 5 Mya after the origin of the solar system (Kleine et al., 2002). Futher, Hf-W systematics reveal that the Earth, which accreted largely from planetesimals that had already themselves separated into a mantle and a core, had fully differentiated by 30 Mya after the beginning of the solar system (Kleine et al., 2002).

As can be seen in figure 1.1, refractory siderophile elements (i.e., elements that preferentially partition into a metallic phase but would not be expected to fractionate due to volatility) are depleted from mantle rocks. The most plausible interpretation of this is that during differentiation, the core-forming metallic alloy equilibrated with the mantle silicates as it sank. The distribution of an element M between the fractionating metal and silicate was governed by the partition coefficient

$$D^{\mathrm{met/sil}}(M) = \frac{X_M^{\mathrm{metal}}}{X_{MO_{n/2}}^{\mathrm{silicate}}}$$

where X is the mole fraction of the element M or its oxide in the metal or silicate and n is its valence state. Siderophile elements, which are defined as having a metal/silicate partition coefficient of greater than 1, would have then partitioned into the metallic phase and thus been sequestered in the core.

While this much is relatively clear, there remains vigourous debate regarding some of the details of core separation beyond this first-order approximation. It has, for instance, long been recognised that a single-stage low-pressure

differentiation event could not reproduce the elemental abundance pattern in the mantle today (e.g., Ringwood, 1966; Wänke, 1981). For example, mantle abundances of the slightly siderophile elements, such as V and Cr, indicate much more reducing conditions than the depletions of moderately or highly siderophile elements (e.g., Frost et al., 2008).

This led to suggestions of heterogeneous accretion models, in which the nature of accreting material changes with time, and the oxygen fugacity at which metal equilbration occurrs increases throughout accretion. (Wänke, 1981; O'Neill, 1991; Wade and Wood, 2005; Wood et al., 2006). O'Neill (1991) suggested a secondary, more oxidised stage of core formation in which the core-forming liquid was no longer metallic iron but a FeS sulfide (the "Hadean matte", see section 1.3.2 for a more detailed review).

Later in the 1990s, it was recognised that some elements become less siderophile with pressure, and that it was possible to reproduce the abundance pattern of many elements with a homogenous accretion model if metal-silicate partitioning had occurred at high pressures and temperatures (e.g., Li and Agee, 1996).

In figure 1.1, it can be seen that the highly siderophile elements (i.e., the platinum group elements or PGE) exist in chondritic ratios relative to each other (e.g., Day et al., 2016). Experiments to determine the metal/silicate partition coefficients of the PGEs, however, have found vastly different partitioning behaviour of the individual elements (Mann et al., 2012). In other words, there is no set of metal-silicate equilibration conditions that can reproduce the observed flat abundance pattern of the highly siderophile elements. These observations led to the suggestion that the PGEs must have been completely stripped from the mantle during core formation, and then subsequently replaced by the addition of more primitive, chondrite-like material that has been termed the "late veneer" (e.g., O'Neill, 1991).

As yet, no model can successfully reproduce every constraint and many details of the differentiation process remain uncertain, however the suggestion that high-pressure metal-silicate equilibration was a feature of core fomation has amassed a fair bit of supporting evidence (Li and Agee, 1996; Rubie et

al., 2003; Chabot et al., 2005; Siebert et al., 2013; Mann et al., 2009). Recent experimental work on sulfide/silicate partitioning behaviour of the highly siderophile elements has also provided further support for the Hadean matte (Laurenz et al., 2016; Rubie et al., 2016), though it should be noted that these possibilities are by no means mutually exclusive.

1.2 Redox evolution of the mantle

1.2.1 During differentiation

Iron is by far the most abundant element in the Earth that can exist in multiple oxidation states, namely Fe^0 (metallic iron), Fe^{2+} (ferrous iron, usually as FeO), and Fe^{3+} (ferric iron, usually as Fe_2O_3). Because iron is so prevalent, the relative abundances of the three possible redox states act to buffer the chemical potential of oxygen in a system, defined as the oxygen fugacity (fO_2), in effect establishing the fO_2 of the entire system (e.g., Frost, 1991). During the formation of the core, metallic iron was present in the mantle. Metallic iron imposes a relatively low oxygen fugacity, setting a level at or below the fO_2 of the iron-wüstite (IW) buffer, which can be determined from the equilibrium constant of the reaction

$$Fe + \frac{1}{2}O_2 = FeO \tag{1.1}$$

given by

$$K_{IW} = \frac{a_{FeO}}{a_{Fe} * fO_2}.$$

1.2.2 Modern upper mantle

Given that the Earth's mantle equilibrated with metallic iron, it could therefore be expected that mantle fO_2 would remain quite low. This is not the case, however. A large amount of work has been done to characterise the oxygen fugacity of the modern mantle, with a diverse suite of methods, and there is broad agreement that the mantle today is uniformly close to the Fayalite-Magnetite-Quartz (FMQ) buffer, which is defined by the reaction

$$3Fe_2SiO_4 \ + \ O_2 \ = \ 2Fe_3O_4 \ + \ 3SiO_2$$

olivine · · · magnetite · quartz
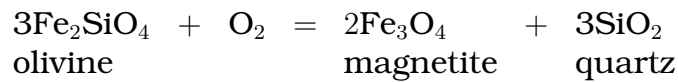
and shown in figure 1.2 to be 4-5 orders of magnitude greater than IW (e.g. Cottrell and Kelley, 2011).
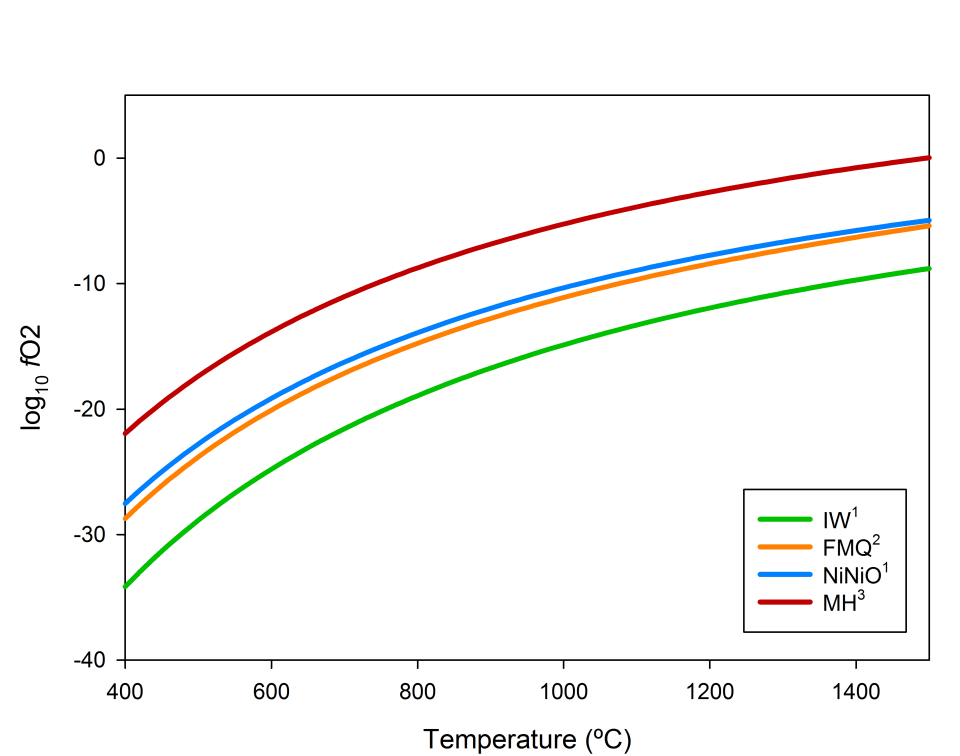
Figure 1.2: Oxygen fugacity of several commonly used buffer reactions as a function of temperature. IW = iron - wustite, FMQ = Fayalite - magnetite - quartz, NiNiO = nickel - nickel oxide, MH = magnetite - hematite. Data are from (1) O'Neill & Pownceby (1993); (2) O'Neill (1987); (3) Meyers & Eugster (1983).

Studies to determine the fO_2 of the mantle today have examined evidence from rocks that represent a partial melt of the mantle, such as mid-ocean ridge basalt (MORB), as well as mantle rocks such as spinel and garnet xenoliths, which were brought up from the mantle within a magma, and peridotite massifs, which are sections of the mantle that have become emplaced in the crust through tectonic forces. Oxybarometry, or calculating the oxygen fugacity of a rock's source magma, can be accomplished with a number of methods.

For MORB glasses, oxybarometry most commonly employs the ferric/ferrous ratio of iron present, which can be determined with an array of techniques,

including Mössbauer spectroscopy (e.g., Jayasuriya et al., 2004), X-ray Absorbtion Near Edge Structure (XANES) spectroscopy (e.g., Cottrell and Kelley, 2011) and wet chemistry methods (e.g., Christie et al., 1986). A number of experimentally calibrated thermodynamic models relating Fe^{3+}/Fe^{2+} and oxide mole fractions directly to fO_2 have been developed (e.g., Sack et al., 1980; Kress and Carmichael, 1991; Jayasuriya et al., 2004), and so the fO_2 of a glass can be reliably determined once the ratio of ferric to ferrous iron has been measured.

Several studies have applied this basic technique to a global data set of MORB glasses, and while there is some variation in the average fO_2 determined between the studies, the differences have been attributed to sampling and/or measurement biases (Bézos and Humler, 2005; Birner et al., 2018). More importantly, the studies have all unanimously confirmed that there does not appear to be any significant global redox variations of the mantle, implying that the entire upper mantle has an oxidation state that is near FMQ (Christie et al., 1986; Bézos and Humler, 2005; Cottrell and Kelley, 2011; Zhang et al., 2018).

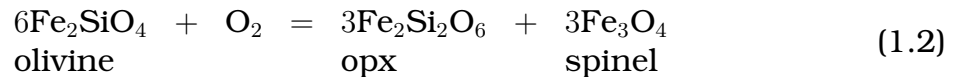For spinel peridotites, the fO_2 can be calculated from the equilibrium reactions of the iron-bearing components of the constituent minerals, e.g.:

$$
\begin{array}{ccccccc}
6Fe_2SiO_4 & + & O_2 & = & 3Fe_2Si_2O_6 & + & 3Fe_3O_4 \\
\text{olivine} & & & & \text{opx} & & \text{spinel}
\end{array}
\tag{1.2}
$$

The equilibrium constant of (1.2) can be rearranged to calculate the fO_2 given the activities of the components (Ballhaus et al., 1991):

$$
\log fO_2 = \frac{-\Delta G_r^0(1.2)}{\ln(10) * RT} + 3\log a_{Fe_2Si_2O_6}^{\text{opx}} + 2\log a_{Fe_3O_4}^{\text{spinel}} - 6\log a_{Fe_2SiO_3}^{\text{olivine}}
\tag{1.3}
$$

where ΔG_r^0 is the standard-state free energy change of reaction 1.2, T is the temperature, a_i is the activity of component i, and R is the universal gas constant. This and other oxybarometers have been calibrated in order to calculate the fO_2 of a rock based on composition measurements, obtained via electron probe microanalysis (EPMA) (e.g., Davis et al., 2017; Gudmundsson and Wood, 1995).

Regardless of the method used, for the upper mantle the result is universally close to FMQ (figure 1.3). This has further been confirmed by recent work (Birner et al., 2018), which has examined the fO_2 of MORB and peridodite that were sourced from the same region, the Southwest Indian Ridge. This allowed for a direct comparison of the two proxies, and verified that both record a consistent upper mantle fO_2 of approximately FMQ (Birner et al., 2018).
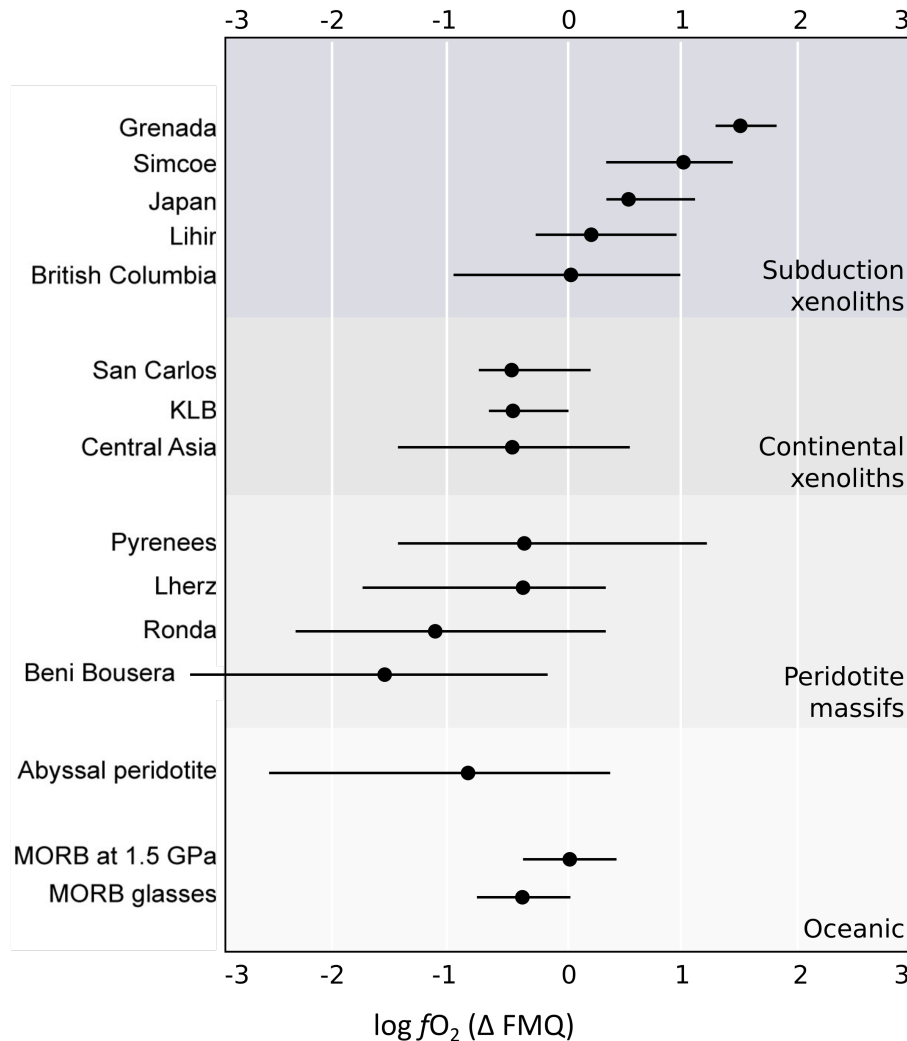

Figure 1.3: Redox state of the modern mantle, determined from peridotites and mid-ocean ridge basalt. As can be seen, the oxygen fuacity of all samples is within 1.5 log units of FMQ. Even the most reduced samples are several log units more oxidised than IW. Figure modified from Frost and McCammon (2008).

1.2.3 Oxidation state at depth

The oxyen fugacity of the mantle does, however, decrease with depth. As can be seen in equation 1.3, in a low-pressure spinel peridotite assemblage, the $f\mathrm{O}_2$ is dependent on the activity of the ferric iron component in phases with low modal abundance: spinel and to a lesser degree cpx and opx. In effect, the ferric iron is concentrated in relatively minor phases and as such the mole fraction and therefore also the activity of Fe^{3+} in those phases is relatively high. At about 200 km depth (6 GPa), however, garnet becomes increasingly stable, and replaces spinel as the primary host of Fe^{3+} (skiagite). Because the modal abundance of garnet continues to increase with depth throughout the transition zone (e.g. Wood et al., 2013), the skiagite component becomes increasingly diluted, decreasing its activity and thereby driving down the $f\mathrm{O}_2$ (Gudmundsson and Wood, 1995; O'Neill et al., 1993; Ballhaus, 1995; Frost and McCammon, 2008). Indeed, if the ratio of $Fe^{3+}/\sum Fe$ measured in the upper mantle today is constant throughout the mantle, i.e. if the mantle is compositionally homogeneous, by the depth of the transition zone, the $f\mathrm{O}_2$ should have decreased to the level of metal saturation (Rohrbach et al., 2007).

Below the transition zone, in the lower mantle, the dominant phase is MgSi perovskite, or bridgmanite. It has been experimentally shown that bridgmanite can accommodate a large amount of ferric iron in its structure, to the degree that it likely forced the disproportionation of FeO into Fe_2O_3 and Fe metal (see section 1.3.1 for a more detailed review) to create more ferric iron (McCammon, 1997; Lauterbach et al., 2000). If this is correct, then the $f\mathrm{O}_2$ can be calculated from the assumed compositions of the precipitated metal and coexisting ferropericlase and bridgmanite and experimentally determined activity coefficients, and has been determined to be between IW and IW-1.5 (Frost et al., 2003; 2004; Frost and McCammon, 2008). Thus the mantle today experiences a gradient in $f\mathrm{O}_2$, in which it is much more oxidised at the surface than at depth.

1.2.4 Timescale of oxidation

Even if the bulk of the mantle is today at metal saturation (i.e. at IW), to raise the oxygen fugacity of the upper mantle from IW to FMQ, FeO in the mantle would have to have been oxidised to Fe_2O_3 via the reaction:

$$2FeO + \frac{1}{2}O_2 = 2Fe_2O_3 \qquad (1.4)$$

As long as metallic iron was still present in the mantle, however, the fO_2 would have been buffered below the level of iron-wüstite, precluding reaction 1.4, at least at upper mantle pressures where the mantle interacts with the surface. Oxidised species, such as CO_2, H_2O, and Fe_2O_3 could not have coexisted with metal, as they would simply react with it and raise the bulk FeO content of the mantle. Fe_2O_3 could not have begun to accumulate in the upper mantle until it had oxidised to a level at which metallic iron is no longer stable (figure 1.4). The implication is that some process(es) oxidised the entire mantle after core formation had ceased. Furthermore, this increase in oxidation state appears to have occurred not only globally, but very rapidly.
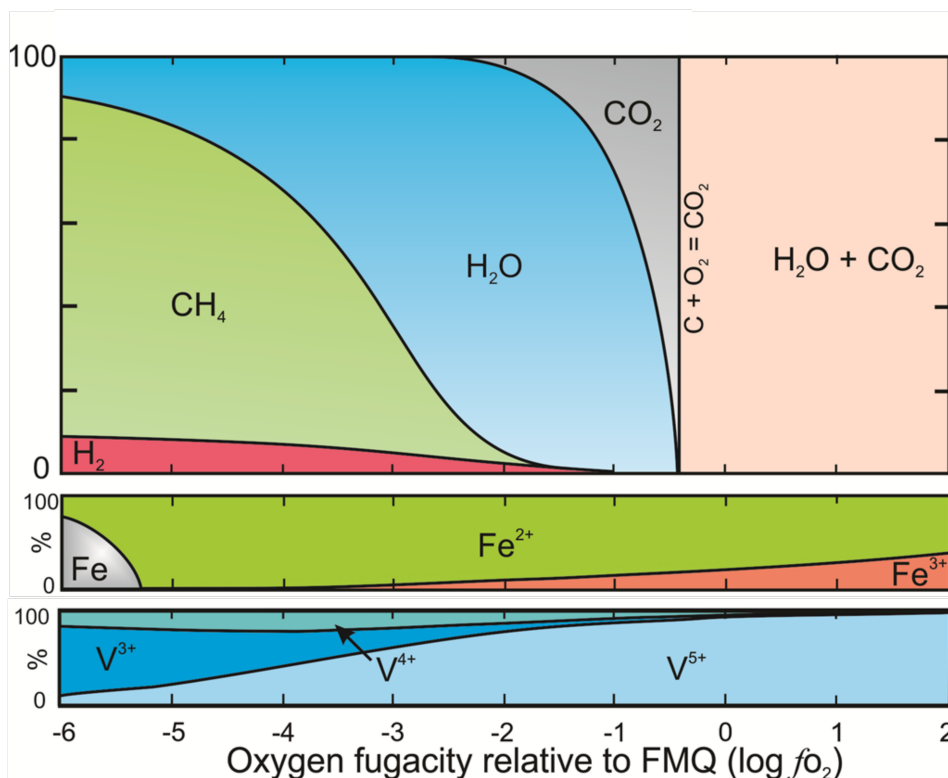
Figure 1.4: Changes in relative abundances of iron, vanadium, and volatiles as a function of oxygen fugacity. At the relatively low fO_2 imposed by iron metal, volatiles degassing to the atmosphere from the mantle would have been predominantly H_2 and CH_4, and ferric iron is essentially nonexistant. Iron and vanadium speciation within minerals can be used to determine the oxygen fugacity of the source magma, and have been used to conclude that the upper mantle has been at $\sim$ FMQ since the beginning of the geoloic record.

Due to aqueous alteration, ferric/ferrous ratios are an unreliable indicator of the oxygen fucagity of the source magmas of ancient rocks. Archaean mantle fO_2 can still be constrained, however, via oxybarometry techniques that exploit redox-sensitive but immobile elements, such as chromium and vanadium. Like iron, fO_2 determines the Cr^{2+}/Cr^{3+} ratio, but unlike iron this ratio is not susceptible to changing with aqueous alteration (e.g., Delano, 2001 and references therein). Canil (1997) used olivine/liquid vanadium partitioning to determine that the Archaean source mantle of several komatiites was close to FMQ, and this result has been repeated in several studies using a variety of techniques. Li and Lee (2004) showed V/Sc ratios to be a robust proxy for fO_2, and determined that Archaean basalt fO_2 differs from that of modern basalt

by less than 0.3 log units (Li and Lee, 2004). Lee et al. (2003) used vanadium systematics in peridotites to reach the same conclusion. Delano (2001) used whole-rock abundances of Cr and V and the composition of Cr-rich spinels to conclude that the mantle reached its current oxidation state by 3600 Ma, though suggests that even 3900 Ma is likely. Trail et al. (2011) proposed that cerium incorporation into detrital zircons could be used as a redox indicator for the Hadean mantle, and suggests that mantle had reached its present-day oxidation state by as early as 4350 Ma. Thus the problem is summarised in figure 1.5: after the end of core formation but before the start of the geologic record, some process(es) oxidised the mantle enough to raise the $f\mathrm{O}_2$ of the upper mantle from IW to FMQ.
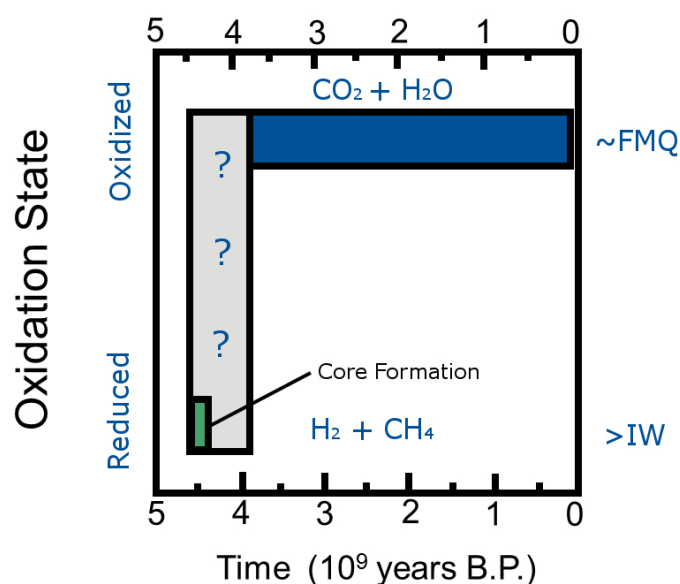
Figure 1.5: The Earth's mantle must have been reduced, with an oxygen fugacity at or below the iron-wüstite buffer, during core formation. Quickly thereafter, however, the upper mantle attained a much more oxidised state, through process(es) that remain unclear. Figure modified from Delano (2001).

1.3 Plausible mechanisms

The timing and mechanism of this increase in oxidation state are consequential not only to the understanding of the atmosphere, but also the proportion of volatiles accreted and retained to the growing Earth. The work presented

here explores the plausibility of two potential oxidation mechanisms.

1.3.1 Disproportionation in a deep magma ocean

The first process considered is built on the observation that pressure appears to stabilise the ferric iron component of lower mantle minerals, specifically bridgemanite. Experiments performed at the pressure/temperature conditions at the top of the lower mantle have indicated that bridgmanite can accommodate a high proportion of ferric iron in its structure, even when the experimental assemblage was in equilibrium with metallic iron and thus at the lowest plausible oxygen fugacity (Frost et al., 2004; Nakajima et al., 2012). This is in stark contrast to spinel and other lower-pressure phases, in which ferric iron content correlates strongly with oxygen fugacity (figure 1.6, Ballhaus, 1995).
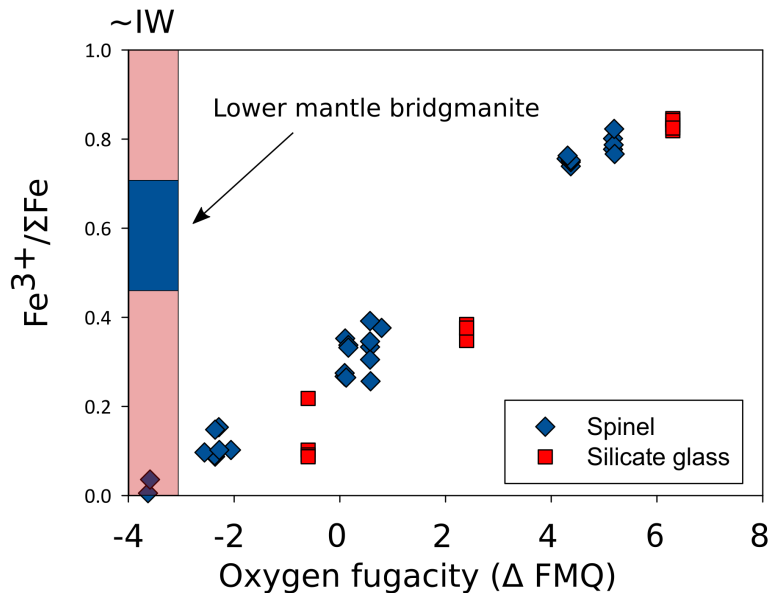
Figure 1.6: The ferric iron content of spinel (and other low-pressure minerals) is clearly dependent on the oxygen fugacity of its surroundings. In contrast, bridgmanite can contain large quantities of ferric iron even at low fO_2. Here silicate glass is shown to mirror the behaviour of minerals at low pressure; an aim of this study is to determine if silicate liquids also can accommodate more ferric iron at high pressure but low fO_2. Spinel data is from Ballhaus (1995), silicate glass data from Jayasuriya (2004) and bridgmanite data from Nakajima (2012).

The Earth's lower mantle is presumed to comprise bridgmanite (magnesium silicate perovskite) and ferropericlase, with the former dominating in terms of volume at 80% (Frost and McCammon, 2008). The unexpectedly high ferric iron content in bridgmanite is the result of an energetically favourable coupled substitution of Fe^{3+} and Al^{3+} for Mg^{2+} and Si^{4+} in the structure (Nakajima et al., 2012). If the lower mantle formed before the end of core formation, it would have formed from material poor in Fe_2O_3. Balancing the Al in the substitution implies that the additional Fe_2O_3 observed in the bridgmanite would have had to form through the disproportionation of FeO, i.e.

$$3FeO = Fe_2O_3 + Fe^0. \qquad (1.5)$$

This would have created ~ 1 wt % metallic iron in the lower mantle. I.e., if the mantle has a uniform bulk oxygen content, the lower mantle should contain metallic iron. Removing approximately 10% of this metallic iron towards the end of core formation (figure 1.7 below) would have left the lower mantle with proportionately more oxygen. Subsequent remixing of the whole mantle could have then raised the oxidation state of the mantle to its present value (Frost et al., 2004). This possibility is reliant on a mechanism that would have removed some of the precipitated metal from the solid mantle to the core. Though not implausible, a potentially simpler solution is possible if silicate melts mirror this behaviour and that an analogous process could have occured at depth within a global magma ocean.
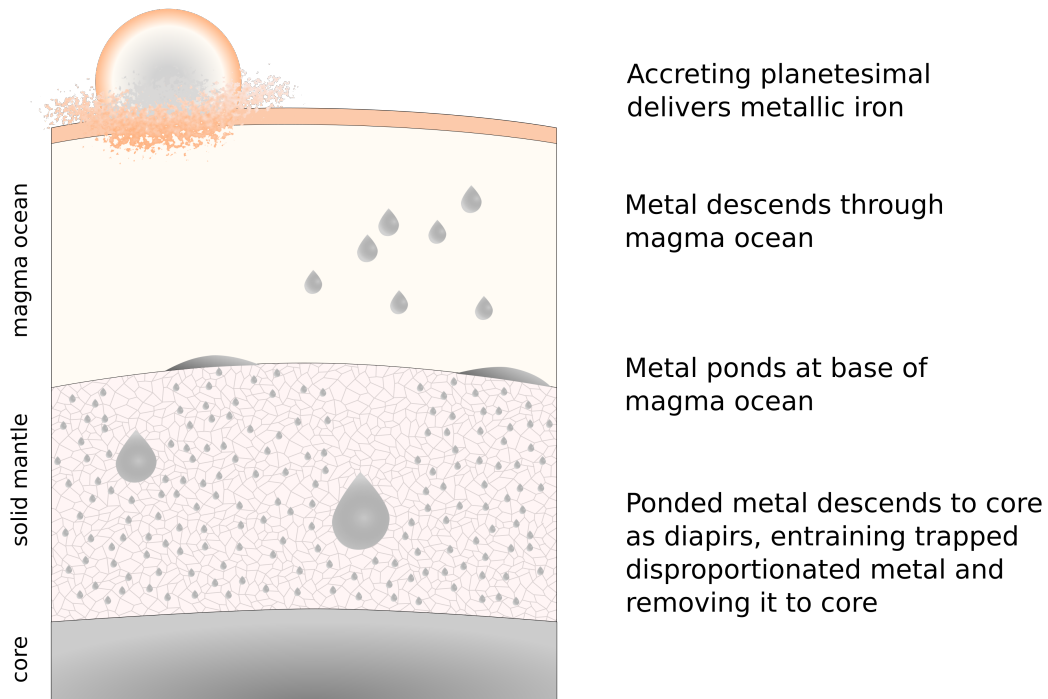
Figure 1.7: A plausible mechanism by which the mantle may have become oxidized. If some iron metal that formed via disproportionation in the lower mantle was removed to the core via decending diapirs, the end result would be a mantle with an elevated O/Fe ratio.

Plausible N-body simulations modelling planetary accretion have in common that the final stages of accretion are characterised by giant impacts between larger planetary embryos (e.g. Chambers, 2001). These collisions would have certainly been energetic enough to vaporise and/or melt a large fraction of the material and create global magma oceans (e.g., Tonks and Melosh, 1993; Rubie et al., 2011). Any metallic iron present, e.g. the core of the impactor, would descend through the molten silicate, equilibrating as it fell. The metal would accumulate in ponds at the top of the solidified mantle, which may be at lower mantle depths (see figure 1.7) (e.g., Rubie et al., 2003; Wade and Wood, 2005).

In this scenario, final metal-silicate equilibration in the Earth would have occured at high pressure/temperature conditions such as would exist at the base of a deep magma ocean. Indeed, this hypothesis is supported by several studies that have experimentally determined the pressure dependence

of metal/silicate partition coefficients of a number of elements (Li and Agee, 1996; Rubie et al., 2003; Chabot et al., 2005; Siebert et al., 2013; Mann et al., 2009).

Numerical models indicate that vigorous convection would mix the molten silicate on a timescale of weeks, and so a global magma ocean would have been homogenous in composition (Solomatov, 2000). If metal-silicate equilibrium occurred at high pressure, and ferric iron is stabilised with pressure, the ferric iron content of the entire, homogenised global magma ocean may have been much higher than the level that would be established through iron equilibration at lower pressure. If the initial silicate materal were low in ferric iron, the pressure effect may even force the disproportionation of FeO (as in equation 1.5) and, in a molten environment, the heavier precipitated iron could have more easily sank through to the base.

This implies that a deep magma ocean that is in equilibirum with iron metal (and therefore at or below IW) at its base may in fact contain an amount of ferric iron such that at the surface its oxygen fugacity, imposed by the ferric/ferrous ratio, is at FMQ (figure 1.8). Such a redox gradient as a function of depth in a magma ocean is an interesting possibility, as it reflects the $f\text{O}_2$ gradient that exists in the mantle today. This suggests that simply crystallising a deep magma ocean could have resulted in the redox state of the whole mantle as it is observed today (Frost and McCammon, 2008).
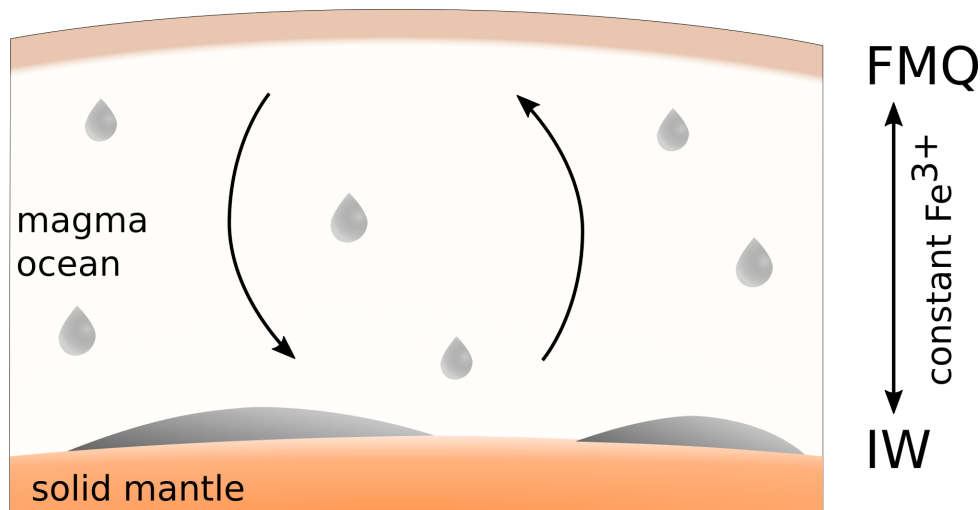
Figure 1.8: If metal-silicate equilibration occurred at the base of a magma ocean, and silicate liquids stabilise ferric iron with pressure, a deep magma ocean, kept homogenous by convection, may have a larger amount of ferric iron than low-pressure data indicate. As the oxygen fugacity of the system is set by the proportions of iron species, such a magma ocean may be at IW at its base but FMQ at the surface.

A testable feature of this hypothesis is that, if fO_2 can vary with pressure given a constant $Fe^{3+}/\sum Fe$ ratio, the reverse should also be true: at a constant fO_2, ferric iron content should vary with pressure. Experimentally, fO_2 is easier to hold constant than ferric iron content, and so it should be possible to test if ferric iron increases as a function of pressure at a constant fO_2. To date, experimental studies have explored the effect of pressure on ferric/ferrous ratios in silicate melts to 7 GPa (O'Neill et al., 2006; Zhang et al., 2017), and the trend is in fact the opposite: ferric iron decreases with pressure (figure 1.9).
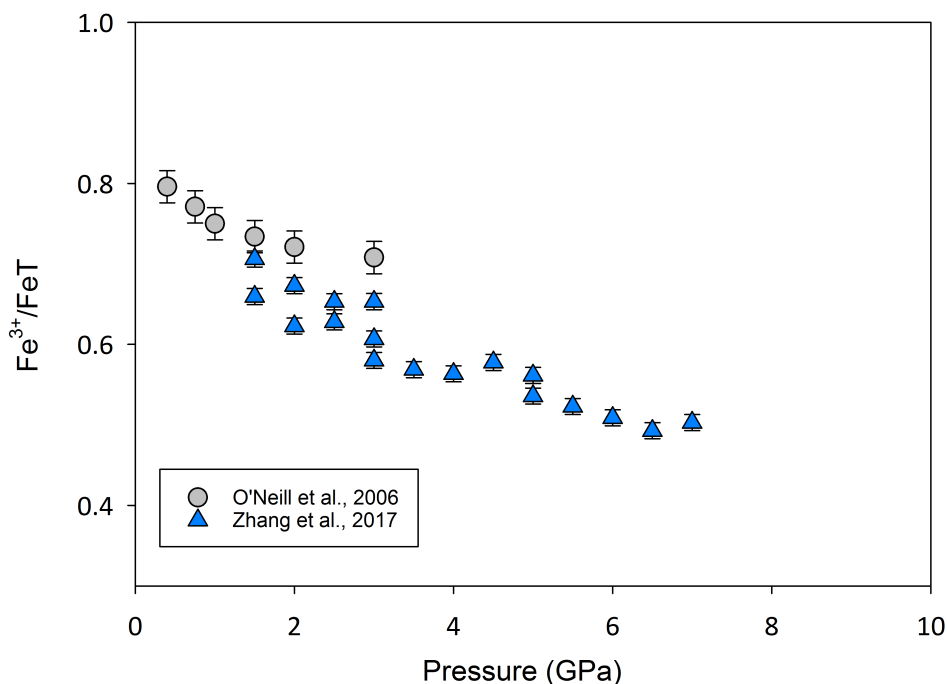
Figure 1.9: Literature data from experiments determining the effect of pressure on the ferric iron content of silicate melts. Clearly, to 7 GPa there is a negative trend. There is reason to suppose, however, that this trend may reverse at higher pressure (see text). Data from O'Neill et al. (2006) and Zhang et al. (2017).

However, as outlined in Hirshmann (2012), it's plausible that this trend may reverse at higher pressure. The reasoning is based around observations and *ab initio* predictions of liquid silicate structures. For one, the greater ability of high pressure minerals such as garnet and bridgmanite to accommodate ferric iron is largely due to the availability of high-coordination sites within their structures (O'Neill et al., 1993; McCammon, 1997; Frost and McCammon, 2008). Similar high-coordination environments, also favoring smaller cations, have been reported in silicate liquids (Ghiorso, 2004; Stixrude and Karki, 2005). In addition, 6-coordinated Fe^{3+} has a smaller partial molar volume than 4-coordinated Fe^{3+}. At high pressures, where 6-coordinated Fe^{3+} is more likely, the volume change of ferric-ferrous equilibrium would decrease and perhaps reverse with increasing pressure (Liu and Lange, 2006; Hirschmann, 2012).

If pressure stabilises the ferric iron component of silicate melts, as in minerals,

then high-pressure metal-silicate equilibration could result in a magma ocean with a higher ferric iron content than would be expected for low pressure metal equilibration. At the surface, a higher ferric iron content would have imposed a relatively high oxygen fugacity, such that the upper portions of the magma ocean may have been in equilibrium with more oxidised voltile species.

1.3.2 Gradual oxidation of the mantle through delivery of H_2O

It is possible that the mantle was oxidised simply through the delivery of more oxidised, water-rich material towards the end of accretion, but this possibilty has several constraints that must be satisfied. To raise the oxidation state of the upper mantle from IW to FMQ would have required the addition of 150 ppm H_2O throughout the mantle, or at least $9 \cdot 10^{20}$ kg of H_2O. This is just over half of the current hydrosphere, and from estimates of the probable mass of the "late veneer", this is a reasonable amount of water to have been added (Sharp et al., 2013).

If indeed the Earth's mantle was fully stripped of highly siderophile elements during differentiation, the concentration of highly siderophile elements in the mantle today provides a constraint as to the total mass accreted as the "late veneer", which is approximately 0.7% of the Earth's total mass (e.g. O'Neill, 1991). If this material was CI-like, which is 20 % water, this could have supplied enough water to oxidise the mantle and provide the hydrosphere. The late veneer, however, has been shown to be isotopically unlike CI chondrite, or, indeed any known chondritic material (Fischer-Gödde and Kleine, 2017).

An additional potential problem is reconciling the inferred rapidity of oxidation with the likely nature of this material. If it accreted as many small, primitive bodies it is unlikely to have mixed into the mantle quickly enough to account for the apparent speed of oxidation discussed in section 1.2.4 (Maier et al., 2009). Alternatively, one large impactor could account for the timescale of the oxidation, since a large enough accreting planetesimal would plunge deep into the interior and create a global magma ocean that would rapidly convect and homogenise. It is difficult, however, to explain how an impactor of that size could have retained its water and remained relatively oxidised. Chondritic me-

teorites that have experienced even small amounts of thermal metamorphism have water contents of $< 1\%$ (Huss, 2006). It thus seems unlikely that an oxidised, primitive body could have been large enough to mix into the early Earth rapidly.

A model similar to that of O'Neill (1991), could, however, loosen the constraint of a rapid timescale. This model suggests that during the early stages of accretion, Earth was forming from primarily reduced, volatile-depleted material (figure 1.10). As core formation proceeded, siderophile elements were completely stripped from the mantle and removed to the core. Then followed a gradual oxidation, through the addition of more oxidized and volatile-rich material, accounting for $\sim 11\%$ of the present Earth's mass. As this would have left the mantle with an overabundance of the highly siderophile elements (HSEs), this process is only plausible if core formation could have continued once the oxygen fugacity of the mantle had risen above the level where metallic Fe would have been stable, in order to continuously remove the HSEs (O'Neill, 1991). This implies the core-forming liquid would have been a liquid FeS sulfide, the "Hadean matte". Finally, the "late veneer" of chondritic material added back the highly siderophile elements after core formation ceased. Hence the mantle may have experienced oxidation over a longer time period than appears plausible from HSE abundances.
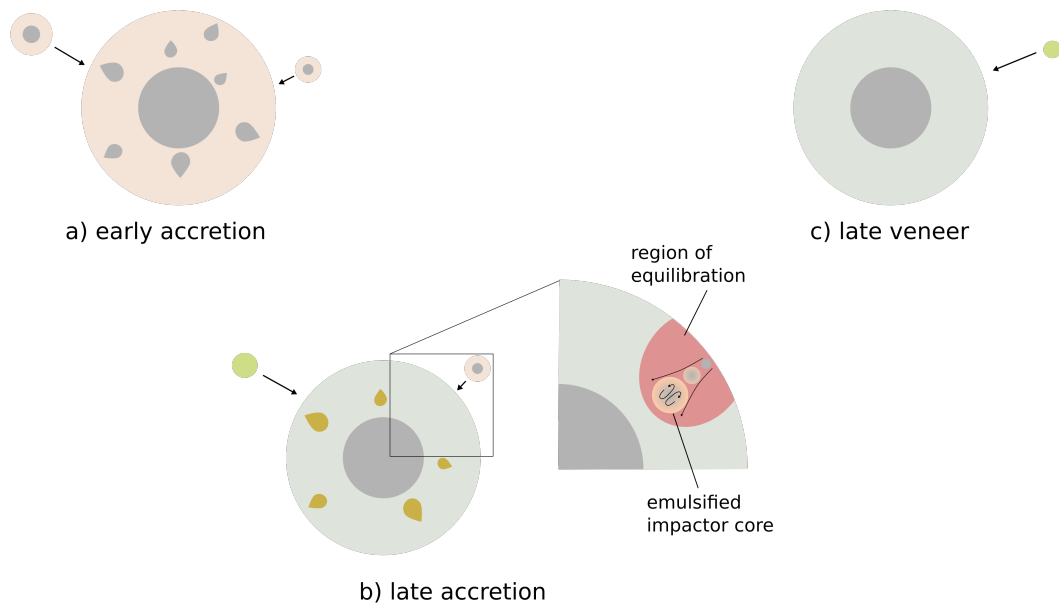
Figure 1.10: A model for the gradual oxidation of the Earth's mantle through the delivery of water. (a) In the early stages of accretion, the Earth was accreting from reduced material, metallic iron was present in the mantle which was therefore at or below IW. (b) More oxidised material delivers water from further out in the solar system. Core formation is ongoing, removing highly siderophile elements to the core. Once the oxidation state of the mantle rises above the level at which metallic iron is stable, the liquid descending to the core is an FeS sulfide. Any metallic iron delivered equilibrates only locally, allowing only part of the mantle to be reset to IW. (c) Finally, after core formation ceases, highly siderophile elements are replaced with the "late veneer".

The N-body simulation model of Rubie et al. (2015) provides some dynamical support for this idea. This model assumes that the Earth accreted from material that condensed at variable distances from the sun, and thus with different amounts of volatiles and at different oxidation states. The results of many simulations indicate that, in general, it would have been more likely for accretion to start with reduced material, and that more oxidized material would have been added towards the end (see figure 1.11). In addition, Rubie et al. (2015) have suggested that at late stages of core formation, when additional metallic iron is primarily added via the cores of differentiated accreting planetesimals, that metal may only have locally equilibrated with the mantle, thereby not necessarily resetting the redox state of the mantle to metal

saturation (see figure 1.10).
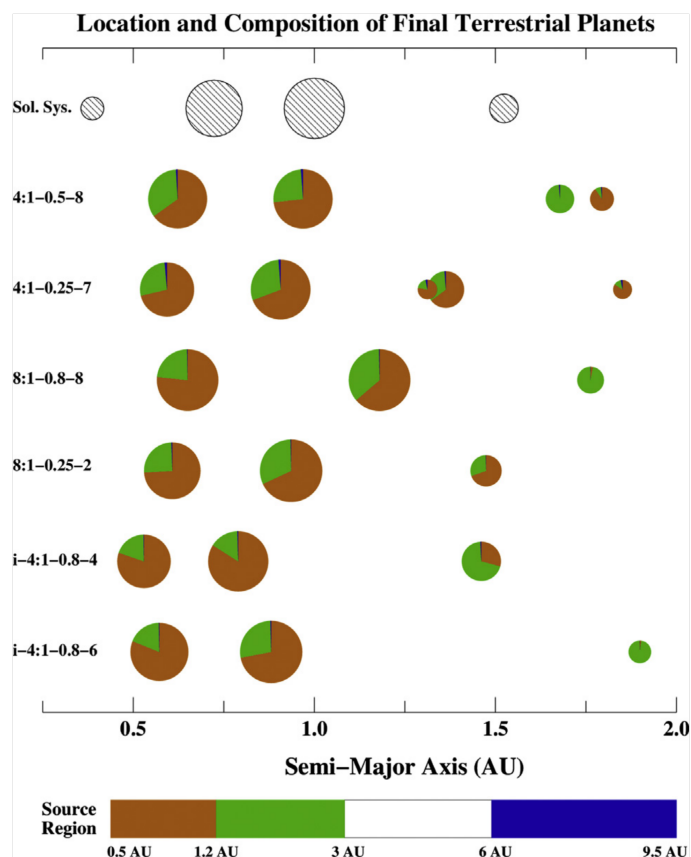
Figure 1.11: Results from six runs of an n-body accretion model, showing the proportions of the terrestrial planets that would have been sourced from different regions of the solar system. Note no material is sourced from between 3-6 AU because that region was cleared by Jupiter. In general, the material accreting during the early part of the simulation was from further in, and so presumably more reduced, with material from being farther out coming in later, after being gravitaionally excited. Figure from Rubie et al. (2015).

New work to characterise the isotopic signature of the late veneer may provide some additional support for this model. As mentioned above, Ru isotopes have been used to conclusively show that the late veneer could not have been derived from material similar to CI, has had previously been proposed (Fischer-Gödde and Kleine, 2017). More recently, a small observed offset in the $\Delta^{17}O$ between water in terrestrial and lunar basalt has been used to suggest that to satisfy the oxygen and ruthenium isotopic constraints, the best approximation for the late veneer is 80% enstatite chondrite and 20% CM chondrite

1 Introduction

(Greenwood et al., 2018). If correct, this implies that only about 5% of the Earth's water was delivered as the late veneer, and the Earth must have acquired much of its water over a longer time period, concurrent with accretion (Greenwood et al., 2018).

A potential problem with gradual oxidation though the delivery of water, however, is that it requires a mechanism to remove any hydrogen produced from the system. H is a powerful reductant, and if it remains in the system it will generally just reverse any oxidation reaction and reform into water. Sharp et al. (2013) envisaged a process by which water oxidises the mantle and H_2 is lost to space. One problem with this, however, is that the process of removing H, while leaving O behind, must have continued once the oxidation state has risen to a level where the degassing species would have been H_2O, which only minimally affects the redox state (Hirschmann et al., 2012). In addition, for hydrogen to be lost into an atmosphere from a magma ocean, the liquid silicate would have to be supersaturated in hydrogen, allowing bubbles to nucleate and form (e.g. Elkins-Tanton, 2012). According to Hirschmann et al. (2012), molecular hydrogen is only present in appreciable quantities at relatively high pressures (> 3 GPa); even at the relatively reducing conditions of $IW - 1$, at 0.1 GPa the ratio of $H_2 /$ ($H_2O + H_2$) is only $\sim 10\%$.

Another possibilty to remove H could be to sequester it into the core. If there was a core-forming sulfide metal present (the "Hadean matte"), hydrogen may have dissolved into the core-forming sulfide liquid, and thereby prevented from subsequently reducing other regions of the mantle. Previous work has shown hydrogen to be quite soluble in metallic iron, suggesting that a large amount of hydrogen could have been removed to the core during differentiation (e.g., Okuchi, 1997; Iizuka-Oku et al., 2017). However, again a potential problem is that this process must have been ongoing once iron metal were no longer stable. Hydrogen has been shown to be soluble in FeS sulfides (Shibazaki et al., 2011), and so this work will attempt to place constraints on the plausibility of whether hydrogen, delivered to the Earth as water, may have dissolved into an FeS melt and been lost to the core, leaving its oxygen behind in the mantle.

1.4 Approach

1.4.1 Accurate determination of oxygen fugacity within experiments

As described above, experimental studies of transition zone and lower mantle minerals have implied that ferric iron components may be increasingly stabilized with depth in the mantle. To fully characterize the thermodynamic stability of such components, however, we need to be able to measure their concentration at a known oxygen fugacity. Currently, the calculated fO_2 of any buffering reaction is relatively poorly constrained above 10 GPa. Few studies have attempted to determine the equation of state properties of the component phases at high pressures and temperatures, and large uncertainties remain. Campbell et al. (2009) used synchrotron X-ray diffraction to determine the thermal equation of state (EoS) properties of the metal-oxide pairs Fe-FeO and Ni-NiO in a multianvil press and laser-heated diamond anvil cells, to 80 GPa and 2500K (Campbell et al., 2009). These parameters were then used to calculate the fO_2 of the Fe-FeO and Ni-NiO buffers, however, the components of these and most other buffer reactions react extensively with the sample material, creating additional uncertainties in the imposed fO_2.

For high-pressure experiments in a multianvil apparatus, sample volumes are too small to solve this problem via techniques that segregate the buffer, such as the double-capsule. Ruthenium and ruthenium oxide, added directly into a capsule with the experimental charge, is an fO_2 buffer ($Ru + O_2 = RuO_2$) that offers multiple advantages (O'Neill and Nell, 1997; O'Neill et al., 2006; Zhang et al., 2017). Its equilibrium fO_2 is relatively high, so Fe loss into Pt capsules is minimised and both ferric and ferrous Fe are present in sufficient quantities to be conveniently measured in silicate phases. Both buffer phases remain pure, as neither reacts with minerals and are relatively insoluble in silicate melts. Additionally, adding the buffer directly into the capsule, as opposed to the double capsule technique, does not require a saturating OH-rich phase which limits experiment to relatively low temperatures and normally to water saturated conditions.

Calculating the absolute $f\mathrm{O}_2$ of the Ru-RuO2 equilibrium at high P/T requires accurate data on the compressibility and thermal expansivity of Ru and RuO_2; current available data for RuO_2 exist only to 3 GPa and 980 K (O'Neill and Nell, 1997). In addition, RuO_2 is known to undergo two phase transitions with increasing pressure and temperature (e.g., Haines and Léger, 1993; Haines et al., 1997) For this work, experiments to characterise the phase relations of RuO_2 and equation of state parameters of Ru and RuO_2 were performed in the large volume press at the Advanced Photon Source, Argonne National Laboratory, USA. X-Ray diffraction data was collected to determine unit cell parameters up to 25 GPa and 2400 K, i.e. conditions over which these redox techniques are potentially useful for multianvil experiments.

Experiments were performed with a 10/4 multianvil assembly design (see section 2.1), previously used successfully to 25 GPa and 2400 K at 13 ID-D, APS (e.g., Chantel et al., 2012). To heat the samples, a rhenium foil furnace was used, which had windows cut in to allow X-rays to enter the assembly in the horizontal direction and the diffracted beam to exit. For each experiment, pressure was first increased to a target, followed by heating to a peak temperature. X-ray diffraction measurements were then be collected on both the sample and the pressure calibrant materials (Au and MgO). Futher measurements were taken as temperature was dropped in steps to room temperature. The assembly was then compressed further at room temperature, and the temperature again raised for another cycle. These cycles were repeated to cover the required range of pressure and temperature (5 to 25 GPa and between 1000 and 2400 K). The P and T conditions were calculated using the P-V- T equations of state of the calibrant materials.

In chapter 3 I present a new phase diagram for RuO_2, as well as new PVT equations of state of Ru and RuO_2. These parameters are then used to calibrate the Ru-RuO_2 system for use as an interal oxygen fugacity buffer in order to use the Ru-RuO_2 buffer at conditions compatible with the transition zone of the mantle.

1.4.2 Disproportionation within a magma ocean

The possibility that a magma ocean that is in equilibrium with iron metal at depth may be in equilibrium with more oxidised species at its surface was explored with a series of high-pressure high-temperature experiments in a multianvil press. If this could be a plausible mechanism by which the mantle may have oxidised, the ferric iron component of silicate melts would become increasingly stabilised with pressure, as has been observed for silicate minerals.

As presented above in section 1.3.1, experiments to date, which have reached 7 GPa, have in fact indicated the opposite: that ferric iron content decreases with pressure. The first set of experiments has extended the datasets of O'Neill et al. (2006) and Zhang et al. (2017), in which an andesitic-composition melt is equilibrated with the Ru-RuO$_2$ oxygen fugacity buffer, to 23 GPa. This explores the possibility, suggested by Hirschmann (2012), that this trend will reverse at higher pressure and ferric iron will begin to be stabilised. Data from these experiments was used to derive a thermodynamic model that is valid to 23 GPa. Further experiments, with different compositions and at lower oxygen fugacities, explored the validity of the model at different conditions.

High pressures and temperatures were achieved with large-volume multianvil presses at the Bayerisches Geointitut. Most experiments were conducted with an 18/11 assembly (see section 2.1), although smaller assembly sizes were required to attain the highest pressures. Ferric iron content of the resulting samples were measured with Mössbauer spectroscopy. In chapter 4 I present experimental results that explore the effect of pressure on the stability of ferric iron in silicate melts at a constant fO$_2$, extending the dataset of O'Neill et al. (2006) and Zhang et al. (2017) to 23 GPa and discuss the plausibility of this mechanism to have oxidised the Earth's mantle.

1.4.3 Gradual oxidation of the mantle through water accretion

For this project, the possibility that the accretion of H$_2$O-rich material led to the gradual oxidation of the mantle was explored. This would have only

been possible provided that this process could have continued once the oxygen fugacity had risen above the level where metallic iron would be stable, implying that the core-forming material would have been an FeS sulfide. There is a fair amount of evidence that as the final magma ocean cool and crystallised, FeS may have exsolved (the "Hadean matte", e.g., O'Neill, 1991; Rubie et al., 2016) and been removed to the core.

In order to examine whether a Hadean matte could have removed hydrogen to the core, experiments were performed to equilibrate a mid ocean ridge basaltic melt with an FeS composition at 3 GPa, in multianvil presses at the Bayerisches Geoinstitut. The experiments contained 0.2 - 0.5 wt % H_2O, and graphite capsules were employed inside outer welded AuPd capsules to minimise water loss during the experiments. Experiments were run at 3 GPa to ensure that a silicate glass was produced upon quenching of the experiments. The resulting run products comprise a large pool of silicate glass and quenched FeS melt. The oxygen fugacity in the experiments was adjusted by changing the bulk FeO content of the silicates and by adding varying amounts of Fe to the experiments.

Hydrogen concentration of the run products was determined with elastic recoil detection analysis (ERDA), performed with a nuclear microprobe at CEA Saclay, France. Hydrogen partition coefficients for the experimental run products were then calculated and the resulting data were used to assess the potential oxidation of the mantle through interaction of H_2O and FeS in a primordial magma ocean. In chapter 5 I present results from hydrogen molten silicate/ liquid sulfide partitioning experiments and discuss the plausibility of water accretion as an oxidation mechanism for the mantle.

2 Methods

2.1 High-pressure experimental techniques

This thesis mainly describes experiments performed at high pressures and temperatures in multianvil presses. In a multianvil apparatus, high pressures are achieved with two stages of anvils to direct the force of up to 5000 tonnes of hydraulic force onto a small sample volume. The first large-volume high-pressure apparatus was developed during the 1950s by Tracy Hall, and featured a tetrahedral design (Hall, 1958). Some years later, the split-sphere multianvil design was introduced by Kawai and Endo (1970), which featured a steel sphere split into 6 wedge-shaped anvils. These were held in a pressurised oil reservoir, and contained an inner array of 8 tungsten carbide anvils. Pressure from the oil was directed through the 2 stages of anvils onto the sample. The design was later changed to supply pressure with a hydraulic press.

All experiments for this study were accomplished using presses of either this design (Kawai-type) or of a second type, introduced in 1991 (Walker, 1991) that features 6 outer cylindrical anvils, coupled with the same array of 8 inner tungsten carbide anvils. Further details as to the history and design of the multianvil apparatus can be found in the literature (e.g., Keppler and Frost, 2005; Liebermann, 2011).
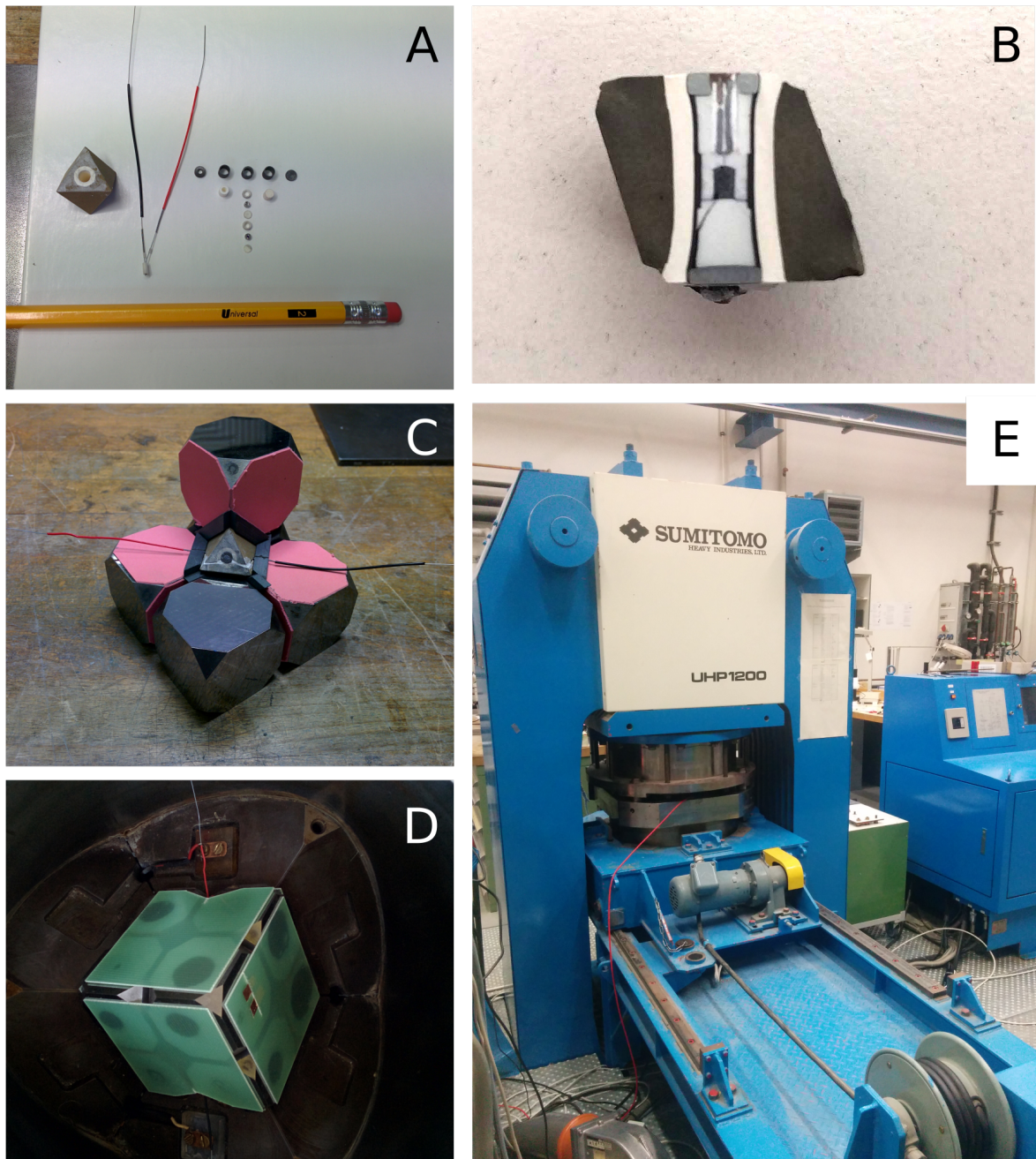
Figure 2.1: The experimental setup of a multianvil press apparatus. (A, B) The sample, along with cylindrical heating elements, MgO spacers, and a thermocouple is placed in an octahedral pressure medium. (C) This is surrounded by an array of 8 tungsten carbide cubes, which have truncated corners (3 cubes missing to show the geometry). (D) This array of cubes is placed in the press, with epoxy sheets insulating the cubes from the outer steel anvils. (E) The hydraulic press compresses the entire setup.

The 8 inner tungsten-carbide anvils have precisely machined truncations of their corners, such that when placed in a cubic array an octahedral cavity is

created in the center, which is where the high-pressure assembly is placed (figure 2.1). The sample is contained within an octahedral pressure medium, which for all experiments performed for this work was made of MgO doped with 5 wt% Cr_2O_3. The octahedron has a hole drilled through, which is fitted with a zirconia sleeve, into which the sample, heating element and a thermocouple are placed. The different experimental requirements called for small variations in the setup within the assembly, and so further details (including figures) of each setup are given in the individual chapters.

Pyrophilite gaskets and the pressure medium itself flow under pressure, creating a quasai-hydrostatic pressure on the sample. Further details of the multianvil technique, including pressure calibrations, can be found in Kawai and Endo (1970), Walker et al. (1990), Rubie (1999), Frost et al. (2004b) and Keppler and Frost (2005). Four different presses were used for this work, with varying maximum loads of 500, 1200, and 5000 tonnes. Three are at the Bayerisches Geoinstitut, and the fourth is installed at beamline 13-ID-D at the Advanced Photon Source (APS), Argonne National Laboratory for use with synchrotron radiation.

A variety of assembly sizes and tungsten carbide anvil truncation edge lengths were used for this study, the most common being an "18/11", which indicates an 18-mm edge-length octahedron, used with tungsten-carbide cubes with 11 mm corner truncations. In the 500 (Walker-type, Voggenreiter) and 5000 (Kawai-type, Zwick) tonne presses, this setup can produce pressures up to 6 and 18 GPa, respectively. For higher pressures (up to 23 GPa), 10/4 and 10/5 assemblies were used. The pressure calibrations employed were those routinely used at the BGI, and are based on univariant phase transitions that occur at known pressures and temperatures. Frost et al. (2004b) contains details on the pressure calibration of the 5000 tonne Zwick press, and calibrations for the other presses are reported in Keppler and Frost (2005).

Heating was achieved through the use of both conductive (graphite or rhenium) and resistive (lanthanum chromite) heaters, depending on the experimental conditions. Temperature is increased by raising the current that is passed through the assembly, and quenched by shutting off the power. For all experiments except those performed at the APS (see chapter 3 for details of

the setup used at the synchrotron), temperature was monitored with an axially inserted, $W_{97}Re_3$ - $W_{75}Re_{25}$ (type D) thermocouple, in which the wires are held in a 4-bore alumina tube. For experiments during which a thermocouple failed, temperature was estimated from previous temperature-power relations from experiments performed with the same type of assembly.

2.2 Analytical techniques

2.2.1 Scanning electron microscopy

In almost all cases, recovered samples were mounted in epoxy, polished, and carbon coated (~ 12 nm thick carbon layer) for examination with the scanning electron microscope (SEM). This instrument (Leo Gemini 1530 at the BGI) was primarily used to evaulate physical properties such as the texture, grain size, and proportion of melt, although qualitative chemical information was also obtained.

Scanning electron microscopes function by rastering an incident electron beam over the sample, which excites atoms within a teardrop-shaped interaction volume. Secondary, auger, and backscatter electrons are produced as a result, only the latter of which was used for this study. X-rays are also emitted from the sample which are used for element identification and qualitative chemical analyses. Many resources detail this technique, for example Reed (2005).

Backscattered electrons (BSE) originate from the incident electron beam, and are scattered by the nuclei of target atoms within the interaction volume. Heavy elements more reliably scatter the incident electrons, and, as such, appear brighter in a resulting image. BSE can therefore be used to image very subtle changes in chemistry throughout a sample. Backscattered electron images were taken of samples in this study to assess sample attributes such as to what degree melting had occurred, textures of any resulting quench assemblage, whether a sample had been contaminated, and whether equilibrium had been attained.

Characteristic X-rays are also produced when electrons from the incident

beam interact with electrons of target atoms, exciting them to higher-energy orbitals. When the electron reverts to its lower-energy orbital, an X-ray photon is emitted which can be detected with energy dispersive or wavelength dispersive spectroscopy (EDS or WDS). For this study, EDS was used to make qualitative determinations of composition, allowing for phase identification, and assessment of equilibrium. In addition, EDS mapping was used, in which chemical data was taken over a large area, allowing for subtle changes over the sample area to be seen.

2.2.2 Electron probe microanalysis

Quantitative determination of the composition of all samples, which were polished and carbon coated (as described above) was performed with a five-spectrometer Jeol JXA 8200 electron microprobe. This instrument uses a tungsten filament to generate an electron beam, which is then focused and accelerated to the sample. Incident electrons interact with sample atoms within an interaction volume, exciting the electrons of target atoms which then emit characteristic X-rays when they fall back to a lower-energy shell. The electron probe uses wavelength dispersive spectroscopy (WDS), for which emitted X-rays are collected by crystal spectrometers, sorted by wavelength, and counted, giving a quantitative analysis (e.g., Reed, 2005).

A WDS spectrometer uses the Bragg relation (see section 2.2.3) between wavelength, angle of incidence, and layer spacing (d-spacing) within a crystalline "filter" (diffraction crystal) to allow X-rays of certain wavelengths to constructively interfere, and suppress others. Limitations from the geometry of the spectrometer itself impose a limit on the angle of incidence, such that it cannot be varied enough to cover the entire range of wavelengths needed. Therefore, multiple spectrometers with crystals of differing d-spacing are used. X-rays that successfully pass through the filter enter a chamber, where they ionise a gas. A potential difference arises between the chamber walls and an insulated wire, which creates a current that is proportional to the energy of the X-Ray (e.g., Reed, 2005).

For each element, the ratio of emitted X-ray intensity compared to that emit-

ted from a standard of known composition is proportional to the concentration of the element in the sample. However, some complications arise from effects that occur as the emitted X-rays further interact with other atoms of the sample. Figure 2.2 shows the variation in interaction volume within a sample arising from incident beams of variable accelerating voltage. Most geological analyses are performed with 15 keV, as some important elements would not be excited by a lower voltage and would therefore not be counted. The consequent larger interaction volumes may therefore include phases other than the phase of interest if grain sizes are small. In addition, artefacts may arise from even from a sample with homogeneous composition as electrons interact with sample atoms . Various "matrix correction" routines have been developed to account for these types of interactions, and error is further diminished by appropriate selection of a standard which is as similar as possible to the unknown. All analyses in this work were matrix corrected with the phi-rho-z correction routine (see e.g., Reed, 2005).
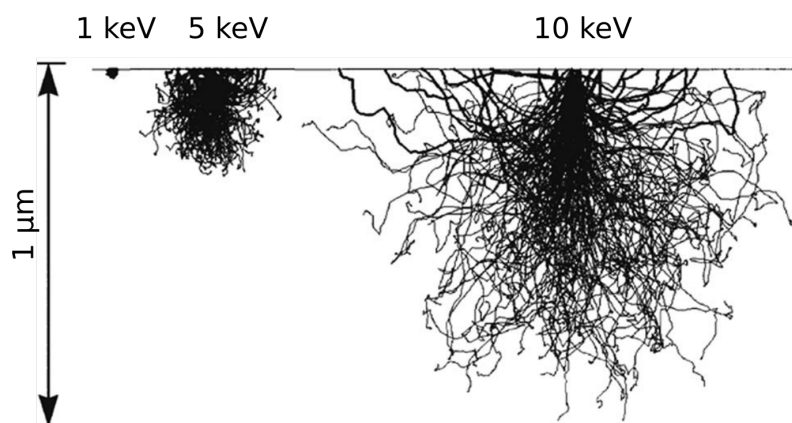
Figure 2.2: Volumes within a sample that are excited by incident beams of variable energy. Image adapted from Rinaldi and Llovet (2015).

Unless otherwise noted in the chapters, analyses were carried out with an accelerating voltage of 15 keV, though beam current and diameter were changed depending on what was most suitable for the sample in question. The spectrometers used for this study were TAP (thallium acid phthalate), PETH (pentaerythritol), LIF (lithium fluoride), and LDE2 (layered dispersion element). Standards used to calibrate the elements were as follows: Si- enstatite; Mg -

forsterite; Al: spinel; Ca: wollastonite; Fe, Ni, Ru: pure metals; Cr: Cr2O3; Ti: rutile; Na: albite.

2.2.3 Synchrotron X-ray diffraction

Crystalline materials comprise arrays of atoms in a regular repeating pattern. X-ray diffraction (XRD) is a technique by which the parameters of this regular array may be deduced, thereby allowing for the determination of crystal structure, unit cell volume, and changes to these with pressure and/or temperature. A beam of monochromatic X-rays (X-rays are used because their wavelength is similar to atomic spacing, which is necessary for diffraction) is focused on the sample, and these incident X-rays interact with the atoms within the sample. The atoms of the sample scatter the incoming X-rays, and because the atoms are aligned and regularly spaced, the scattered waves are likewise regular. These scattered waves will constructively interfere according to Bragg's law:

$$n\lambda = 2d\sin\theta$$

where λ is the wavelength of the incident X-rays, d is the atomic spacing, and θ is the angle of incidence (see figure 2.3). When n is a whole number integer, the scattered waves will constructively interfere and produce a diffraction pattern. The resulting spectrum can then be used to define the crystal structure. A vast amount of literature details the technique (e.g., Cullity, 2001).
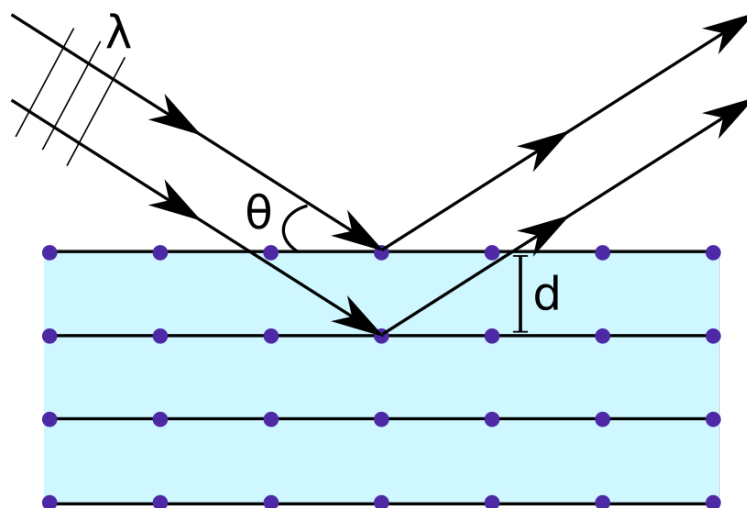
Figure 2.3: X-ray diffraction is a technique by which incident X-rays, of wavelength λ, strike the sample and are diffracted by the array of atoms that comprise a crystalline lattice. Diffracted rays constructively interfere and can be analysed for information on the crystal structure according to Bragg's law (see text).

For this work (detailed in chapter 3), XRD was performed with synchrotron radiation at the 13-ID-D beamline of the Advanced Photon Source (APS), Argonne National Laboratory. Powder X-ray diffraction data were collected using an energy-dispersive system at a diffraction angle of 6.1°, which was calibrated at room pressure using the diffraction patterns of Au and MgO. Images were acquired by placing A YAG (yttrium aluminium garnet) phosphor crystal in the beam path behind the sample to convert transmitted X-rays into visible light, which was then collected with a charge-coupled device (CCD). Diffracted rays were collected with a solid state detector. Figure 2.4 shows a schematic of the setup.
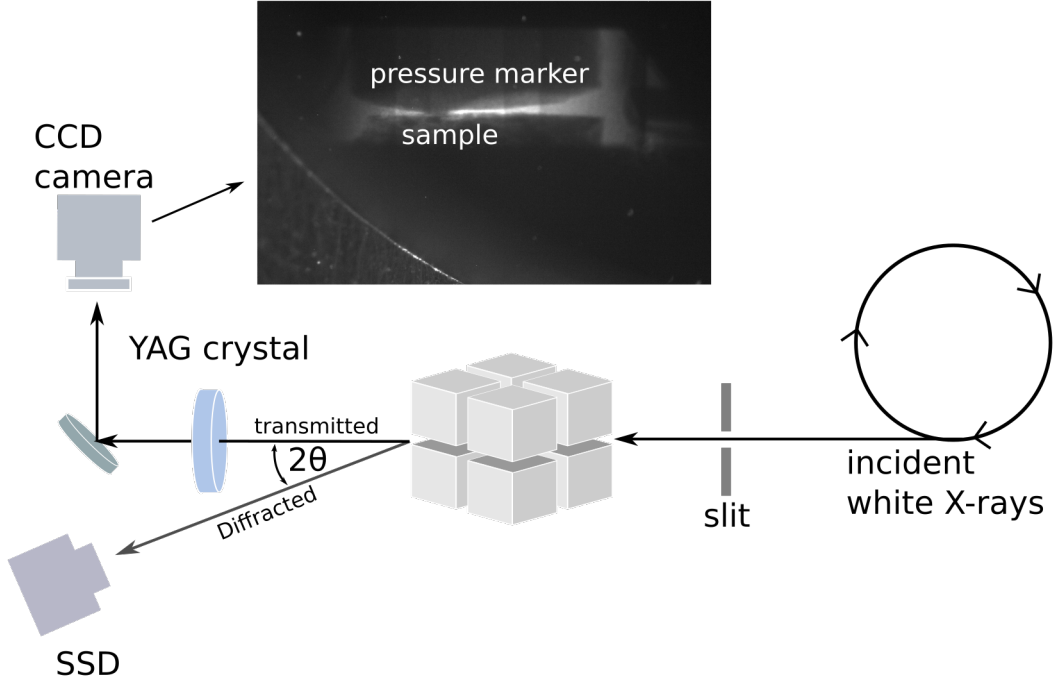
Figure 2.4: Schematic of the experimental setup used to collect diffraction patters at the APS.

Pressure was determined using measurements of the unit-cell volumes of Au and MgO and employing equation of state parameters of Tsuchiya (2003) and Dewaele et al. (2000), respectively, which are given in table 2.1. Total pressure is given by $P(V) = P_0(V) + P_{th}$, where $P_0(V)$ is the pressure calculated at room-temperature, and P_{th} is a thermal contribution to pressure. For this study, a room-temperature third-order Birch-Murnaghan was employed in conjunction with a Debye-Mie-Grüneisen model to account for the effect of temperature. The third-order Birch-Murnaghan is given by:

$$P_0(V) = \frac{3}{2}\kappa_0 \left[\left(\frac{V_0}{V}\right)^{7/3} - \left(\frac{V_0}{V}\right)^{5/3} \right] \cdot \left(1 + \frac{3}{4}(\kappa_0' - 4) \cdot \left[\left(\frac{V_0}{V}\right)^{2/3} - 1 \right] \right)$$

where V_0 is the volume at ambient conditions, and κ_0 and κ_0' are the isothermal bulk modulus and its first derivative, respectively. The Debye-Mie-Grüneisen formalism for thermal pressure is given by:

$$P_{th}(V,T) = \frac{\gamma}{V} E_{th}(V,T)$$

where γ is the thermodynamic Grüneisen parameter. E_{th} can be computed using the quasai-harmonic Debye model:

$$E_{th}(T, \theta_D) = 9nRT \left(\frac{T}{\theta_D}\right)^3 \int\limits_0^{\theta_D/T} \frac{x^3}{e^x - 1} dx$$

where θ_D is the Debye temperature, $n = 1$ for Au and $n = 2$ for MgO, R is the universal gas constant, and T is the temperature. A volume dependence for γ is assumed such that $\gamma = \gamma_0(V/V_0)^\zeta$ (e.g., Poirier, 1991). The values of θ_D, ζ and γ_0 have been calculated from first principles for Au by Tsuchiya (2003), and refined from data by Dewaele et al. (2000) for MgO (table 2.1). P_{th} was thus calculated as:

$$P_{th} = \frac{\gamma}{V} E_{th}(V, T) - E_{th}(V, T_0)$$

where T_0 is a reference temperature, here 298 K.

Table 2.1: Equation of state parameters for Au and MgO as determined by Tsuchiya (2004) and Dewaele (2000) used to calculate the experimental pressure.

	κ_0 (GPa)	κ_0'	γ_0	ζ	θ_0 (K)
Au	166.7	6.12	3.16	2.15	180
MgO	161	3.94	1.45	0.8	800

2.2.4 Mössbauer spectroscopy

Determinations of iron oxidation state were integral to the work presented here, and all measurements were made with transmission Mössbauer spectroscopy. This technique uses a radioactive source to produce gamma (γ) radiation, which is transmitted through the sample. Some of the γ rays are absorbed and re-emitted by atoms of the target material, while the remainder pass through the sample without interacting and are collected by a detector behind the sample (see figure 2.5). Therefore, the spectrum that is produced records dips in the count rate, at discrete energies that were absorbed (e.g., Dyar et al., 2006).

Atoms can only absorb and emit gamma rays at certain discrete, quantized energies, and so the source must emit radiation that is at the necessary energy

for the isotope of interest. In the case of iron, a source of ^{57}Co is conventionally used. Radioactive sources emit monochromatic gamma rays; i.e., at a fixed energy. This value can, however, be modulated by moving the source (or the target) and thereby Doppler-shifting the emitted γ radiation. Thus, gamma rays with a range of energies can be transmitted through the sample, and the detector can record count rate as a function of the source velocity (e.g., McCammon, 2004; Dyar et al., 2006).
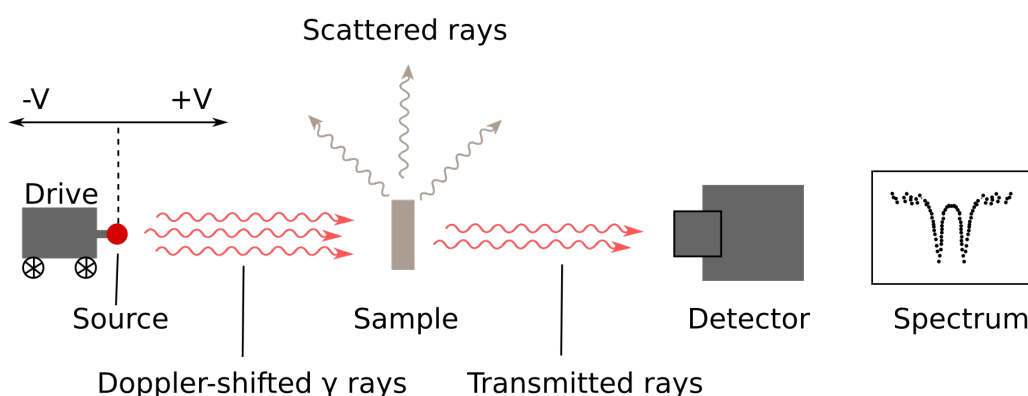
Figure 2.5: Cartoon of a Mössbauer spectrometer. The radioactive source is mounted on a drive, moving it relative to the sample and thereby Doppler-shifting the incident γ rays. Some of the atoms in the sample scatter the incident waves, so the detector behind the sample records only transmitted rays; the signal is in the absence of the rays that were scattered. Figure adapted from Dyar et al. (2006) and McCammon (2004).

Further, the energies that are absorbed can be modified (shifted or split) depending on the specific environment (coordination, number of electrons, symmetry of the site) of the iron nucleus in the sample. This is a result of interactions between the nucleus and electrons, or the hyperfine interaction (e.g., Dyar et al., 2006). The result is a spectrum that can be used to determine valence state, spin state, and coordination of the target atoms.

Mössbauer spectra comprise sets of peaks, usually Lorentzian doublets and sextets, the shapes of which are dependent on the hyperfine parameters from every structural site occupied by iron in the sample. The primary hyperfine parameters used are the isomer centre shift and quadrupole splitting. The former is a shift of the peak energy absorbed (relative to α-Fe), and falls into a defined range as a result of coordination, valence state, and spin state (Ban-

croft et al., 1967; McCammon, 2004). The latter is a split of a single peak into a doublet, and reflects an asymmetry of valence electron charge distribution, as well as non-cubic symmetry in a crystalline lattice (Ingalls, 1964; McCammon, 2004). Fitting a spectrum involves deconvolving the sum spectrum into its component doublets and sextets, which are each then assigned to Fe^{3+} or Fe^{2+} depending on the hyperfine parameters determined from them (Figure 2.6). Fe3+ / $\sum$Fe is then determined from the relative areas beneath the component spectra.
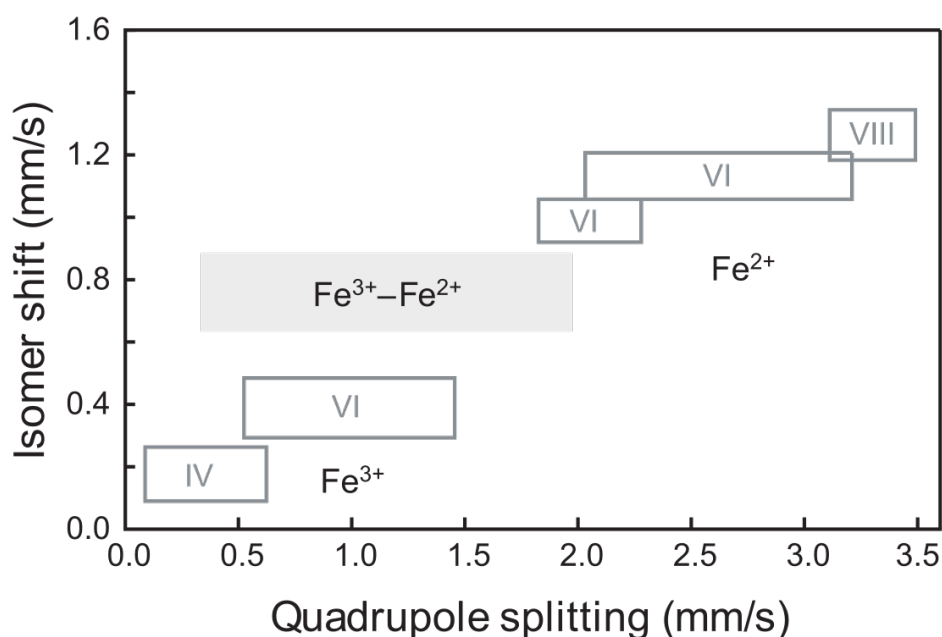
Figure 2.6: Assigning a component subspectrum to Fe2+ or Fe3+ is accomplished with the values of the hyperfine parameters. Figure adapted from Dyar et al. (2006)

Spectra can be quite complicated, with several sets of overlapping peaks. It may not be possible to determine a unique solution (McCammon, 2004). For this study, this work of fitting the spectra was done with the MossA software (Prescher et al., 2012). This program allows for a visual inspection of the spectrum, enabling the user to define parameters of the subspectra that are physically plausible. Deviations in a subspectra could be accounted for by effects such as site distortion, preferred orientation, or a signal from iron in another crystallographic site (McCammon, 2004). The proper selection of a model can effect the final result, and care must be taken to account for not

only a good fit of the model to the data but ensuring that the result is physically possible (Prescher et al., 2012). If possible, additional constraints from other analysis techniques (e.g. to determine the identity of the phases present) may be necessary.
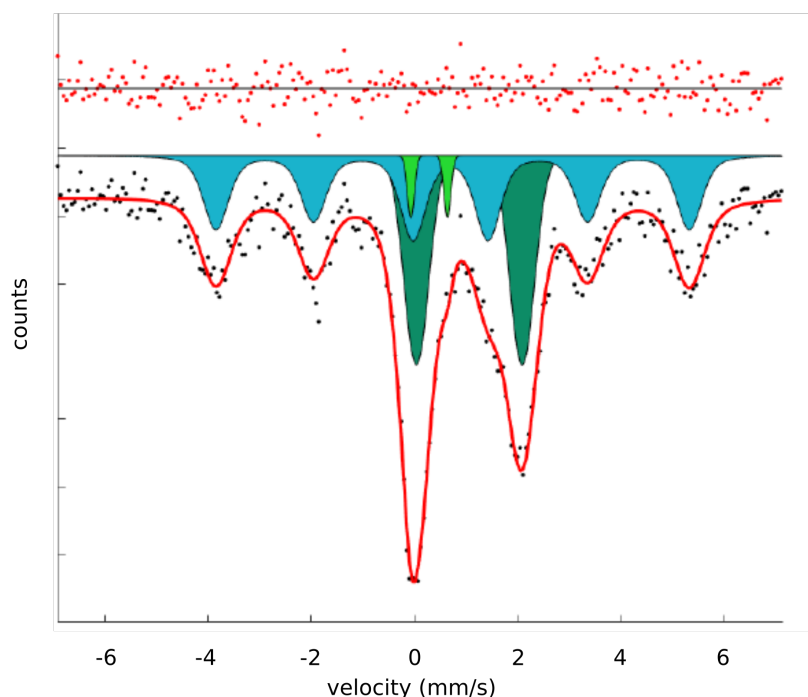
Figure 2.7: Example of a Mössbauer spectrum collected for this study (chapter 5). Evident in the spectrum is a sextet from the iron in the FeS sulfide, as well as two doublets, assigned to Fe^{3+} (light green) and Fe^{2+} (dark green) based on their centre shift and quadropole splitting.

Many of the samples analysed for this study were quenched silicate glasses. Glassy and other amorphous materials do not have a repeating structural array, so the sites that contain iron are therefore locally less regular and more distorted. This generally manifests as a broadening of the spectra obtained from amorphous samples. The hyperfine parameters obtained, however, arise from interactions of the iron nucleus with atoms up to two coordination shells out, and so structural information can still be obtained.

As for crystalline materials, the relative areas of the subspectra are used to determine the site abundances. Due to the broadening of the spectra, however, this procedure is more sensitive to an appropriate choice of fitting model. For example, a broad spectrum can be fit by adding successive Lorentzian lines

for multiple quadrupole doublets until a fit is achieved. Another approach assumes hyperfine parameters, and then solves for their probability (Vandenberghe et al., 1994), thus finding the most likely set of Lorentzian doublets to fit the data. A third technique is built on the approximately Gaussian distributions of hyperfine parameter probabilities, and so spectra are fit using sums of Gaussian (Rancourt and Ping, 1991). Whichever technique is used, the centre shift and quadrupole splitting of each doublet can then be used to determine relative abundance of Fe^{3+} and Fe^{2+} as described above for crystalline material (McCammon, 2004).

Broadening of the spectrum can also occur if the sample is not prepared adequately. The optimum thickness for a sample depends on the chemical composition, as there are trade-offs between signal strength (for which more iron is better) and nonresonant scattering which creates noise. For the compositions used in this study (~ 10 wt % FeO), samples were thinned to ~ 500 μm, giving an apparent thickness of ~ 10 mg Fe/cm^2 (Long et al., 1983). For this work, all spectra were taken at room temperature on a constant acceleration Mössbauer spectrometer in transmission mode. The velocity scale was calibrated by collecting a spectrum from Fe foil at the same conditions of measurement.

2.2.5 Elastic recoil detection analysis

Quantitative analyses of hydrogen in quenched sulfides and silicate melts were obtained with elastic recoil detection analysis (ERDA) performed at with the nuclear microprobe at the Laboratoire Pierre Süe, Commissariat à l'énergie atomique (CEA) Saclay, France (Barbour and Doyle, 1995; Raepsaet et al., 2008; Bureau et al., 2009; Withers et al., 2012).

This analysis is performed with an incident beam of helium (^{4}He$^+$), which is focused onto the polished and carbon-coated sample. The incident beam interacts with hydrogen in the sample, and the resulting elastic recoil ejects the hydrogen from the sample, and it can then be detected. Care must be taken to ensure that the sample remains as dry as possible before the analysis, and all sample polishing is performed with ethanol rather than water.

The incident beam of the nuclear microprobe at CEA Saclay is powered by a 3.75 MV Van de Graaff accelerator; the instrument is described in detail by Khodja et al. (2001). The incident beam cross-sectional area where it hits the sample is 4×4 μm^2, however the sample is tilted at $75°$ for the analysis, and so the area of the incident beam on the sample is about 4×16 μm^2. For this study, The beam was scanned over areas of about 100×100 μm^2 to obtain maps, which increase the statistics.

Three detectors were used simultaneously to obtain the analysis. Particle-induced X-ray emission (PIXE) is used to determine trace element content and is used to select the area of interest. Another collector detects Rutherford backscattering of incident particles (RBS) and is used to detect major and minor elements of the sample. Finally, the ERDA detector collects the ejected hydrogen. An analysis with the RBS detector is first made to determine sample composition, with the sample normal to the incident beam, and combined with PIXE to select the region of interest. The sample is then tilted to $75°$, which allows for the forward ejection of H particles by the incident beam, and the ERDA analysis is performed (see figure 2.8).
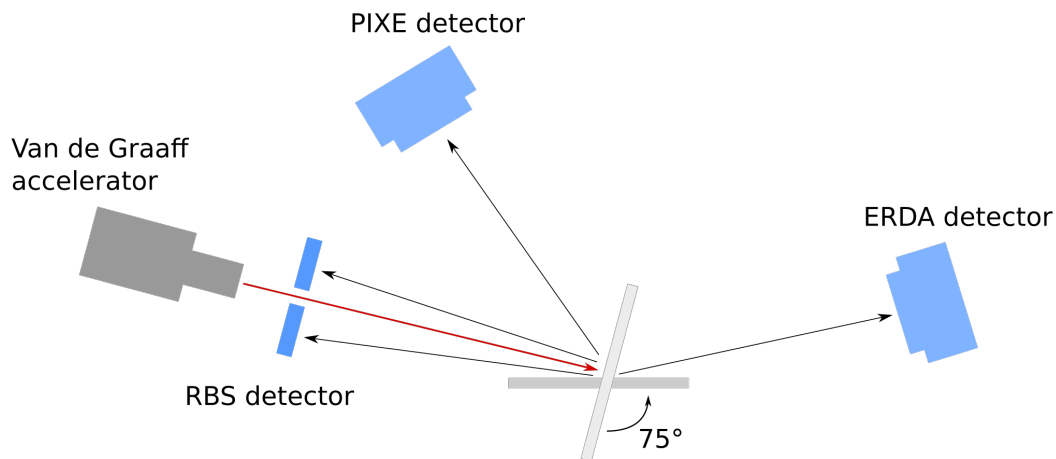
Figure 2.8: Schematic of the ERDA analysis instrumentation. An incident beam of ^{4}He$^+$ is first directed normal to the sample. X-rays and surface charge are measured by the PIXE and RBS detectors. The sample is then tilted at 75° to the incident beam, and protons ejected from the sample are collected by the ERDA detector. Figure modified from Bureau et al. (2009).

The RBS spectrum is also important to the ERDA analysis in that it can be used to deduce a quantitative determination of the total number of incident

particles on the sample during spectrum acquisition. This is a critical parameter for the ERDA determination, and it is obtained by measuring the charge deposited on the sample by the incoming particles. This measurement is not possible in the tilted position required for ERDA, however it is directly proportional to the intensity of the RBS measurement and so may be determined from an analysis of the RBS spectrum.

Data processing occurs in several steps. First, all data are processed with RISMIN software (Daudin et al., 2003). Data are checked for overall quality and compositional homogeneity. The required RBS and ERDA spectra are then extracted; the resulting maps of the analyses can be used to select the best region of interest (see figure 5.6). E.g., data from a cracked or uneven surface can be excluded, or if sum spectra comprise data from two distinct phases they can be separated. Once RBS and ERDA spectra are obtained, these are analysed with the SIMNRA software (Mayer, 1999), to account for effects of sample composition. The RBS spectrum is first used to determine the number of incident particles, which is then inserted into the ERDA analysis, and the concentration of H particles can then be determined (further explanation in chapter 5, see figure 2.9).

It should be noted that one feature of ERDA analysis is that the total spectrum comprises a signal from surface contamination of water from the atmosphere, as well as a signal produced from the hydrogen ejected from deeper within the sample. These manifest differently in the spectrum, and so H originating from surface contamination can be identified and thus subtracted from the H determination (see figure 2.9; Bureau et al., 2009).
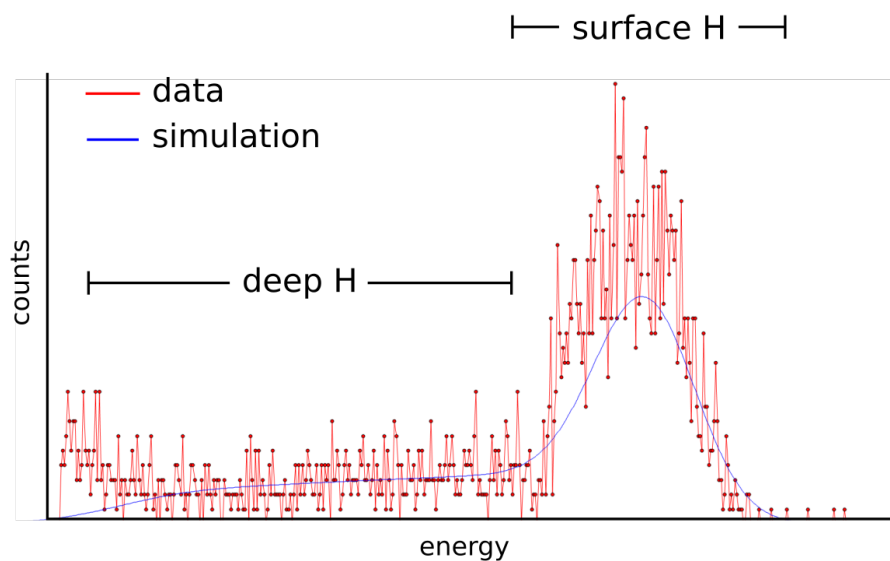
Figure 2.9: Accounting for surface contamination of H. The ERDA spectrum is a histogram, with number of counts (directly proportional to H content) is plotted against energy. Higher energy (to the left) corresponds to the surface, while particles of lower energy (to the right) are sourced from deeper within the sample and are therefore not affected by any surface effects.

Detection limits of H for the types of samples analysed are approximately 50 wt ppm for sulfides, and 100 wt ppm for silicate glass (Bureau, personal communication; Bureau et al., 2009). Uncertainty in the measurement is calculated from a combination of sources: statistical uncertainty, energy calibration of the ERDA spectrum, angle of tilt, and solid angle of RBS detection (Ω_{RBS}), giving a total uncertainty of:

$$\sigma_{tot} = \sqrt{\left(\sigma_{statistic}\right)^2 + \left(\sigma_{calibration}\right)^2 + \left(\sigma_{tilt}\right)^2 + \left(\sigma_{\Omega RBS}\right)^2}$$

which was found to be 14%.

3 Equations of state, phase relations and oxygen fugacity of the Ru-RuO$_2$ buffer at high pressures and temperatures

3.1 Introduction

Knowledge of the redox conditions, or more specifically the oxygen fugacity (fO$_2$), at which rocks and melts formed is important for understanding a host of phenomena such as the partitioning of variably valent elements, the speciation of volatiles, and the formation of accessory phases such as sulfides, diamond and metal alloys (Hirschmann et al., 2012; Gaillard et al., 2015; Smith et al., 2016; Davis and Cottrell, 2018). Perhaps most importantly, the fO$_2$ of the mantle has influenced the nature of volcanically degassed species throughout Earth's history (Hirschmann, 2012), as well as transport properties such as diffusion, creep and electrical conductivity by controlling the Fe^{3+}/Fe^{2+} ratio and OH$^-$ contents of minerals and melts (e.g., Pommier et al., 2010; Keefner et al., 2011; Yoshino and Katsura, 2013). In order to place quantitative constraints on the effects of any redox or redox-influenced process at mantle conditions, experimental studies that either control or measure the fO$_2$ are necessary.

Recent studies on the speciation of ferric iron in minerals and melts at high pressure have further indicated the need for quite specific controls on oxygen fugacity (Tao et al., 2018; Zhang et al., 2017). Although the concentration of ferric iron in upper mantle rocks is relatively low (Canil and O'Neill, 1996; Woodland et al., 2006), studies of sublithospheric diamonds (Kiseeva et al., 2018) and experimental studies at transition zone and lower mantle conditions appear to indicate that ferric iron components are increasingly stabilized with depth in the mantle (Lauterbach et al., 2000; Rohrbach et al., 2007). In order to explore this tendency, it is important to be able to determine the chemical potentials of ferric iron-bearing components in minerals and melts. This can tractably be achieved by fixing the oxygen fugacity of an experiment at conditions where measurable amounts of ferric iron components are present and then determining their concentration (O'Neill et al., 2006).

Standard methods for fixing fO$_2$ that use redox buffering assemblages in experiments face major challenges when applied at pressures consistent with the deep mantle. They require too much space in the experimental apparatus to be practical, and uncertainties arise in both the activities and standard state properties of the components involved. The use of an outer capsule containing an H$_2$O-saturated redox buffer (Eugster, 1957), for example, is problematic above 3 GPa because the solute content of the fluid makes it difficult to determine the activity of H$_2$O in the inner capsule, which is required to calculate the fO$_2$ (Matjuschkin et al., 2015). Noble metal redox sensors can be used to determine the fO$_2$ of iron-bearing assemblages (Woodland and O'Neill, 1997), however at pressures above 15 GPa uncertainties in the effect of pressure on the excess molar volumes of the alloy solid solutions contribute to very large errors in calculated fO$_2$ (Stagno et al., 2011).

One solution is to use pure solid buffering assemblages inside the experimental capsule, allowing the buffer to be in close proximity to the sample, which ensures that they can equilibrate directly. The best buffers for this purpose are those that undergo minimal chemical interaction with the sample under investigation, other than exchanging oxygen, such as Re + O$_2$ = ReO$_2$ and Ru + O$_2$ = RuO$_2$ (Smyth et al., 2014; Righter et al., 2004). At the other end of the scale, Fe metal is similarly effective at rendering an fO$_2$ close to the

iron-wüstite (IW, $2Fe + O_2 = 2FeO$) buffer, although the chemical potential of a least one coexisting ferrous iron phase is also required (Rohrbach et al., 2007). This technique is potentially the most reliable for calculating oxygen fugacities of sufficient accuracy to determine the chemical potentials of ferric iron components at pressures compatible with the deep mantle. However, the thermal equations of state and phase relations of the buffering assemblage need to be accurately known.

A metal-oxide oxygen fugacity buffer has the form

$$M + \left(\frac{x}{2}\right) \cdot \mathbf{O}_2 = M\mathbf{O}_{(x/2)} \tag{3.1}$$

where M is a metal and x is its valence state in the oxide. As long as both solid phases are pure, the oxygen fugacity can be calculated from

$$\left(\frac{x}{2}\right) \cdot RT \ln f\mathbf{O}_2 = -\Delta_r G^0_{(T,1\text{bar})} + \int_{1\,\text{bar}}^{P} \Delta V \cdot dP \tag{3.2}$$

where R is the universal gas constant, T is temperature, $\Delta_r G^0_{(T,1\,\text{bar})}$ is the standard-state Gibbs free energy of the equilibrium at ambient pressure and the temperature of interest, and ΔV is the volume change of the solid phases. As the pressure increases, the accuracy to which ΔV needs to be determined also increases. Above 10 GPa, thermal equations of state (EoS) for the metal and oxide phases at conditions close to those of interest are required to reduce the uncertainties. Potentially of even greater importance, the phases of the buffering assemblage may undergo phase transitions at high pressures and/or temperatures. If so, the thermodynamic properties of these phases are also required to calculate the $f\mathbf{O}_2$.

Campbell et al. (2009) used synchrotron X-ray diffraction to determine the thermal equations of state for the metal-oxide pairs Fe-FeO and Ni-NiO in a multianvil press and laser-heated diamond anvil cells, to 80 GPa and 2500 K (Campbell et al., 2009). These data were then used to calculate the $f\mathbf{O}_2$ of the Fe-FeO and Ni-NiO buffers over this range of conditions, which are to date the only buffering assemblages that are accurately calibrated to lower mantle settings. By determining the EoS of both metal and oxide in a single exper-

iment, the properties become internally consistent and the absolute errors have limited effects because they cancel out across the buffering equilibrium.

Here we report synchrotron X-ray diffraction data on an assemblage of Ru and RuO$_2$ collected to pressures of 19.4 GPa and temperatures up to 1473 K in a multianvil press. This assemblage has particular advantages for buffering the fO$_2$ of silicate melts in order to examine the pressure effect on melt ferric/ferrous ratios (O'Neill and Nell, 1997; O'Neill et al., 2006; Zhang et al., 2017). Both metal and oxide undergo minimal reaction with coexisting silicate melts and can therefore be mixed directly with the melt phase or silicate minerals. Ruthenium also has a relatively low solubility in silicate melts. In addition, as the buffered fO$_2$ is relatively high, Fe loss into Pt capsules is not significant and ferric Fe is present in sufficient concentrations to be accurately measured.

Though thermal expansion data at room pressure are available for both Ru and RuO$_2$, and compression studies at room temperature have been performed (Clendenen and Drickamer, 1964; Rao and Iyengar, 1969; Schroeder et al., 1972; Hazen and Finger, 1981), no volume data at simultaneous high pressures and temperature are available. More importantly, however, RuO$_2$, which has a tetragonal rutile-type structure at room pressure, undergoes a series of phase transformations with increasing pressure. At room temperature, a second-order ferroelastic phase transformation to an orthorhombic CaCl$_2$-type structure has been observed above 7 GPa (Haines and Léger, 1993; Rosenblum et al., 1997; Ono and Mibe, 2011). Further, a cubic pyrite-type structure has been observed above 11 GPa (Haines and Léger, 1993), which has also been synthesised and recovered from 20 GPa and 1373 K (Haines et al., 1998). We have determined the phase relations and thermal EoS properties of these phases in order to use the Ru-RuO$_2$ buffer at conditions compatible with the transition zone and top of the lower mantle.

3.2 Methods

Samples of reagent-grade ChemPur Ru metal and RuO$_2$ powders were mixed together in the ratio 30:70, respectively, by weight and cold pressed into pellets 1.7 mm in diameter and 1 mm thick. Pellets of the same size were also prepared of MgO mixed with Au powder in the ratio 90:10 for use as a pressure calibrant. Pellets of both were loaded into a 10-mm edge-length Cr-doped MgO octahedral pressure medium inside an MgO sleeve, separated by thin (0.3 mm) Al$_2$O$_3$ spacers of the same diameter. MgO filled the space above and below the samples and calibrant.

A 25 μm thick rhenium foil furnace was used to heat the sample, with windows cut in to allow X-rays to enter the assembly and the diffracted beam to exit. The furnace was surrounded by a ZrO$_2$ sleeve to provide thermal insulation. Temperature was monitored by a W$_{97}$Re-W$_{75}$Re (type D) thermocouple, inserted normal to the X-ray beam with the foil furnace serving as the high-T junction (figure 3.1).
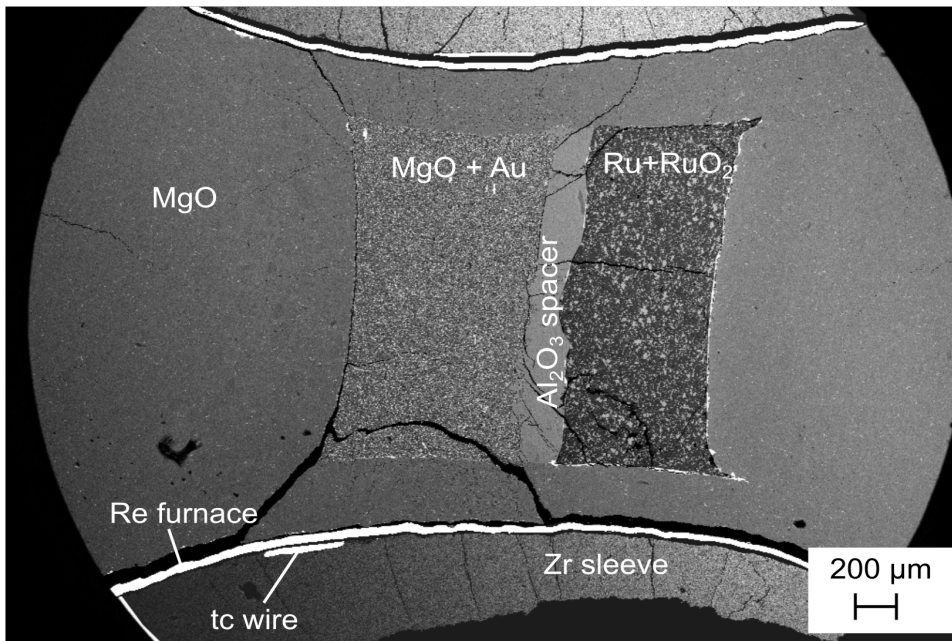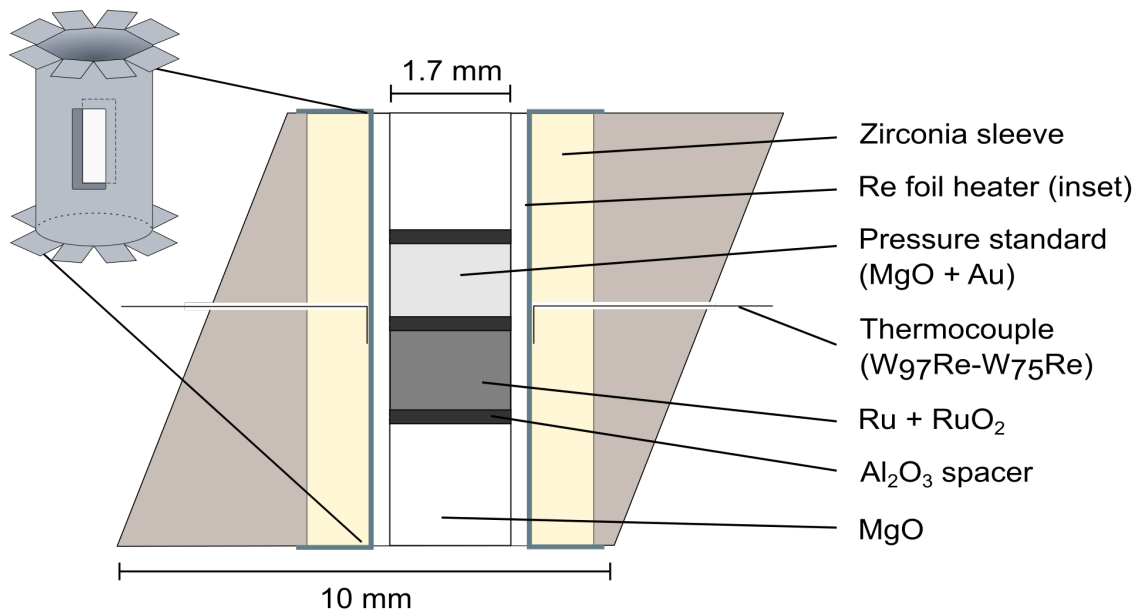
Figure 3.1: (Top) schematic of the experimental assembly used in the multianvil press. Pellets of sample material and pressure calibrant, 1.7 mm in diameter and approx 1 mm thick were stacked vertically in a 10-mm edge-length octahedral pressure medium (see text), separated by alumina discs. The sample was heated with a Re foil furnace, which had windows cut in to allow the beam to pass through (inset image). (Bottom) BSE image of recovered run product, showing pressure calibrant, sample, furnace and thermocouple. Composite image from several different brightness settings to show detail.

The assembly was compressed with high-hardness Fujilloy TF05 tungsten car-

bide (WC) anvils with 4-mm edge length truncated corners (Ishii et al., 2016) in the large volume press at beamline 13-ID-D at the Advanced Photon Source, Argonne National Laboratory (e.g. Wang et al., 2009; Chantel et al., 2012). Powder X-ray diffraction data from the sample and the pressure calibrants were collected using an energy-dispersive system at a diffraction angle of 6.1°, calibrated at room pressure using the diffraction patterns of Au and MgO. A YAG phosphor crystal was placed in the beam path behind the sample to convert the X-ray absorption contrast of the assembly into visible light. A charge-coupled device (CCD) was used to record images of the sample assemblage in order to focus the diffraction beam either on the Ru-RuO$_2$ pellets or on the Au-MgO mixture. Pressure was determined using measurements of the unit-cell volumes of Au and MgO and employing the equations of state of Tsuchiya (2003) and Dewaele et al. (2000), respectively (see section 2.2.3).

In addition, a series of quench experiments were performed at the Bayerisches Geoinstitut using 18 mm and 10 mm edge length octahedral assemblies of very similar design as described above, but with LaCrO$_3$ furnaces. These assemblies were employed with either 8 mm WC anvil truncations in a 5000 tonne press or 4 mm truncations in a 1200 tonne press, respectively. Ru and RuO$_2$ mixtures were employed as a buffering assemblage inside platinum capsules. After the experiments were quenched, the RuO$_2$ phase was identified using either X-ray powder diffraction or Raman spectroscopy by comparison with spectra previously reported (Haines et al., 1998; Rosenblum et al., 1997).

Table 3.1: Experiment pressure and temperature conditions.Pressures calculated using equations of state for Au and MgO, of Tsuchiya (2003) and Dewaele (2000), respectively. The temperature uncertainty is ±40 K due to the thermal gradient over the diffraction volume. The pressure uncertainties are approximately ±0.3 GPa.

Run #	Au a (Å)	MgO a (Å)	P Au (GPa)	P MgO (GPa)	T (K)
T2135.001	4.0812 (2)	4.2116 (2)	0.0001	0.0001	298
T2135.004	4.0773 (3)	4.2024 (3)	7.4	7.0	1273
T2135.006	4.0684 (3)	4.1944 (2)	7.2	6.7	1073
T2135.009	4.0569 (2)	4.1851 (3)	6.7	6.0	773
T2135.012	4.0455 (2)	4.1762 (3)	4.8	4.3	298
T2135.015	4.0578 (3)	4.1841 (4)	9.9	9.3	1273
T2135.017	4.0536 (2)	4.1796 (2)	9.2	8.6	1073
T2135.019	4.0434 (3)	4.1691 (2)	8.5	8.1	773
T2135.022	4.0302 (4)	4.1578 (5)	7.1	6.7	298
T2135.025	4.0425 (3)	4.1705 (5)	12.0	11.0	1273
T2135.026	4.0342 (3)	4.1580 (7)	11.9	11.4	1073
T2135.029	4.0249 (2)	4.1537 (5)	11.3	10.1	773
T2135.030	4.0161 (3)	4.1410 (5)	9.4	9.1	298
T2135.034	4.0238 (3)	4.1439 (2)	13.5	13.4	1073
T2135.036	4.0150 (2)	4.1348 (2)	12.9	12.8	773
T2135.038	4.0045 (2)	4.1228 (2)	11.3	11.7	298
T2139.001	4.0780 (2)	4.2108 (2)	0.0001	0.0001	298
T2139.006	3.9803 (2)	4.1000 (2)	15.2	15.1	298
T2139.012	3.9737 (2)	4.0935 (3)	16.4	16.2	298
T2139.017	3.9687 (2)	4.0875 (2)	17.4	17.1	298
T2139.022	3.9590 (2)	4.0764 (3)	19.4	19.0	298
T2140.001	4.0788 (2)	4.2122 (2)	0.0001	0.0001	298
T2140.004	4.0256 (4)	4.1487 (4)	15.4	15.3	1473
T2140.007	4.0219 (3)	4.1447 (4)	14.7	14.6	1273
T2140.008	4.0178 (3)	4.1390 (4)	14.1	14.1	1073
T2140.011	4.0081 (3)	4.1286 (6)	13.6	13.8	773
T2140.012	3.9995 (2)	4.1218 (5)	11.8	11.9	298
T2140.015	4.0181 (3)	4.1382 (7)	16.5	16.8	1473
T2140.018	4.0124 (3)	4.1345 (2)	16.3	16.0	1273
T2140.019	4.0077 (3)	4.1304 (3)	15.8	15.4	1073
T2140.022	4.0015 (2)	4.1233 (3)	14.8	14.6	773
T2140.023	3.9944 (3)	4.1145 (3)	12.7	13.1	298
T2140.026	4.0080 (3)	4.1253 (2)	18.2	18.7	1473
T2140.029	4.0008 (2)	4.1207 (3)	18.2	18.1	1273
T2140.030	3.9964 (2)	4.1182 (4)	17.7	17.2	1073
T2140.033	3.9899 (4)	4.1040 (5)	16.8	17.5	773
T2140.034	3.9831 (3)	4.0996 (3)	14.8	15.4	298

Table 3.2: Experimental conditions and results of additional multianvil quench experiments containing Ru and RuO$_2$

Run #	P (GPa)	T (K)	Duration (min)	RuO$_2$ product
S6973	4	1873	20	Tetragonal
S6928	4	1673	15	Tetragonal
S6820	6	2023	10	Tetragonal
S6889	6	2023	15	Tetragonal
S6811	6	2173	5	Tetragonal
S6879	6	2173	15	Tetragonal
S6977	8	2173	30	Tetragonal
S6777	8	2173	30	Tetragonal
Z1791	10	2173	15	Tetragonal
S6510	10	2173	30	Tetragonal
Z1468	15	2373	45	Tetragonal
Z1621	17	2473	10	Tetragonal
Z1666	18	2473	10	Cubic
S6654	20	2473	5	Cubic
S6606	23	2573	5	Cubic
S6776	23	2573	10	Cubic

3.3 Results

Three experiments were performed, with each experiment comprising three to four temperature cycles. For each cycle, pressure was first increased to a target, followed by heating to a peak temperature. X-ray diffraction measurements were then performed on both the sample and on the pressure calibrant materials as the temperature was dropped in steps of 200 K to 773 K and then in one step to room temperature. The assembly was then compressed further at room temperature and the temperature was again raised for another cycle (figure 3.2). The peak temperature was 1273 K for the first experiment and 1473 for the third. In the second experiment the thermocouple broke but data at room temperature were still collected at various pressures after heating to a temperature estimated to be ∼1273 K based on the power supplied to the furnace. During heating at constant load, sample pressure generally increased slightly, whereas it dropped during cooling. The only exception to this was during the first heating cycle of the third experiment, where cubic RuO$_2$ formed and the pressure was observed to drop during heating, most likely due

to the large volume change.
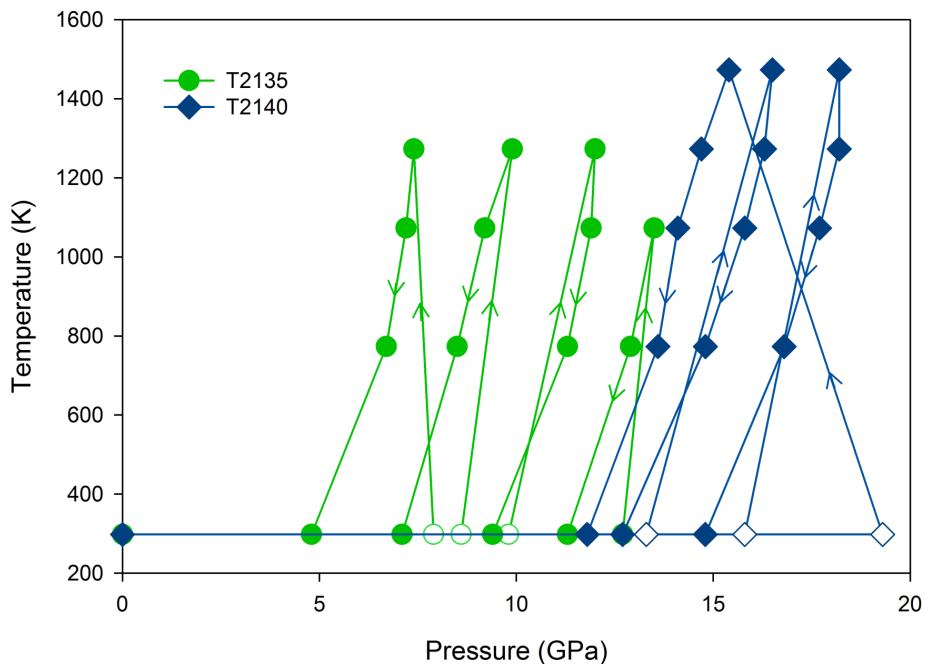
Figure 3.2: Pressure-temperature paths of two in situ X-ray diffraction experiments. Pressures were calculated using the P-V-T EoS of Au. The pressure was increased after each cycle of heating. In experiment T2140 the pressure was first increased to ~ 19 GPa but dropped significantly, at constant press load, during heating, most likely due to the large volume change as cubic RuO_2 was synthesized. In a third experiment, T2139, the thermocouple was broken and only room temperature results are used.

In general there was good agreement between the pressure calculated from the Au and from the MgO, but the Au was taken to be more reliable as many of the assembly component parts are MgO and interference of the diffraction lines from MgO that was not within the furnace hot spot could not be excluded. Experimental conditions at each data point are reported in table 3.1.

Energy dispersive powder X-ray diffraction patterns (fig 3.3) were processed using full profile LeBail refinements with the GSAS software package used in the EXPGUI interface (Larson and Von Dreele 2004; Toby, 2001). Unit-cell lattice parameters determined at the different P-T conditions are reported in Tables 3.3 and 3.4. To make the errors on the unit cell volumes more realistic we multiply the values provided by GSAS by 10. The results of X-ray diffraction and Raman analyses on quenched samples of Ru and RuO_2 from various pressures and temperatures are reported in Table 3.2. Pressure and

temperature uncertainties at these conditions are of the order of 0.5 GPa and 100 K, respectively.
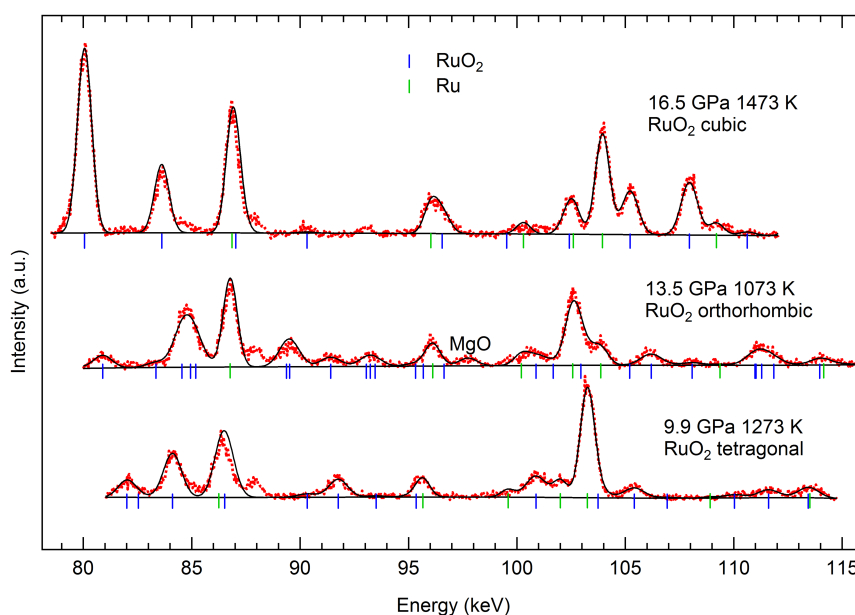
Figure 3.3: Examples of energy dispersive diffraction patterns collected for Ru/RuO$_2$ samples at different pressures and temperatures. Dotted red curves: observed intensity data; black solid curves: results from Le Bail fits (calculated intensities + background). The reflections positions for the Ru (green) and RuO$_2$ (blue) phases are shown as vertical ticks. Fluorescence peaks at ~85 and ~88 keV due likely to some lead components of the diffraction line have been ignored during Le Bail fitting.

3.4 Data fitting procedure

The room-temperature volume (V) data were fitted with the modified Tait EoS (Holland and Powell, 2011; Huang and Chow, 2002), which gave identical fitting parameters when compared to the second-order Birch-Murnaghan EoS. The former method was employed because its form is more amenable for ultimately calculating the fO$_2$. The fitting was performed with the EoSFit7 software (Angel et al., 2014). The room-T modified Tait equation of state (Huang and Chow, 2002) is given as

$$\frac{V}{V_0} = 1 - a(1 - (1 + bP)^{-c}) \tag{3.3}$$

or in terms of pressure

$$P = \frac{1}{b}\left(\left[\frac{V/V_0 + a - 1}{a}\right]^{-1/c} - 1\right)$$ (3.4)

where

$$
\begin{aligned}
a &= \frac{1 + \kappa_0'}{1 + \kappa_0' + \kappa_0\kappa_0''} \\
b &= \frac{\kappa_0'}{\kappa_0} - \frac{\kappa_0''}{1 + \kappa_0'} \\
c &= \frac{1 + \kappa_0' + \kappa_0\kappa_0''}{\kappa_0'^2 + \kappa_0' - \kappa_0\kappa_0''}.
\end{aligned}
$$

V_0 is the volume at ambient pressure and temperature, and κ_0, κ_0', and κ_0'' are the isothermal bulk modulus and its first and second derivatives, respectively. The experimental data were used to refine V_0 and κ_0, however the data were insufficient to refine κ_0' and so its value was fixed at 4 and a value of κ_0'' was assigned such that

$$\kappa_0'' = -\frac{\kappa_0'}{\kappa_0}.$$

Two methods were used to derive equations of state terms at high temperature. In the first, the room pressure volume is described with a thermal expansion expression

$$V_T = V_0 \cdot \exp\left[\int_{T_0}^{T} \alpha dT\right]$$ (3.5)

and the effect of temperature on the bulk modulus is given by

$$\kappa_T = \kappa_0 + (\partial\kappa_T/\partial T)_P (T - T_0)$$ (3.6)

where α is the volumetric coefficient of thermal expansion, here approximated with a linear function $\alpha(T) = \alpha_0 + \alpha_1 T$. Using this approach, $\partial\kappa_T/\partial T$, α_0, and α_1 are refined from the high temperature data. This was found to be the necessary approach for fitting the data for ruthenium metal.

For the second approach, an expression for thermal pressure was refined from the high-temperature data, which is then used in conjunction with an isother-

mal EoS. The thermal pressure term is defined as

$$P_{\text{th}} = \int_{T_0}^{T} \alpha\kappa dT \mid_V .$$ (3.7)

The function $\alpha\kappa$ is assumed to have the form of a heat capacity curve; i.e., becoming constant at high temperature and decreasing to zero at 0 K, and so is modeled with an Einstein function:

$$\xi = \left(\frac{\alpha_0 \kappa_0}{\xi_0} \right) \frac{u^2 e^u}{(e^u - 1)^2}$$ (3.8)

where α_0, κ_0, and ξ_0 are the values at ambient conditions, $u = {}^\theta/_T$, and θ is the Einstein temperature. An approximate value for θ can be estimated for each phase via the relation $\theta = 10636/(S/n + 6.44)$, where S is the molar entropy (in JK^{-1}mol^{-1}) and n is the number of atoms per formula unit (Holland and Powell, 2011). P_{th} can then be rewritten:

$$\begin{aligned}
P_{\text{th}} &= \int_{T_0}^{T} \frac{\alpha_0 \kappa_0}{\xi_0} \xi dT \\
&= \frac{\alpha_0 \kappa_0 \theta}{\xi_0} \left(\frac{1}{e^u - 1} - \frac{1}{e^{u_0} - 1} \right) .
\end{aligned}$$ (3.9)

In this approach only α_0 is fit to the high temperature data. This EoS contains an implicit thermal effect on the compressibility.

3.4.1 P-V-T data and equation of state for ruthenium metal

Table 3.3: Ru metal lattice parameters. Temperature uncertainty is ±30 K.

Run #	P Au (GPa)	T (K)	Ru metal a (Å)	c (Å)	V (Å3)
T2135.001	0.0001 (0)	298	2.708 (3)	4.280 (6)	27.18 (5)
T2135.004	7.4 (0.2)	1273	2.704 (3)	4.285 (14)	27.12 (8)
T2135.006	7.2 (0.2)	1073	2.701 (3)	4.283 (8)	27.04 (5)
T2135.009	6.7 (0.2)	773	2.697 (3)	4.274 (6)	26.93 (5)
T2135.012	4.8 (0.1)	298	2.694 (2)	4.260 (6)	26.77 (4)
T2135.015	9.9 (0.2)	1273	2.697 (2)	4.272 (11)	26.91 (6)
T2135.017	9.2 (0.2)	1073	2.696 (5)	4.270 (12)	26.88 (9)
T2135.019	8.5 (0.3)	773	2.693 (3)	4.266 (8)	26.78 (6)
T2135.022	7.1 (0.1)	298	2.687 (4)	4.256 (5)	26.62 (4)
T2135.025	12.0 (0.2)	1273	2.686 (3)	4.287 (3)	26.78(14)
T2135.026	11.9 (0.2)	1073	2.686 (2)	4.267 (10)	26.65 (5)
T2135.029	11.3 (0.2)	773	2.684 (3)	4.253 (6)	26.53 (5)
T2135.030	9.4 (0.1)	298	2.680 (2)	4.248 (8)	26.42 (5)
T2135.034	13.5 (0.2)	1073	2.681 (2)	4.254 (10)	26.47 (6)
T2135.036	12.9 (0.2)	773	2.677 (2)	4.254 (7)	26.41 (5)
T2135.038	11.3 (0.1)	298	2.674 (2)	4.244 (7)	26.28 (5)
T2139.001	0.0001 (0)	298	2.707 (2)	4.279 (5)	27.16 (4)
T2139.006	15.2 (0.1)	298	2.662 (3)	4.225 (9)	25.93 (6)
T2139.012	16.4 (0.1)	298	2.658 (3)	4.221 (8)	25.84 (5)
T2139.017	17.4 (0.1)	298	2.657 (2)	4.213 (5)	25.77 (4)
T2139.022	19.4 (0.1)	298	2.652 (3)	4.213 (7)	25.67 (5)
T2140.001	0.0001 (0)	298	2.707 (2)	4.280 (4)	27.17 (3)
T2140.004	15.4 (0.2)	1473	2.681 (2)	4.263 (4)	26.54 (3)
T2140.007	14.7 (0.2)	1273	2.683 (2)	4.256 (13)	26.47 (8)
T2140.008	14.1 (0.2)	1073	2.681 (3)	4.250 (8)	26.40 (5)
T2140.011	13.6 (0.3)	773	2.677 (2)	4.248 (9)	26.32 (6)
T2140.012	11.8 (0.1)	298	2.673 (2)	4.235 (7)	26.19 (5)
T2140.015	16.5 (0.2)	1473	2.677 (2)	4.259 (7)	26.43 (5)
T2140.018	16.3 (0.2)	1273	2.675 (2)	4.2505 (3)	26.33 (15)
T2140.019	15.8 (0.2)	1073	2.675 (2)	4.249 (9)	26.31 (5)
T2140.022	14.8 (0.2)	773	2.673 (2)	4.238 (6)	26.20 (4)
T2140.023	12.7 (0.1)	298	2.669 (2)	4.231 (5)	26.10 (3)
T2140.026	18.2 (0.2)	1473	2.672 (3)	4.253 (14)	26.29 (8)
T2140.029	18.2 (0.2)	1273	2.671 (4)	4.248 (13)	26.24 (7)
T2140.030	17.7 (0.2)	1073	2.670 (3)	4.230 (9)	26.10 (6)
T2140.033	16.8 (0.3)	773	2.669 (2)	4.230 (5)	26.08 (3)
T2140.034	14.8 (0.1)	298	2.664 (4)	4.223 (20)	25.98 (11)

Ruthenium metal has a hexagonal (hcp) unit cell with the space group $P6_3/mmc$. No structural transitions were observed with increasing pressure and/or temperature. Data from this study up to 19.4 GPa and temperatures to 1473 K were employed to refine the EoS terms along with room pressure thermal expansion data from Schroeder et al. (1972). Using the modified Tait EoS, the resulting bulk modulus, 301 ± 2 GPa with $\kappa_0' = 4$, is identical within error to that obtained with a second order Birch-Murnaghan EoS. Clendenen and Drickamer (1964) reported lattice parameters for Ru from compression experiments up to 40 GPa and their data are compared in Figure 3.4. Fitting this previous data results in a κ_0 of 287 ± 36 GPa and $\kappa_0' = 5 \pm 2$, which is within the uncertainty of our value. However, more recent density functional theory calculations on Ru by Lugovskoy et al. (2014) yield a κ_0 of 332.5 GPa at 0 K, which is also in reasonable agreement with our result.

When fitting the thermal terms to the Ru EoS, the room pressure thermal expansion data of Shroeder et al. (1972) were also included, which extend to 2000 K. Although the Einstein thermal pressure model has been shown to successfully describe data on silicate minerals (Holland and Powell, 2011), it was found to be insufficiently flexible to fit the high-temperature data of Schroeder et al. (1972). Thus, for Ru metal, the polynomial thermal expansion model resulted in the only successful fit. Isotherms from this model are plotted in figure 3.4 and the fitting parameters are given in Table 3.5.
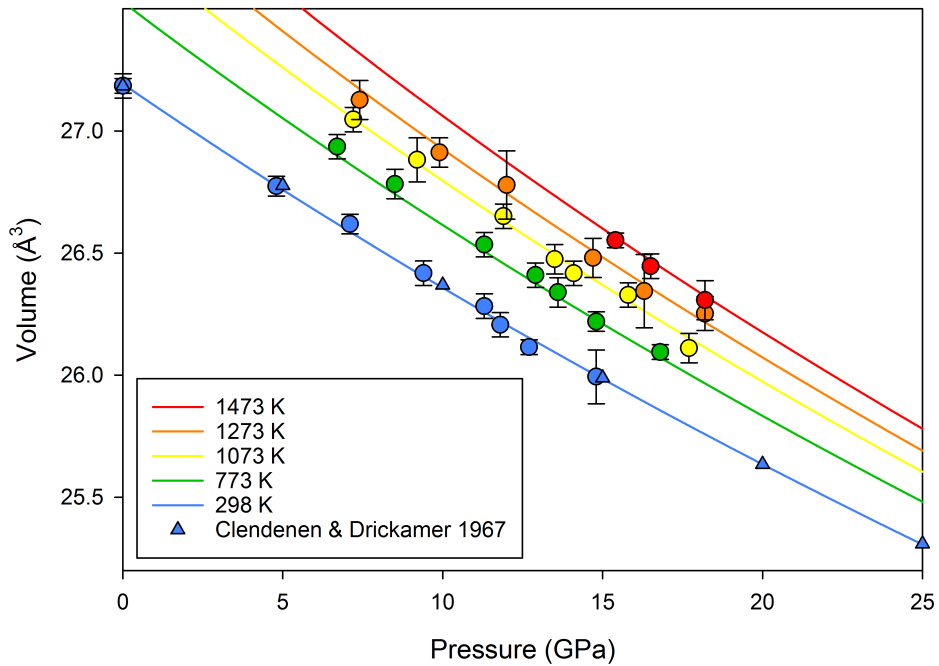
Figure 3.4: Experimental P-V-T data collected for ruthenium metal at the temperatures indicated by the colors of the fitting curves (circles: this study). Curves show the fit of the equation of state that employs the modified Tait equation (Huang and Chow, 2002; Holland and Powell, 2011), with a two-term polynomial expression for the thermal expansion. The room pressure thermal expansion data of Schroeder et al. (1972) were included in the fitting procedure but the compression data of Clendenen and Drickamer (1967; triangles) were not.

3.4.2 P-V-T data, phase relations, and equations of state for ruthenium dioxide

Table 3.4: Lattice parameters of ruthenium dioxide.

Run #	P Au (GPa)	T (K)	a (Å)	b (Å)	c (Å)	V (Å^3)	phase
T2135.001	0.0001 (0)	298	4.4993 (3)		3.1067 (3)	62.889 (8)	tetragonal
T2135.004	7.4 (0.2)	1273	4.5020 (4)		3.0753 (4)	62.330 (10)	tetragonal
T2135.006	7.2 (0.2)	1073	4.4883 (3)		3.0806 (3)	62.056 (8)	tetragonal
T2135.009	6.7 (0.2)	773	4.4764 (4)		3.0870 (4)	61.858 (9)	tetragonal
T2135.012	4.8 (0.1)	298	4.4646 (4)		3.1000 (4)	61.791 (12)	tetragonal
T2135.015	9.9 (0.2)	1273	4.4848 (4)		3.0730 (4)	61.808 (11)	tetragonal
T2135.017	9.2 (0.2)	1073	4.4788 (4)		3.0770 (4)	61.723 (9)	tetragonal
T2135.019	8.5 (0.3)	773	4.4668 (4)		3.0834 (4)	61.522 (9)	tetragonal
T2135.022	7.1 (0.1)	298	4.4569 (4)		3.0889 (4)	61.357 (9)	tetragonal
T2135.025	12.0 (0.2)	1273	4.5685 (7)	4.3666 (9)	3.0700 (4)	61.243 (13)	orthorhombic
T2135.026	11.9 (0.2)	1073	4.5553 (6)	4.3588 (8)	3.0732 (5)	61.021 (10)	orthorhombic
T2135.029	11.3 (0.2)	773	4.5467 (7)	4.3499 (9)	3.0763 (5)	60.842 (11)	orthorhombic
T2135.030	9.4 (0.1)	298	4.4726 (8)	4.3850 (10)	3.0866 (5)	60.535 (14)	orthorhombic
T2135.034	13.5 (0.2)	1073	4.5760 (8)	4.3047 (8)	3.0618 (6)	60.313 (12)	orthorhombic
T2135.036	12.9 (0.2)	773	4.5616 (9)	4.2900 (7)	3.0703 (5)	60.082 (12)	orthorhombic
T2135.038	11.3 (0.1)	298	4.5376 (14)	4.2901 (9)	3.0736 (6)	59.833 (14)	orthorhombic
T2139.001	0.0001 (0)	298	4.4964 (3)		3.1062 (2)	62.801 (8)	tetragonal
T2139.006	15.2 (0.1)	298	4.7737 (3)			108.787 (19)	cubic
T2139.012	16.4 (0.1)	298	4.7668 (2)			108.312 (17)	cubic
T2139.017	17.4 (0.1)	298	4.7610 (2)			107.917 (13)	cubic
T2139.022	19.4 (0.1)	298	4.7509 (3)			107.236 (19)	cubic
T2140.001	0.0001 (0)	298	4.4977 (2)		3.1081 (2)	62.875 (7)	tetragonal
T2140.004	15.4 (0.2)	1473	4.8217 (2)			112.100 (16)	cubic
T2140.007	14.7 (0.2)	1273	4.8164 (2)			111.727 (14)	cubic
T2140.008	14.1 (0.2)	1073	4.8110 (2)			111.351 (12)	cubic
T2140.011	13.6 (0.3)	773	4.8046 (2)			110.912 (12)	cubic
T2140.012	11.8 (0.1)	298	4.7976 (2)			110.423 (12)	cubic
T2140.015	16.5 (0.2)	1473	4.8165 (2)			111.734 (12)	cubic
T2140.018	16.3 (0.2)	1273	4.8077 (2)			111.127 (14)	cubic
T2140.019	15.8 (0.2)	1073	4.8044 (2)			110.904 (13)	cubic
T2140.022	14.8 (0.2)	773	4.7984 (2)			110.485 (11)	cubic
T2140.023	12.7 (0.1)	298	4.7918 (2)			110.025 (11)	cubic
T2140.026	18.2 (0.2)	1473	4.8059 (2)			111.003 (14)	cubic
T2140.029	18.2 (0.2)	1273	4.7994 (2)			110.550 (15)	cubic
T2140.030	17.7 (0.2)	1073	4.7944 (2)			110.207 (14)	cubic
T2140.033	16.8 (0.3)	773	4.7878 (2)			109.756 (12)	cubic
T2140.034	14.8 (0.1)	298	4.7822 (2)			109.369 (16)	cubic

At ambient conditions, RuO$_2$ has a tetragonal space group ($P4_2/mnm$, $z = 2$) with a rutile-type structure. As this is isostructural with SiO$_2$ stishovite, there has been significant previous experimental and *ab initio* work to characterize its structure as a possible analogue for SiO$_2$ in the lower mantle. RuO$_2$ has been found to undergo two phase transitions with pressure. At room temperature it first undergoes a second-order ferroelastic phase transformation above 7 GPa, to an orthorhombic CaCl$_2$-type structure with space group $Pnnm$ ($z = 2$). At pressures above 12 GPa, a first-order phase transition occurs to a cubic pyrite-type (or modified fluorite) structure with space group $Pa\bar{3}$ ($z = 4$) (Haines et al., 1996; 1997; 1998; Haines and Léger, 1993; Ming and Magnhani, 1982; Ono and Mibe, 2011; Ahuja et al., 2001; Rosenblum et al., 1997). All three phases were encountered in this study and the transitions and volume changes are visible in the ambient-temperature data (figure 3.5), although it should be noted that in this study the cubic phase was formed upon heating to over 1000 K.
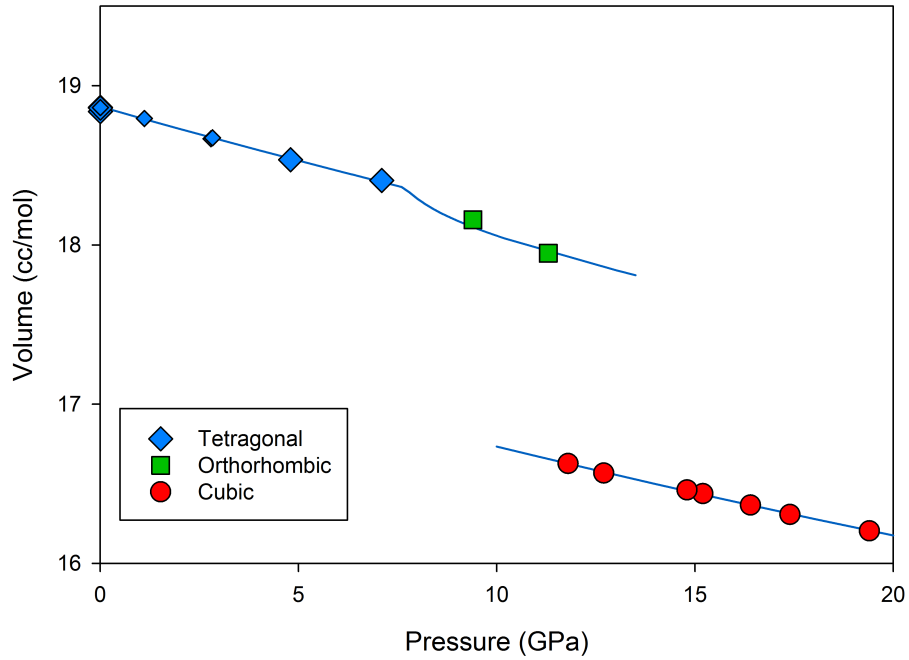
Figure 3.5: Molar volumes of RuO2 phases at room temperature. Single crystal compression data from Hazen and Finger (1981; small diamonds) are also shown. The curves show the results of EoS fitting, with the effect of the tetragonal to orthorhombic second order phase transition described with a model based on Landau theory. The cubic phase was synthesized after a phase of heating to over 1000 K.

In our experiments, the transition from the tetragonal to orthorhombic structure was found to occur between 7.5 and 9.8 GPa at ambient temperature (figure 3.6). Several previous studies have determined pressures for this transition. Using powder X-ray diffraction in a diamond anvil cell Haines and Léger (1993) report observation of the CaCl$_2$ phase at 8 GPa and proposed based on a back extrapolation of the unit cell parameters that the phase transition occurred at 5 GPa. A subsequent study with neutron diffraction (Haines et al., 1997) found the transition at 5.3 GPa, although pressure was determined using the equation of state of the tetragonal RuO$_2$ phase itself. Rosenblum et al. (1997) used Raman spectroscopy in a diamond anvil cell and splitting of the E_g mode to determine a transition pressure of 11.8 GPa, while Ono and Mibe (2011) used essentially the same methodology to determine a transition at 7.6 GPa, which is in very good agreement with our result. Ono and Mibe (2011) discuss a number of possible explanations for the difference in pressure of the

transition compared to the study of Rosenblum et al. (1997), however, we note that both our result and the result of Ono and Mibe have the advantage that the samples were heated between measurements, which should reduce differential stresses that might influence the transition. This result is also in good agreement with the *ab initio* value of 8 GPa (Gupta and Jha, 2014), though lower than the 9 GPa determined by Tse et al. (2000). The slope of the phase boundary determined from our experiments differs only very slightly from that of Ono and Mibe (figure 3.6) and is quite tightly constrained by both data sets.
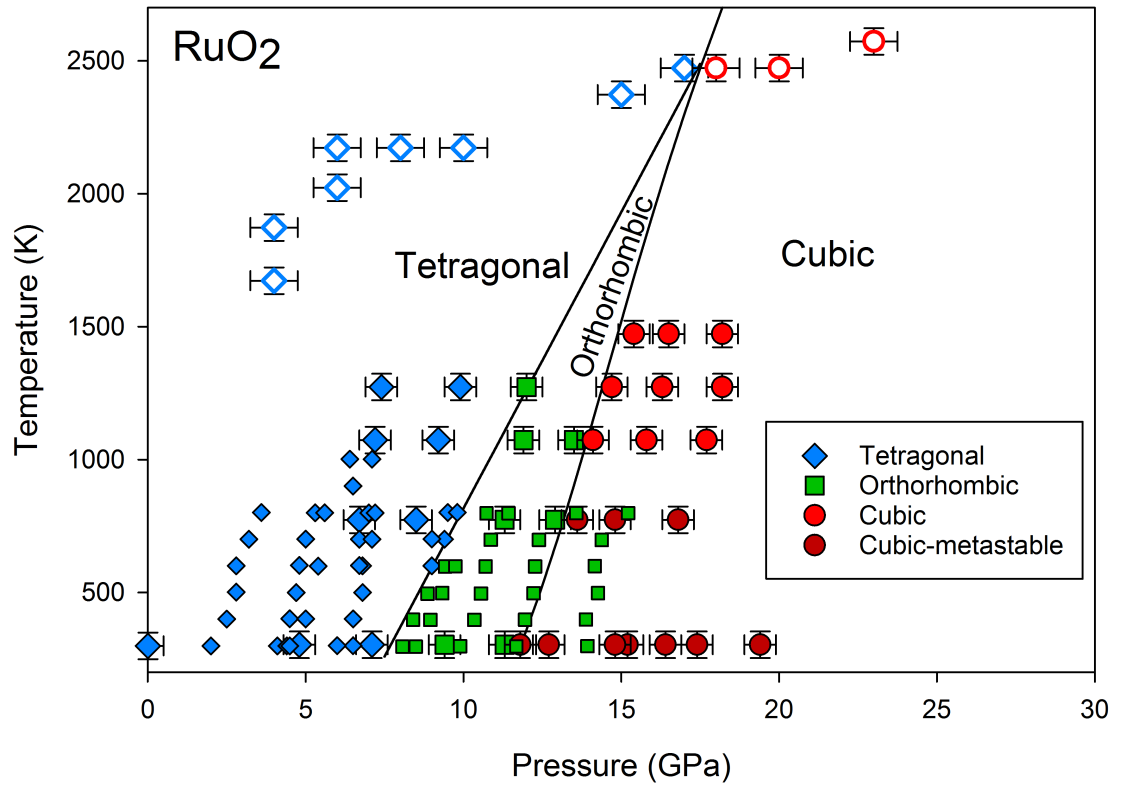
Figure 3.6: Phase relations of RuO$_2$ as a function of P and T. Mid-sized symbols indicate individual in situ XRD analyses from this study, larger symbols show the results from quench experiments at higher temperatures and small symbols show the in situ results of Ono & Mibe (2011) for the tetragonal-orthorhombic transition. Darker red symbols for the cubic phase indicate conditions where the data are not employed in fitting due to lower temperatures and potential metastability. Curves show the fit of thermodynamic models for both transitions as described in the text.

The results of higher-temperature quench experiments that contained mix-

tures of Ru and RuO$_2$ are also shown in figure 3.6. Although information on the orthorhombic phase would not be preserved in these recovered experiments, the phase boundaries determined imply that the orthorhombic phase is barely stable at these higher temperatures. To fit the EoS of the tetragonal phase, we also include room temperature single-crystal compression data from Hazen and Finger (1981) up to 2.8 GPa and room-pressure thermal expansion data from Rao and Iyengar (1969) up to 975 K.

The results of simultaneous fitting of these and our data are reported in Table 3.5 and give a bulk modulus of 261 ± 4 GPa, with κ' set to 4. This is in reasonable agreement with the *ab initio* calculations of Tse et al. (2000), who, depending on the density gradient corrections employed, obtained either 299 or 249 GPa, with $\kappa' \sim 4$. The thermal expansion coefficient (α_0) obtained, $1.57 \cdot 10^{-5}$ K^{-1}, is very similar to that of stishovite (Ito et al., 1974). Interestingly, the RuO$_2$ tetragonal phase c-axis shows a negative thermal expansion at room pressure (Rao and Iyengar, 1969), which is not only preserved in our high-pressure data but also appears to be the case for the orthorhombic phase. This is probably not related to the phase transition but may result from rotation of octahedra during heating.

It is clear that a significant softening of the structure occurs upon the second-order phase transition to the orthorhombic phase (figure 3.5). If we were to fit the available data for the orthorhombic phase to a separate EoS the bulk modulus would be ~ 110 GPa. However, given the paucity of the volume data and the fact that we expect the elastic properties to change rapidly in the region of such a transition, a more effective approach is to adopt dependencies described by Landau theory, which defines an excess Gibbs free energy term ($G^{ex}_{(P,T)}$) to describe the energetic consequences of a transition.

The advantage of this approach is that both the phase relations and the relationship between the volumes of the two phases, and in principal also the changes in elastic constants, can be derived from a single $G^{ex}_{(P,T)}$ expression. This provides internal consistency through a relatively small number of adjustable parameters. The high symmetry tetragonal phase is considered to form above a critical temperature T_c, which is anchored at room pressure at the value T_c^0. Following Holland and Powell (1998), and a lack of evidence to

the contrary, we assume that T_c is linear with pressure and that the slope of the transition is related to the maximum volume (V_{max}) and entropy (S_{max}) encountered during the transition, i.e.

$$\frac{dT_c}{dP} = \frac{V_{\mathrm{max}}}{S_{\mathrm{max}}}. \tag{3.10}$$

The phase relations can then, therefore, be fitted to the expression:

$$T_c = T_c^0 + \frac{V_{\mathrm{max}}}{S_{\mathrm{max}}}P. \tag{3.11}$$

The volume at pressure and temperature is described by

$$V_{(P,T)} = V_{(P,T)}^0 + V_{(P,T)}^{ex} \tag{3.12}$$

where $V_{(P,T)}^0$ is the volume of the tetragonal phase but excluding any contribution from the phase transition, as explained later. $V_{(P,T)}^0$ can be determined with the P-V-T EoS methods previously described. $V_{(P,T)}^{ex}$ is the excess volume arising from the transition. In Landau theory the excess properties vary across the phase transition as a function of an order parameter, Q, which can be defined in various ways depending on the type of data available. The rutile to CaCl$_2$-type transition ($P4_2/mnm \leftrightarrow Pnnm$) in RuO$_2$ and SiO$_2$ stishovite is second-order (Haines and Léger 1993; Carpenter et al., 2000), such that the temperature dependence of the order parameter is given by

$$Q^2 = (1 - \frac{T}{T_c}). \tag{3.13}$$

Higher order terms of Q (Carpenter et al., 2000) are neglected, as their influence on the volume and $G_{(P,T)}^{ex}$ would be relatively minor and we are not attempting to model the elastic behavior. The excess volume is then calculated as,

$$V_{(P,T)}^{ex} = V_{\mathrm{max}}(Q_{298}^2 - Q^2) \tag{3.14}$$

where Q_{298} is the value at the reference temperature of 298 K.

Q is set to 0 in the tetragonal stability field, i.e. where $T > T_c$, so $V_{(P,T)}^{ex}$ then becomes equal to $V_{\mathrm{max}}Q_{298}^2$. Consequently, the volume in the tetragonal field

contains a contribution from $V^{ex}_{(P,T)}$ and $V^0_{(1\,bar,298)}$ must be corrected for this (Carpenter et al., 2000; Angel et al., 2017) and is, therefore, lower than the measured volume of the tetragonal phase at ambient conditions by $\sim V_{\max}$.

We can determine values of $V^0_{(1\,bar,298)}$, $V_{\max}$, $S_{\max}$ and T^0_c by fitting both the experimental phase transition conditions using the data in figure 3.6 and the volume data for the orthorhombic phase simultaneously, however, to make the fitting internally consistent for both phases we also refine κ_0 and α_0 of the tetragonal phase in a weighted least squares refinement. The resulting parameters are reported in table 3.5. The refined phase transition boundary is shown in figure 3.6 and the volumes predicted by the model along different isotherms are shown in figure 3.7. The refined gradient of the phase boundary is 223 KGPa^{-1}. This is at the high end of the values proposed for the isostructural SiO$_2$ stishovite to CaCl$_2$-structure transition, for which proposed values range from 180 to 64.6 KGPa^{-1} (Akins and Ahrens, 2002; Fischer et al., 2018 and references therein).

It is, however, in very good agreement with several *ab initio* determinations for the slope of the SiO$_2$ transition boundary (Tsuchiya et al., 2004; Yang and Wu, 2014). As shown in figure 3.7, the volumes are predicted to drop more rapidly with pressure as the phase transition is crossed, but this effect gets smaller at higher temperatures. If such behaviour is also followed by the isostructural stishovite to CaCl$_2$-structure transition in SiO$_2$, the effects, at least on the volume, due to the transition may get weaker at high temperatures. The same model is used to calculate the Gibbs free energy of the orthorhombic phase in section 3.4.3.
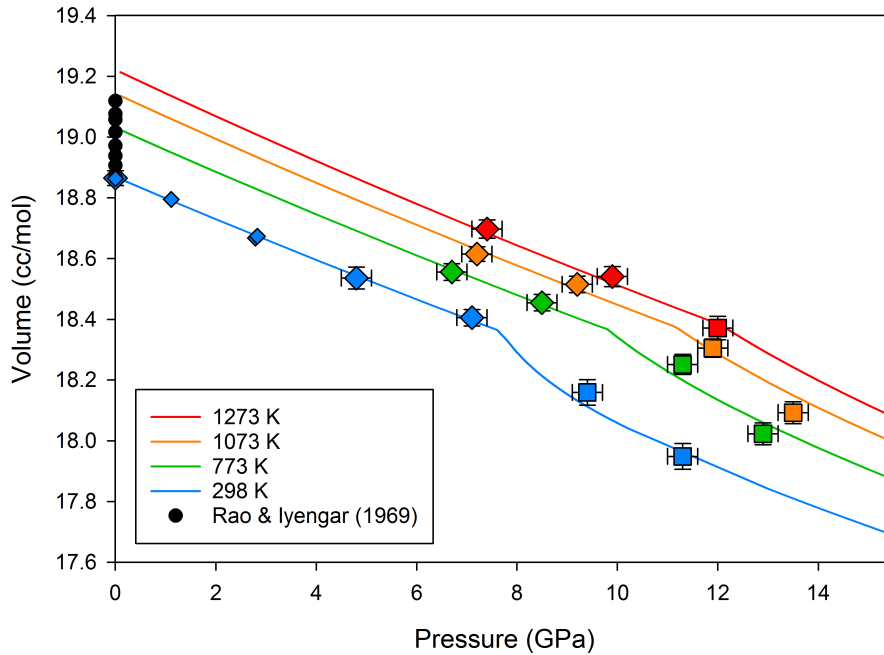
Figure 3.7: P-V-T compression data for the tetragonal (diamonds) and orthorhombic (squares) phases of RuO2. Curves show the equation of state model which accounts for the effect of the second order phase transition using Landau theory. Results of single crystal compression experiments by Hazen and Finger (1981; small diamonds) and room pressure thermal expansion measurements to 975 K (Rao and Iyengar 1969) are also shown and were included in the fitting procedure.

The cubic RuO$_2$ phase was formed on heating to 1473 K at 15.8 GPa. Although the observations are not reversed, cooling of the cubic phase to 1273 K at 15 GPa and 1073 K at 14.1 GPa resulted in no back transformation and we tentatively assume that the cubic phase remained in its stability field at these conditions. Furthermore, an experiment at 13.7 and 1073 K remained in the orthorhombic structure, providing a tight bracket on the transition conditions at this temperature. Multianvil quench experiments at 2473 K that produced the tetragonal and cubic phases at 17 GPa and 20 GPa, respectively, also constrain the transformation boundary, which is fitted with a thermodynamic model described in section 3.4.3.

If the resulting boundary, shown in Figure 3.6, is extrapolated to room temperature, the transition pressure is at ~ 11.5 GPa. This is in good agreement with the appearance of X-ray diffraction lines for the cubic phase that were

observed above 12 GPa at room temperature by Haines and Léger (1993), who found this to be a kinetically slow transition, with some crystals still in the orthorhombic structure to 40 GPa. Both the cubic and the orthorhombic phases must have the potential to remain metastable at temperatures below 1073 K, however, as Ono and Mibe (2011) report the occurrence of the orthorhombic phase at pressures where our reaction boundary would imply that the cubic phase is stable. For this reason we do not employ data below 1073 K to constrain the stability field of the cubic phase, as the potential for metstability exists. *Ab initio* simulations (Tse et al., 2000) predict the room temperature transition at a slightly greater pressure of 13 GPa.

The P-V-T EoS of the cubic phase was fitted using the data shown in figure 3.8. This yields a significantly lower bulk modulus (237 ± 5 GPa) than previously proposed (399 GPa, Haines and Léger, 1993). *Ab initio* studies have predicted lower values of the bulk modulus, between 299 and 380 depending on method (Lundin et al., 1998; Tse et al., 2000), but even the lowest calculated value is significantly greater than our refined value. It is possible that the sparse data coverage provides insufficient constraints on κ_0, particularly if κ_0' for this phase is different to 4. However, as the objective of this work is to facilitate calculating the Gibbs free energy of RuO$_2$ phases at high P and T, finding fit parameters that accurately describe the elastic properties is a secondary concern to deriving a model that suitably describes the volumes. As will be shown, large uncertainties in κ_0 for cubic RuO$_2$ result in relatively small uncertainties in the calculated fO$_2$ for the Ru-RuO$_2$ buffering equilibrium. Our data indicate a ΔV of the orthorhombic-cubic transition at room temperature to be 7.3% at the approximate pressure of the transition. This is between the previously reported values of 6.1% (Haines et al., 1996) and 10% (Ming and Magnhani, 1982).
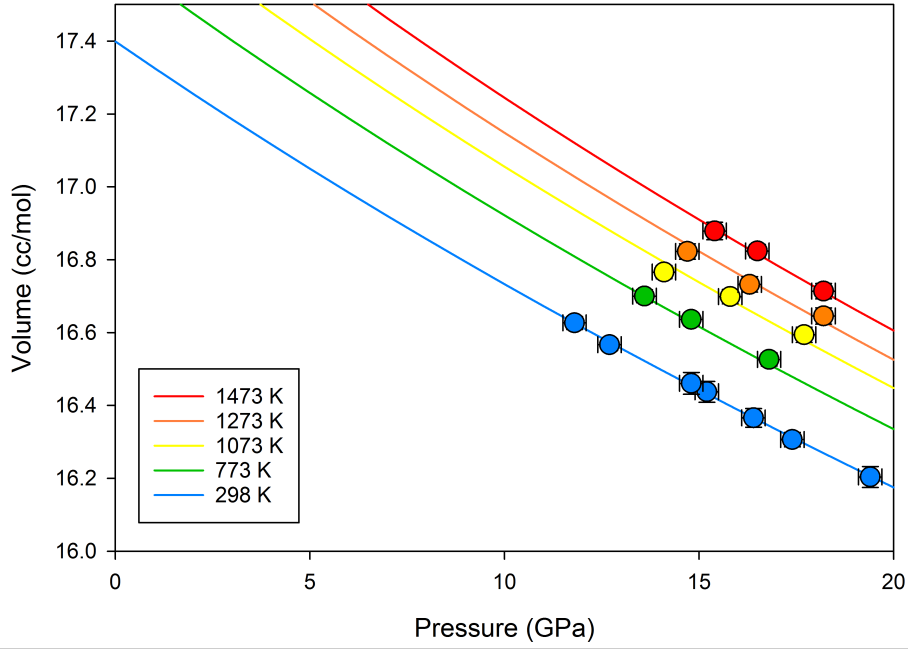
Figure 3.8: Experimental P-V-T data for cubic RuO$_2$ and curves showing the results of EoS fitting at the temperatures indicated.

Table 3.5: Equation of state fitting parameters. Einstein temperature, θ, was estimated from the molar entropy as described in the text.

Phase	V_0 (Å^3)	κ_0 (GPa)	$\partial\kappa/\partial T$	θ (K)	α_0 ($\times10^{-5}$)	α_1($\times10^{-8}$)
Ru Metal	27.185 (4)	301 (2)	-0.050 (4)		2.15 (22)	0.78 (24)
RuO$_2$						
Tetragonal	62.89 (5)	261 (4)		487	1.57 (7)	
Cubic	115.61 (12)	237 (5)		513	2.32 (5)	

Landau Terms	V_{max} (J $\cdot$ bar^{-1})	S_{max} (J $\cdot$ K^{-1})	T_c^0 (K)
	0.0253	1.14	-1413

3.4.3 Thermodynamic analysis of RuO$_2$ phase relations

In order to calculate oxygen fugacities for the Ru-RuO$_2$ buffer, descriptions for the Gibbs free energies of all three RuO$_2$ phases are required. The Gibbs free energy for both the tetragonal and orthorhombic phases can be determined

from the Landau theory expression,

$$G^{\text{tet/orth}}_{(P,T)} = G^0_{(P,T)} + G^{ex}_{(P,T)} \tag{3.15}$$

where $G^0_{(P,T)}$ is the Gibbs free energy of the high-symmetry tetragonal phase at the pressure and temperature of interest, determined using the standard state thermodynamic terms in Table 3.6 and the EoS data in Table 3.5. $G^{ex}_{(P,T)}$ is the excess free energy arising from the second-order phase transition, which can be calculated from

$$G^{ex}_{(P,T)} = H^{ex}_{1,T} + T S^{ex}_{1,T} + V_{\max} Q^2_{298} P \tag{3.16}$$

where the excess enthalpy and entropy are determined from:

$$
\begin{aligned}
H^{ex}_{1,T} &= S_{\max} \left[T^0_c (Q^2_{298} + \frac{1}{2}(Q^4 - Q^4_{298})) - T_c Q^2 \right] & (3.17) \\
S^{ex}_{1,T} &= S_{\max} \left[Q^2_{298} - Q^2 \right]. & (3.18)
\end{aligned}
$$

The standard state Gibbs free energy of formation for the cubic phase at 1 bar at the temperature of interest, $\Delta_f G^{0\,\text{cubic}}_{1,T}$, was calculated from the determined phase boundary conditions using $G^{\text{orth}}_{P,T}$ determined from equation 3.16 with the Landau terms previously reported, and the EoS of the cubic phase, i.e.:

$$\Delta_f G^{0\,\text{cubic}}_{1,T} = G^{\text{tet/orth}}_{P,T} - \int_{1\,\text{bar}}^{P} V^{\text{cubic}} dP. \tag{3.19}$$

The advantage of using the modified Tait EoS is that $\int_{1\,\text{bar}}^{P} V dP$ (equation 3.7) is relatively straightforward and gives:

$$PV_0 \cdot \left(1 - a + \left(\frac{a((1 - bP_{\text{th}})^{1-c} - (1 + b(P - P_{\text{th}}))^{1-c})}{b(1-c)P} \right) \right) \tag{3.20}$$

all terms of which can be directly determined using equations 3.6-3.20, without the need for iteration. In the absence of heat capacity (C_p) data for the cubic phase we use the same values as for the tetragonal phase but then refine the first C_p polynomial term a along with S and $\Delta_f H$ in a weighted least squares fit to the phase boundary data shown in figure 3.6. The resulting boundary is that plotted in figure 3.6, which, when compared to the slope

of the tetragonal to orthorhombic transition, implies that the orthorhombic phase field may pinch out at high temperatures.

Table 3.6: Molar thermodynamic properties for calculating the fO$_2$ for the Ru-RuO$_2$ buffer. The C_p equation is $a + bT + cT^{-2} + dT^{-0.5}$. The * indicates values refined in this study, whereas all other data were either determined or compiled by O'Neill and Nell (1997). § the volume is lower than the measured value due to the contribution from $V^{ex}_{(P,T)}$ through equation 3.14.

| Phase | S | $\Delta_f H$ | V_0 | C_p | (kJ$\cdot$K^{-1}) | | |
	(J$\cdot$K^{-1})	(kJ)	(J$\cdot$bar^{-1})	a	b	c	d
RuO$_2$ (tetrag)	46.15	-314.13	1.856*§	119.277	0.000626	-105800	-1074.6
RuO$_2$ (cubic)	41.94*	-299.88*	1.736*	121.951*	0.000626	-105800	-1074.6
Ru	28.5			13.054	0.010052	-345700	205.2
O$_2$	205.15			47.255	-0.00046	440200	-393.5

3.5 The Ru-RuO$_2$ oxygen buffer

The oxygen fugacity of the Ru $+$ O$_2$ $=$ RuO$_2$ buffer can be calculated using the relation:

$$RT \ln f\mathrm{O}_2 = \Delta_r G^0_{T,1\,\mathrm{bar}} + \int_{1\,\mathrm{bar}}^{P} \Delta V dP. \tag{3.21}$$

The thermodynamic data for calculating $\Delta_r G^0_{T,1\,\mathrm{bar}}$ for the component phases is listed in table 3.6. A continuous Gibbs free energy is calculated for the tetragonal and orthorhombic phases using equations 3.15-3.18, following the methodology of Holland and Powell (1998), although noting that Holland and Powell provide Landau equations for a tricritical transition, whereas the RuO$_2$ transition, as for stishovite, is second-order.

The only other redox buffers where EoS data allow oxygen fugacities to be reliably determined at pressures > 10 GPa are for the equilibria 2Fe+O$_2$ $=$ 2FeO (IW) and 2Ni $+$ O$_2$ $=$ 2NiO (NNO) (Campbell et al., 2009). In figure 1.2 oxygen fugacities calculated for the Ru-RuO$_2$ buffer are normalised against the NNO buffer in order to remove the strong pressure variation. The curve for the equilibrium involving tetragonal and orthorhombic RuO$_2$ shows that there is no perceptible influence on the fO$_2$ due to the second-order phase transition, which occurs at ~ 12 GPa at 1273 K. The transition to the cubic phase has

a much larger effect on both the slope and the absolute value of the fO$_2$, which is lower by ~ 0.5 log units at 25 GPa than the value extrapolated for the orthorhombic RuO$_2$ phase. This difference decreases significantly at high temperature, however, and both values are within 0.2 log units at 2473 K and 25 GPa.

In figure 1.2 we also make two types of comparisons with extrapolations based on only low pressure data. At 1273 K a dashed curve is calculated assuming a constant ΔV for the solid phases of the buffering reaction, i.e. ignoring phase transformations and equations of state. The calculated oxygen fugacity is over 1 log unit higher than that determined for the cubic phase at 25 GPa. If, however, the previously available EoS data are employed (compiled by O'Neill and Nell, 1997) but the phase transformations are again ignored, as shown by the dashed curve at 2473 K, the resulting oxygen fugacities are still 0.5 log units higher even than those calculated for the extrapolated orthorhombic phase. This demonstrates that simultaneous high P and T EoS data are indeed important for determining accurate oxygen fugacities at pressures approaching those of the lower mantle.

However, the uncertainties in the determined EoS properties have a relatively small influence on the resulting oxygen fugacities, provided they are approximately of the correct magnitude. κ_0 of the cubic RuO$_2$ phase, for example, would have to change by 40 GPa in order to change the fO$_2$ of the buffer at 1273 K and 25 GPa by 0.1 log units. An uncertainty of 20 % on α_0 also propagates to only 0.1 log units in fO$_2$ at the same conditions, although it corresponds to volume uncertainties that are ten times larger than those measured.

Propagating all EoS uncertainties over the conditions shown in figure 1.2 results in a maximum fO$_2$ uncertainty of 0.1 log units. We can determine the uncertainties arising from the phase boundary determination of the cubic RuO$_2$ transformation by changing the boundary gradient. The experimentally determined boundary has a gradient of 390 KGPa^{-1}. If we increase this to 570 KGPa^{-1}, while maintaining approximately the same transition pressure at 298 K, this equates to an uncertainty in the determined pressure of ~ 1 GPa at 1273 K and ~ 1.8 GPa at 2473 K, well outside of the experimental uncertainties of 0.3 and 0.5 GPa, respectively. The resulting change in thermodynamic

properties determined for the cubic RuO$_2$ phase propagates to a change in calculated fO$_2$ at 1273 K and 25 GPa of only 0.06 log units. The same changes in properties result in even smaller shifts in fO$_2$ at higher temperatures or lower pressures. As a result the maximum uncertainty in fO$_2$ over the conditions shown in figure 1.2 is less than 0.2 log units.
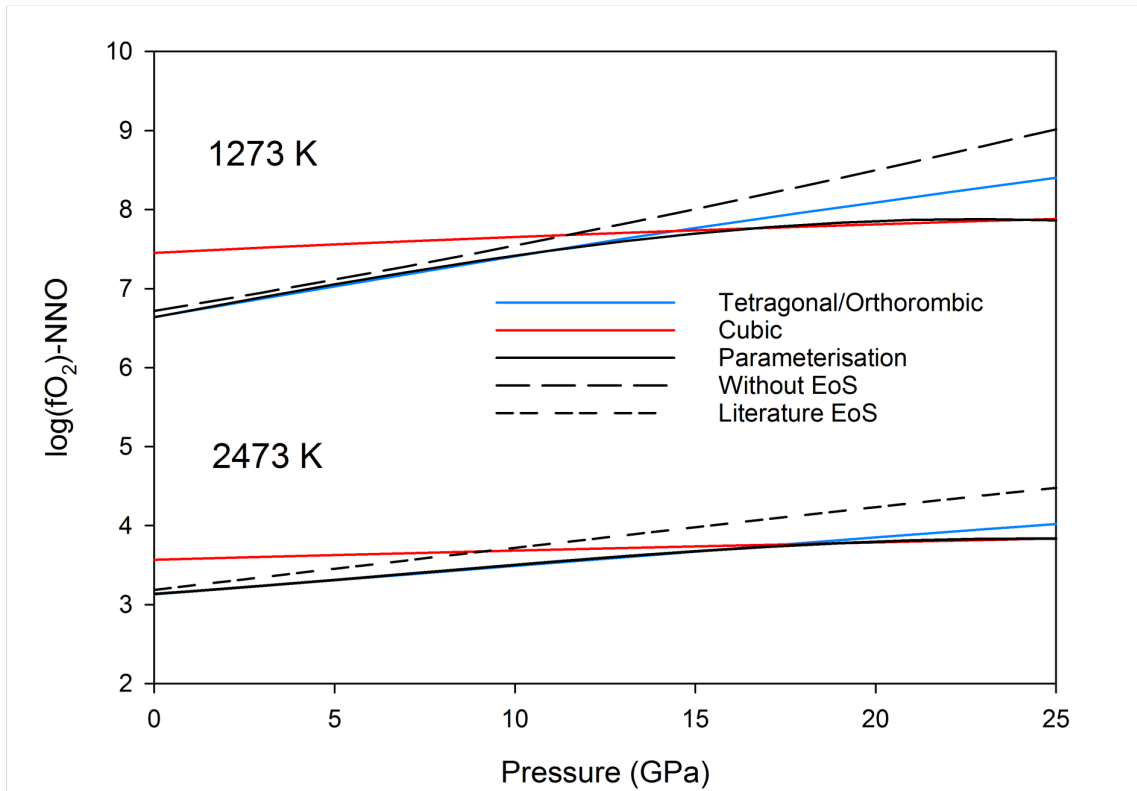
Figure 3.9: The $\log f$O$_2$ for the Ru $+$ O$_2$ $=$ RuO$_2$ buffering equilibrium at 1273 K and 2473 K calculated for the three RuO$_2$ polymorphs as a function of pressure, and normalized to the oxygen fugacity of the nickel-nickel oxide (NNO) buffer (Campbell et al., 2009). The black curve shows the polynomial parameterisation which predicts the $\log f$O$_2$ for the Ru-RuO$_2$ buffer to within 0.05 of a log unit over this pressure and temperature range. For comparison, the dashed grey curve at 1273 K shows the extrapolated fO$_2$ assuming a constant room P and T volume change for the buffering reaction, whereas the dashed grey curve at 2473 K shows the fO$_2$ calculated using the previous EoS parameters summarized by O'Neill and Nell (1997). Both extrapolations ignore the occurrence of RuO$_2$ phase transitions.

We have parameterised the oxygen fugacity of the Ru-RuO$_2$ buffer across the stability fields of all three RuO$_2$ phases using a single polynomial of a similar

form to that used by Campbell et al. (2009) i.e:

$$\log_{10} f\mathrm{O}_2(\mathrm{Ru} - \mathrm{RuO}_2) = \left(a_0 + a_1 P + a_2 P^2 + a_3 P^3\right) + \left(b_0 + b_1 P + b_2 P^2\right)/T + (c_0 + c_1 P)/T^2$$

Using a least squares fitting routine the following parameters were refined:

a_0	a_1	a_2	a_3	b_0	b_1	b_2	c_0	c_1
7.783	-0.0113	0.00209	$-4.10 \cdot 10^{-5}$	-13764	593.4	-4.08	$-1.05 \cdot 10^6$	-4511

where P is in GPa and T in K. Curves calculated from this parameterisation are shown in figure 1.2, although they are to some extent eclipsed by the thermo-dynamically calculated curves to which they have been fitted. The maximum difference with the thermodynamically calculated curves occurs near the orthorhombic to cubic phase transition but is never greater than 0.05 log units over the range of fitted conditions, which cover 773-2773 K and to 25 GPa. The polynomial likely becomes rapidly unreliable if extrapolated outside of this range.

3.6 Conclusions

In order to experimentally investigate the stability of ferric iron bearing phases at conditions compatible with the Earth's deep mantle, oxygen fugacity buffers are required that can be mixed directly with experimental samples and undergo minimal chemical interaction other than exchanging oxygen. The Ru-RuO$_2$ oxygen buffer fulfills this criterion, but the volumes of both phases and phase transition boundaries need to be accurately known at high pressures and temperatures if oxygen fugacities are to be correctly calculated. We have determined the phase relations and P-V-T equation of state properties for Ru and RuO$_2$ phases using in situ x-ray diffraction and additional quench experiments in multianvil devices.

While no phase transformations were found for Ru metal, RuO$_2$ which is tetragonal (rutile-structure) at room pressure undergoes a second-order phase transformation to an orthorhombic CaCl$_2$ structured phase and then a first order transformation to a cubic (pyrite-type) structured phase. We have used a

model based on Landau theory combined with the modified Tait EoS (Holland and Powell, 1998) to derive a continuous Gibbs free energy expression for the tetragonal and orthorhombic phases by fitting the second-order phase transition boundary and P-V-T data for both phases. The phase relations for the transition between the orthorhombic and cubic phases were then used along with EoS data for both phases to determine a Gibbs free energy expression for the cubic phase.

The refined gradients for the second- and first-order phase boundaries are 223 KGPa^{-1} and 390 KGPa^{-1}, respectively, which implies that the stability field of the orthorhombic phase pinches out at temperatures > 2500 K. A number of studies have emphasized the importance of RuO_2 transformations as analogues for those encountered by SiO_2 at lower mantle conditions (Haines et al., 1996; 1997; 1998; Haines and Léger 1993; Ming and Magnhani, 1982; Ono and Mibe, 2011; Ahuja et al., 2001; Rosenblum et al., 1997).

While the RuO_2 second order rutile to $CaCl_2$-type transition is isostructural to that observed for stishovite, the first-order transition to the pyrite structure differs, as SiO_2 first assumes an orthorhombic αPbO_2-type structure above 100 GPa and only assumes the pyrite-type structure above 270 GPa (Kuwayama et al., 2005). In the pyrite-type structure, the Ru cations occupy the corners and the face centers of the unit cell whereas in the αPbO_2-type structure the Ru cations would be required to occupy positions well inside the unit cell. This would likely result in Ru-O bonds that are too short, whereas this is quite possible for the smaller Si cations. For this reason we probably cannot draw conclusions as to the shape of the $CaCl_2$-type stability field for SiO_2 based on our results for RuO_2, because the breakdown transition at high pressure is quite different.

It has been proposed that the stishovite second-order transition could create an observable seismic anomaly, or cause scattering of seismic waves in the lower mantle, because the shear modulus goes through a minimum at the transition (Andrault et al., 1998; Carpenter et al., 2000). Although we can place no constraints on this elastic behavior for the RuO_2 phases, we note that the influence of the transition on the volume of RuO_2, while quite strong at room temperature, is predicted by our model to decrease with increasing

temperature. This emphasizes the need to support room temperature investigations of the elastic properties across such transitions with high temperature data if conclusions concerning seismic behavior in the lower mantle are to be drawn.

Using the refined thermodynamic and EoS properties for both Ru and RuO$_2$ phases the oxygen fugacity of the buffering assemblage can be calculated reliably to 25 GPa and between 773-2500 K, with an estimated uncertainty of 0.2 log units. A polynomial expression fit to these data provides an accurate description for the oxygen fugacity of the Ru-RuO$_2$ buffer to conditions at the top of the lower mantle.

4 Self-oxidation within a magma ocean

4.1 Motivation

As detailed in section 1.3.1, it is possible that a deep global magma ocean could have been relatively oxidised at its surface whilst remaining in equilibrium with metallic iron at its base. Briefly, if pressure stabilises the ferric iron (Fe^{3+}) component of silicate melts, and final metal-silicate equilibrium occurred at the base of a deep magma ocean, then the ferric iron content, imposed by the presence of iron metal on the magma ocean, may have been higher than expected for iron metal equilibration at low pressure. If the ferric iron content of the entire magma ocean was relatively constant as a result of convective mixing, then, at low pressure near the surface the oxygen fugacity may have been much higher. Thus the oxygen fugacity of a deep magma ocean could plausibly decrease with depth, given a constant ferric/ferrous iron ratio (figure 1.8).

If correct, the ferric iron content of a silicate melt should increase with pressure at a constant relative fO_2. This can readily be seen from the equilibrium of the reaction

$$FeO + \frac{1}{4}O_2 = FeO_{1.5}. \tag{4.1}$$

In terms of Gibbs free energy, the relationship between pressure (i.e., the changes in molar volume of FeO and $FeO_{1.5}$), ferric iron content and fO_2 at

equilibrium is given by

$$-(\Delta G_r^0(4.1) + \int_1^P \Delta V(4.1) \mathrm{d}P) = RT \ln \frac{X_{\mathrm{FeO}_{1.5}} \cdot \gamma_{\mathrm{FeO}_{1.5}}}{X_{\mathrm{FeO}} \cdot \gamma_{\mathrm{FeO}}} - \frac{1}{4} RT \ln f\mathrm{O}_2 \qquad (4.2)$$

where ΔG_r^0 is the Gibbs free energy of reaction 4.1, ΔV is the volume change of reaction 4.1, T is the temperature (in K), X_i and γ_i are the mole fraction and activity coefficient of i, respectively, and R is the universal gas constant.

Clearly, at a constant $X_{\mathrm{FeO}}/X_{\mathrm{FeO}_{1.5}}$ ratio, the oxygen fugacity of equilibrium 4.1 will change with pressure as a result of the volume change associated with the reaction. If the oxygen fugacity is buffered at a constant relative value, however, the ratio of $X_{\mathrm{FeO}}/X_{\mathrm{FeO}_{1.5}}$ will change with pressure. As seen in section 1.3.1, at the relatively low pressures tested to date, up to 7 GPa (O'Neill et al., 2006; Zhang et al., 2017), the volume change of reaction 4.2 has been shown to be positive. For this reason, MORB magmas have an associated $f\mathrm{O}_2$ which is more oxidised at the source than at the surface, as shown in figure 1.3. Magmas become more reduced as they ascend due to the positive ΔV of reaction 4.1. Therefore, at a constant relative $f\mathrm{O}_2$, pressure favors Fe^{2+} (figure 1.9), rather than Fe^{3+}, precluding the possilibilty of a magma ocean that is reduced at depth becoming more oxidised in the direction of the surface. However, as discussed in section 1.3.1, this trend may reverse at higher pressure.

4.2 Approach

In order to examine the volume change of reaction 4.1 at pressures above 7 GPa, three sets of experiments were performed, for different bulk compositions at different relative oxygen fugacities and pressures. The ferric iron content of the resulting glass or quench assemblage was then measured. The primary set of experiments extends the dataset in figure 1.9 to 23 GPa, and were performed with an andesitic composition (O'Neill et al., 2006; Zhang et al., 2017). The higher SiO_2 content and degree of polymerisation of this melt were selected in order to extend the pressure range over which the melt will

quench to a glass compared to more mafic compositions. Constant relative oxygen fugacity was accomplished through the addition of ruthenium metal and ruthenium dioxide directly inside the experimental capsule (see figure 4.1). This particular buffer assemblage was employed for two reasons: first, it is quite oxidising (ΔIW = +11.28 log units at 1000 °C), which results in relatively high and easily measureable ferric iron contents of the melts. Additionally, RuO_2 has an extremely low solubility in silicate melts, which allows the buffer assemblage to be added into the sample charge directly, with minimal chemical interaction with the sample other than the exchange of oxygen (O'Neill et al., 2006; Zhang et al., 2017; chapter 3 this work). The results from this set of experiments were used to develop a thermodynamic model to describe the pressure dependence of reaction 4.1 (section 4.5).

A second set experiments were performed to test the resulting model's sensitivity to melt composition, using a mid-ocean ridge basalt (MORB) composition (Gale et al., 2013) at the same oxygen fugacity (i.e., as defined by the Ru and RuO_2 equilibrium). The compositions of both starting materials are reported in table 4.1.

A third set of experiments was conducted with the andesitic composition, but at metal iron saturation, with powdered metallic Fe added directly to the sample charge (figure 4.1), in order to constrain the pressure effect of equilibrium 4.1 at a much lower oxygen fugacity.

Table 4.1: Andesitic and mid-ocean ridge basalt starting compositions, in weight %

	SiO_2	TiO_2	Al_2O_3	Fe_2O_3	MgO	CaO	Na_2O	K_2O
Andesite	57.3	3.0	14.8	9.4	2.1	7.4	4.4	1.1
MORB	50.9	1.7	14.8	10.1	8.1	11.5	2.8	0

4.3 Experimental methods

Starting materials were prepared from reagent grade oxides and carbonates, which were ground under ethanol with an agate mortar and pestle. Oxides

were devolatilised at 1000 °C for three hours before weighing, and after preparation the bulk composition was devolatilised at 1000 °C for 12 hours. For the primary andesitic and MORB experiments, powdered starting material plus approximately 20 wt% of a Ru/RuO$_2$ mixture (previously mixed together in the proportion 1:1 by weight) was sealed by welding into platinum capsules. For the metal saturated experiments, graphite capsules were used. Capsules were placed in an octahedral Cr-doped MgO pressure medium (figure 4.1), and then equilibrated at high pressure and superliquidus temperature in a multi-anvil press at the Bayerisches Geoinstitut. Refer to section 2.1 for a detailed description of the multianvil technique.
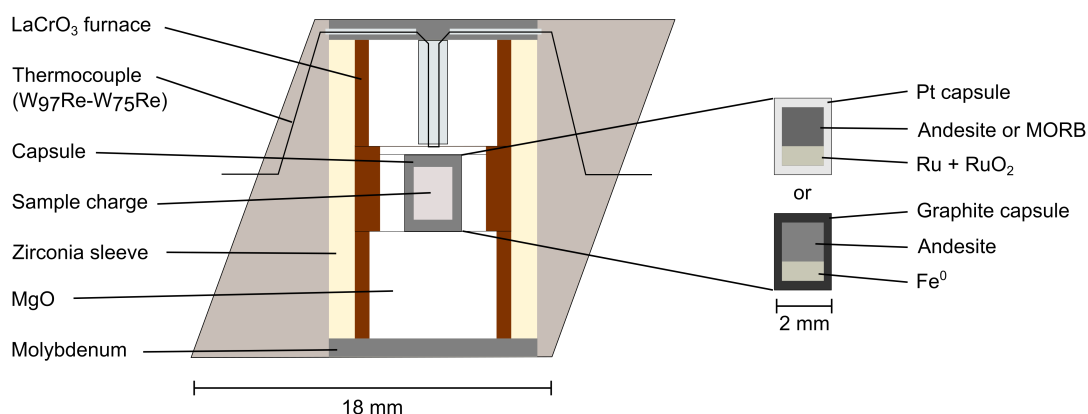

Figure 4.1: Schematic of the experimental assembly used for the majority of experiments (18/11, see section 2.1). Higher-pressure assemblies (10/4 and 10/5) differ only in that they are 10 mm edge-length, and capsules are 1.2 or 1.7 mm in diameter, respectively. In addition, the LaCrO$_3$ heating element is a straight cylinder, rather than stepped. For experiments under 10 GPa, stepped graphite rather than LaCrO$_3$ heating elements were used.

Most of the experiments were performed with a fully oxidised starting material, where all Fe was initially Fe$_2$O$_3$, but in order to confirm redox equilibrium had been achieved several reversal experiments were conducted. For these, the starting material had been initially reduced in a 1-atm CO-CO$_2$ gas-mixing furnace overnight at 1100 °C and an oxygen fugacity $\sim$ FMQ $- 2$, such that all Fe was FeO, verified by Mössbauer spectroscopy (figure 4.2). Refer to table 4.2 for a list of all experiments and their conditions. The majority of experiments were performed with an 18/11 assembly (see section 2.1), but for the higher-pressure experiments other assembly sizes were used (table 4.2). Temperature was monitored with a W$_{97}$Re$_3$ $-$ W$_{75}$Re$_{25}$ (type D) thermocouple, except in one

case when temperature was estimated from a power curve (table 4.2). The duration of the experiments was between 5 and 30 minutes, which previous studies and the reversal experiments indicate is sufficient to reach redox equilibrium (Zhang et al., 2017, figure 4.5 this work). Temperature was quenched by turning off power to the heater, which yields a rapid quench rate of >500 K/sec.

Table 4.2: Conditions for all experiments in this study. An (*) indicates that the starting materials had initially been reduced in a 1-atm gas-mixing furnace such that all Fe present would be FeO. Otherwise the starting material was fully oxidised, such that all Fe was Fe_2O_3. A (**) indicates that the thermocouple broke and temperature was estimated from the input power. Experiment Z1794 was prepared with oxidised starting material, and Ru was added only as metal. RuO_2 was formed during the experiment.

| Expt #	Pressure (GPa)	Temp (°C)	Duration (min)	Assembly	Redox buffer	Starting composition
S6928	4	1400	15	18/11	Ru+ RuO_2	Andesite
S6889	6	1750	15	18/11	Ru + RuO_2	Andesite
S6879	6	1900	15	18/11	Ru + RuO_2*	Andesite
S6820	6	1750	10	18/11	Ru + RuO_2	Andesite
S6811	6	1900	5	18/11	Ru + RuO_2*	Andesite
S6777	8	1900	30	18/11	Ru + RuO_2	Andesite
S6510	10	1900	30	18/11	Ru + RuO_2	Andesite
Z1794	10	1900	30	18/11	Ru metal only	Andesite
Z1468	15	2100	45	18/11	Ru + RuO_2	Andesite
Z1621	17	2200	10	18/11	Ru + RuO_2	Andesite
Z1666	18	2200	10	18/11	Ru + RuO_2*	Andesite
S6654	20	2200	5	10/5	Ru + RuO_2	Andesite
S6606	23	2300**	5	10/4	Ru + RuO_2	Andesite
S6776	23	2300	10	10/4	Ru + RuO_2*	Andesite
S6973	4	1600	20	18/11	Ru + RuO_2*	MORB
S6977	8	1900	30	18/11	Ru + RuO_2*	MORB
Z1791	18	2200	15	18/11	Ru + RuO_2*	MORB
Z1850	18	2200	10	18/11	Ru + RuO_2*	MORB
S6775	3	1750	10	18/11	Fe metal	Andesite
S6729	8	1900	10	18/11	Fe metal	Andesite
S6665	10	1900	30	18/11	Fe metal	Andesite
Z1626	15	2200	10	18/11	Fe metal	Andesite
Z1630	17	2200	15	18/11	Fe metal	Andesite
Z1647	20	2200	10	18/8	Fe metal	Andesite
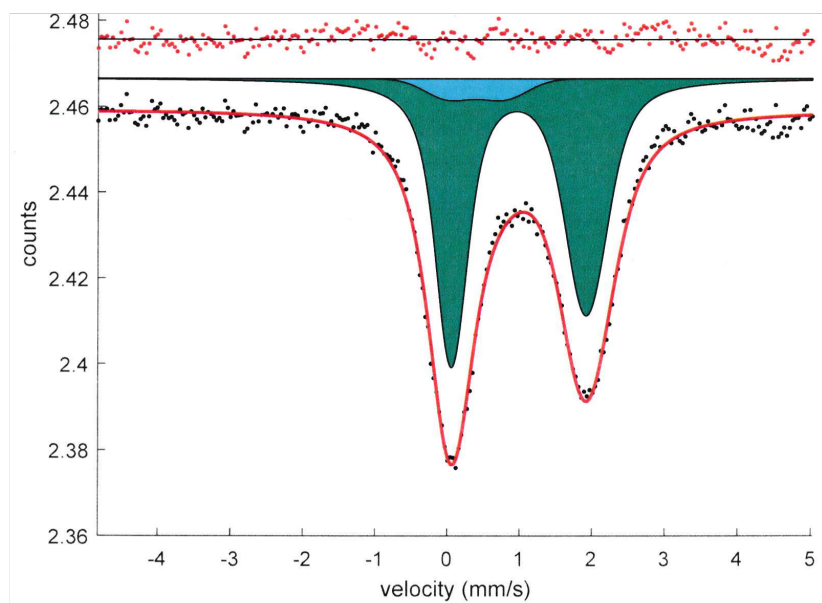
Figure 4.2: Transmission Mössbauer spectrum of the starting material for reversal experiments, which had been reduced in a 1-atm CO-CO$_2$ gas-mixing furnace overnight in order to ensure all Fe was present as FeO. A small amount- 5%- of Fe$_2$O$_3$ remains (blue doublet) however the majority of Fe has reacted.

4.4 Results

4.4.1 Texture, phase assemblage, and bulk chemical composition

Recovered samples were sectioned and ground down to a thickness of 500 µm for transmission Mössbauer spectroscopy, with one side polished for analysis with scanning electron microscopy (SEM), Energy-dispersive spectroscopy (EDS), X-ray diffraction (XRD), and electron microprobe analyses (EPMA). In all experiments conducted with the andesitic composition, the sample melted completely. The experiments with MORB composition at 4 and 8 GPa melted completely, but attempts at 18 GPa yielded only a partial melt (see section 4.7). Below 10 GPa sample melt quenched to a glass, but above 10 GPa the melt crysallised during the quench (see section 4.10 and figure 4.3). Backscattered electron imaging, EDS, XRD, and EPMA indicate that all crystalline samples comprise homogeneous assemblages of clinopyroxene and/or garnet; coesite

or stishovite; and the buffer phases (either Ru + RuO$_2$ or iron metal). In all experiments performed with Ru and RuO$_2$ both phases were always present. However, in some experiments Ru alloyed with Pt from the capsule as will be discussed in section 4.8. Bulk compositions of all samples, obtained with EPMA, are given in table 4.3. Microprobe analyses were carried out with an accelerating voltage of 15keV, and a current between 10-15 nA depending on the phase being analysed. Analysis spot sizes were ~ 1 μm for glasses but defocused to ~ 15 μm for the crystalline samples, due to the different crystals present in the assemblage. Standards used to calibrate the elements were: Si - enstatite; Mg - forsterite; Al: spinel; Ca: wollastonite; Fe, Ru: pure metals; Cr: Cr$_2$O$_3$; Ti: rutile; Na: albite.
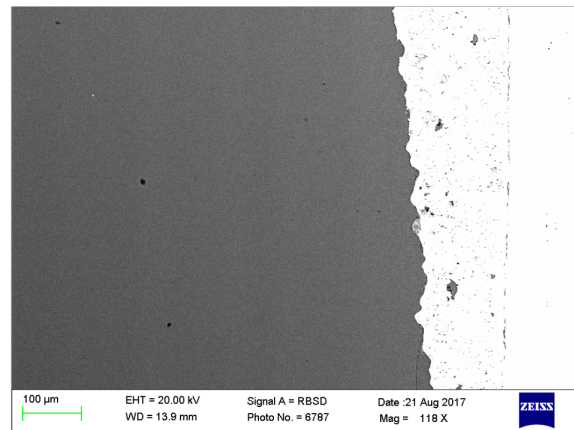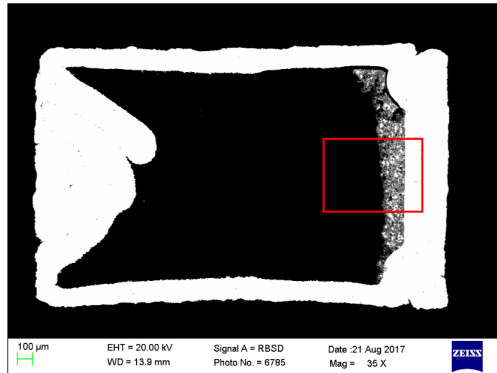
S6889

Z1621

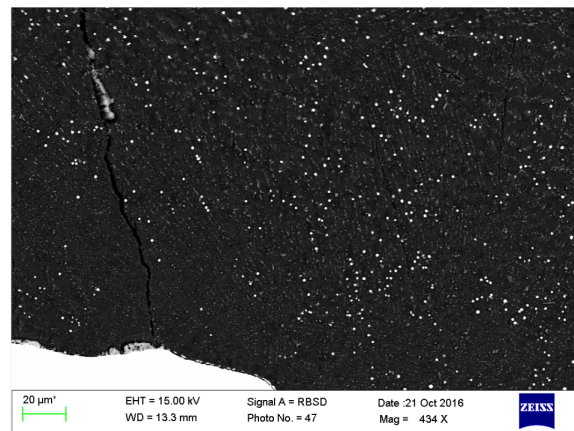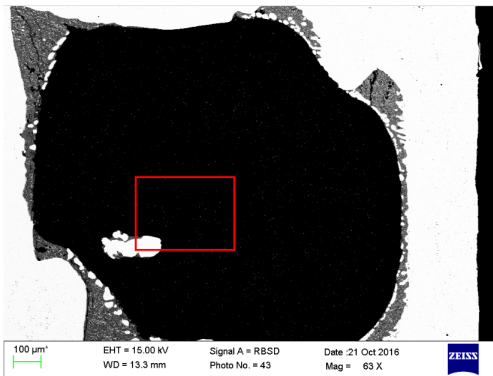**Figure 4.3:** Backscattered electron images of typical run products. S6889, top, was run at 6 GPa and 1750 °C, and quenched to a glass (top right image). Z1621, bottom, was run at 17 GPa and 2200 °C, and quenched to a homogenous assemblage of clinopyroxene and stishovite (bottom right image). Bright spots in the assemblage are RuO_2. Red rectangles on the left images indicate the region of the zoomed image on the right.

Table 4.3: Bulk composition (EPMA) of run products

| Expt #	SiO$_2$	TiO$_2$	Al$_2$O$_3$	MgO	FeO (total Fe)	CaO	Na$_2$O	K$_2$O	RuO$_2$	PtO
S6928	59.06 (1.43)	2.78 (0.12)	15.27 (0.29)	2.21 (0.08)	8.68 (0.17)	7.23 (0.10)	3.99 (0.09)	0.79 (0.03)	0.04 (0.02)	0.13 (0.14)
S6889	56.68 (0.29)	2.39 (0.10)	14.46 (0.09)	2.04 (0.04)	8.37 (0.13)	7.08 (0.04)	4.61 (0.07)	0.78 (0.03)	0.03 (0.03)	0.10 (0.13)
S6879	56.20 (0.47)	2.22 (0.08)	14.81 (0.05)	2.09 (0.02)	5.87 (0.07)	7.19 (0.05)	4.61 (0.05)	0.80 (0.01)	0.53 (0.14)	0.17 (0.10)
S6820	56.19 (0.29)	2.37 (0.05)	14.57 (0.09)	2.05 (0.04)	8.23 (0.12)	7.12 (0.07)	4.57 (0.07)	0.77 (0.02)	0.02 (0.02)	0.21 (0.18)
S6811	59.06 (0.22)	2.80 (0.06)	14.57 (0.08)	2.56 (0.03)	7.35 (0.14)	7.27 (0.08)	4.49 (0.07)	0.82 (0.02)	0.72 (0.23)	0.19 (0.18)
S6777	55.99 (2.67)	2.76 (0.06)	14.65 (0.16)	2.13 (0.03)	6.65 (0.08)	7.02 (0.09)	4.43 (0.06)	0.82 (0.03)	0.82 (0.14)	0.19 (0.19)
S6510	56.41 (1.14)	2.77 (0.40)	14.66 (0.61)	2.14 (0.13)	7.84 (0.25)	7.21 (0.25)	4.45 (0.38)	0.68 (0.16)	1.25 (0.62)	0.12 (0.14)
Z1794	56.90 (2.55)	3.23 (0.73)	14.77 (1.56)	2.24 (0.32)	8.57 (0.72)	7.57 (0.59)	4.87 (1.14)	0.57 (0.25)	0.58 (0.11)	0.17 (0.15)
Z1468	56.23 (2.19)	2.40 (1.01)	15.14 (1.97)	2.11 (0.19)	7.02 (1.32)	7.04 (0.64)	4.78 (1.31)	0.53 (0.22)	1.47 (0.75)	0.16 (0.13)
Z1621	55.70 (1.43)	1.87 (0.71)	16.19 (1.37)	2.44 (0.18)	6.50 (0.65)	7.56 (0.77)	5.66 (0.98)	0.48 (0.16)	1.24 (0.59)	0.16 (0.15)
Z1666	55.16 (0.95)	2.75 (1.27)	15.59 (2.05)	2.41 (0.17)	7.53 (1.62)	7.58 (0.59)	5.20 (1.55)	0.73 (0.31)	2.13 (0.43)	0.24 (0.21)
S6654	55.13 (0.28)	2.36 (0.34)	16.75 (0.70)	2.05 (0.05)	6.13 (0.56)	7.07 (0.32)	4.32 (0.14)	0.57 (0.08)	1.39 (0.31)	0.17 (0.16)
S6606	57.76 (0.61)	2.47 (0.20)	15.31 (1.29)	1.77 (0.20)	6.53 (0.53)	6.39 (0.48)	4.79 (1.16)	1.03 (0.17)	3.01 (0.34)	0.14 (0.15)
S6776	56.40 (2.25)	3.53 (0.77)	13.31 (4.78)	2.77 (0.58)	8.66 (0.33)	7.49 (0.47)	4.42 (1.09)	0.63 (0.12)	2.67 (0.13)	0.15 (0.14)
S6973	47.48 (0.61)	1.34 (0.04)	13.89 (0.15)	7.83 (0.10)	9.48 (0.10)	10.96 (0.08)	2.91 (0.03)	-	0.03 (0.02)	0.05 (0.08)
S6977	47.30 (3.32)	1.59 (0.67)	14.04 (0.89)	7.87 (0.76)	8.17 (0.82)	10.93 (1.03)	3.03 (0.44)	-	1.02 (0.57)	0.18 (0.13)
Z1791	51.22 (0.19)	2.37 (0.09)	15.70 (0.18)	8.57 (0.39)	7.25 (0.40)	12.34 (0.17)	3.30 (0.13)	-	0.56 (0.05)	0.13 (0.18)
Z1850	45.06 (0.52)	0.75 (0.39)	18.33 (0.64)	12.20 (0.96)	8.11 (0.68)	12.87 (0.25)	2.23 (0.22)	-	1.43 (0.74)	0.17 (0.14)
S6775	53.98 (0.51)	2.72 (0.08)	13.76 (0.13)	3.45 (0.09)	12.22 (0.45)	7.50 (0.10)	4.09 (0.06)	0.72 (0.02)	-	-
S6729	55.23 (0.33)	2.59 (0.08)	14.50 (0.11)	2.42 (0.06)	12.18 (0.22)	7.27 (0.10)	4.33 (0.09)	0.52 (0.02)	-	-
S6665	55.67 (0.11)	1.03 (0.04)	15.79 (0.04)	5.55 (0.09)	11.25 (0.36)	8.48 (0.08)	5.81 (0.14)	0.10 (0.01)	-	-
Z1626	52.45 (0.39)	2.40 (0.41)	14.47 (0.80)	2.22 (0.13)	13.82 (1.07)	6.53 (0.12)	5.17 (0.52)	0.58 (0.16)	-	-
Z1630	51.00 (1.13)	2.68 (0.55)	12.77 (2.84)	2.04 (0.48)	14.74 (1.92)	6.46 (0.80)	4.20 (0.99)	0.70 (0.17)	-	-
Z1647	49.59 (3.91)	3.10 (0.31)	14.48 (0.20)	2.18 (0.01)	12.61 (4.17)	7.45 (0.31)	4.81 (0.28)	0.80 (0.09)	-	-

4.4.2 Ferric iron content
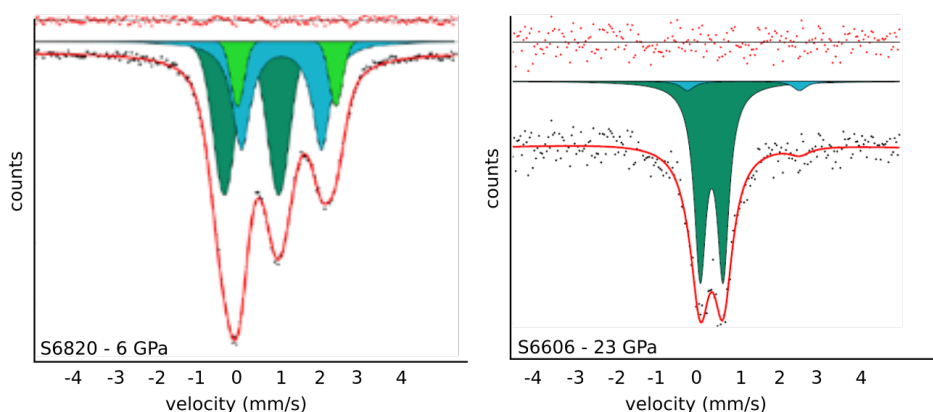
Figure 4.4: Examples of transmission Mössbauer spectra taken for this study. The left spectrum is from a 6 GPa experiment, and its $Fe^{3+}/\sum Fe$ ratio is 0.5. The sample is an amorphous glass, and so the spectrum is broadened. The dark green doublet represents Fe^{3+}, while the two lighter doublets correspond to Fe^{2+} in two different structural environments. On the right is a spectrum from a crysalline sample from an experiment at 23 GPa. The spectrum comprises two subspectra, the darker green represents Fe^{3+}, which has clearly increased in proportion. The small lighter green doublet corresponds to Fe^{2+}, and the $Fe^{3+}/\sum Fe$ of the sample is 0.95.

Transmission Mössbauer spectra were collected over a 500-1000 µm diameter spot in the centre of samples that were parallel ground to a thickness of 500 µm, giving an effective Mössbauer thickness of roughly 10 mg Fe/cm^2 (see figure 4.4 for example spectra, section 2.2.4 for details of the technique, and tables 4.5 and 4.6 for the reported hyperfine parameters). Melt $Fe^{3+}/\sum Fe$ ratios are reported in table 4.4 and plotted in figure 4.5. As will be discussed in section 4.8, the Ru metal of the buffer of some experiments became contaminated with Pt, yielding a higher oxygen fugacity in the experiment and therefore anomalously high $Fe^{3+}/\sum Fe$ ratios. In section 4.7, results of the MORB-composition experiments at 18 GPa, which only underwent partial melting, are discussed. Aside from these outliers, however, it is clear from the data that the trend observed in previous, lower-pressure data sets does indeed begin to reverse above 15 GPa, and ferric iron is increasingly stabilised with pressure above this point. This appears to be true independent of the oxygen fugacity, as shown by the metal-saturated experiments, discussed in section 4.6.
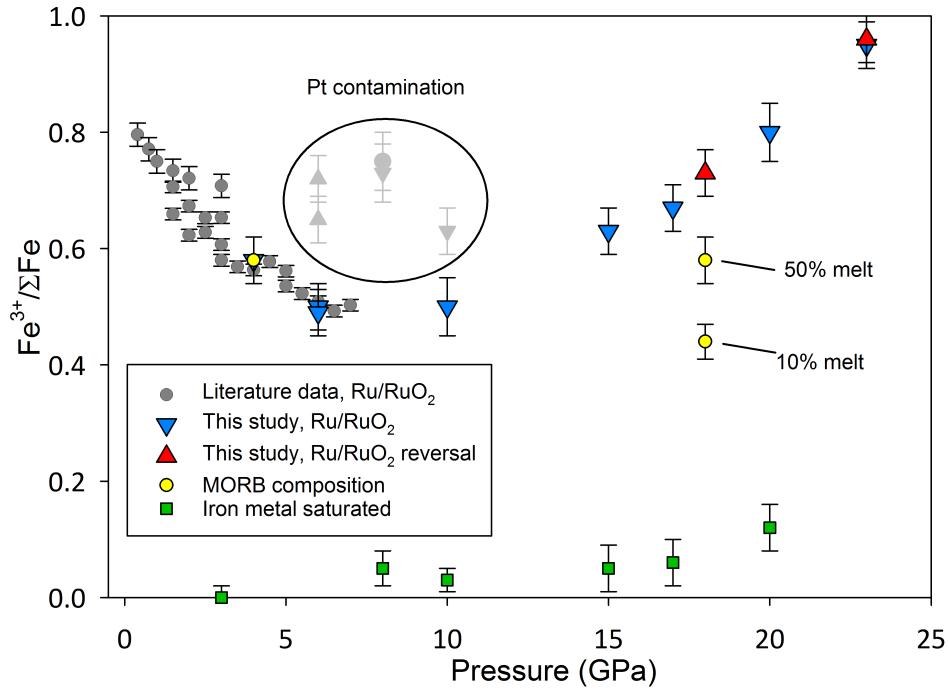
Figure 4.5: Melt ferric iron over total iron ratio, determined from Mössbauer spectroscopy, as a function of pressure at a fixed relative oxygen fugacity, defined by the equilibrium between Ru and RuO_2. Blue symbols indicate the starting composition was initially oxidised and contained all iron as Fe_2O_3, red symbols that it was reduced and contained all iron as FeO (see text). Greyed symbols indicate the oxygen buffer became contaminated during the experiment (section 4.8). MORB-composition samples at 18 GPa did not reach superliquidus conditions (section 4.7).

Table 4.4: Ferric iron content and phases present in the recovered experimental charges. Samples marked with a (*) indicate that they suffered from inhomogenous Pt contamination of the oxygen buffer, and are therefore an unreliable result (see section 4.8). Uncertainties are shown in brackets.

Sample	Pressure (GPa)	Fe^{3+}/ Total Fe	Phases present
S6928	4	0.58 (0.04)	glass
S6889	6	0.49 (0.04)	glass
S6879	6	0.65 (0.04)*	glass
S6820	6	0.50 (0.04)	glass
S6811	6	0.72 (0.04)*	glass
S6777	8	0.73 (0.04)*	glass
S6510	10	0.63 (0.04)*	cpx, coesite
Z1794	10	0.50 (0.05)	cpx, coesite
Z1468	15	0.63 (0.04)	cpx, coesite
Z1621	17	0.67 (0.04)	cpx, stishovite
Z1666	18	0.73 (0.04)	cpx, garnet, stishovite
S6654	20	0.80 (0.05)	cpx, garnet, stishovite
S6606	23	0.95 (0.04)	garnet, stishovite
S6776	23	0.96 (0.04)	garnet, stishovite
S6973	4	0.58 (0.04)	glass
S6977	8	0.75 (0.04)*	glass
Z1791	18	0.44 (0.04)	garnet, stishovite
Z1850	18	0.58 (0.04)	garnet, stishovite
S6775	3	0.00 (0.02)	glass
S6729	8	0.04 (0.03)	glass
S6665	10	0.03 (0.03)	cpx, coesite
Z1626	15	0.05 (0.04)	cpx, garnet, coesite
Z1630	17	0.06 (0.04)	rwd, cpx, stishovite
Z1647	20	0.12 (0.04)	rwd, garnet, stishovite

Table 4.5: Hyperfine parameters from Mössbauer spectra of experiments performed with andesitic composition at the Ru-RuO$_2$ oxygen fugacity buffer

Exp #	CS	FWHM	Intensity	QS	BHF	χ^2
S6928	1.038 (0.014)	0.611 (0.043)	42.323 (3.098)	1.997 (0.026)	NaN	1.3
	0.321 (0.008)	0.648 (0.027)	57.677 (3.098)	1.211 (0.018)	NaN	
S6889	1.004 (0.020)	0.515 (0.111)	39.233 (6.360)	1.841 (0.103)	NaN	1.37
	1.124 (0.046)	0.372 (0.069)	11.752 (7.367)	2.272 (0.058)	NaN	
	0.312 (0.005)	0.616 (0.015)	49.015 (6.038)	1.253 (0.010)	NaN	
S6879	1.017 (0.027)	0.545 (0.132)	35.358 (4.302)	1.999 (0.050)	NaN	1.03
	0.317 (0.013)	0.701 (0.046)	64.642 (4.302)	1.238 (0.026)	NaN	
S6820	1.015 (0.041)	0.561 (0.174)	37.646 (11.367)	1.862 (0.202)	NaN	1.08
	1.152 (0.083)	0.402 (0.124)	12.535 (13.050)	2.273 (0.093)	NaN	
	0.324 (0.008)	0.612 (0.017)	49.819 (10.856)	1.228 (0.016)	NaN	
S6811	0.376 (0.032)	0.219 (0.056)	28.198 (3.165)	-0.186 (0.064)	45.925 (0.187)	1.66
	0.353 (0.034)	0.346 (0.173)	11.239 (3.658)	-0.318 (0.072)	41.795 (0.373)	
	1.012 (0.021)	0.695 (0.060)	28.386 (3.051)	1.989 (0.037)	NaN	
	0.342 (0.013)	0.697 (0.041)	32.177 (3.020)	1.177 (0.031)	NaN	
S6777	0.389 (0.019)	0.577 (0.102)	18.748 (4.523)	-0.163 (0.037)	45.137 (0.201)	2.55
	0.430 (0.033)	1.022 (0.134)	24.595 (4.898)	-0.182 (0.064)	41.441 (0.592)	
	1.038 (0.017)	0.194 (NaN)	27.250 (2.581)	1.974 (0.029)	NaN	
	0.284 (0.017)	0.737 (0.047)	29.407 (2.801)	1.303 (0.022)	NaN	
S6510	0.345 (NaN)	0.811 (NaN)	2.970 (1.481)	-0.100 (NaN)	44.820 (NaN)	2.9
	1.184 (0.005)	0.396 (0.026)	20.674 (2.501)	2.697 (0.028)	NaN	
	1.127 (0.027)	0.465 (0.117)	15.842 (2.903)	2.013 (0.135)	NaN	
	0.385 (0.005)	0.328 (0.011)	60.514 (2.904)	0.617 (0.010)	NaN	
Z1794	1.153 (0.008)	0.442 (0.065)	31.494 (5.124)	2.660 (0.084)	NaN	1.2
	1.150 (0.020)	0.432 (0.180)	18.671 (5.879)	1.823 (0.188)	NaN	
	0.381 (0.005)	0.340 (0.025)	49.836 (4.960)	0.649 (0.012)	NaN	
Z1468	0.345 (0.055)	0.811 (0.301)	16.798 (5.942)	-0.100 (NaN)	44.821 (0.589)	2
	1.194 (0.007)	0.381 (0.064)	16.126 (8.041)	2.708 (0.075)	NaN	
	1.203 (0.019)	0.641 (0.278)	20.537 (8.518)	1.932 (0.344)	NaN	
	0.383 (0.004)	0.313 (0.018)	46.540 (7.177)	0.636 (0.009)	NaN	
Z1621	0.480 (NaN)	1.123 (NaN)	20.423 (3.174)	-0.081 (NaN)	46.881	1.3
	1.199 (0.008)	0.196 (0.044)	17.057 (2.769)	2.749 (0.028)	NaN	
	1.164 (0.025)	0.428 (0.086)	16.044 (3.221)	2.049 (0.108)	NaN	
	0.377 (0.006)	0.266 (0.012)	46.476 (2.892)	0.652 (0.013)	NaN	
Z1666	0.478 (0.107)	1.009 (0.630)	27.223 (14.665)	-0.081 (NaN)	43.702 (0.958)	1.04
	1.188 (0.061)	0.352 (0.168)	20.855 (10.561)	2.592 (0.105)	NaN	
	0.950 (0.140)	0.265 (0.396)	6.122 (10.431)	2.392 (0.195)	NaN	
	0.401 (0.017)	0.356 (0.038)	45.801 (11.571)	0.681 (0.030)	NaN	
S6654	0.478 (NaN)	0.558 (1.040)	15.789 (19.840)	-0.081 (NaN)	43.702 (NaN)	1.12
	1.086 (0.058)	0.453 (0.198)	19.697 (6.616)	2.698 (0.110)	NaN	
	0.393 (0.014)	0.291 (0.038)	64.514 (15.672)	0.499 (0.020)	NaN	
S6606	1.150 (NaN)	0.400 (NaN)	5.261 (4.271)	2.776 (0.506)	NaN	0.97
	0.362 (0.016)	0.362 (0.043)	94.739 (4.271)	0.566 (0.023)	NaN	
S6776	1.293 (0.058)	0.097 (0.186)	4.203 (1.919)	3.351 (0.115)	NaN	1.23
	0.366 (0.007)	0.304 (0.017)	95.797 (1.919)	0.696 (0.010)	NaN	

Table 4.6: Hyperfine parameters from Mössbauer spectra of experiments performed with MORB composition at the Ru-RuO$_2$ oxygen fugacity buffer, and those performed with an andesitic composition at metal saturation.

Exp #	CS	FWHM	Intensity	QS	BHF	χ^2
S6973	1.034 (0.012)	0.572 (0.045)	41.582 (2.749)	1.989 (0.024)	NaN	1.32
	0.315 (0.007)	0.670 (0.024)	58.418 (2.749)	1.250 (0.015)	NaN	
S6977	1.082 (0.026)	0.559 (0.072)	24.653 (4.218)	2.502 (0.048)	NaN	1.14
	0.396 (0.009)	0.406 (0.040)	75.347 (4.218)	0.771 (0.017)	NaN	
Z1791	1.250 (0.003)	0.171 (0.028)	55.954 (1.336)	3.512 (0.007)	NaN	1.17
	0.364 (0.008)	0.274 (0.048)	44.046 (1.336)	0.533 (0.012)	NaN	
Z1850	1.252 (0.008)	0.184 (0.060)	42.276 (2.163)	3.532 (0.015)	NaN	1.04
	0.368 (0.011)	0.255 (0.106)	57.724 (2.163)	0.563 (0.017)	NaN	
S6775	1.089 (0.037)	0.194 (NaN)	64.263 (15.466)	2.110 (0.058)	NaN	1.09
	0.955 (0.032)	0.786 (0.130)	35.737 (15.466)	1.592 (0.230)	NaN	
S6729	0.042 (0.064)	0.380 (0.218)	2.682 (1.412)	0.000 (NaN)	33.424 (0.437)	1.5
	0.208 (0.010)	0.451 (0.029)	24.322 (1.114)	0.000 (0.020)	20.426 (0.068)	
	1.085 (0.007)	0.194	69.422 (1.566)	2.068 (0.012)	NaN	
	0.237 (0.060)	0.452 (0.107)	3.574 (0.985)	0.731 (0.152)	NaN	
S6665	0.188 (0.025)	0.312 (0.067)	13.385 (2.679)	0.009 (0.051)	20.433 (0.140)	0.94
	1.139 (0.007)	0.442 (0.054)	47.990 (6.306)	2.925 (0.022)	NaN	
	1.292 (0.018)	0.263 (0.061)	8.995 (2.450)	3.541 (0.032)	NaN	
	1.172 (0.025)	0.724 (0.119)	27.322 (6.622)	2.044 (0.146)	NaN	
	0.307 (0.061)	0.255 (0.179)	2.308 (1.386)	0.592 (0.131)	NaN	
Z1626	0.092 (NaN)	0.295 (NaN)	4.877 (NaN)	0.000 (NaN)	32.877	1.66
	0.185 (0.005)	0.466 (0.019)	50.080 (NaN)	0.030 (0.010)	20.399 (0.038)	
	1.196 (0.013)	0.763 (0.062)	27.122 (NaN)	2.449 (0.040)	NaN	
	1.286 (0.007)	0.336 (0.027)	15.224 (NaN)	3.441 (0.014)	NaN	
	0.201 (0.023)	0.247 (0.069)	2.698 (NaN)	0.855 (0.047)	NaN	
Z1630	-0.046 (0.034)	0.226 (0.100)	4.816 (1.655)	0.000 (NaN)	33.225 (0.235)	0.91
	0.171 (0.019)	0.509 (0.051)	34.145 (2.227)	0.007 (0.036)	20.200 (0.132)	
	1.168 (0.016)	0.194 (NaN)	57.084 (2.425)	2.462 (0.031)	NaN	
	0.076 (0.121)	0.497 (0.229)	3.955 (1.889)	0.817 (0.318)	NaN	
Z1647	0.184 (0.007)	0.468 (0.019)	42.966 (1.623)	0.050 (0.013)	20.481 (0.047)	3.29
	1.267 (0.005)	0.389 (0.017)	28.854 (1.382)	3.519 (0.010)	NaN	
	1.179 (0.020)	0.703 (0.086)	16.948 (1.821)	2.365 (0.055)	NaN	
	-0.002 (0.038)	0.377 (0.127)	5.086 (1.511)	0.000 (NaN)	33.371 (0.251)	
	0.168 (0.033)	0.483 (0.089)	6.147 (0.875)	0.757 (0.068)	NaN	

4.5 Thermodynamic treatment

As outlined above, the relationship between the Fe^{3+} / Fe^{2+} ratio, oxygen fugacity, and pressure can be expressed with equation 4.2, which can be rearranged

into:

$$\ln \frac{X_{\mathrm{FeO}_{1.5}}}{X_{\mathrm{FeO}}} = -\left(\frac{(\Delta G_r^0(4.1)}{RT} + \frac{\int_1^P \Delta V \mathrm{d}P(4.1)}{RT} \right) - \ln \frac{\gamma_{\mathrm{FeO}_{1.5}}}{\gamma_{\mathrm{FeO}}} + \frac{1}{4} \ln f\mathrm{O}_2. \tag{4.3}$$

To model the ferric iron content of a silicate melt as a function of oxygen fugacity, the components of this expression were evaluated as follows.

4.5.1 Oxygen fugacity

For the primary set of experiments as well as those conducted with a MORB composition, the oxygen fugacity of the experiments was imposed by the coexistence of Ru and RuO_2, the determination of which as a function of pressure and temperature is thoroughly detailed in chapter 3. For the experiments conducted at metal saturation, the oxygen fugacity was assumed to be buffered by presence of iron metal, discussed further in section 4.6.

The $f\mathrm{O}_2$ of the Ru + RuO_2 has been parameterised as the following (detailed in this work, chapter 3):

$$\log_{10} f\mathrm{O}_2(\mathrm{Ru} - \mathrm{RuO}_2) = \left(a_0 + a_1 P + a_2 P^2 + a_3 P^3 \right) + \left(b_0 + b_1 P + b_2 P^2 \right) / T + \left(c_0 + c_1 P \right) / T^2$$

with the coefficients:

a_0	a_1	a_2	a_3	b_0	b_1	b_2	c_0	c_1
7.783	-0.0113	0.00209	$-4.10 \cdot 10^{-5}$	-13764	593.4	-4.08	$-1.05 \cdot 10^6$	-4511

4.5.2 Standard-state free energy change

Three models for the standard-state Gibbs free energy of reaction 4.2 were considered when fitting our data to a thermodynamic model. The first was presented by Jayasuriya et al. (2004), from the premise that equation 4.2 can be taken as the sum of the two reactions

$$\underset{\mathrm{metal}}{\mathrm{Fe}} \quad + \quad \tfrac{3}{4}\mathrm{O}_2 \quad = \quad \underset{\mathrm{melt}}{\mathrm{Fe}^{3+}\mathrm{O}_{1.5}} \tag{4.4}$$

and

$$
\begin{array}{ccccc}
\text{Fe} & + & \frac{1}{2}\text{O}_2 & = & \text{Fe}^{2+}\text{O} \\
\text{metal} & & & & \text{melt}
\end{array}
\tag{4.5}
$$
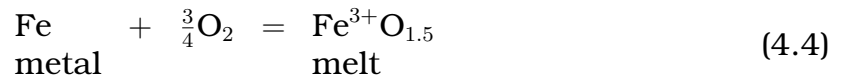
hence, $\Delta G_r^0(4.1) = \Delta G_r^0(4.4) - \Delta G_r^0(4.5)$. O'Neill and Eggins (2002) provide the free energy change of reaction 4.5 as $\Delta_r G(4.5) = -244118 + 115.559T - 8.474T \ln T$ $(\text{J} \cdot \text{mol}^{-1})$. Thermodynamic data for the free energy of reaction 4.4 is less certain, due to the decomposition of Fe_2O_3 into Fe_3O_4 at 1730 K, even in pure oxygen above 1 bar (Wriedt, 1991). Jayasuriya et al. (2004) therefore provide an estimate for the free energy of reaction 4.4 as follows. The free energy of reaction
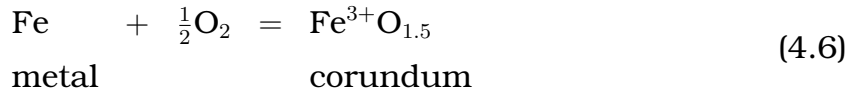
$$
\begin{array}{ccccc}
\text{Fe} & + & \frac{1}{2}\text{O}_2 & = & \text{Fe}^{3+}\text{O}_{1.5} \\
\text{metal} & & & & \text{corundum}
\end{array}
\tag{4.6}
$$

is given by Robie and Hemingway (1995) as $\Delta_r G(4.6) = -411565 + 167.095T - 5.350T \ln T$ $(\text{J} \cdot \text{mol}^{-1})$. Jayasuriya et al. (2004) assume a melting temperature for Fe_2O_3 of 2100 K, based on melting relations presented by Phillips and Muan (1960); an extrapolation of the liquidus of the Fe_2O_3-rich side of their phase diagram indicates a melting temperature for Fe_2O_3 of > 1900 K. In conjunction, Jayasuriya et al. (2004) assume an entropy of melting ΔS_m^0, based on values for other corundum-structured oxides, of 24.5 J/mol·K. The free energy of melting for $FeO_{1.5}$ is therefore approximated by $\Delta G_m(FeO_{1.5}) = 24.5(T - 2100)$ $\text{J} \cdot \text{mol}^{-1}$. The free energy of reaction 4.4 can then be approximated as:

$$
\Delta G_r^0(4.4) = -360115 + 142.595T - 5.350T \ln T
$$

and the free energy of equilibrium 4.1 is thus:

$$
\Delta G_r^0(4.1) = -115997 + 27.036T + 3.124T \ln T.
$$

The second was taken from an evaluation of thermodynamic data presented in Kowalski and Spencer (1995), which was determined from the melting phase relations in the Fe-O system. The authors use data on solid FeO and Fe_2O_3, compiled and presented by Sundman (1991, and references therein) to obtain:

$$
{}^0G_{FeO}^{solid} = -279318 + 252.848T - 46.12826T \ln T - 5.7402984 \cdot 10^{-3}T^2
$$

and

$$^0G^{\text{solid}}_{\text{Fe}_2\text{O}_3} = -858683 + 827.946T - 137.0089T \ln T + 1453810T^{-1},$$

which are both valid for temperature ranges $298.15 \leq T \leq 3000$ K. From the melting phase relations, Kowalski and Spencer (1995) give the Gibbs free energy of liquid FeO and $\text{FeO}_{1.5}$ as:

$$^0G^{\text{liquid}}_{\text{FeO}} = {}^0G^{\text{solid}}_{\text{FeO}} + 34008 - 20.969T$$

and

$$^0G^{\text{liquid}}_{\text{FeO}_{1.5}} = 0.5{}^0G^{\text{solid}}_{\text{Fe}_2\text{O}_3} + 39712 - 20.007T.$$

These expressions are here combined and, with thermodynamic data for oxygen compiled by O'Neill and Nell (1997, reported in table 3.6) parameterised to give:

$$\Delta G^0_r(4.1) = -131062 + 42.321T + 1.929T \ln T.$$

The third, and ultimately most successful for reproducing our data, is the model that was determined by Jayasuriya et al. (2004) as a fit from their experimental data. The authors determined $\text{Fe}^{3+}/\sum\text{Fe}$ values for glasses of an anorthite-diposide eutectic composition as a function of oxygen fugacity and fit their data to a regular solution model, with $\Delta_r G(4.1)$ as a refinable parameter, to obtain:

$$\Delta G^0_r(4.1)/RT = 16201/T - 8.031.$$

4.5.3 Volumes of FeO and $\text{FeO}_{1.5}$ at high P/T

Fitting the high-pressure data requires an expression for $\int \Delta V \, dP$, where ΔV is the volume change for equilibrium 4.1. Although this volume change is positive at low pressures, our data indicate it must become negative at pressures greater than 10 GPa. In order for this to occur, the $\text{FeO}_{1.5}$ component must be more compressible then the FeO component. We found the Murnaghan equation of state, employed by O'Neill et al. (2006) and Zhang et al. (2017) to

be insufficiently flexible to describe this rapid change in compressibility, and so the effect of pressure on the volumes of FeO and FeO$_{1.5}$ was evaluated with a modified Tait equation of state (TEOS, Huang and Chow, 2002; Holland and Powell, 2011). This form of EoS has the additional advantage that it is easily rewritten as a function of pressure and solved without the need for iteration. The isothermal TEOS is given by:

$$\frac{V}{V_{0,T}} = 1 - a(1 - (1 + bP)^{-c})$$

or in terms of pressure:

$$P = \frac{1}{b}\left(\left[\frac{(V/V_{0,T}) + a - 1}{a}\right]^{-1/c} - 1\right)$$

where

$$a = \frac{1 + \kappa_0'}{1 + \kappa_0' + \kappa_0\kappa_0''}$$

$$b = \frac{\kappa_0'}{\kappa_0} - \frac{\kappa_0''}{1 + \kappa_0'}$$

$$c = \frac{1 + \kappa_0' + \kappa_0\kappa_0''}{\kappa_0'^2 + \kappa_0' - \kappa_0\kappa_0''}.$$

$V_{0,T}$ is the volume at ambient pressure and the temperature of interest, κ_0 is the bulk modulus at ambient conditions, and κ_0' and κ_0'' are the first and second derivatives, respectively. Integrating V with respect to P yeilds the contribution to $\Delta G_r^0(4.1)$ from pressure:

$$\int_1^P V\,dP = V_{0,T}P\left[\frac{a(bP + 1)^{1-c}}{bP(1 - c)} + (1 - a)\right].$$

To account for the effect of temperature, the partial molar volumes (i.e., $V_{0,T}$) of FeO and FeO$_{1.5}$ that have been determined by Lange and Carmichael (1987, 1990) to be $13650 + 2.92(T - 1673)$ and $21070 + 4.54(T - 1673)$ J/GPa, respectively, were used to evaluate the thermal expansion and determine $V_{0,T}$ at the temperature of interest.

4.5.4 Compositional interactions

The effects of non-ideal interrelations arising from the various components of the silicate melts on the Fe^{3+}/Fe^{2+} ratio are described by the terms $\gamma_{Fe^{3+}O_{1.5}}$ and $\gamma_{Fe^{2+}O}$ in equation 4.3. Each component (e.g., MgO, CaO, etc.) will interact with both the $Fe^{2+}O$ and the $Fe^{3+}O_{1.5}$, and, in addition, there are interactions between the iron components themselves. Sack et al. (1980) and Jayasuriya et al. (2004) describe a regular solution model to account for non-ideal interactions in a multi-component system. For this model, the excess free energy of mixing is given by

$$G_{ex} = \sum_{i=1}^{n-1} \sum_{j>1}^{n} X_i X_j W_{ij}$$

where X_i and X_j are the single-cation molar fractions of the components in the melt (e.g., $FeO_{1.5}$, MgO, $NaO_{0.5}$), and W_{ij} is the interaction (Margules) parameter between components i and j (e.g., Cemič, 2005; Sack et al., 1980). An activity coefficient is then given by

$$\ln \gamma_i = \sum_{j \neq i}^{n} X_{\mathbf{i}} W_{ij}/RT - G_{ex}.$$

Hence, the ratio of the activity coefficients for the iron components can be written

$$\ln \frac{\gamma_{FeO_{1.5}}}{\gamma_{FeO}} = \sum_{j}^{n} X_j (W_{Fe^{3+}-j} - W_{Fe^{2+}-j})/RT + (X_{Fe^{2+}O} - X_{Fe^{3+}O_{1.5}})W_{Fe^{2+}Fe^{3+}}/RT \quad \text{(4.7)}$$

with the term $W_{Fe^{2+}Fe^{3+}}$ describing the interaction between $FeO_{1.5}$ and FeO. Jayasuriya et al. (2004) provide a review of previous work to relate the fO_2 of a multicomponent melt to Fe^{3+}/Fe^{2+} ratio, and focus in particular on the importance of the $W_{Fe^{2+}Fe^{3+}}$ term, which had not been previously included in empirically-calibrated thermodynamic models. Substituting equation 4.7 into 4.3, and using values for the interaction terms empirically determined by Jayasuriya et al. (2004) yeilds the full expression for the model:

$$\ln \frac{X_{FeO_{1.5}}}{X_{FeO}} = \frac{1}{4} \ln f_{O_2} - \frac{(\Delta G_r^0(4.1) + \int_1^P \Delta V(4.1)dP)}{RT} - 2248\frac{X_{MgO}}{T} + 7690\frac{X_{CaO}}{T}$$

$$+8553\frac{X_{\mathrm{NaO_{0.5}}}}{T} + 5644\frac{X_{\mathrm{KO_{0.5}}}}{T} - 6278\frac{X_{\mathrm{AlO_{1.5}}}}{T} + 6880\left(\frac{X_{\mathrm{Fe^{2+}O}} - X_{\mathrm{Fe^{3+}O_{1.5}}}}{T}\right). \text{ (4.8)}$$

4.5.5 Resulting model

The above components of equation 4.3 were combined in order to model the Fe^{3+}/Fe^{2+} ratio of silicate melts as a function of pressure, temperature, composition, and oxygen fugacity. Values for κ_0 and κ_0' for FeO and $FeO_{1.5}$ were then fit from our data. Previous studies (O'Neill et al., 2006, Zhang et al., 2017) had used values of κ_0 for FeO and $FeO_{1.5}$ determined by Kress and Carmichael (1991) to be 30.3 and 16.6 GPa, respectively, though O'Neill et al. (2006) suggested that a better fit of their data could have been obtained with a higher value for FeO and a lower value for $FeO_{1.5}$. Indeed, our data are best represented by a κ_0 for FeO of 37 GPa, and 12.6 for $FeO_{1.5}$. Additionally, previous studies had used a value of 4 for κ_0' for both phases, whilst here we determine values of 8 for FeO and 1.3 for $FeO_{1.5}$.

Plots of the resulting model curves are in figure 4.6.
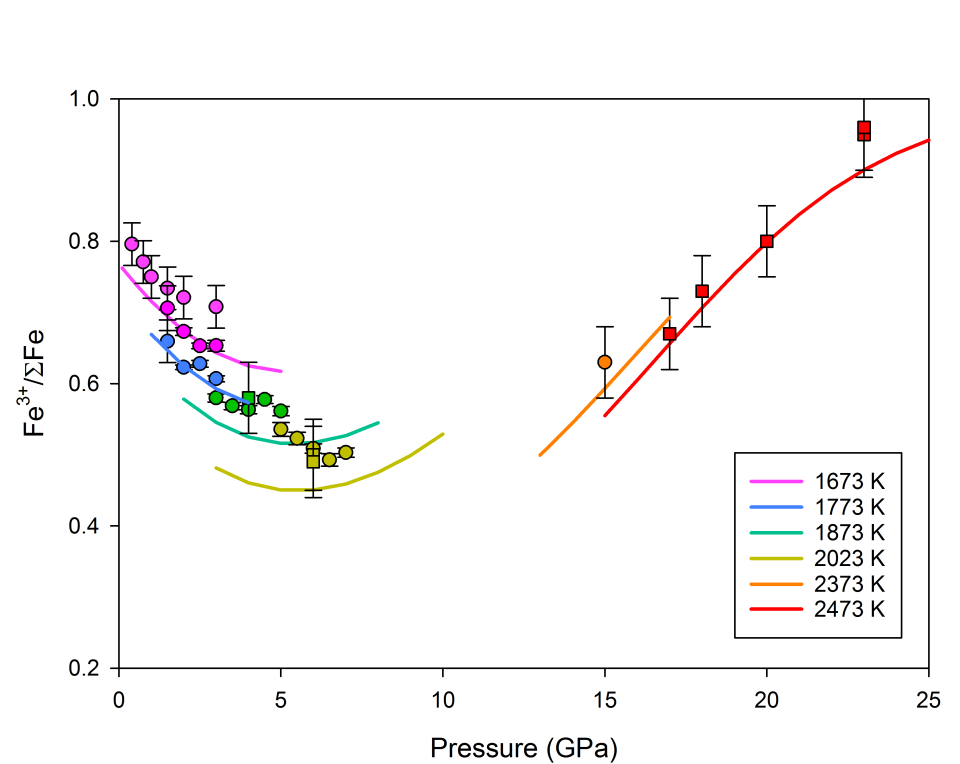
Figure 4.6: Calculated model curves, predicting ferric iron content given the Ru/RuO$_2$ oxygen fugacity buffer, pressure, and temperature, plotted with the data from the primary set of experiments (square data points). Literature data (O'Neill et al., 2006; Zhang et al., 2017) is plotted as well (circles).

This model fits low-pressure data less well than the models of O'Neill et al. (2006) and Zhang et al. (2017), but faithfully represents the data above 15 GPa, with the exception of the data at 23 GPa. The reason for this is likely in the value for κ_0'', which, as described above, was fixed to a value equivalent to that of a third-order equation of state, rather than refined. Due to the paucity of data above 20 GPa, however, it would not be possible to refine a meaningful value for κ_0, κ_0', and κ_0'' simultaneously.

The values for κ_0 and κ_0' reported here for FeO and FeO$_{1.5}$ account for the changes in compressibility that must occur with pressure in order to produce the observed increase in ferric iron content. While the volume change of reaction 4.1 is positive below 10 GPa, at higher pressures it must become negative. In order for this to occur, the FeO$_{1.5}$ component must be more compressible then the FeO component, and the decrease in compressibility with pressure must be much greater for FeO than FeO$_{1.5}$; i.e., κ' FeO $\gg \kappa'$ FeO$_{1.5}$. ($\kappa_0' < 4$).

It has been suggested that ferric iron may more readily be incorporated into high-coordination sites within a melt structure with increasing pressure (e.g., Hirschmann, 2012; Stixrude and Karki, 2005). Such a change in coordination would explain the the relatively rapid changes in volume necessary to account for the experimental observations. The higher compressibility of the $FeO_{1.5}$ component cannot continue indefinitely to higher pressures, however. It must ultimately become less compressible after the coordination change is complete, as implied by the model at pressures above 23 GPa. Currently, the data at higher pressures are insufficient to refine the κ_0'' terms, which are highly correlated with the other equation of state terms.

4.6 Metal-saturated samples

The resulting model was used to calculate predicted ferric/total iron ratios for both an andesite and a peridotite composition melt at the oxygen fugacity imposed by the presence of iron metal, which can be determined from the equilibrium of the iron-wüstite (IW) reaction:

$$2Fe + O_2 = 2FeO. \tag{4.9}$$

The $f O_2$ at equilibrium can be expressed:

$$\log f O_2 = \frac{2\Delta_r G^0 (4.9)}{\ln(10)} + 2\log \frac{a_{FeO}^{melt}}{a_{Fe}^{alloy}}.$$

For pure phases, the activities are unity, and the oxygen fugacity of IW is given by the first term. We estimate the oxygen fugacity of the metal-saturated experiments discussed here by assuming pure iron metal (i.e., $a_{Fe}^{alloy} = 1$) and approximating a_{FeO}^{melt} as X_{FeO}^{melt}. The $f O_2$ of the experiments is therefore estimated as

$$\log f O_2 = \log f O_2(IW) + 2\log X_{FeO}^{melt}.$$

Campbell et al. (2009) parameterised the oxygen fugacity of the IW buffer as a function of pressure and temperature as:

$$\log_{10} f\mathbf{O}_2 = (6.541 + 0.001P) + (-28163.6 + 546.32P + -1.1341P^2 + 0.001927P^3)/T$$

The compositions of the metal-saturated experiments in mole percent are reported in table 4.7

Table 4.7: Melt compositions of the metal-saturated experiments, given in mole percent.

exp#	SiO$_2$	TiO$_2$	Al$_2$O$_3$	MgO	FeO	CaO	Na$_2$O	K$_2$O
S6777	58.72 (0.56)	2.22 (0.06)	8.82 (0.08)	5.59 (0.15)	11.11 (0.41)	8.74 (0.11)	4.31 (0.06)	0.50 (0.02)
S6778	60.15 (0.36)	2.12 (0.07)	9.30 (0.07)	3.93 (0.10)	11.09 (0.20)	8.48 (0.11)	4.57 (0.10)	0.36 (0.01)
S6779	56.69 (0.12)	0.79 (0.03)	9.47 (0.02)	8.42 (0.13)	9.58 (0.31)	9.24 (0.08)	5.74 (0.14)	0.06 (0.01)
S6780	58.26 (0.43)	2.01 (0.34)	9.47 (0.52)	3.68 (0.21)	12.83 (1.00)	7.77 (0.15)	5.57 (0.56)	0.41 (0.11)
S6781	58.40 (1.29)	2.31 (0.47)	8.61 (1.91)	3.48 (0.81)	14.11 (1.83)	7.92 (0.98)	4.66 (1.10)	0.51 (0.12)
S6782	56.74 (4.47)	2.67 (0.26)	9.76 (0.14)	3.71 (0.02)	12.06 (3.99)	9.13 (0.39)	5.34 (0.31)	0.58 (0.07)

Figure 4.7 shows the result of this calculation compared with the same computation for the andesitic composition and the results from experiments performed with an andesite composition. To 20 GPa, the highest achieved pressure at this oxygen fugacity in this study, the model faithfully represents the experimental values, implying as expected that the increase in FeO$_{1.5}$ results from a change in sign of the ΔV of reaction 4.1. Additionally, the ferric iron content of a peridotite melt reaches the modern MORB average value, ~ 12 % total iron, at around 20 GPa.
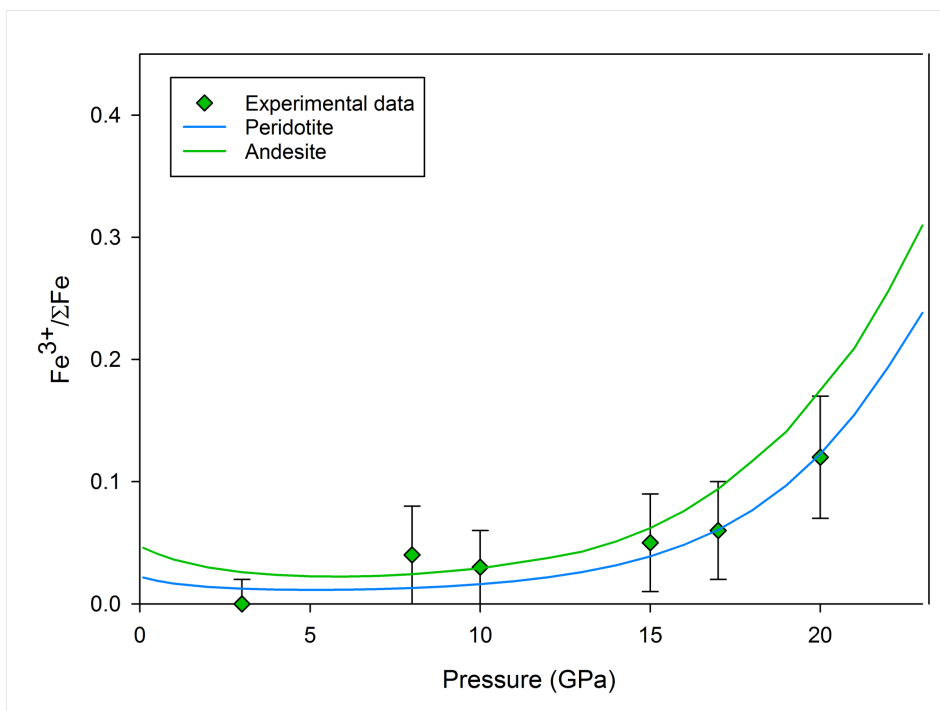
Figure 4.7: Ferric iron content of the metal saturated experiments, compared to the model predictions for peridotite and andesite composition.

The slight pressure dependence between the two compositions is a result of the $X_{Fe^{2+}} - X_{Fe^{3+}}$ interaction term, which changes with pressure as the ferric/ferrous abundances change, and different compositions have different total iron. It should be noted that any changes in activity-composition effects, i.e., the activity coefficients (Jayasuriya et al., 2004), as a function of pressure are not known. However, the effect is expected to be small as the partial molar volumes of FeO and $FeO_{1.5}$ have been shown to be independent of melt composition (O'Neill et al., 2006). In addition, the experiments performed with MORB composition at 4 GPa show no indication whatsoever of a compositional dependence, and the results from the partial melt obtained at 18 GPa, if extrapolated to 100% melt, likewise suggest a small change at most.

An additional consideration addressed by the metal-saturated samples is the possibility that FeO may disproportionate on quench, creating Fe metal and Fe_2O_3. If this were to occur, the quench product would not be accurately reflecting the ferric iron content of the melt. However, no metallic iron was detected in the quench assemblage by either SEM or XRD analyses.

4.7 MORB composition

The experiments conducted with MORB composition at the Ru+ RuO$_2$ oxygen fugacity buffer were plagued by the difficulty of reaching superliquidus temperatures above 15 GPa without also melting the platinum capsule. An initial attempt at 18 GPa yeilded only incipient melt, though it should be noted that the starting composition for the MORB experiments had been fully reduced, and so the result of 50% ferric iron still represents a large increase. A second attempt, in which the melting temperature of the MORB was lowered by the addition of liquid water into the experimental capsule, yeilded approximately 50% melt, and, as shown in figure 4.5, an increase in ferric iron, approaching the value expected for 100% melt. Electron backscattered images of the experimental products are shown in figure 4.8. It is thus plausible that the area over which the Mössbauer spectrum was collected included both melt and residue, and that a fully molten sample, if achieved experimentally, would match the predicted melt ferric iron content at this oxygen fugacity.
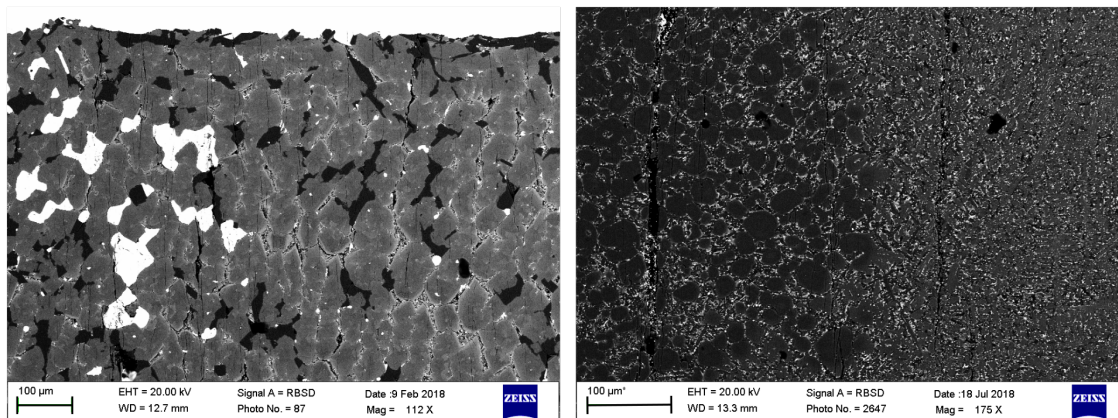
Figure 4.8: Electron backscattered images showing the textures of the recovered experiments with MORB composition performed at 18 GPa. On the right is exp # Z1791, in which garnet (gray), stishovite (dark), and RuO2 (bright) coexist. Only a small amount of melt has formed interstitial to the garnets. The left image is exp # Z1850, in which the melt proportion was increased by the addition of liquid water into the experimental charge. On the right of the image, there is a clear quench assemblage, however the darker grains to the left are unmelted garnets.

Table 4.8: Composition of the garnet phase in recovered experiments Z1791 (incipient melt only) and Z1850 ($\sim 50\%$ melt), as compared to the initial bulk MORB composition. Ferric iron content of the bulk composition is calcualted from the model, assuming a full melt. All are in mole percent.

	Bulk	Z1791	Z1850
$Fe^{3+}/\sum Fe$	0.69 (0.04)	0.44 (0.04)	0.58 (0.04)
SiO_2	54.59	47.53 (0.20)	46.10 (0.88)
TiO_2	1.37	0.36 (0.07)	0.14 (0.02)
Al_2O_3	9.35	12.02 (0.11)	12.32 (0.19)
MgO	12.95	16.34 (0.60)	22.76 (0.50)
CaO	13.21	15.81 (0.19)	13.27 (0.26)
Na_2O	2.91	2.27 (0.13)	1.67 (0.07)
FeO	2.81	3.93 (0.20)	2.16 (0.19)
Fe_2O_3	2.81	1.39 (0.20)	1.34 (0.19)
Ru_2O_3		0.31 (0.02)	0.19 (0.02)
PtO		0.04 (0.05)	0.04 (0.03)

The measured ferric iron content of the garnet in the unmelted sample, compared with the predicted ferric iron content of a full melt of the same composition at the same pressure and temperature allow for an estimate of the ferric iron garnet/melt partition coefficient at 18 GPa and 2473 K. Compositions of the garnets, determined from EPMA, are reported in table 4.8, in mole percent. The mineral/melt partition coefficient is given as

$$D_{Fe_2O_3}^{garnet/melt} = \frac{X_{Fe_2O_3}^{garnet}}{X_{Fe_2O_3}^{melt}}$$

Where X is the mole fraction of the ferric iron component. Taking the ferric iron concentration of experiment Z1791 (incipient melt only) as representative of $X_{Fe_2O_3}^{garnet}$, and using the calculated ferric iron content of a full melt of the same composition, gives $D_{Fe_2O_3}^{garnet/melt} = 0.49 \pm 0.05$.

This is the first time to our knowledge that such an estimate has been made for garnet or for any mineral at transition zone pressures. This value indicates incompatible behaviour for ferric iron, as expected, but is greater than most other mineral/melt partition coefficients that have been reported for ferric iron. Mallmann and O'Neill (2009) report a value determined from data from partitioning experiments of 0.45 ± 0.02 for clinopyroxene, but lower values (~ 0.2) for orthopyroxene and spinel. Whole-rock mineral/melt partition coef-

ficients for ferric iron have likewise been estimated at ~ 0.1 (Canil et al., 1994) and ~ 0.2 (Sorbadere et al., 2018).

Partitioning, however, is strongly dependent on pressure, temperature, and oxygen fugacity, and these previous estimates have been considered for P/T conditions relevant to MORB formation; i.e., $\sim 1-3$ GPa and $\sim 1200\,°C$, and a range of oxygen fugacities. Our result for garnet implies that ferric iron may in fact become more compatible lower in the mantle, at higher pressures and temperatures, and when garnet becomes the most abundant phase. Small degrees of melt at lower depths may therefore be less enriched in ferric iron than their lower-pressure counterparts.

4.8 Platinum contamination of the $f\mathrm{O}_2$ buffer

Most of the samples in this study that were equilibrated in platinum capsules had some Pt alloying with the Ru of the oxygen buffer. This dilutes the Ru, lowering the Ru activity and thereby increasing the imposed $f\mathrm{O}_2$. This can readily be seen from the buffer reaction:

$$\mathrm{Ru} + \mathrm{O}_2 = \mathrm{RuO}_2 \tag{4.10}$$

at equilibrium the imposed oxygen fugacity can be calculated from the expression

$$\ln f\mathrm{O}_2 = \frac{\Delta G_r^0}{RT} + \ln \frac{X_{\mathrm{RuO_2}}^{\mathrm{oxide}}}{X_{\mathrm{Ru}}^{\mathrm{alloy}}} + \ln \frac{\gamma_{\mathrm{RuO_2}}^{\mathrm{oxide}}}{\gamma_{\mathrm{Ru}}^{\mathrm{alloy}}}.$$

Table 4.9: Activity coefficients for the Ru-Pt system, as given by Frank and Neuschutz (2006).

	X_{Ru}	γ_{Ru}	a_{Ru}
fcc	0	0.946	0
	0.1	0.797	0.0797
	0.2	0.748	0.1496
	0.3	0.766	0.2298
	0.4	0.837	0.3348
	0.5	0.957	0.4785
	0.6	1.118	0.6708
	0.654	1.22	0.79788
hcp	0.784	1.018	0.798112
	0.8	1.016	0.8128
	0.9	1.005	0.9045
	1	1	1

If the alloy composition is homogeneous, this can be easily be accounted for given the activity coefficient that governs the interaction between Ru and Pt, the values of which are given by Franke and Neuschutz (2006) and are repeated in table 4.9. Five samples (see table 4.10) in this study, however, suffered from an extremely inhomogeneous Ru-Pt alloy composition, rendering a very large uncertainty in experimental fO_2 (figure 4.9). These samples have anomalously high ferric iron contents that do not match the model. This implies that although the heterogeneity in Ru-Pt composition was high, the samples appear to have experienced the higher end of the oxygen fugacity range. This is possibly because the Pt contents were highest at the grain boundaries of the alloy, which is likely where the oxygen fugacity fixed. These samples are indicated in grey in figure 4.5, and were excluded from the thermodynamic analysis described in section 4.5.

The samples that suffered from contamination were those that were from the low-mid range of pressures (6-10 GPa) and higher temperatures. Buffer alloys from experiments at the same pressures but lower temperatures did not experience contamination, nor did those at higher temperatures but also higher pressures, indicating that temperatures facilitates alloying between Ru and Pt, but pressure inhibits it.
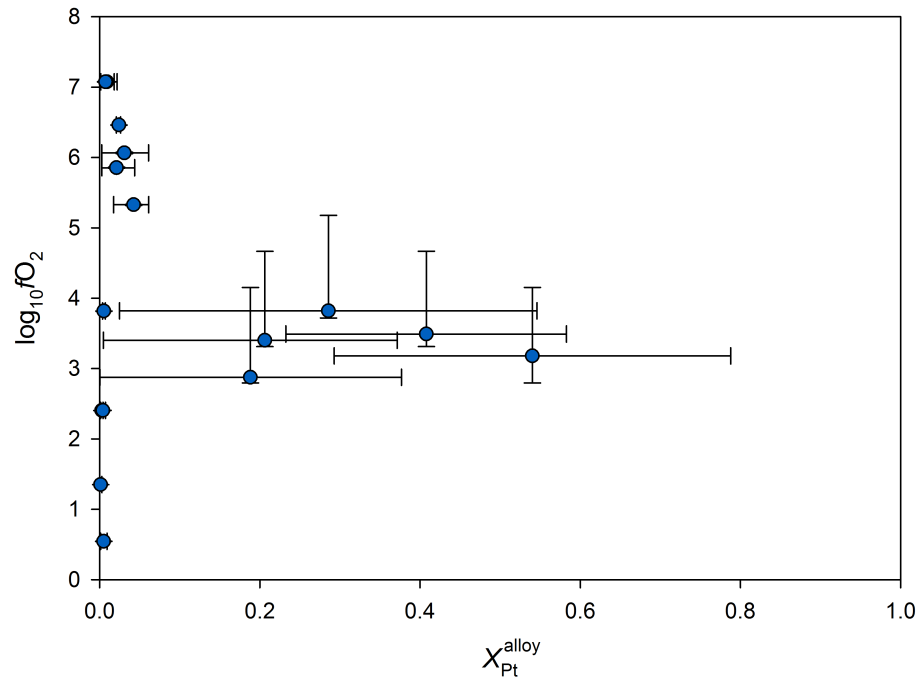
Figure 4.9: $\log_{10} fO_2$ plotted against Pt content in the buffer alloy. When the Pt content is low and fairly homogenous, the imposed fO_2 of the Ru+RuO2 assemblage is very accurately known (vertical error bars are in some cases eclipsed by the data point), whereas high, inhomogenous Pt contents impart an incredibly large uncertainty in oxygen fugacity.
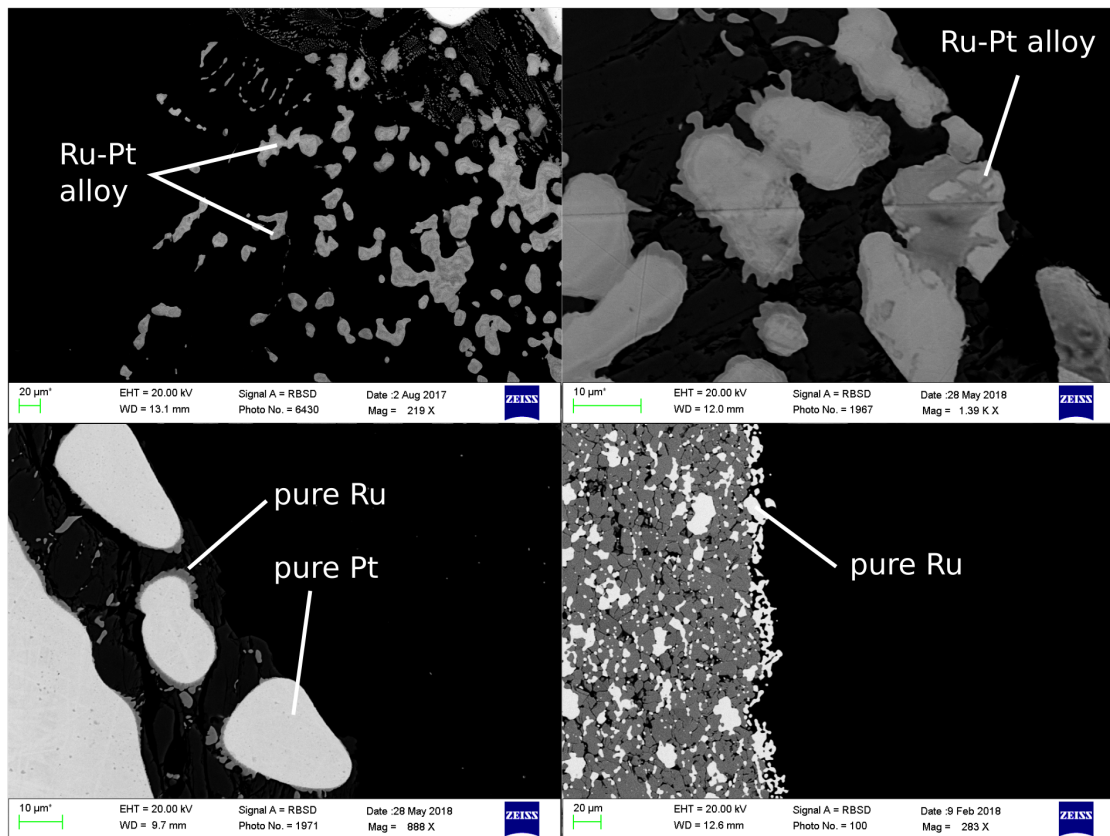
Figure 4.10: Backscattered electron images of contaminated (top two images), and pure (bottom two images) RuPt alloys of the oxygen fugacity buffer assemblage. Inhomogeneity in the alloys yeilded large uncertainties in the imposed oxygen fugacity.

Table 4.10: Buffer alloy compositions (Atom %). An (*) indicates extremely large inhomogeneity in the buffer, and therefore very large uncertainty in the imposed oxygen fugacity. These samples were excluded from the thermodynamic analysis.

| Sample	Ru	Pt
S6928	99.75 (0.14)	0.25 (0.14)
S6889	99.61 (0.20)	0.39 (0.20)
S6879*	81.20 (18.86)	18.80 (18.86)
S6820	99.76 (0.14)	0.24 (0.14)
S6811*	45.97 (24.76)	54.03 (24.76)
S6777*	81.26 (16.52)	18.74 (16.52)
S6510*	71.45 (26.07)	28.55 (26.07)
Z1794	99.49 (0.14)	0.51 (0.14)
Z1468	95.78 (2.19)	4.22 (2.19)
Z1621	97.91 (1.31)	2.09 (1.31)
Z1666	96.93 (1.82)	3.07 (1.82)
S6654	97.60 (0.20)	2.40 (0.20)
S6606	99.11 (0.70)	0.89 (0.70)
S6776	99.26 (0.66)	0.74 (0.66)
S6973	99.89 (0.11)	0.11 (0.11)
S6977*	59.23 (17.53)	40.77 (17.53)
Z1791	80.04 (2.24)	19.96 (2.24)
Z1850	95.49 (2.39)	4.51 (2.39)

4.9 Ru and Pt contents of silicate melts at high pressure and temperature

The experimental data also provide information on the Ru and Pt solubilities in silicate melts at high pressures and temperatures. The solubilities of highly siderophile elements such as Ru and Pt in melts are strongly dependent on oxygen fugacity, which in the current experiments is known very accurately. Analysis of the experimental data has the advantage that the metal concentrations at oxygen fugacities buffered by the presence of RuO_2 are relatively high in the silicate melts, and so their uncertainties are low. More importantly, the fO_2 dependence of the solubilities can also be used to place constraints on the valence state of the metal dissolved in the silicate.
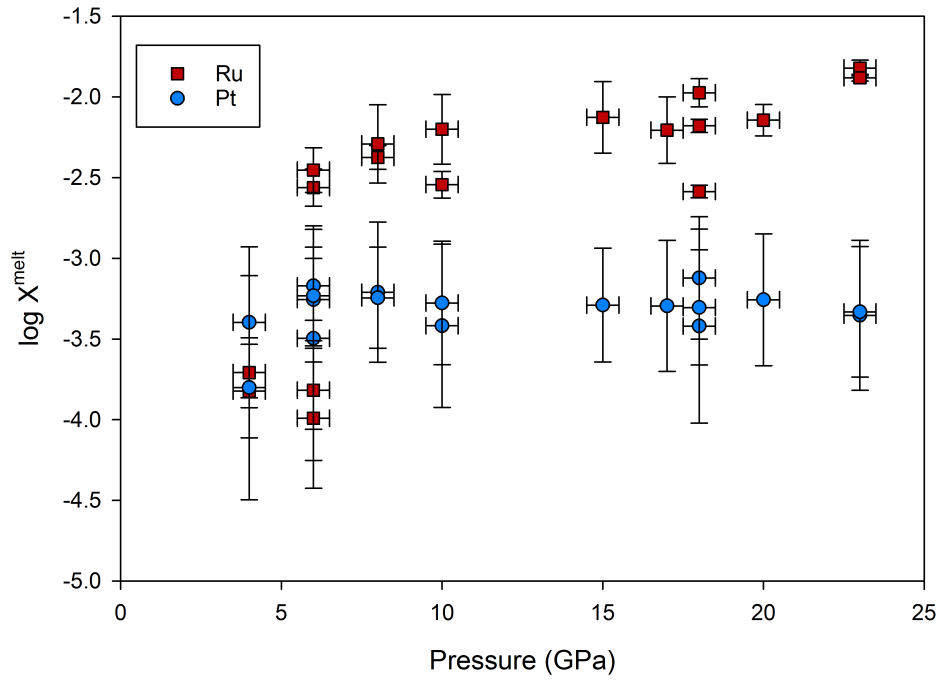
Figure 4.11: Mole fractions in log units of Ru and Pt in silicate melt as a function of pressure.

Figure 4.11 shows the concentrations of Ru and Pt in the silicate melt as a function of pressure. While Pt values remain virtually constant over the P and T range, Ru shows a sharp rise at low pressure but also a gradual rise at higher pressures. To analyse these data in terms of Ru oxide valence and to separate any effect of pressure, however, effects of $f\mathrm{O}_2$ and temperature need to be considered. In order to define the oxygen fugacity dependence, we need to be able to compare with previous studies that have examined metal silicate partitioning (e.g. Mann et al., 2012). The partitioning of a highly siderophile element M between metal and silicate is controlled by the redox equilibrium:

$$M^{\mathrm{metal}} + \frac{n}{4}\mathrm{O}_2 = M\mathrm{O}^{\mathrm{silicate}}_{n/2}$$
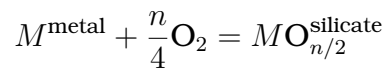
where n is the valence state of the metal in the silicate melt. The partition coefficient D for element M can be defined from the mole fractions (X) of the element in the metal and melt, i.e:

$$D = \frac{X_M^{\mathrm{metal}}}{X_M^{\mathrm{silicate\ melt}}}.$$

For solubility measurements, the pure metal is present such that $X_M^{\mathrm{metal}} = 1$. A plot of the variation of $\log D$ with oxygen fugacity can be used to obtain an idea of the valence state n of the metal dissolved in the silicate melt, as it should follow the relation

$$\log D = -\frac{n}{4}\Delta\mathrm{IW} + \mathrm{const}$$

where ΔIW is the oxygen fugacity, which in this case is normalised to the iron-wüstite oxygen buffer.
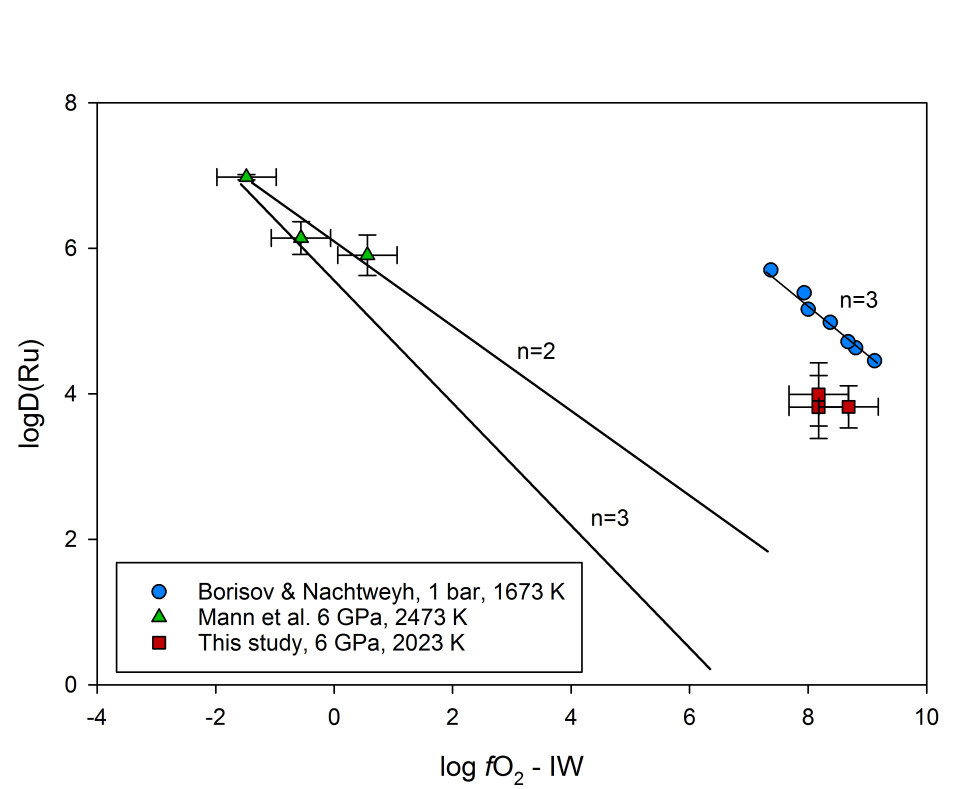
Figure 4.12: Plot of $\log D$ of ruthenium in silicate melt against oxygen fugacity, normalised to iron-wüstite. At ambient pressures, the gradient determined by Borisov and Nachtweyh (1998) is consistent with a 3+ valence for Ru in the melt. At higher pressures, however, Ru appears to have a 2+ valence state, based on the data of Mann et al., which is consistent with the data from this study once the effect of temperature is considered.

Figure 4.12 shows such a plot determined from Ru solubility data from this study, compared with that of Mann et al. (2012) and Borisov and Nachtweyh (1998). The gradient of the data of Borisov and Nachtweyh (1998) is consistent with a valence of 3+ for Ru in the silicate melt at 1 bar, whereas Mann et al. (2012) proposed that at higher pressures the gradient was more consistent

with a valence of 2+ in the melt. Data from the current study at the same pressure plot above this extrapolated 2+ curve, but this is expected as there is a temperature difference between the data of 450 K, which can account for this difference. If the valence state of Ru were 3+ at 6 GPa, the curve extrapolated from the data of Mann et al. (2012) would miss the solubility data by almost 5 log units, which is unrealistic. For this reason, it is likely that the melt valence state remains 2+ even at these much higher oxygen fugacities. Melt composition also seems to have very little effect on Ru solubility because both MORB and andesitic melt compositions result in very similar values.

In order to compare the P and T effect of the datasets we can define an exchange coefficient K_D,

$$\log K_D = \log D + \frac{n}{4}\Delta IW,$$

which should remove the effect of fO$_2$ if the valence state for the metal in the melt is chosen correctly. The consistency between K_D values from this study and those of Mann et al. (2012), from similar P and T conditions but 10 log units lower in fO$_2$, confirms that the choice of 2+ for the valence of Ru in the melt must be correct (figure 4.13). Most of the variation in K_D over both data sets can be attributed to changes in temperatures. However, there is an apparent displacement in the temperature - log K_D trend at approximately 2000 K, the origin of which remains uncertain. Nevertheless, the results from this study makes this one of the most complete high P and T datasets for any highly siderophile element.
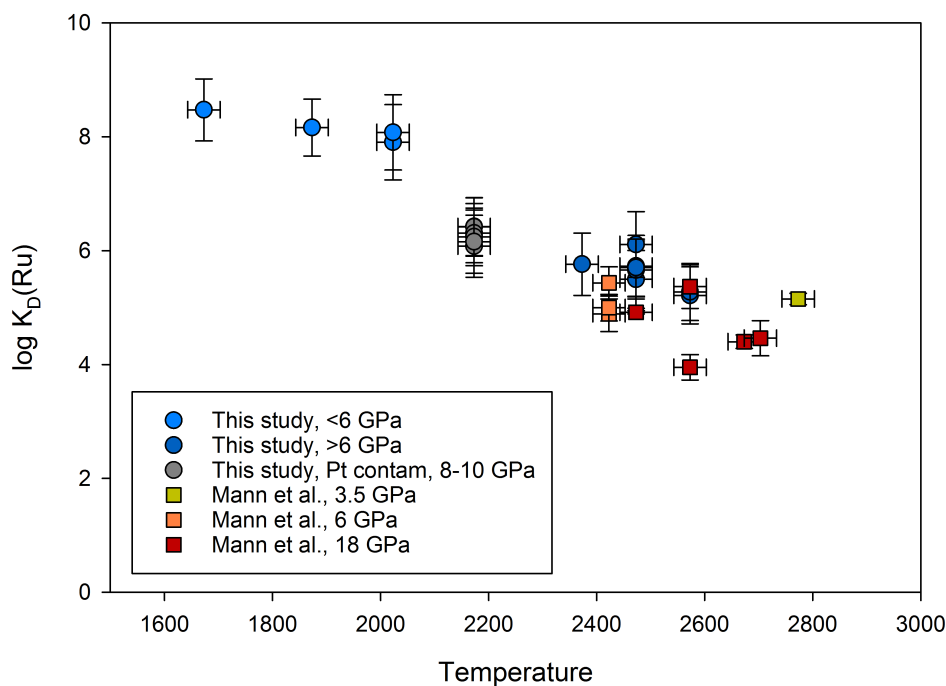
Figure 4.13: Plot of $\log K_D$ of Ru , which removes the effect of oxygen fugacity, in the silicate melt against temperature. The data from this study are consistent with the results of Mann et al., (2012), despite a difference of 10 log units in oxygen fugacity, indicating that the valence state of Ru was indeed 2+.

4.10 Effect of crystallisation on ferric/ferrous ratio

Experiments above 10 GPa crystallised on quenching into a homogeneous assemblage (see table 4.4). There remains some uncertainty as to whether the crystalline samples faithfully record the ferric iron content of the silicate, or if a a redox exchange reaction on crystallization could affect the $Fe^{3+}/\sum Fe$ ratio, as has been proposed for Fe^{3+} and Cr^{2+} bearing melts (Berry and O'Neill, 2004). Figure 4.14 shows the transition from a glassy sample to a crystalline assemblage, with no change in measured ferric iron content observed between samples at similar pressures but different textures. This is good evidence that there is no major redox reaction that occurs on crystallisation in these samples, suggesting that the crystalline samples do in fact record the ferric iron content of their previous molten state, at least as well as the glassy samples.
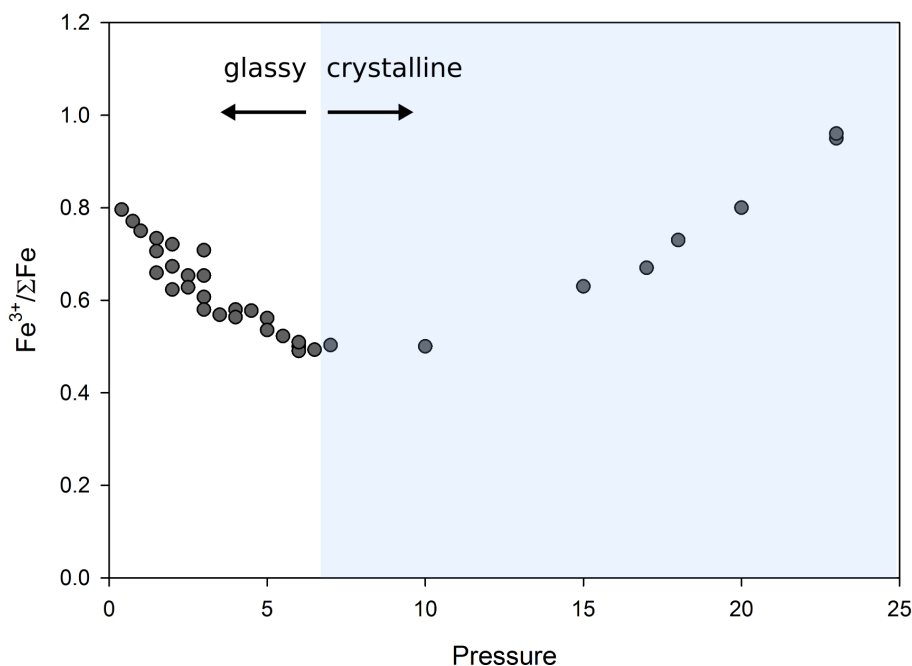
Figure 4.14: The transition from a glassy quench to a crystalline assemblage, for our samples and the literature data, occurrs at approximately 8 GPa. No change in ferric iron content is seen as a result, suggesting that there is no redox reaction occurring during crystallisation.

One possible exchange reaction would involve RuO dissolved in the melt. As described above in section 4.9, even at high oxygen fugacities the oxidation state of Ru in the melt is 2+, i.e., RuO. It is possible that some of the dissolved RuO reduced to Ru metal on quench, in turn oxidising FeO in the melt and thereby increasing the ferric/ferrous ratio; i.e., $RuO + 2FeO = Fe_2O_3 + Ru$. While the solubility of Ru does increase with temperature, the highest-pressure silicates contain only about ~ 1 mole percent RuO_x (see table 4.3). Even if 100% of this RuO reduced to Ru on quenching, it would not have changed the ferric/ferrous ratio enough to explain the increase in ferric iron content that we observe. Furthermore, X-ray diffraction analyses of the quenched silicates indicate that Ru has crystallised on quenching to form RuO_2, indicating that, if anything, RuO oxidised to RuO_2 during crystallization, which would raise the ferric iron contents of the actual melts to an even higher level at high pressures. It should be noted, however, that small concentrations of Ru metal would be unlikely to be detected by X-ray diffraction. Figure 4.15 shows the

maximum plausible effect of RuO reduction and FeO oxidation during quench crystallization, which is still relatively small. The effect of RuO oxidation to RuO_2 would move the data by the same amount only in the opposite direction. The most likely reaction of the RuO in the melt would have been for it to disproportionate during quenching, such that $2RuO = Ru + RuO_2$, resulting in no change at all to the oxidation state of the iron.
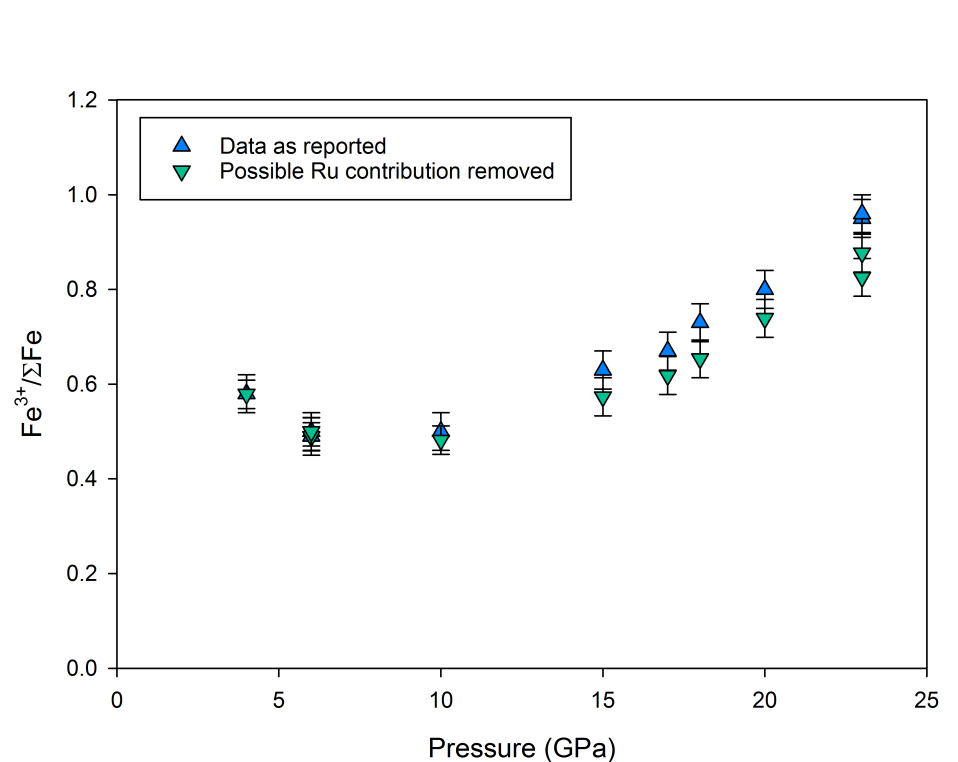
Figure 4.15: The $Fe^{3+}/\sum Fe$ of samples as determined my Mössbauer spectroscopy as reported above (blue symbols), compared with the ratio as it would have been during the experiment, if 100% of the RuO dissolved in the melt reduced on quench, oxidising FeO (green symbols). It is possible that the reduction of RuO on quenching increased the observed $Fe^{3+}/\sum Fe$ ratios; however, (1) it would not have been enough to explain the increase in ferric iron with pressure, and (2), XRD analyses of the quenched silicates indicate that, if anything, RuO oxidised during the quench.

Another possible exchange reaction could have occurred if water had been inside the capsule and oxidised FeO on quenching, i.e., $H_2O + 2FeO = H_2 + Fe_2O_3$. We consider this to have likely been a similarly negligible reaction, as water contents were measured for two of the glassy samples, and also found to be ~ 1 mole percent. Furthermore, the oxygen fugacity in the experiments was so high that it would have been unlikely for the reaction above to have

proceeded significantly to the right.

4.11 Discussion and implications

Our experiments demonstrate a clear increase in the $Fe^{3+}/\sum Fe$ ratio of silicate melt with increasing pressure at a fixed relative oxygen fugacity. This dependence can be attributed to a greater compressibility of the ferric iron melt component compared to the ferrous component, most likely due to ferric iron being more readily incorporated into a higher-coordination environment with pressure (Mysen and Virgo, 1985; Brearly, 1990; Stixrude and Karki, 2005; Hirschmann, 2012). Although we determine this effect principally in an andesitic melt at a relatively high oxygen fugacity (Ru-RuO$_2$), the effect of pressure on the volume difference of the iron melt components is a constant at any oxygen fugacity. This is confirmed by our results obtained from melts equilibrated with iron metal. At pressures above 15 GPa, the ferric iron contents of these melts increase in good agreement with the prediction of equation 4.8 calculated at the conditions of the experiments, even though this equation was only fitted to the results obtained in equilibrium with Ru and RuO$_2$.

Activity coefficients for the individual melt components will influence the relationship between oxygen fugacity and melt $Fe^{3+}/\sum Fe$ ratio for different melt compositions. Our attempts to examine the effects of melt composition, however, were hampered at high pressure by the high liquidus temperature of MORB composition melts, which resulted in only partially molten assemblages. However, successful experiments at 4 GPa indicate no discernible effect of composition, and the results obtained at 18 GPa, if extrapolated to 100 % melt, indicate that any effect must be relatively small.

The stabilisation of the ferric iron component in silicate melts with increasing pressure therefore mirrors similar changes that have been reported for mantle minerals over similar pressure intervals (Frost et al., 2004; Rohrbach et al., 2007; Shim et al., 2017). These results imply that the equilibrium,

$$3FeO = Fe_2O_3 + Fe^0,$$
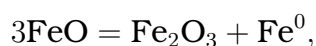
involving ferric and ferrous iron mineral components, will shift to the right with increasing pressure. This will force the precipitation of metallic iron in systems that are initially poor in Fe_2O_3 at low pressures, such as that of the Earth's mantle during and just after differentiation. Our experiments indicate that a similar effect will occur in silicate melts at high pressures, which will have a number of important implications for the oxygen fugacity and volatile speciation in magma oceans.

Accretion and core separation of the Earth were likely accompanied by extensive melting of the mantle. Numerical simulations indicate that after an initial stage of runaway growth that produced Moon to Mars sized planetary embryos, the final stages of formation was mainly through giant impacts involving these embryos. (e.g., Chambers and Wetherill, 1998; Agnor et al., 1999; Morbidelli et al., 2000; Raymond et al., 2004). These final collisions, the very last of which is considered to have resulted in the formation of the Moon, would have led to melting of the entire Earth. This would have been followed by crystallisation of a global magma ocean. Such magma oceans would not only have been in at least partial equilibrium with core forming metallic and sulfide phases, but also with the protoatmosphere, a significant proportion of which must have degassed from this silicate melt. As a result, the magma ocean stages of planetary formation likely had a major influence over the distribution of volatiles in the Earth system (Hirschmann, 2012).

By rearranging equation 4.8, the oxygen fugacity of a magma ocean composition can be calculated for a given bulk $Fe^{3+}/\sum Fe$ ratio as a function of pressure, as shown in figure 4.16. The modern upper mantle is often cited as having approximately 3 % of iron in the ferric state (Canil et al., 1994; Frost and McCammon, 2008) but, given that this is mainly based on analyses of xenoliths from the lithosphere, a slightly higher value may also be justified. In figure 4.16 the oxygen fugacities of magma oceans with bulk silicate Earth compositions are calculated as a function of pressure for $Fe^{3+}/\sum Fe$ ratios of 0.03, 0.045 and 0.1 along a magma ocean adiabat (Miller et al., 1991). It is assumed that a magma ocean would convect sufficiently rapidly to ensure homogeneous ferric iron content throughout the depth of the magma ocean (Solomatov, 2000). As shown, regardless of the bulk $Fe^{3+}/\sum Fe$ ratio, a gradi-

ent in oxygen fugacity is established for each constant bulk $Fe^{3+}/\sum Fe$ ratio, such that the magma ocean can be near or above FMQ near the surface but at or below the iron-wüstite buffer, where iron-nickel metal would become stable, (O'Neill and Wall, 1987; Frost and McCammon, 2008) at pressures above 20 GPa.
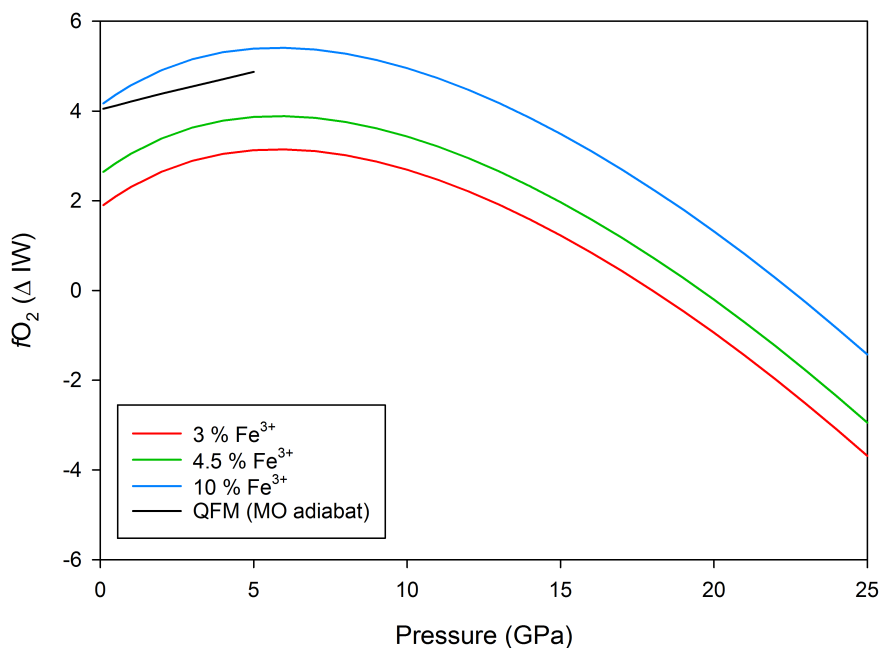
Figure 4.16: Plots of the oxygen fugacity profile of a magma ocean with 3%, 4.5%, and 10% $Fe^{3+}/\sum Fe$ ratios along a magma ocean adiabat. The 3% and 4.5% values bracket the estimates for modern upper mantle ferric iron content (e.g., Cottrell and Kelley 2011). Also plotted is the QFM buffer at the same conditions to 5 GPa. A magma ocean with 3% ferric iron would be well below IW at 25 GPa but nearly 4 log units more oxidised at low pressures.

This has two main implications. First, it can explain how the oxygen fugacity of the whole mantle was raised after core formation ceased. During core formation, upper mantle materials at pressures < 15 GPa would have contained insignificant levels of ferric iron, as the oxygen fugacity would have been fixed by equilibration with core-forming metallic iron. If the magma ocean extended to depths where pressures were > 20 GPa, FeO would have disproportionated in order to produce sufficient ferric iron in the silicate melt to satisfy the melt ferric/ferrous iron equilibrium (4.1) at these redox conditions (Figure 4.7). Metallic iron would have therefore precipitated out of the silicate melt. This

would raise the ferric iron content of the magma ocean in the regions where metallic iron precipitated, but, after convective mixing, the bulk $Fe^{3+}/\sum Fe$ ratio of the entire magma ocean would increase. If the precipitated iron metal then separated to the core, potentially along with accreted metal that had ponded after raining out from the magma ocean, the bulk oxygen content of the entire mantle would have increased, potentially to the present-day level that appears to have been already established by the start of the geological record (Canil, 1997; Delano, 2001; Trail et al., 2011).

Second, after any phase of deep magma ocean formation (i.e., to > 20 GPa), once metal had rained out, a gradient in oxygen fugacity would be established, as described above, such that while the base of the magma ocean may have been in equilibrium with metallic iron, at the surface, redox conditions at or even above FMQ would have prevailed, depending on the depth of the magma ocean. At FMQ or above, CO_2 and H_2O would be the main components degassing from the mantle to form an atmosphere (figure 1.4). This probably means that once the Earth had accreted to a size where mantle pressures exceeded 20 GPa, continued accretion of planetary embryos would have rendered magma oceans of a sufficient depth to ensure that the degassing atmosphere was oxidised, i.e., CO_2 and H_2O. On the other hand, magma oceans on smaller bodies such as the moon, Mars, and Vesta would have been of insufficient depth to stabilise significant ferric iron in equilibrium with iron metal. This can explain why their mantles appear today to be more reduced, i.e., closer to IW (Herd et al., 2002; Wadhwa, 2008; Pringle et al., 2013), than the Earth's, despite Mars and Vesta being further out from the sun and therefore, presumably, deriving from more oxidised, volatile-rich material. At these more reduced conditions, the main degassing species would have been H_2, CO and H_2O which, on cooling, would have rendered an atmosphere rich in H_2O, CH_4 and H_2 (Hirschmann, 2012). These lighter species would have been more susceptible to atmospheric loss, which may have implications for the cooling history of a magma ocean and the volatile inventory of a planet. A thick CO_2 and H_2O atmosphere would have insulated the underlying magma ocean, maintaining a molten surface and thus facilitating exchange between the two reservoirs, while a thinner or nonexistent atmosphere may have allowed for

the surface of the magma ocean to form a quench lid, effectively isolating the mantle from the atmosphere (e.g., Abe and Matsui, 1985; Elkins-Tanton, 2012).

Previous studies have proposed that a similar shift in equilibrium 4.1 to the right would occur as the lower mantle crystallised to form the mineral bridgmanite, which also contains high levels of ferric iron in equilibrium with iron metal (Frost et al., 2004; Shim et al., 2017; Andrault et al., 2018). Loss of precipitated iron metal from the solid lower mantle through further core formation could then have raised the bulk oxygen content of the entire mantle after convection. This process may have also contributed to the increase in the bulk oxygen content of the mantle, however, the homogenisation process is dependent on solid-state whole mantle mixing, which would have almost certainly required a longer time scale than homogenisation of a magma ocean. The current scenario, involving a magma ocean, makes the oxidation processes inevitable, provided the magma ocean is sufficiently deep. Due to the rapid homogenisation of the $Fe^{3+}/\sum Fe$ ratio, oxygenated atmospheres may prevail even before the end of accretion. As soon as metal has rained out, which has been suggested to be efficient process (Ichikawa et al., 2010), an oxygen fugacity gradient would be established, allowing for an oxidised atmosphere.

Our current results imply the precipitation of metallic iron at pressures above 20 GPa, but a magma ocean can potentially have encompassed the entire mantle. This leaves open the question as to the behaviour of iron components at much higher pressures. Ultimately, the compressibility of the FeO1.5 melt component will likely start to rival that of FeO, and the rising trend in melt $Fe^{3+}/\sum Fe$ ratio with pressure may start to reverse, as implied by our model fit shown in figure 4.6. A magma ocean that bottoms out in the deep lower mantle may not necessarily have high equilibrium ferric iron contents. Although the crystallisation of a magma ocean may be complicated by regions of mineral flotation and neutral buoyancy (e.g., Elkins-Tanton, 2012 and references therein), most of the lower mantle should have crystallised from near the base upwards as cooling occurs. Although initial crystallisation of the magma ocean may have had to occur, a depth would be eventually reached where metallic iron would precipitate if the previous crystallisation had not

already rendered a magma ocean composition with raised ferric iron content.

Hirschmann (2012) has speculated that if a deep magma ocean featured a gradient in oxygen fugacity, a carbon "pump" could have operated that would have removed CO_2 from the atmosphere and precipitate it as diamond in the interior. This would explain the relatively high abundance of carbon compared to other volatile elements in the present-day mantle. The carbon dioxide content of a melt which is in equilibrium with graphite or diamond would drop with depth as the oxygen fugacity decreases. This is shown in figure 4.17 calculated using the model of Duncan et al. (2017) for the oxygen fugacity of a magma ocean with a $Fe^{3+}/\sum Fe$ ratio of 0.045. Although this model is extrapolated far above the pressures over which it was calibrated, its thermodynamic basis and the fact that CO_2 will inevitably reduce to graphite or diamond with decreasing fO_2 (Stagno and Frost, 2010) ensures that the predicted trend is at least qualitatively correct. If the magma ocean remains in equilibrium with a CO_2-rich atmosphere, then the concentration of CO_2 in downwelling magma, although likely very low, must eventually reach carbon saturation. This would most likely occur at pressures over 15 GPa where the CO_2 content of the melt at saturation drops to below 10 ppm. At this depth, diamond would precipitate and should also be neutrally buoyant at approximately the same depth (Ohtani and Maeda, 2001). With time, the carbon content of the mantle would gradually rise, even if the flux of CO_2 in the melt itself from the surface was very low. One caveat to this scenario is that at low oxygen fugacities the concentration of CH_4 in the melt may also start to increase. This is difficult to asses as methane solubility would also depend on the hydrogen fugacity of the melt, although this may have been relatively low due to degassing (Hirschmann, 2012). Simple C-O-H fluid calculations also predict low CH_4 concentrations in the gas at conditions where the CO_2 content also drops to low levels, which seems to agree with the available results on the behaviour of silicate melt CH_4 contents (Ardia et al., 2013). As the Earth experienced a relatively late stage giant impact, this carbon pump mechanism might have been important in removing carbon dioxide from the atmosphere, while the absence of a late giant impact on Venus may have left the atmosphere, by comparison, more enriched in CO_2.
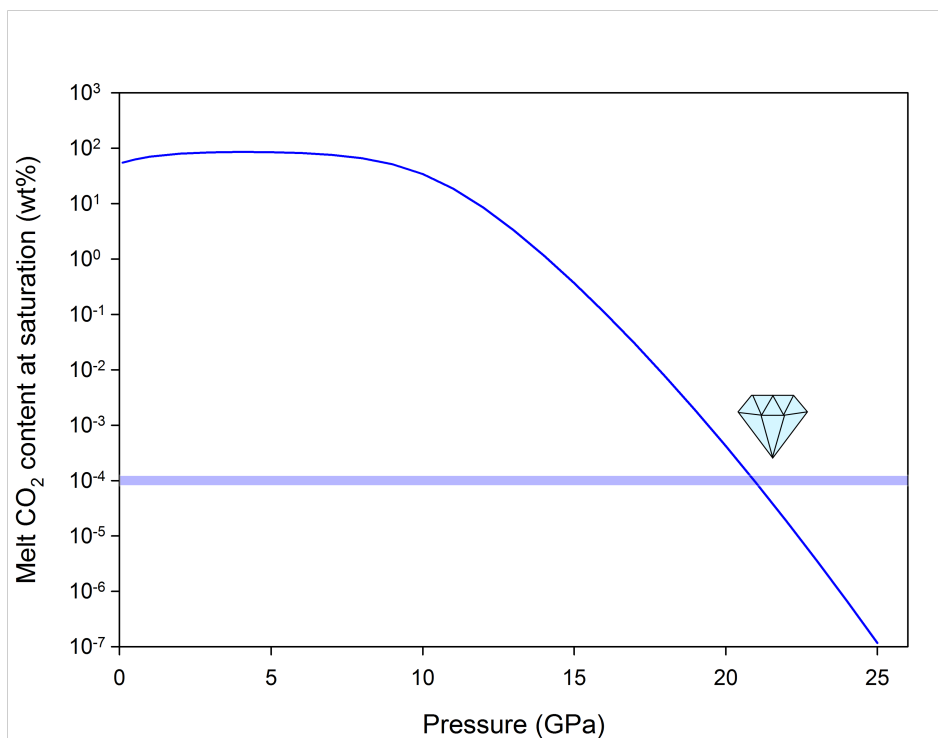
Figure 4.17: The carbon dioxide content of a silicate melt in equilibrium with graphite or diamond as a function of depth along an oxygen fugacity constrained by a bulk silicate Earth composition with a constant $Fe^{3+}/\sum Fe$ ratio of 0.045. With these parameters, the horizontal line shows that a magma containing only 1 ppm carbon would reach carbon saturation at ~ 20 GPa, at which point diamond would exsolve. Calculated using the model of Duncan et al. (2017).

In summary, our results demonstrate that the ferric iron component of silicate melts becomes increasingly stabilised with pressure at a fixed relative oxygen fugacity, at least to ~ 25 GPa. This implies that a deep magma ocean that is in equilibrium with metallic iron at its base could have a relatively high ferric iron content throughout, such that the upper portions may have been at a much higher oxygen fugacity. This may explain why the Earth's upper mantle appears to have been at FMQ since the beginning of the geologic record, despite necessarily having been at equilibrium with iron metal during core formation and therefore at or below IW.

A magma ocean with such a gradient in oxygen fugacity may have established a carbon pump, in which downwelling magma containing even very small amounts of CO_2 would at some depth become carbon saturated and exsolve diamond or graphite. This could explain why the mantle today has

an overabundance of carbon, and possibly why the atmosphere of Venus is comparatively enriched in CO_2.

Finally, this oxidation mechanism can also potentially explain why the mantles of the moon, Mars, and Vesta are comparatively more reduced than the Earth's. Magma oceans on smaller bodies may not have attained the depths necessary to stabilise ferric iron to the extent required for the production of appreciable amounts of ferric iron, resulting in more reduced mantles despite accreting from material that was presumably more oxidised.

5 Gradual oxidation of the mantle through accretion of water

5.1 Motivation

As introduced in section 1.3.2, the delivery of water late in the Earth's accretion may have been a plausible mechanism to oxidise the mantle, however it requires a process by which hydrogen would have been removed from the system. Any hydrogen released through the disproportionation of H_2O in the mantle that is not removed in some way would simply reduce overlying mantle and result in no net oxidation. One possibility for removing hydrogen would be to dissolve it into a phase that is subsequently removed to the core, sequestering the hydrogen. Previous work has investigated hydrogen partitioning between a silicate melt and metallic iron, and found that, hydrogen is quite soluble in metallic iron at high H_2O fugacities (e.g. Okuchi, 1997). However, it has been recently proposed that hydrogen metal/silicate partition coefficients may be much lower and closer to ~ 0.2 (Clesi et al., 2018), indicating lithophile behaviour. Furthermore, raising the oxygen fugacity of the upper mantle from metal saturation to FMQ requires the accumulation of Fe_2O_3, which precludes the coexistence of metallic iron, at least at lower pressures. The process of removing hydrogen from the mantle would, therefore, have had to have continued even after the oxygen fugacity of the mantle had risen above the level at which iron metal is stable.

It has long been suggested that many of the geochemical signatures of the Earth's mantle could be explained if the segregating liquid during the final stage of core formation were a sulfide, rather than metallic iron (e.g., O'Neill,

125

1991; Rubie et al., 2016). It is therefore perhaps more relevant to consider whether hydrogen could be lost to the core by partitioning into a descending sulfide liquid, as this appears to have been the final stage of core formation after which the mantle could be oxidised. Any increase in Fe_2O_3 in the upper mantle prior to this would have been reduced by more incoming metallic iron.

The recent work of Rubie et al. (2016) used the mantle abundances of the highly siderophile elements to argue that sulfur, along with other volatile elements, must have been delivered to Earth throughout accretion and not solely as a late addition. In their model, core formation proceeds as planetesimals and planetary embryos are accreted to the growing Earth, each delivering a metallic core, and/or varying amounts of volatiles, depending on its original heliocentric distance. Some percentage of the Earth's mantle equilibrates with the core of the impacting planetesimal, depending on its size, and elements are tracked as they partition into the core or mantle, depending on their pressure and temperature-dependent partition coefficients (Rubie et al., 2015; 2016). Abundances of the elements in the mantle are thus quantified over time throughout accretion.

The sulfur concentration in the mantle resulting only from metal silicate partitioning is higher than in the present day mantle concentration. The maximum attainable sulfur concentration of a magma ocean that is in equilibrium with iron sulphide liquid, i.e. the sulphur concentration at sulphide saturation (SCSS), has been found to be a function of both pressure and temperture. A magma will start to exsolve sulfide, however, if the concentration of sulfur in the silicate melt exceeds a saturation limit (Mavrogenes and O'Neill, 1999). Mavrogenes and O'Neill (1999) quantified the sulfur concentration at sulfide saturation for a peridotite liquid, and showed that it decreases with pressure and increases with temperature.

While average values along a magma ocean adiabat are large enough to accommodate the full complement of sulfur delivered to the growing Earth in the model, as a deep magma ocean cools towards crystallisation temperatures, FeS sulfide would exsolve as the SCSS drops. High convection velocities would have ensured that sulfur would have been well-mixed into the magma ocean (Solomatov, 2000). FeS exolution would have therefore occurred throughout

the magma ocean as it cooled, and the entire magma ocean would thus have been in equilibrium with the FeS (Rubie et al., 2016). The higher density of the sulfide would have meant it would sink and segregate to the core, removing sulfur from the mantle and accounting for the difference in sulfur abundance predicted by the accretion model and observed today. This would also explain the slightly superchondritic abundance of some highly siderophile elements (Laurenz et al., 2017; Rubie et al., 2017). In fact, these abundance provide good evidence in support of the late stage separation of sulphide which was originally proposed by O'Neill (1991) and referred to as a Hadean matte.

The separation of the Hadean matte would have been one of the final phases of planetary differentiation. The question then arises of how its separation may have affected the oxygen fugacity of the mantle, through the potential disso-lution of either oxygen, hydrogen, or both. Experimental evidence suggests that up to ~ 10 mole percent of hydrogen may dissolve into solid FeS at 3 GPa (Shibazaki et al., 2010). If hydrogen, supplied originally as water in accret-ing planetesimals, was removed to the core in a sulfide melt, leaving oxygen behind, the net result would be an increase in the mantle's oxidation state. Similarly, if oxygen dissolves in the sulphide melt as O rather than FeO, then the oxygen fugacity of the mantle could have decreased.

The difficulty of such a study has been pointed out by previous workers, specifically the fact that sulfide will necessarily crystallise during quenching, and thus cannot record the entire H content. Recent work, however, has re-ported measurements of some H in crystallised melts of metallic iron (Clesi et al., 2018). The idea is that the solid metal has a finite H solubility, i.e., if partitioning experiments are performed involving metallic and silicate melts, the partition coefficient can be determined as long as the metal liquid hydro-gen content is below the solid metal solubility limit. This, of course, requires that bulk H concentrations are below the Henry's law limit, but, the parti-tion coefficient should be applicable to all concentrations below this limit. In this work, we performed exploratory experiment measurements in order to de-termine whether it may be possible to measure any H in quenched sulphide melts. If this is the case, then by keeping the bulk H concentration lower than the solubility in the quenched solid sulfide, it may still be possible to estimate

a partition coefficient. Although it is also likely that the partition coefficient changes at higher bulk H concentrations, lower concentrations may anyway be more applicable to a terrestrial magma ocean.

Wykes and Mavrogenes (2005) proposed that sulfide melts may dissolve H_2O and release it on crystallisation. The authors used indirect observations to propose that H_2O is soluble in sulfide melts by performing piston-cylinder experiments on oxide-free sulfides with added liquid H_2O. While the authors were unable to quantify the water concentration of the sulfide, they found a depression of the sulfide melting temperature of 35 K as compared to dry experiments. In addition, they report textural evidence in the quenched liquid sulfide for a fluid phase, specifically vessicles and fluid pores. No oxides or other indication that the H_2O had decomposed to H_2 and O, were present, suggesting that the H_2O itself was soluble in the liquid sulfide. They suggest that their results support the interpretation that hydrous phases that have been found around sulfide ore deposits originated from water that exsolved from the sulfide as it cooled (Li et al., 1992; Wykes and Mavrogenes, 2005 and references therein). Buono and Walker (2015) proposed similarly that a decrease in the FeS-Fe eutectic temperature may also be caused by the solubility of H in the melt.

Quenched sulphide melts are also the main inclusions found in diamonds (e.g., Pearson et al., 1998). Knowledge of the H content might provide some useful information on the melt from which diamonds formed or the H contents of the silicate or carbonate melts from which the iron sulphide melts may have separated. To date, no one has ever attempted to measure the H content of a quenched sulfide melt, and so the results presented here provide useful constraits on whether a liquid sulfide may retain any dissolved hydrogen during crystallisation. H and O contents of sulphides coexisting with silicate melt are then used to examine the effects of Hadean matte separation on the redox state of the mantle.

5.2 Approach

In order to investigate whether the interaction between core-forming sulfide and mantle materials may have influenced the oxidation state of the mantle, we have performed multianvil experiments in which a liquid FeS sulfide was equilibrated with molten silicate. As the major goal of this study is to examine how the oxygen fugacity of the mantle may have been raised from iron metal saturation to the level recorded in the upper mantle today, it is critical to be able to both vary and measure the oxygen fugacity within the experiments. The measurement of $f\mathrm{O}_2$ is particularly challenging because noble metal sliding redox sensors (e.g. Stagno et al., 2011) will simply dissolve in the sulphide melt. Varying the oxygen fuacity between experiments was accomplished by changing the initial Fe concentration of both the sulfide and the silicate. Primarily, the oxygen fugacity of the experiments was determined from the recovered samples by measuring the $\mathrm{Fe}^{3+}/\sum\mathrm{Fe}$ ratios of the silicate glasses with Mössbauer spectroscopy, and employing a thermodynamic model with empirically fit parameters that relates ferric iron content to oxygen fugacity (i.e., the model developed in this work, chapter 4, as well as the one presented by O'Neill et al., 2006). In addition, Ni, V, and Mo were added as oxides to the silicate (1 wt% each) in an attempt to provide an estimate of the oxygen fugacity using the partitioning of these elements between the sulphide and silicate melt.

Secondly, the behaviour of oxygen in sulfide melts was also examined. The study of Fonseca et al. (2008), conducted in a 1-atm gas-mixing furnace at 1200-1400 °C, has shown that oxygen content in a sulfide liquid increases as sulfur content decreases, potentially indicating that O replaces S in the sulfide. Further, O solubility increases with oxygen fugacity, and the authors observed up to 7 wt % in the FeS, and at high $f\mathrm{O}_2$ also occurs as FeSO (Fonseca et al., 2008). Therefore, a sulfide melt equilibrating with mantle material may in fact remove oxygen from the system, thereby reducing the redox state of the mantle. Studies of oxygen solubility in liquid sulfides at high pressure are scarce, however, though the studies of Wendlandt (1982) and Mavrogenes and O'Neill (1999) suggest that the oxygen content of sulfides decreases at

increasing pressures and temperatures. However, their experiments were focused on determining SCSS, and oxygen content was not measured directly but a low oxygen content in the sulfide liquid was inferred from a lack of oxides. The study of Fonseca et al. (2008) was focused on oxygen solubility rather than partitioning, and so to date there are no experimental studies to examine the partitioning behaviour of oxygen between a liquid sulfide and a silicate melt.

Finally, as described above, if water accreting to the early Earth supplied the oxygen necessary to raise the fO$_2$ of the mantle, some process must have been removing hydrogen from the system. In order to place constraints on whether hydrogen may have been removed to the core via a sulfide melt, we attempt to determine a partition coefficient between a liquid sulfide and a molten silicate. Here we present results from an explorative study in which we attempt to determine the possibility of measuring hydrogen in a quenched sulfide melt. It must be emphasised that any H content measured in the sulphide melt can only be treated as a minimum. However, before taking steps to examine in detail the solubility of H in the solid quenched sulphide it is first necessary to determine if any H can be detected at all. This work will therefore investigate the partitioning of oxygen and hydrogen between liquid sulfide and silicate melts in order to better understand the possible effects that episodes of sulfide-dominated core formation may have had on the oxidation state of the mantle.

5.3 Experimental methods

To investigate whether a descending sulfide could have influenced the redox state of the mantle, a series of experiments was performed to determine hydrogen and oxygen partitioning between liquid sulfide and molten silicate. The composition of the silicate was average mid-ocean ridge basalt (MORB, Gale et al., 2013) mixed from reagent-grade oxides and carbonates, ground together under ethanol with an agate mortar and pestle. Oxides had been devolatilised at 1000 °C for three hours prior to weighing, and the bulk composition was

further devolatilised after preparation for 12 hours at 1000 °C. To change the oxygen fugacity between the experiments, the iron content of both the silicate (three compositions, compensated for by more or less MgO, see table 5.1) and the sulfide was varied. To obtain the correct stoichiometry, FeO was added as Fe_2O_3, and so after preparation the silicate portions were reduced overnight in a CO-CO_2 1-atm gas-mixing furnace at 1100 °C and an oxygen fugacity $\sim FMQ - 2$, i.e., conditions at which the Fe_2O_3 would fully reduce to FeO. Each of the three MORB compositions was then mixed with pure reagent-grade FeS sulfide, with a 60:40 silicate:sulfide weight ratio. Portions of the MORB/sulfide mixtures then had an additional 5 wt% metallic iron powder added, yielding a total of six different starting materials. Finally, water was added as brucite ($Mg(OH)_2$), the MgO component of which is included in the reported silicate composition. See table 5.2 for quantities(see table 5.2).

Table 5.1: The three MORB-like starting compositions used in this study, in wt %.

oxide	Fe-2	Fe-5	Fe-10
SiO_2	49.21	49.21	49.21
TiO_2	1.64	1.64	1.64
Al_2O_3	14.33	14.33	14.33
CaO	11.10	11.10	11.10
Na_2O	2.72	2.72	2.72
FeO	2.00	5.00	10.00
MgO	16.00	13.00	8.00
NiO	1.00	1.00	1.00
V2O3	1.00	1.00	1.00
MoO3	1.00	1.00	1.00

Two sets of experiments were performed, all in a 500 tonne multianvil press with an 18/11 assembly at the Bayerisches Geoinstitut (see section 2.1 for details of the multianvil technique). For the first set, two sample charges, containing the same FeO content, both with and without added metallic Fe were run simultaneously in stacked graphite capsules, which were in turn sealed in welded $Au_{80}Pd_{20}$ capsules. Gold is less permeable to H as other metals, and so was used in order to minimise water loss during the experiment (see figure 5.1). These experiments were first pressurised to 3 GPa. The temperature was increased to 800 °C and held for three hours to allow the graphite cap-

sules to sinter, minimising their porosity, in order to prevent melt escaping the capsule. Experiments were subsequently heated to 1400 °C, superliquidus temperature, and allowed to equilibrate for 15 minutes before rapidly quenching by shutting off the power to the heater.

The procedure for the second set of experiments was similar, except that only the MORB + FeS starting powder was used (i.e., with no additional Fe metal), in a single graphite capsule, which was sealed in an outer $Au_{80}Pd_{20}$ capsule as in the first set. The amount of water added was greater than in the first set; 0.4 wt% as opposed to 0.1-0.2 wt%, and they were run at a lower temperature (1300 °C).
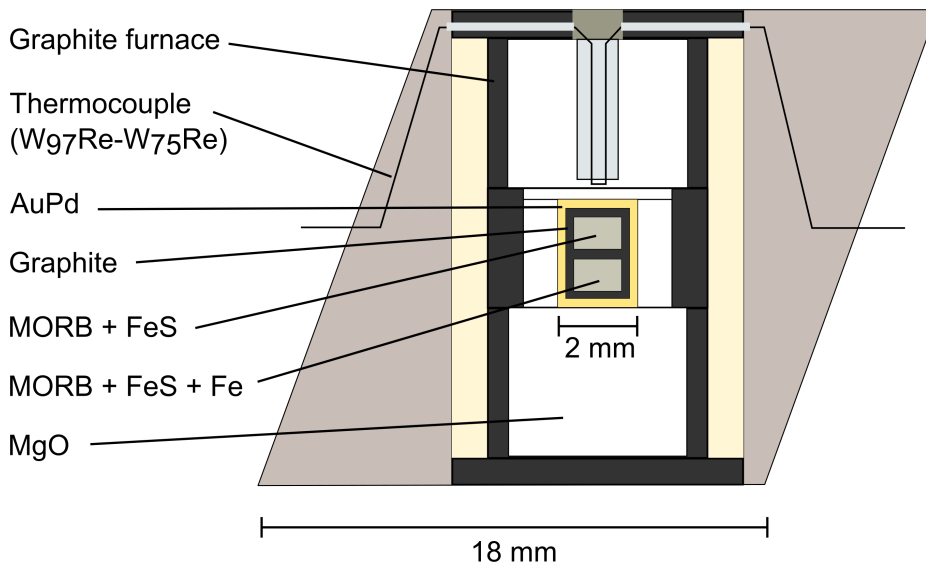
Figure 5.1: Experimental setup for hydrogen partitioning experiments.

Table 5.2: Conditions for all experiments. All were performed at 3 GPa

Exp	Starting material	Temperature (°C)	added water (wt%)
V1043a	Fe-2 + FeS	1400	0.15
V1043b	Fe-2 + FeS + Fe^0	1400	0.29
V1044a	Fe-5 + FeS	1400	0.15
V1044b	Fe-5 + FeS + Fe^0	1400	0.29
V1045a	Fe-10 + FeS	1400	0.15
V1045b	Fe-10 + FeS + Fe^0	1400	0.29
V1052	Fe-2 + FeS	1300	0.43
V1053	Fe-5 + FeS	1300	0.43
V1054	Fe-10 + FeS	1300	0.43

Recovered samples were mounted in epoxy resin and polished for analysis with scanning electron microscope (SEM), electron probe microanalysis (EPMA), and elastic recoil detection analysis (ERDA). Samples were then ground down to 500 μm for transmission Mössbauer spectroscopy, and subsequently further thinned to 100 μm for Fourier-transform infrared spectroscopy (FTIR).

5.4 Results

5.4.1 Texture and bulk composition

All samples were fully molten during the experiment. Recovered run products in all cases comprised one or more spheres of sulfide embedded in the silicate glass (see figure 5.2). The silicate in experiments V1052 and V1053 crystallised on quench, and so were excluded from the study, as H_2O contents could not be determined. Bulk chemistry of the silicates and sulfides was determined with EPMA and the results are in table 5.3. In order to obtain bulk melt compositions the electron beam was defocused, which was particularly important to integrate the quenched crystallized sulphide composition. Silicate analyses were performed with a 15 keV accelerating voltage and 15 nA, and a spot size of 10 μm, with the following standards: Al- spinel; Ca- andradite; Na- albite; Si, Mg, Fe- olivine; S- FeS2; Ti- MnTiO3; V, Mo- metal; Ni- NiO. Sulfides were analysed with 20 keV and 20 nA and a 30 μm spot size with the following standards: O- Fe_2O_3; Si- FeSi; Fe- Fe metal; S- FeS_2; Ni, V, Mo, Au, Pd- metals.
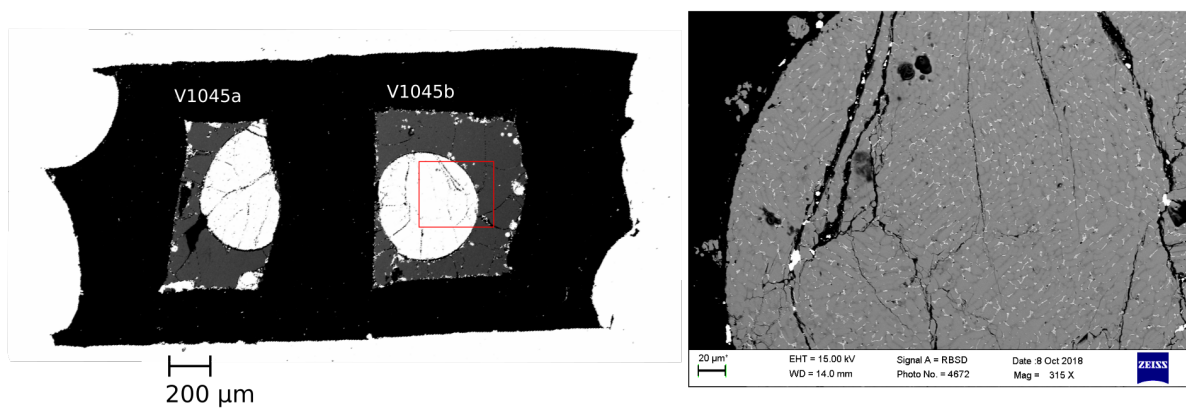
Figure 5.2: Backscattered electron image of a typical run product. Spheres of quenched, crystalline sulfide are embedded in the silicate glass. The red box indicates the zoomed area shown in the right image. The brighter regions of the sulfide are small amounts of pentlandite, which contains some Pd contamination from the outer capsule. Darker regions of the sulphide appear to be comprised of a stoichiometric FeSO phase, as described in Fonseca et al. (2008).

The sulfide quench textures showed evidence of a crystallisation sequence in which a monosulfide solid solution crystallised first, ultimately forming pyrrhotite. Residual liquid around the pyrrhotite grains boundaries became enriched in Pd, Ni, and O, and possibly H, ultimately forming pentlandite and a stoichiometric FeSO, as reported by Fonseca et al. (2008). Some of these pentlandite/FeSO-rich regions exhibited small voids (see figure 5.3). It is unclear whether these are a result of the loss of solid pieces of pentlandite which were plucked during sample preparation, or if these voids represent a volatile-rich fluid that was exsolved during quenching. The FeSO phase was reported to be amorphous by Fonseca et al. (2008) but it likely accounts for much of the oxygen content measured for the sulphide melt by defocusing the EMPA electron beam.
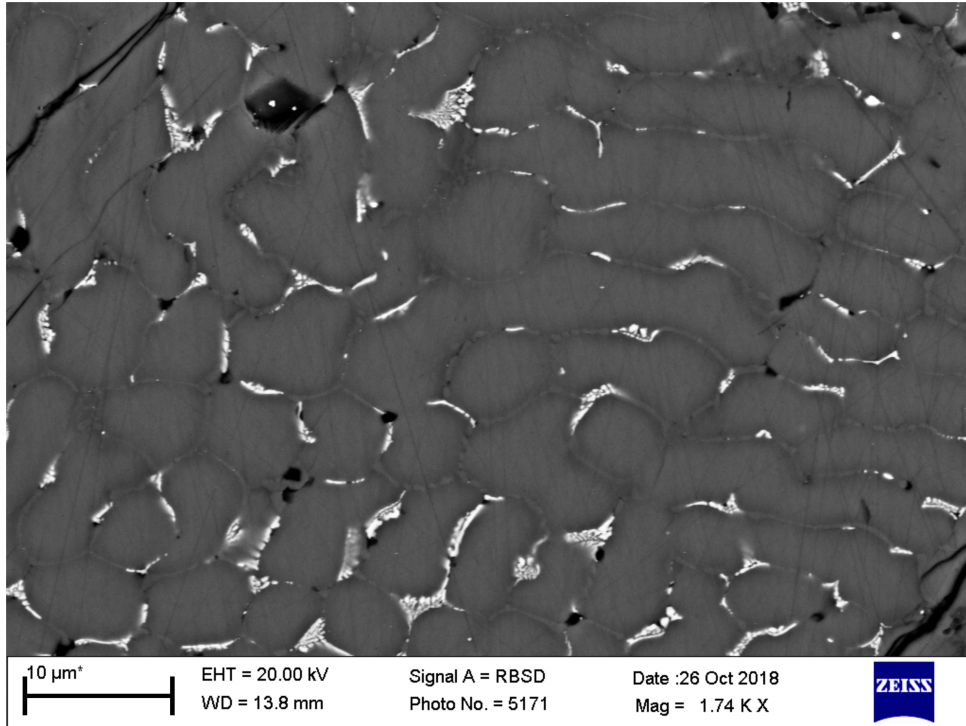
Figure 5.3: Quench texture of the crystallised sulfide. The dominant originally monosulphide solid solution (MSS) ultimately forms pyrrhotite. Surrounding these grains are rims comprised of brighter and darker materials that likely remained liquid after MSS had crystallized. These rims comprise pentlandite (bright), containing some Pd from the outer capsule, and FeSO (darker areas). Small voids may have formed by the separation of fluid phase, but could equally be pentlandite grains that were plucked during sample preparation.

Table 5.3: Results from EPMA analysis of all samples, in wt%

		1043a	1043b	1044a	1044b	1045b	1054-T
silicates	SiO_2	46.68 (0.11)	44.78 (0.13)	45.97 (0.24)	42.76 (0.17)	46.14 (0.12)	45.73 (0.22)
	TiO_2	1.48 (0.03)	1.37 (0.03)	1.46 (0.02)	1.37 (0.03)	1.56 (0.05)	1.51 (0.05)
	Al_2O_3	13.77 (0.07)	12.93 (0.06)	13.38 (0.11)	12.57 (0.11)	13.61 (0.06)	13.57 (0.11)
	FeO	4.07 (0.19)	10.03 (0.32)	7.68 (0.33)	14.61 (0.65)	14.23 (0.46)	11.89 (0.37)
	Fe_2O_3	0.72 (0.19)	0.64 (0.32)	0.67 (0.33)	1.62 (0.65)	1.07 (0.46)	0.50 (0.37)
	MgO	16.12 (0.10)	14.62 (0.10)	14.24 (0.09)	11.69 (0.10)	7.72 (0.03)	8.77 (0.07)
	CaO	11.06 (0.05)	10.14 (0.10)	10.59 (0.09)	9.56 (0.10)	10.35 (0.08)	10.36 (0.08)
	Na_2O	2.81 (0.05)	2.55 (0.06)	2.69 (0.05)	2.46 (0.06)	2.69 (0.05)	2.75 (0.09)
	SO_3	0.48 (0.02)	0.62 (0.02)	0.57 (0.03)	0.95 (0.26)	0.63 (0.04)	0.44 (0.03)
	NiO	0.008 (0.01)	0.006 (0.01)	0.007 (0.01)	0.009 (0.01)	0.006 (0.01)	0.011 (0.01)
	V_2O_3	0.53 (0.02)	0.56 (0.01)	0.59 (0.01)	0.58 (0.02)	0.61 (0.02)	0.66 (0.02)
	MoO_3	0.02 (0.02)	0.02 (0.01)	0.03 (0.02)	0.09 (0.02)	0.02 (0.01)	0.05 (0.02)
sulfides	Si	0.10 (0.19)	0.01 (0.00)	0.04 (0.05)	0.03 (0.02)	0.04 (0.05)	0.09 (0.11)
	Fe	52.48 (1.88)	61.13 (0.66)	56.46 (0.66)	60.29 (0.57)	61.48 (0.44)	56.64 (1.54)
	S	34.09 (0.91)	33.72 (0.52)	33.79 (0.77)	32.60 (0.48)	32.67 (0.71)	34.39 (0.56)
	O	0.78 (0.35)	2.09 (0.40)	1.50 (0.44)	2.78 (0.54)	2.23 (0.47)	1.95 (0.50)
	Pd	5.37 (1.38)	0.03 (0.02)	3.64 (1.40)	0.83 (0.39)	0.24 (0.10)	0.13 (0.07)
	Au	4.60 (2.01)	0.02 (0.02)	0.59 (0.47)	0.30 (0.11)	0.32 (0.12)	0.13 (0.08)
	V	0.21 (0.02)	0.19 (0.03)	0.22 (0.06)	0.16 (0.02)	0.20 (0.03)	0.15 (0.04)
	Mo	1.41 (0.09)	1.46 (0.08)	1.61 (0.11)	1.47 (0.10)	1.37 (0.06)	1.70 (0.15)
	Ni	1.07 (0.05)	1.02 (0.04)	1.23 (0.03)	1.22 (0.03)	0.82 (0.11)	1.29 (0.03)

5.4.2 Oxygen fugacity

An important goal of this study was to understand oxygen and hydrogen partitioning between silicate and sulphide melts, at oxygen fugacities that would have prevailed as the mantle oxidized from iron metal saturation to its present day level. To that end, accutarely quantifying the oxygen fugacity that prevailed during the experiment is critical. This was accomplished by measuring the ferric iron content of the silicate glasses with transmission Mössbauer spectroscopy. Samples were prepared as double-polished 500 μm thick sections, and data was collected for $\sim$ 10-20 hours. An example spectrum is shown in figure 5.4. Each spectrum was fit with MossA software (Prescher et al., 2012), using two Loretzian doublets, one each for Fe^{2+} and Fe^{3+}, and a single sextet for iron in sulphide. Determined $Fe^{3+}/\sum Fe$ ratios are reported in table 5.4 and hyperfine parameters are reported in table 5.5.
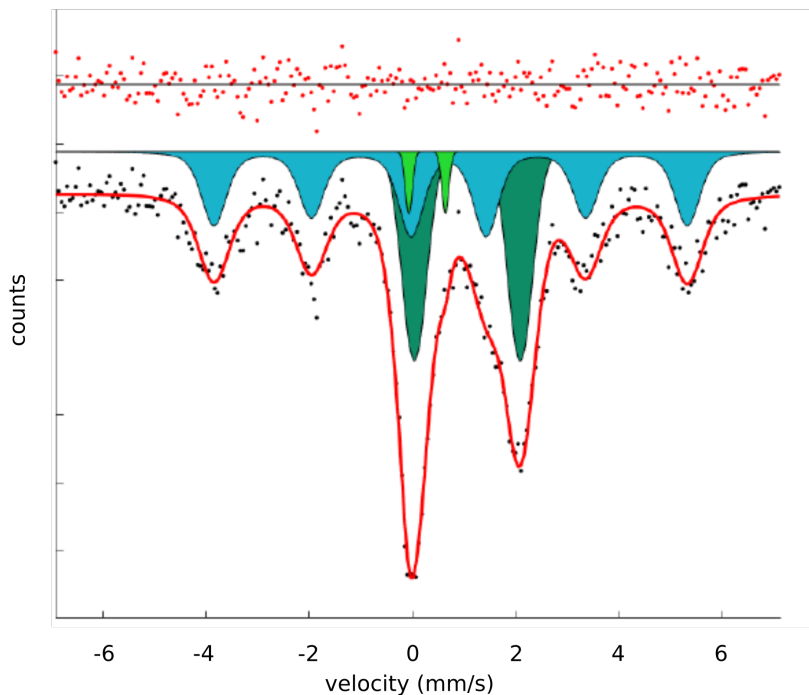
Figure 5.4: Example of a Mössbauer spectrum taken from one of the resulting experimental charges. The spectrum is somewhat broadened due to the amorphous structure of the glass, and was fit with two Lorentzian doublets, for ferrous (dark green) and ferric (light green) iron in the glass, and one sextet (blue), arising from the iron in the sulfide.

Two models relating ferric iron content to oxygen fugacity for silicate melts

were then used to calculate oxygen fugacity: the model developed here in chapter 4, and the model presented by O'Neill et al., (2006). Results are in table 5.4, and have been normalised to the quartz-fayalite-magnetite buffer. The models were in good agreement with each other, with the model developed in this work consistently approximately 0.3-0.5 log units lower than the O'Neill model. In either case, the samples spanned a range of $f\mathrm{O}_2$ from approximately QFM - 2 to QFM + 2, ($\sim$ IW + 2.2 to IW + 5.3), which is a good range for exploring the oxidation of a magma ocean from metal saturation. For this study, the $f\mathrm{O}_2$ calculated by the model of O'Neill et al. (2006) was preferred, as the model developed in chapter 4 was less accurate at low pressures.

Table 5.4: Ferric iron content of the samples as determined by Mössbauer spectroscopy. The oxygen fugacity of the samples was calculated from the ferric iron content of the silicate glass, using both the model presented in this work (chapter 4) and the model developed by O'Neill et al. (2006).

Sample	$Fe^{3+}/\Sigma Fe$	$\log_{10} f\mathrm{O}_2$	$\log_{10} f\mathrm{O}_2$
		(Δ FMQ, this work)	(Δ FMQ, O'Neill et al., 2006)
V1043a	0.15 (0.04)	0.85	1.35
V1043b	0.06 (0.03)	-0.71	-0.42
V1044a	0.08 (0.04)	-0.40	-0.11
V1044b	0.10 (0.04)	0.04	0.33
V1045b	0.07 (0.03)	-1.06	-0.77
V1054	0.04 (0.03)	-2.25	-1.84

Table 5.5: Hyperfine parameters obtained from transmission Mössbauer spectra

Exp #		Center shift	FWHM	Intensity	Quad. split	BHF	χ^2
V1043a	sulfide	0.753 (0.035)	0.626 (0.120)	57.918 (10.480)	0.117 (0.069)	28.212 (0.233)	1
	Fe^{2+}	1.053 (0.033)	0.543 (0.099)	35.712 (9.687)	2.017 (0.067)	NaN	
	Fe^{3+}	0.230 (0.062)	0.097 (0.834)	6.371 (3.771)	0.566 (0.130)	NaN	
V1043b	sulfide	0.751 (0.025)	0.289 (0.175)	43.229 (6.921)	-0.178 (0.049)	31.000 (0.178)	1.06
	Fe^{2+}	1.072 (0.018)	0.553 (0.076)	53.119 (6.775)	2.050 (0.043)	NaN	
	Fe^{3+}	0.184 (0.089)	0.220 (0.389)	3.652 (2.925)	0.615 (0.194)	NaN	
V1044a	sulfide	0.736 (0.026)	0.582 (0.110)	54.316 (6.914)	0.040 (0.050)	28.429 (0.198)	0.93
	Fe^{2+}	1.079 (0.017)	0.565 (0.054)	42.100 (6.606)	2.050 (0.035)	NaN	
	Fe^{3+}	0.301 (0.062)	0.163 (0.315)	3.585 (2.831)	0.710 (0.126)	NaN	
V1044b	sulfide	0.745 (0.033)	0.700 (0.117)	45.016 (8.983)	-0.004 (0.063)	28.913 (0.243)	1.31
	Fe^{2+}	1.081 (0.021)	0.601 (0.054)	49.280 (8.543)	2.070 (0.044)	NaN	
	Fe^{3+}	0.320 (0.084)	0.341 (0.323)	5.704 (5.027)	0.739 (0.208)	NaN	
V1045b	sulfide	0.764 (0.013)	0.269 (0.084)	41.821 (4.207)	-0.211 (0.027)	31.064 (0.087)	1.14
	Fe^{2+}	1.053 (0.015)	0.549 (0.054)	54.043 (4.084)	2.079 (0.031)	NaN	
	Fe^{3+}	0.210 (0.071)	0.183 (0.476)	4.136 (1.656)	0.564 (0.148)	NaN	
V1054	sulfide	0.726 (0.032)	0.487 (0.147)	47.820 (7.689)	-0.229 (0.062)	29.581 (0.225)	0.95
	Fe^{2+}	1.068 (0.012)	0.583 (0.049)	50.156 (7.536)	2.137 (0.043)	NaN	
	Fe^{3+}	0.443 (0.071)	0.097 (0.584)	2.024 (2.177)	0.638 (0.160)	NaN	

5.4.3 Behaviour of the minor elements and their potential use as a proxy for fO_2
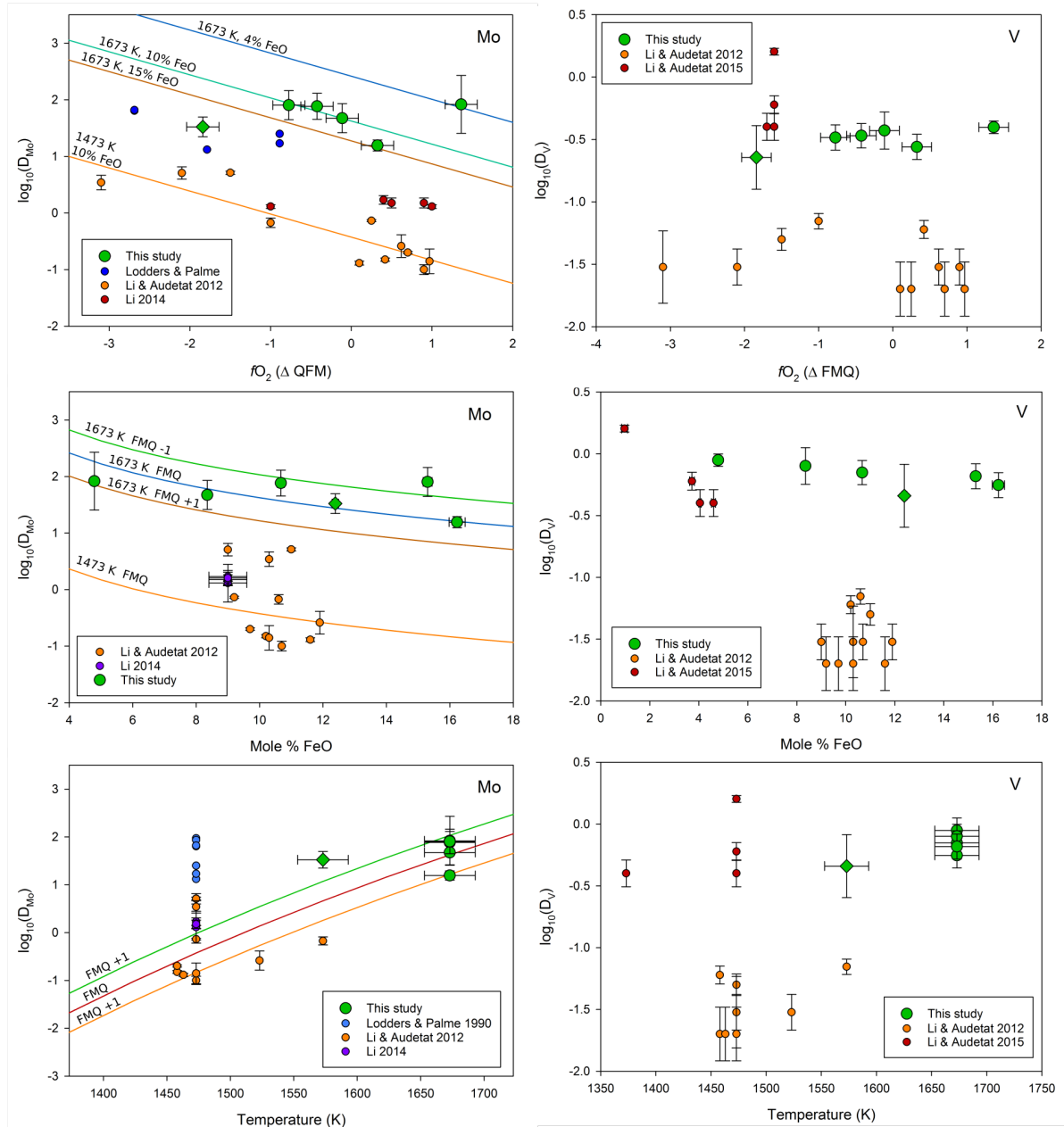
Figure 5.5: Sulfide/silicate partitioning behaviour of molybdenum and vanadium as a function of oxygen fugacity, FeO content of the silicate, and temperature. The diamond symbol denotes the experiment performed at a lower temperature. Literature data from Li and Audétat (2012), Li (2014), and Lodders and Palme (1991) is plotted for comparison. Data from Li and Audétat (2012) was used with our data to fit a parameterised model for $D_{Mo}^{SL/SM}$ as a function of fO_2, FeO content of the silicate melt, and temperature (see text); the resulting curves are also plotted.

If an oxygen fugacity dependence can be calibrated for minor element partitioning between sulphide and silicate melt it could be used in later experiments to determine the oxygen fugacity without the need to determine the melt ferric/ferrous ratio. The nickel concentrations in the silicate glasses of our recovered samples were in general very close to the detection limit of the electron microprobe. As such our results have extremely large uncertainties, and so are not considered useful. Molybdenum concentrations in the silicate melt were also low but certainly above detection limits and, as will be shown, could be routinely used to determine the oxygen fugacities in such experiments.

The obtained molybdenum sulfide liquid/silicate melt partition coefficients, $D_{\mathrm{Mo}}^{\mathrm{SL/SM}}$, appear to have a weak dependence on the silicate melt FeO concentration but no clear $f\mathrm{O}_2$ dependence (Figure 5.5). Li and Audétat (2012) studied a basanitic melt composition at 1.5 and 2.5 GPa and $\sim$1200-1300 °C. Their data, also shown in figure 5.5, have a stronger $f\mathrm{O}_2$ trend but were also collected over a narrower range in silicate melt FeO content. Li and Audétat (2015) proposed an empirical expression to describe $D_{\mathrm{Mo}}^{\mathrm{SL/SM}}$ as a function of T, silicate melt FeO content (in weight %) and oxygen fugacity normalised to the FMQ oxygen buffer, i.e.,

$$D_{\mathrm{Mo}}^{\mathrm{SL/SM}} = 8.66 - 94000/T - 0.27 \cdot (\Delta\mathrm{FMQ}) - 2.34 \cdot \log(\mathrm{FeO}_{\mathrm{melt}}). \qquad (5.1)$$

This equation provides a poor description of our experimental results, to some extent because our data extend to a higher temperature than that at which the expression was calibrated. As the partitioning of Mo is clearly $f\mathrm{O}_2$ dependent, at least in the data of Li and Audétat (2012), a change of oxidation state of Mo between the sulfide and silicate melt is implied. The most likely change would be from Mo^{4+} in the sulphide to Mo^{6+} in the melt (Lodders and Palme, 1991; O'Neill and Eggins, 2002), which can be described through the exchange reaction:

$$\mathrm{MoO}_3^{\mathrm{silicate}} + 2\mathrm{FeS}^{\mathrm{sulfide}} = \mathrm{MoS}_2^{\mathrm{sulfide}} + 2\mathrm{FeO}^{\mathrm{silicate}} + \frac{1}{2}\mathrm{O}_2. \qquad (5.2)$$
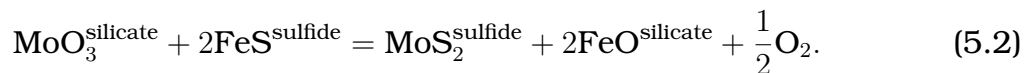
If it is assumed that the equilibrium is not pressure dependent, then the Gibbs

free energy for the equilibrium can be written as

$$\Delta_r G = \Delta H^0 - T\Delta S^0 + RT \ln \frac{\left[X_{\text{Mo}}^{\text{SL}}\right]\left[X_{\text{FeO}}^{\text{SM}}\right]^2 [f\text{O}_2]^{0.5}}{\left[X_{\text{Mo}}^{\text{SM}}\right]\left[X_{\text{FeS}}^{\text{SL}}\right]^2} \tag{5.3}$$

Where SL, SM and X denote sulfide liquid, silicate melt, and mole fraction, respectively, ΔH^0 and ΔS^0 are the standard state enthalpy and entropy of the equilibrium, and R is the universal gas constant. The activity-composition relations are, therefore, ignored and X_{FeS} is then assumed to be 1. The expression can be rearranged:

$$\log \frac{\left[X_{\text{Mo}}^{\text{SL}}\right]}{\left[X_{\text{Mo}}^{\text{SM}}\right]} = \log D_{\text{Mo}}^{\text{SL/SM}} = \frac{-\Delta H^0}{RT \ln(10)} + \frac{\Delta S^0}{RT \ln(10)} - \frac{1}{2}\log f\text{O}_2 - 2\log X_{\text{FeO}}^{\text{SM}}, \tag{5.4}$$

which has a very similar form to equation 5.1. This expression, however, predicts that the $f\text{O}_2$ dependence should have the coefficient -0.5, and the X_{FeO} dependence -2, which is slightly different to the terms obtained by Li and Audétat (2015). Through a combined fit of the data from this study and that of Li and Audétat (2012) we derive the expression:

$$\log D_{\text{Mo}}^{\text{SL/SM}} = \frac{-25300}{T} + 14.75 - 0.41\log f\text{O}_2 - 1.988\log X_{\text{FeO}}^{\text{SM}}. \tag{5.5}$$

The derived coefficients for X_{FeO} is exactly that predicted for equilibrium 5.3, and that for $f\text{O}_2$ is very close. In fact, very little difference in the quality of the fit occurs if an $f\text{O}_2$ coefficient of 0.5 is used, in accordance with the most plausible redox change of Mo. Curves for this equation are plotted in Figure 5.5. As can be seen, the $f\text{O}_2$ dependence is quite strong but is to some extent obscured in the current dataset by the FeO dependence. This seems to confirm the proposed change in oxidation state of Mo between the sulfide and the silicate melts, and also raises the possibility that the Mo partition coefficient could be employed to determine the oxygen fugacity in such experiments.

Li and Audétat (2015) also report Mo sulfide/silicate melt partition coefficients but the silicate melt compositions employed range through andesite to dacite, and the partition coefficients do not agree with the parameterisation in equa-

tion 5.5. This is most likely due to the raised level of polymerisation in the melts. Similarly, the hydrous basanitic melts employed by Li (2014), which contain several weight % H_2O, are in poor agreement with equation 5.5 and with the results of Li and Audétat (2012). This is possibly due to the very raised H_2O contents. Finally, data from Lodders and Palme (1990) from experiments performed at 1 bar are also shown in Figure 5.5. In these data, the effects of varying Fe/S ratio on Mo partitioning was also examined, and only the data close to stoichiometric FeS melt are shown in Figure 5.5. Nevertheless, these data seem to show a much shallower fO_2 dependence, and they also extend to lower values of fO_2. This probably implies a change in the redox state of Mo in the silicate melt either at lower pressures or lower oxygen fugacities.

By rearranging equation 5.5 we obtain

$$\log fO_2 = 2\left(\frac{-25300}{T} + 14.75 - \log D_{Mo}^{SL/SM} - 1.988 \log X_{FeO}^{SM}\right).$$

By assuming that the fO_2 dependence is that expected from equation 5.4, there is a slight improvement in the reproduction of the experimental oxygen fugacities for the current data set, where the oxygen fugacities are reproduced to $\sim$0.3 log units with only one outlier of 0.5 log units difference.

As shown in figure 5.5, there is no clear fO_2 dependence in the partitioning of V, either in the current data set or in that of Li and Audétat (2012). This is somewhat surprising, because V is known to undergo a change in oxidation state in silicate melts as a function of fO_2, and mineral/melt partition coefficients have been used to infer oxygen fugacity (Mallmann and O'Neill, 2009).

However, it should also be noted that the partition coefficients obtained in the current study are about 1 order of magnitude higher than those obtained by Li and Audétat (2012). Although T may have some effect, there are data points from both studies at 1573 K and they differ by amounts that are far outside of the uncertainties. The difference is also probably not caused by pressure, as Li and Audétat (2012) examine one different pressure and no noticeable difference occurs. The data of Li and Audétat (2015), on the other hand are in

much better agreement with the results of this study. Further studies would be required to identify the cause of this difference, which may arise through some quite subtle, and therefore very interesting, chemical difference.

5.4.4 Hydrogen content

Hydrogen contents of the silicate glasses and quenched sulfide liquids was subsequently determined with elastic recoil detection analysis (ERDA), at the nuclear microprobe at CEA Saclay, France. Details of this method can be found in section 2.2.5. For an ERDA analysis, great care must be taken with sample preparation. Samples must be mirror-polished; due to the extreme tilt angle required for analysis ($75°$), any topography of the sample could block the ejected protons from reaching the detector. In addition, epoxy, glues, and most solvents contain H and so care must be taken to ensure that no contamination can be introduced to the sample from these sources. For this study, samples were embedded in indium and then mounted in epoxy. The indium thus provided a 1-3 mm buffer zone between the sample and the epoxy, ensuring that the analysis results would not be contaminated with a signal from the epoxy.

As described in section 2.2.5, the nuclear microprobe uses a focused beam of $^4He^+$ for the analysis. Two types of measurements are required. For the first, the incident beam is normal to the sample and chemical data is collected with the particle induced X-ray emission (PIXE) and Rutherford backscatter (RBS) detector. The RBS data also includes information on the charge on the samples surface, which is directly proportional to the number of incident particles, which is important for the interpretation of the ERDA spectrum. The second measurement is made with the incident beam at $75°$ to the sample, which is necessary to allow the ejected protons to be collected by the detector (see figure 2.8).

The beam was scanned over the sample to create maps, which were 50×50 μm^2, except in one case which was 30×50 μm^2, in order to obtain spectra that are a more statistical representation of the bulk sample. For most samples separate maps were taken of both the silicate glass and the sulfide, but in two

cases maps spanning both phases were taken, and the appropriate regions were extracted from the maps during data analysis (see figure 5.6). ERDA data acquisition for sample V1045b was not possible, due to surface irregularities of the sulfide.

For analysis, the software RISMIN (Daudin et al., 2003) was employed to extract the RBS and ERDA spectra from the data (this process is discussed further in section 2.2.5 and Bureau et al., 2009). These spectra were then processed with the software SIMNRA (Mayer, 1999). Table 5.6 contains the normalised atom % compositions, including H, of all analysed samples.
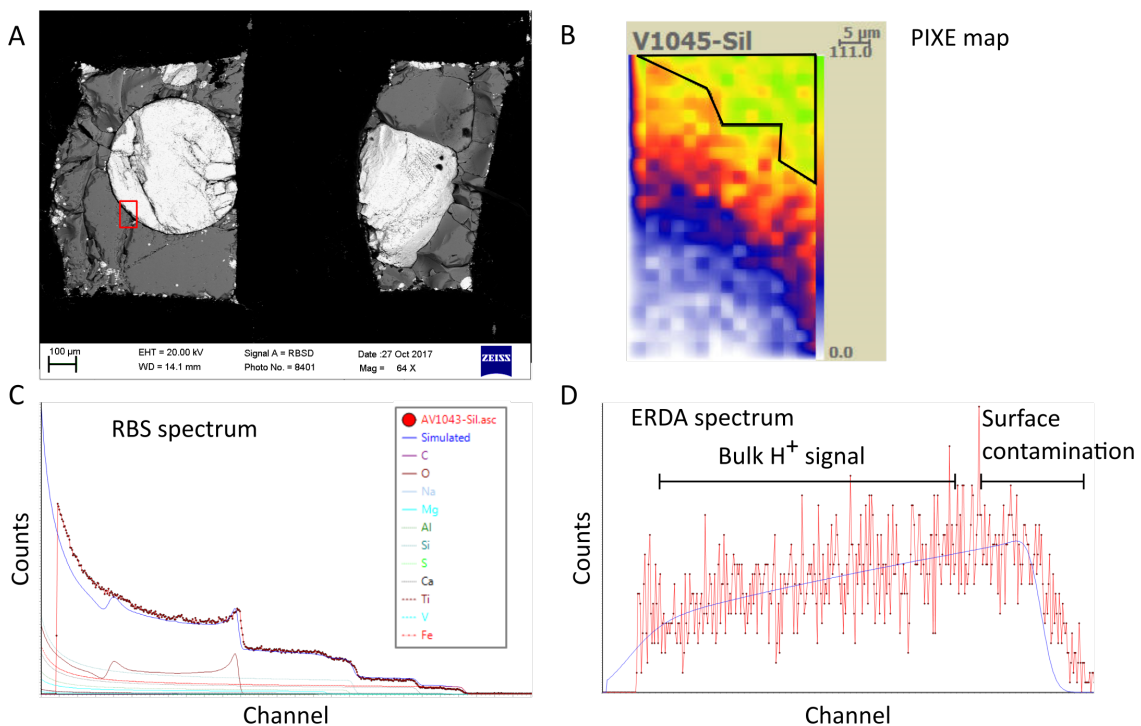
Figure 5.6: The steps of processing ERDA data. (A) Backscattered electron image, with the region that was analysed highlighted. (B) X-ray map of silicon, clearly showing the two phases. Outlined is the area from which the RBS and ERDA spectra were extracted for the silicate. (C) RBS spectrum of of the silicate glass. The edges result from the different elements, but the overall intensity is a direct function of the number of incident particles. (D) ERDA spectrum, used to determine the number of protons ejected from the sample.

Table 5.6: Atom % composition

		1043a	V1043b	V1044a	V1044b	V1045b	V1054
silicate	SiO2	47.27	45.82	47.21	44.96	49.30	51.84
	TiO2	1.13	1.05	1.13	1.08	1.25	1.23
	Al2O3	8.22	7.80	8.10	7.79	8.57	8.91
	FeO	4.06	9.13	7.17	14.27	13.67	9.09
	MgO	24.33	22.30	21.80	18.32	12.30	13.64
	CaO	12.00	11.12	11.65	10.77	11.85	12.30
	Na2O	2.76	2.53	2.68	2.51	2.79	2.69
	SO3	0.36	0.48	0.44	0.75	0.51	0.35
	NiO	0.006	0.002	0.006	0.008	0.004	0.006
	V2O3	0.22	0.23	0.24	0.24	0.26	0.27
	MoO3	0.01	0.01	0.01	0.04	0.01	0.01
	H	1.13	2.07	0.93	1.61	1.74	1.57
sulfide	Si	0.16	0.02	0.06	0.05	0.06	0.05
	Fe	43.21	47.16	44.92	46.43	47.46	46.01
	S	48.89	45.32	46.83	43.74	43.94	48.53
	O	2.24	5.63	4.17	7.47	6.01	3.27
	Pd	2.32	0.01	1.52	0.34	0.10	0.00
	Au	1.07	0.00	0.13	0.07	0.07	0.00
	V	0.19	0.16	0.19	0.14	0.17	0.15
	Mo	0.68	0.66	0.75	0.66	0.62	0.61
	Ni	0.84	0.75	0.93	0.89	0.60	0.76
	H	0.26	0.20	0.33	0.15	0.65	0.42

In order to provide an independent evaluation of the ERDA results with a more conventional technique, the water contents of the silicate glasses was also determined with fourier-transform infrared spectroscopy (FTIR) at the Bayerisches Geoinstitut. Absorption peaks resulting from the stretch of the O-H bond, observed at $\lambda = 2.8\ \mu$m, for the glasses were used to calculate water contents using the method described in Stolper (1982):

$$c = \frac{18.02A}{d\rho\varepsilon}$$

where c is the weight fraction of water, A is the height of the absorption peak, d is the thickness of the sample (cm, samples were thinned to 100 μm), ρ is the density of the sample (estimated at 3000 g/l), and ε is an extinction coefficient, determined by Stolper (1982) to be 67 l/mol cm. The calculated water contents are in table 5.7. The results are in good agreement with the water

content of the glasses determined by ERDA, as is shown in figure 5.7. The only sample for which the two methods do not agree is V1054, for which FTIR returns a much larger value. It is possible that this is a result of accidental surface contamination of the sample during storage or preparation for FTIR measurements.

Table 5.7: FTIR-determined water content (wt ppm H_2O) compared to ERDA results

Sample	Peak height	FTIR	ERDA
V1043a	0.5060	4725	4856
V1043b	0.912	8516	8760
V1044a	0.487	4547	3925
V1044b	0.780	7284	6590
V1045b	0.887	8283	7165
V1054	1.145	10692	6618
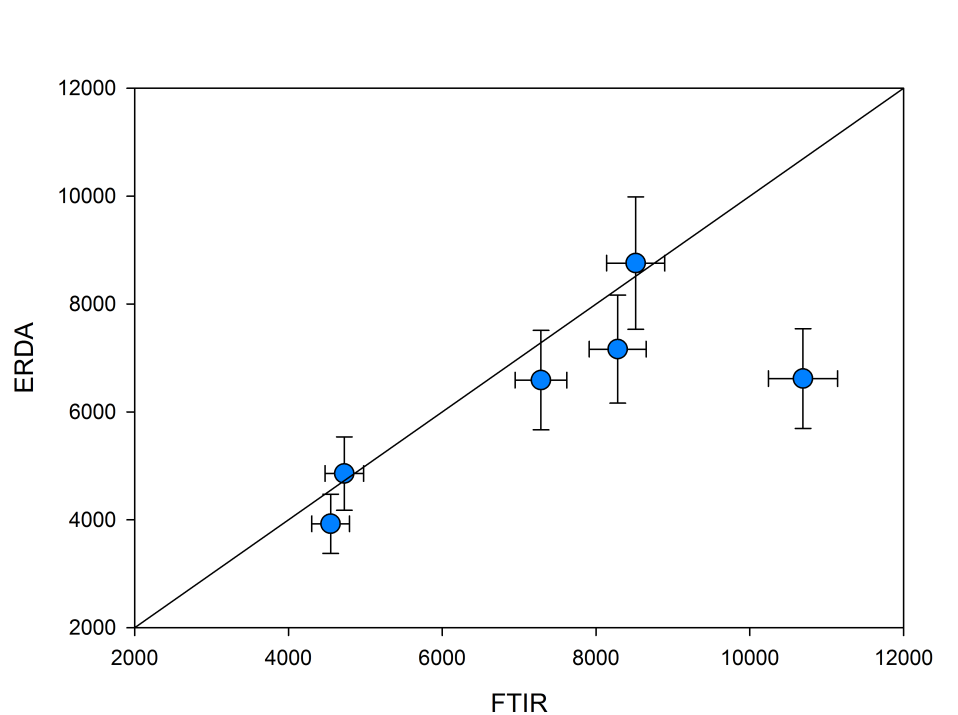
Figure 5.7: Weight ppm of H_2O in the silicate glasses of the samples as determined by both ERDA and FTIR. In general there is good agreement between the two methods, except for sample V1054, for which the value determined by FTIR was much higher than the ERDA result.

The hydrogen contents of the sulfides are plotted in figure 5.8, as a function of oxygen fugacity, Fe/S ratio of the sulfide, FeO content of the coexisting silicate,

and pressure. For comparison, the data of Clesi et al. (2018) obtained on quenched metallic liquids at pressures between 5 - 21 GPa and temperatures between 2020 - 2775 K is also plotted. Although the concentrations of H vary up to close to 1 atomic % there does not appear to be a consistent trend that explains this variation. Although there might appear to be a weak fO_2 dependence, this does not persist once the partitioning with the silicate melt is also considered, as discussed later. The amount of H measured in the sulfide is similar to that found in quenched iron melts by Clesi et al. (2018) at similar conditions.
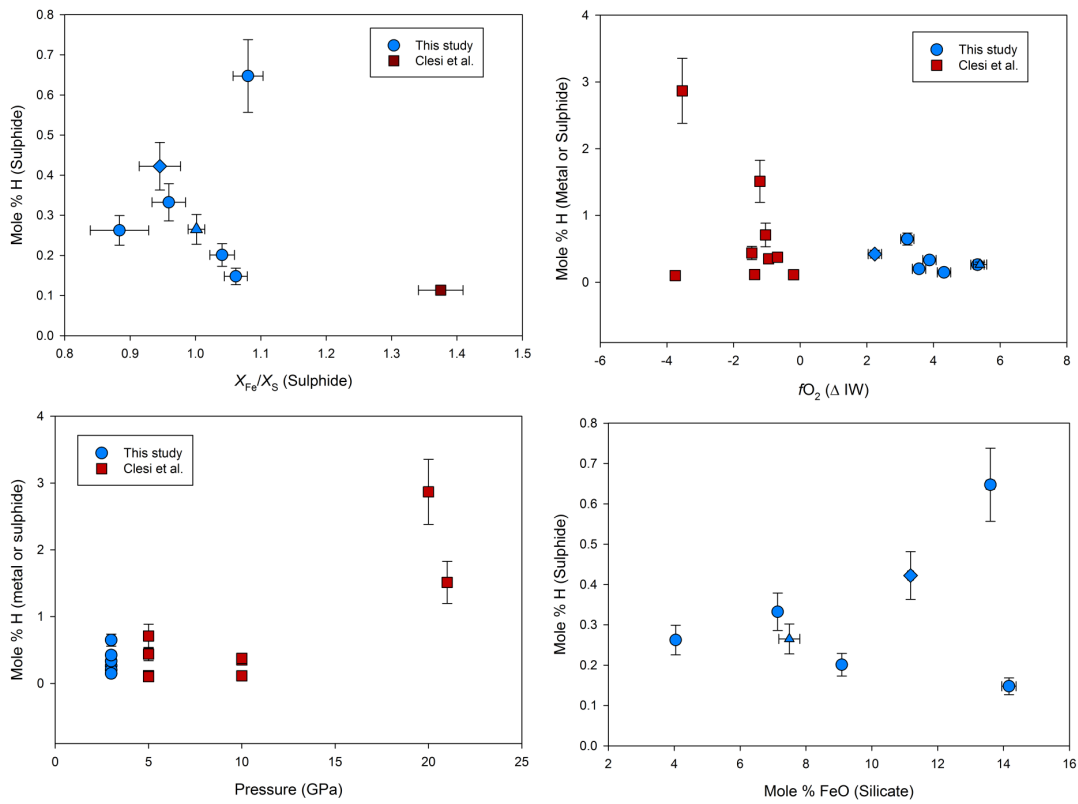
Figure 5.8: Mole fraction of hydrogen in the sulfide as a function of Fe/S ratio in the sulfide, fO_2, pressure, and mole fraction FeO in the coexisting silicate. Data from metal/silicate partitioning experiments (Clesi et al., 2018) is shown for comparison. For all plots, the diamond symbol denotes the experiment with greater bulk water and a lower temperature equilibration. Triangle symbols denote a data point from a separate study, performed at 3 GPa and 1823 K.

5.5 Discussion

5.5.1 Oxygen partitioning

As shown in Figure 5.9, oxygen replaces sulfur in the FeS liquid. Fonseca et al. (2008) identified a quenched stoichiometric FeSO phase in their experiments performed at 1 bar, and in the current study this phase was also identified in the quenched sulfide, as shown in figure 5.3. If the melt were considered a solution of FeS and FeSO, the Fe content of the melt would also decrease with increasing O, however, the FeSO phase is always in close proximity to pentlandite $(Fe,Ni)_9S_8$, which balances the local decrease in metal cations.
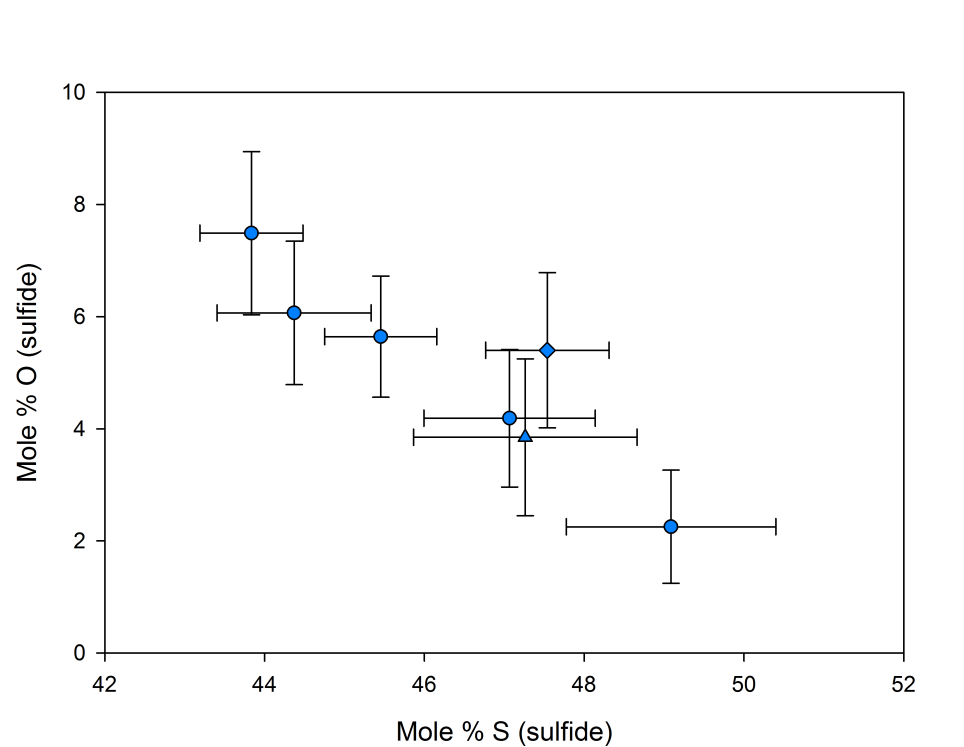
Figure 5.9: The sulfur content of the sulfide melt decreases with increasing oxygen content indicating that oxygen is replacing sulfur in the melt structure, indicating that oxygen is substituting for sulfur.

As only oxygen is entering the sulfide, the Fe/O ratio of a silicate melt in equilibrium with a sulfide would increase as this occurs, whereas it would remain constant if oxygen were entering the sulfide as an FeO component. A magma ocean which is exolving FeS might therefore lose oxygen into a descending sulfide phase, resulting in a net reduction of the remaining silicate as Fe_2O_3

is reduced to FeO. The oxygen content in the sulfide increases as a function of the FeO content of the silicate, as can be seen in figure 5.10A. Data from previous studies (Laurenz et al., 2016) indicate that the oxygen content in the sulfide also increases with temperature. What is quite surprising, is that the oxygen contents of the sulfides show no dependence on oxygen fugacity, only on the silicate melt FeO content, as shown in Figure 5.10. The reaction can be considered to be

$$\mathrm{FeO^{silicate} = (Fe + O)^{sulfide}}. \tag{5.6}$$
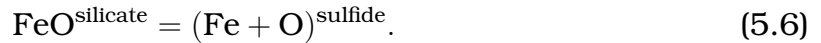
The compositional influence on the partitioning of oxygen can be removed by defining an exchange coefficient for reaction 5.6, expressed as

$$K_D = \frac{X_O^{\text{sulfur site}} \cdot X_{\text{Fe}}^{\text{sulfide}}}{X_{\text{FeO}}^{\text{silicate melt}}}$$

In Figure 5.10, the calculated oxygen K_D is plotted and can be seen to be a constant as a function oxygen content. Data from temperatures between 1573 and 2473 K also give a similar K_D indicating little temperature dependence. The data point from Laurenz et al. (2016) is from 7 GPa which also implies very little pressure dependence.
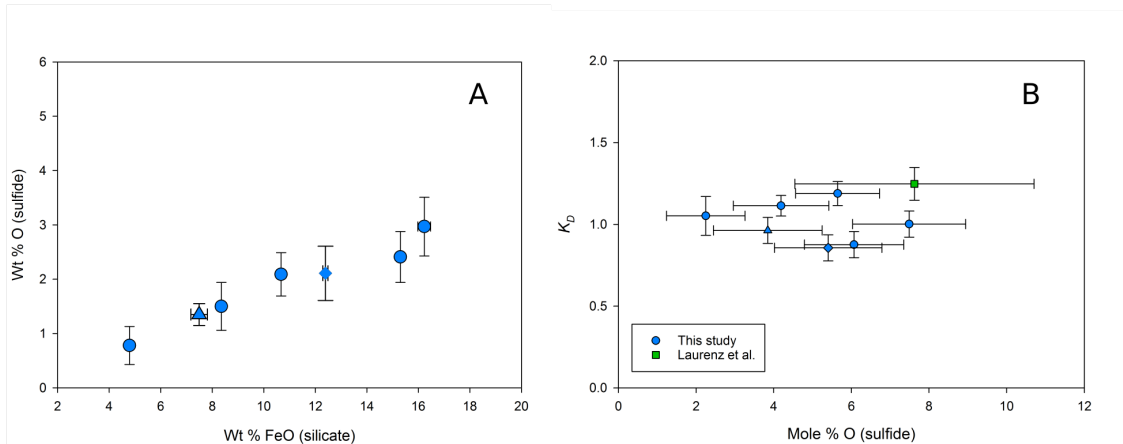
Figure 5.10: Oxygen content of the sulfide. (A) Oxygen content of the sulfide increases with FeO content of the silicate, but as shown in (B), the partitioning behaviour is constant with temperature and composition. The data point from Laurenz et al. (2016) is at 2473 K and 7 GPa, while the triangle was 1823 K, circles at 1673 K, and diamond symbol at 1573 K, all at 3 GPa.

Using the determined value of K_D, it is possible to estimate the extent of reduc-

tion that a silicate magma ocean as a function of the total amount of sulfide separating from the melt, i.e., to calculate the amount of oxygen lost per mole of exsolved sulfide. We consider a peridotite melt that has an FeO content of 8.7 wt% and an initial $Fe^{3+}/\sum Fe$ ratio of 15%, that is at 1673 K and 3 GPa. According to our data, at these conditions a coexisting sulfide should contain ~ 4.1 mole % oxygen. Assuming this oxygen is deriving from the reduction of Fe_2O_3 to FeO, the subsequent change in ferric/ferrous ratio will change the oxygen fugacity as shown in figure 5.11, calculated with the model of O'Neill et al. (2006). Therefore, the formation and separation of a Hadean matte would result in the partial reduction of the silicate magma ocean from which it is was separating. Although the effect is relatively small, oxygen would act in opposition to any oxidation by H_2O made possible through the loss of H in the sulfide. See section 5.5.3 for further discussion.
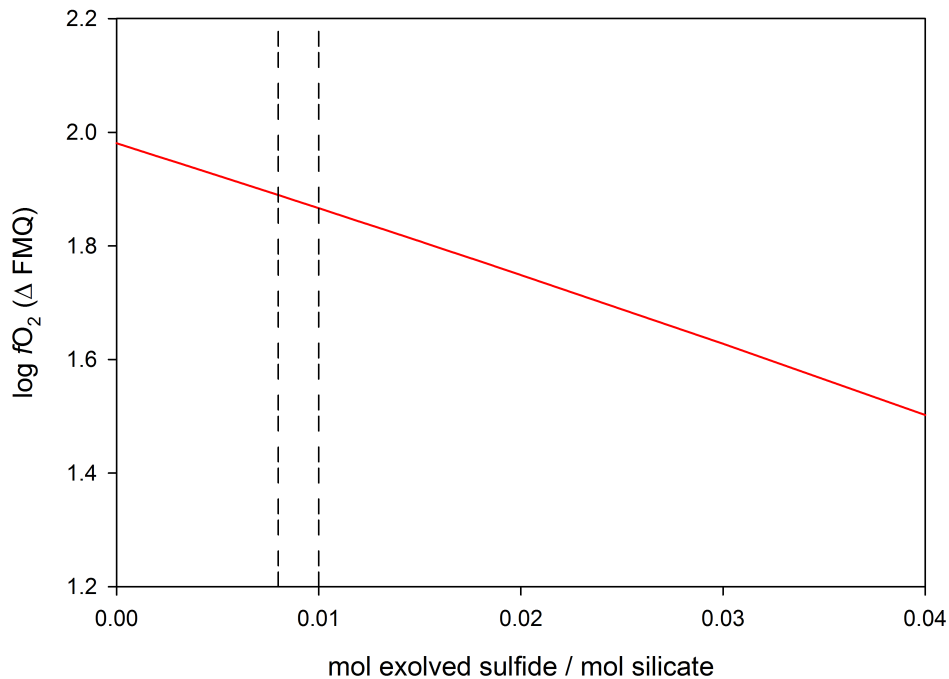
Figure 5.11: Reduction of a silicate magma ocean that would occur from the dissolution of oxygen into a coexisting sulfide melt that is subsequently removed. The model of Rubie et al. (2016) suggests that ~ 0.008 - 0.01 moles of sulfide per mole of silicate would have been required to exsolve from the magma ocean in order to explain the present-day abundance of sulfur and superchondritic values of some HSEs in the mantle (indicated by the vertical lines). The effect on the oxyfen fugacity of the magma ocean, therefore, would have been a reduction of ~ 0.2 log units.

5.5.2 Hydrogen partitioning

The partitioning of hydrogen between the sulfide and silicate melt is quantified by the molar partition coefficient, defined as

$$D_H^{\text{sulf/silicate}} = \frac{X_H^{\text{sulfide}}}{X_H^{\text{silicate}}}$$

where X_H is the mole fraction of H in the silicate or sulfide. In this designation no inference is made concerning the nature of the H species, which is certainly H_2O in the silicate melt and may well also be in the sulfide. In this study, this value ranged between 0.1 and 0.4, suggesting nominally lithophile, rather than chalcophile behaviour, and showing little variation with oxygen fugacity or bulk water content. In figure 5.8, for the sulfide experiments conducted for this study, there does appear to be a slight increase in hydrogen content of the sulfide as oxygen fugacity decreases. When the partition coefficient is considered, however, that dependence disappears and D_H appears relatively constant with fO_2 (figure 5.12). The lack of fO_2 dependence also makes it difficult to determine whether H or H_2O is present in the sulfide phase. A lack of any dependence also raises questions as to whether the entire H content of the sulfide was captured by the quenched assemblages or whether H or H_2O could have separated from the sulfide melt during quenching.
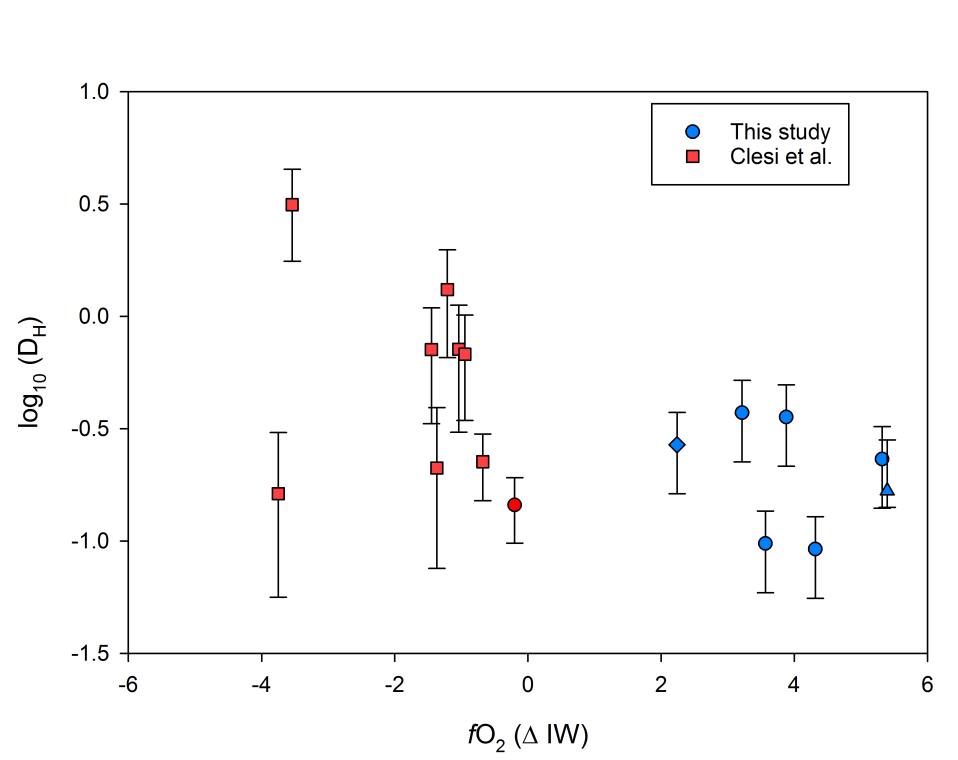
Figure 5.12: Silicate/sulfide partition coefficient for hydrogen determined for this study (blue symbols) plotted with those determined for metal/silicate (red squares, Clesi et al., 2018), including one sulfide (red circle). Diamond symbol denotes experiment with greater bulk water content added and run at a 1573K rather than 1673 K. Triangle denotes experiment from a separate study run at 3 GPa at 1823 K.

Experiments to investigate whether hydrogen could be an important light element in the core have suggested that at high pressures (above 3 GPa) a significant amount of hydrogen could dissolve into metallic iron (Fukai and Suzuki, 1986; Okuchi, 1997; Iizuka-Oku et al., 2017). These partitioning experiments, however, were performed with starting materials that contained water contents of several weight percent, creating very high water fugacities within the experimental charge and thereby saturating the iron. In these experiments, the exsolution of hydrogen during quenching creates bubbles in the resulting metals. By determining the volume of these bubbles and using estimates of the hydrogen equation of state, it is possible to determine the original melt hydrogen contents. In the study of Okuchi (1997), for example, these reach approximately 40 atom % of the metal. Using X-ray diffraction and an estimate of the effect of H on the volume of FeS liquid, Shibazaki et al. (2011)

estimated that 9−10 mole percent H may enter the structure of solid FeS at 3 GPa. It must be appreciated however, that there are large uncertainties in these determinations. There is the potential for significant amounts of H to enter these phases but to be mainly lost during the crystallization that occurs on quenching.

Following this reasoning, the recent work of Clesi et al. (2018) determined metal/silicate partition coefficients for hydrogen using a similar procedure as the one described here, employing H contents that are more applicable to the plausible H_2O content in a bulk silicate earth magma ocean, i.e. < 3000 ppm (Marty, 2012). Their resulting partition coefficients are plotted alongside those determined for a sulfide for this study in figure 5.13. As in the current experiments, it would seem that there is a finite and non trivial amount of H in both metal and sulfide. The idea is that by lowering the bulk H content of the experiment it may be possible to reach a metal or sulfide H content that can be entirely preserved in the crystallized solid phase. In general, there is good agreement between the datasets for both metal and sulfide, indicating that hydrogen partitioning between a silicate and a sulfide is similar to that between a silicate and metallic iron. Both suggest lithophile behaviour for hydrogen, particularly at lower pressures.
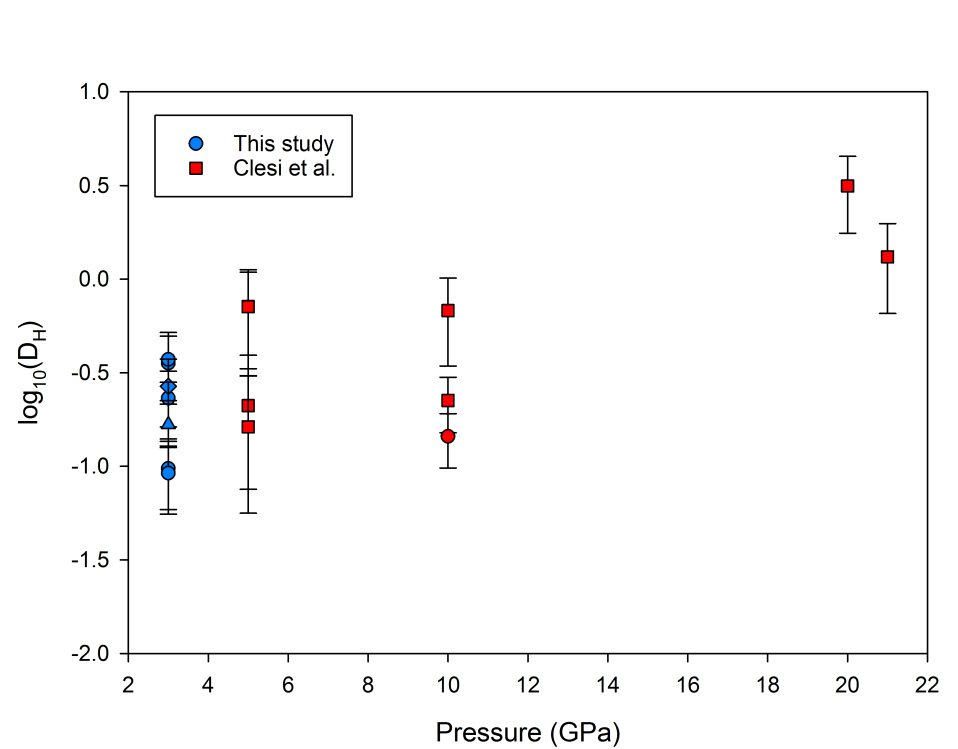
Figure 5.13: $\log D_H$ between sulfide/silicate (this study, blue circles) and iron metal/silicate (Clesi et al., 2018, red squares). There is general agreement between the datasets; one of the data points from the previous study was a sulfide, rather than Fe metal (red circle). Diamond symbol denotes experiment with a higher added water content and run at 1573K, triangle denotes experiment from a separate study run at 1823 K.

It is possible that more hydrogen could have been dissolved in the sulfide during the experiment, and was lost upon quench crystallisation. Wykes and Mavrogenes (2005) used the depression of melting to propose H_2O dissolved in sulphide melts, whereas at lower oxygen fugacities Buono and Walker (2015) proposed that H dissolved in them based on the same argument. Similarly, Shibazaki et al. (2011) proposed that 9–10 mole percent H may enter the structure of solid FeS at 3 GPa, based on X-ray diffraction measurements. Our results allow only a minimum possible H content of the sulphide to be determined. Loss of H or H_2O on crystallisation cannot be excluded. As explained previously, the H contents vary between 0.2 and 0.7 atomic %, but over this range show no correlation with other potentially controlling parameters. The lack of variation in the H partition coefficient with fO_2 also prevents the speciation of H in the sulphide from being assessed. This lack of correlation, which is also present in the results of Clesi et al., (2018) compounds the

suspicion that not all H was preserved.

Along the grain boundaries of the quenched crystalline monosulfide solid solution from our samples are crystals of pentlandite and FeSO. From textures and the Fe-Ni-S phase diagram, it is clear that MSS crystallized first and left a remaining melt which then crystallized pentlandite and FeSO. This melt might be expected to become concentrated in dissolved H or H_2O. In some grain boundary areas, there are small void spaces, which may have been the result of a volatile-rich fluid phase exolving during quenching, as exhibited by H in metallic melts (Fukai and Suzuki, 1986; Okuchi, 1997). The voids are, however, relatively sparse and it is also possible that they are simply the result of some grains of pentlandite having been plucked and lost during sample preparation (see figure 5.3). In addition, we note that the final quenched assemblages containing pentlandite are also rich in Pd from capsule contamination. H can dissolve readily in Pd, however there is insufficient Pd in the majority of the samples to account for the entire H content.

If the crystallised assemblage is capable of preserving 0.7 % H, then any partition coefficients based on sulphide H concentrations below this potential threshold might be considered to have preserved the entire sulphide H content. However, here it must also be considered that the sulfide may contain both H and H_2O at high temperatures, and only preserve the H_2O or a component thereof. In a scenario where the bulk H_2O content of the melt is raised until the entire H content of the sulphide cannot be preserved, then a plateau in D should be followed by a decrease in D. At H_2O contents below the threshold, at which H can be preserved in the quenched sulphide, the plateau in D should occur due to the concentrations being below the Henry's law limit. Once the threshold is reached, however, D should drop, because H is being lost from the sulfide. Figure 5.14 does not reveal a plateau, but it does broadly indicate a drop in D as the melt H_2O content increases, consistent with a threshold being overstepped. This would imply that the highest H partition coefficient obtained, i.e. $\sim$0.4, is still a minimum and further experiments at even lower H_2O contents would be required to investigate if a plateau eventually does arise. For this reason the results of Clesi et al., (2018) must also be considered with suspicion.
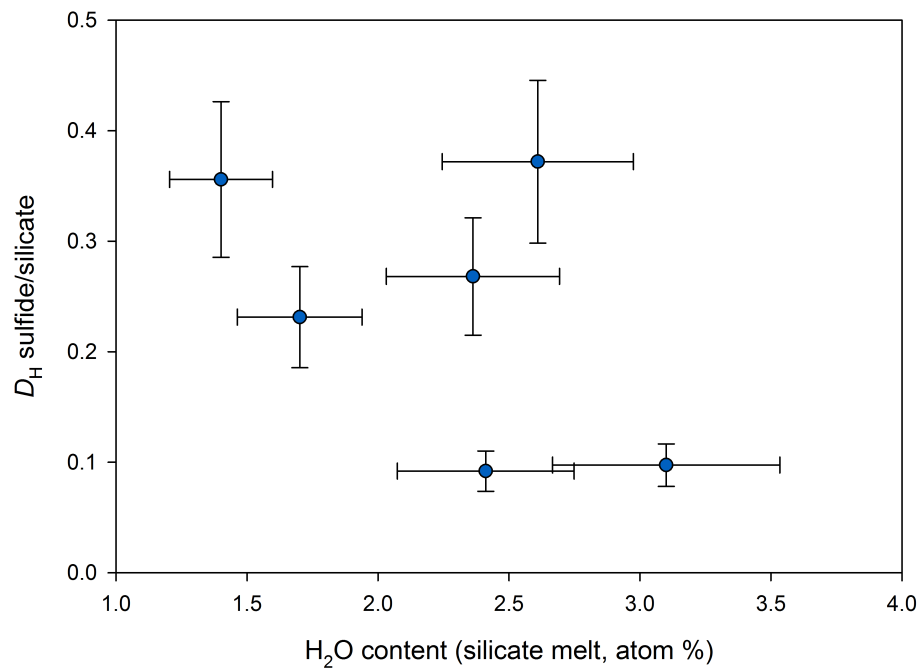
Figure 5.14: Sulfide/silicate H partition coefficient as a function of the melt H_2O content. If the quenched sulfide reaches a threshold in the H that it can retain, then D should drop as the melt H_2O content increases. This is in broad agreement with the data.

5.5.3 Effect of sulfide equilibration on the oxidation state of the mantle

The experimental results support a minimum partition coefficient for H partitioning between a molten silicate and a liquid sulfide of $\sim$0.2, which implies that there will be some amount of hydrogen that is removed into the core. For H_2O to be an effective mantle oxidising agent, however, the resulting oxygen would have had to have been left behind in the silicate and not also partitioned into the core-forming phase. Hirschmann et al. (2012) have speculated on the likely effectiveness of oxidation by H_2O with respect to hydrogen partitioning into metallic iron. The authors point out that at the low oxygen fugacities and high pressures of metal-silicate equilibration, it is likely hydrogen would have already been present as H_2, therefore not necessarily associated with any oxygen to oxidize the mantle. Furthermore, reaction of H_2O with iron metal, at least at upper mantle conditions, can only produce more FeO in the mantle

and will not raise the ferric iron content and thus the oxygen fugacity of the upper mantle. However, loss of H_2 to the core would lower the magmatic $H_2/$ (H_2+H_2O) ratios, which would have driven the magma to more oxidised conditions. They conclude, however, that the presence of metallic iron buffers the system, resisting oxidation, and that therefore the effect of H_2 removal would have been relatively small (Hirschmann et al., 2012).

Even if metallic iron could have efficiently removed hydrogen to the core, the upper mantle is still several orders of magnitude more oxidised than the co-existence of metal permits; i.e., hydrogen removal must have been ongoing even at more oxidised conditions, allowing ferric iron to accumulate in the upper mantle. In the case of a sulfide, the oxygen fugacity of the magma ocean would have already risen above the level at which metallic iron can be stable, and so it is possible that H was present in the melt mainly as H_2O, particularly at lower pressures (Hirschmann et al., 2012). The study of Buono and Walker (2015) indicates that H_2O can indeed disproportionate, with O bonding to Fe creating ferropericlase and H entering the FeS, constrained through a depression of the melting temperature.

Our data can be used to perform a similar calculation as presented above in section 5.5.1, to determine the degree of oxidation possible from water disproportionation and hydrogen segregation to the core. A peridotite melt at 1673 K with 1 wt % H_2O would be ~1.8 mole percent H. Using our highest value for D_H of 0.4 (which can be taken as a minimum for reasons described above), a coexisting liquid sulfide would then be 0.7 mole % H. Assuming that this hydrogen derived from H_2O, and the oxygen is taken up by oxidising FeO to Fe_2O_3, the change in oxygen fugacity expected can be calculated as a function of amount of sulfur exsolved, and is plotted in figure 5.15. As we are uncertain that our quenched sulfide managed to capture the full complement of hydrogen that may have dissolved into the liquid during the experiment, also plotted in figure 5.15 is the amount of oxidation that would be expected if the sulfide became hydrogen saturated (Shibazaki et al., 2011). For comparison, the amount of reduction caused by the loss of oxygen (section 5.5.1) is also plotted.
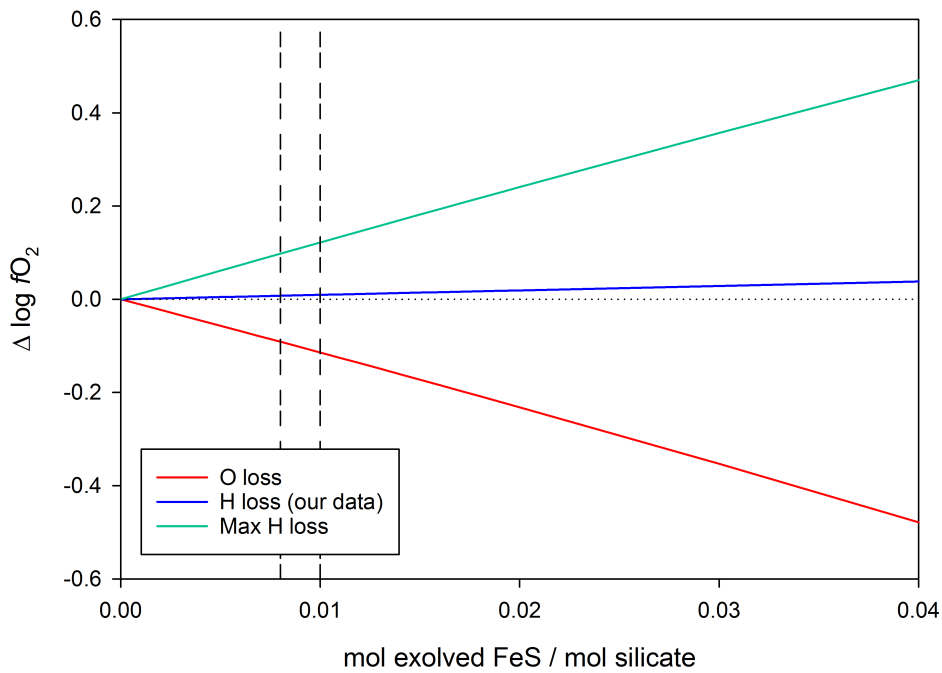
Figure 5.15: Change in oxygen fugacity of a silciate melt caused by the loss of oxygen and hydrogen via dissolution into a core-forming sulfide melt. The blue line indicates the increase in oxygen fugacity that would be expected if our measurements are an accurate representation of the amount of dissolved hydrogen. The green line indicates the amount of possible oxidation if a sulfide were to become hydrogen saturated, using the saturation limit reported by Shibazaki et al. (2011). Vertical dashed lines represent the approximate amount of exsolved sulfide predicted by Rubie et al. (2016).

As can be seen, the amount of oxidation caused by the removal of hydrogen is, at absolute maximum, negated by the reduction that is caused by the simultaneous loss of oxygen. If the sulfide is at all undersaturated in hydrogen, the net effect on the oxidation state of a silicate magma ocean of sulfide exolution and removal would more than likely have been an overall reduction. Furthermore, the effect is likely to have been very small. The vertical lines in figure 5.15 represent the amount of sulfide that is likely to have exsolved, estimated from the work of Rubie et al. (2016). Their model predicts that before sulfide segregation, the Earth's mantle would have been overabundant in sulfide by a factor of ~ 30. To bring the mantle concentration of sulfur to the present-day value of ~ 200 ppm (McDonough and Sun, 1995) would have required about $\sim$0.8 - 1 mole % of sulfide to have exsolved. As shown in figure 5.15, this

amount of sulfide exolution could have, at most, changed the oxygen fugacity of the coexisting silicate by about 0.1 log unit. Changing the fO$_2$ by even just 0.5 log units would have required the exolution of 5 mole % FeS, which is unlikely.

Futhermore, the effects of removing oxygen and hydrogen simultaneously act to cancel each other out, resulting in an even smaller net effect. It is even possible that H$_2$O does not disproportionate, and dissolves into the sulfide as a whole molecule, as there is evidence that H$_2$O is soluble in sulfide melts (Wykes and Mavrogenes, 2005). The low amount of hydrogen in our quenched sulfide melts inhibited attempts to determine the speciation of the hydrogen, but it is entirely possible that water may dissolve in sulfide without disproportionating and therefore the exolution of a sulfide may not affect the oxidation state of the coexisting magma ocean at all.

In summary, it appears problematic for oxidation by H$_2$O to have raised the oxidation state of the mantle significantly above the level of iron metal saturation (Sharp et al., 2013). The hydrogen evolved would simply reduce the surrounding mantle material back to the original level and a separating sulfide phase would be of insufficient volume to remove significant H. Only by releasing H at the very surface of the magma ocean might it be possible for oxidation to take place. Models of magma ocean dynamics would be necessary to determine if such a mechanism could lead to oxidation of the entire mantle by mixing. In contrast, the stabilization of ferric iron in a deep magma ocean in association with precipitation of iron metal would appear to be a much more effective mechanism for raising the redox state of Earth-sized planetary bodies.

5.6 Conclusions and possible future directions

There is a significant amount of evidence to suggest that the Earth experienced at least one episode of core formation in which the descending liquid was not Fe metal, but an FeS sulfide. If the Earth's mantle had been gradually oxidised by the accretion of water-rich material, a mechanism to remove

hydrogen from the system is required in order to raise the bulk oxygen content of the mantle. We have presented high-pressure experimental results to investigate the effects of the exolution of an FeS sulfide from a silicate magma ocean on the oxidation state of the residual silicate.

Oxygen fugacity of the experiments was determined by measuring the $Fe^{3+}/\sum Fe$ ratios of the quenched silicate glasses with transmission Mössbauer spectroscopy. By changing the iron content of both sulfides and silicates, we have achieved a variation in oxygen fugacity between our samples of ~ 4 log units. Somewhat surprisingly, oxygen fugacity had little effect on the partitioning behaviour of either oxygen or hydrogen between a liquid sulfide and a molten silicate. The partitioning of Mo between the sulfide and the silicate was found to be a useful function of oxygen fugacity. Mo partitioning was found to be also temperature and silicate FeO content dependent, but not to vary significantly with pressure. V partitioning on the other hand, shows no apparent dependence on fO_2. The concentrations of Mo measured in the sufide and silicate were of a level that could be accurately determined with the electron microprobe. In future experiments, it may be possible therefore to estimate fO_2 through the Mo partition coefficient, with the current calibration giving an uncertainty of ~ 0.3 log units.

The oxygen content of our quenched sulfides varied with FeO content of the silciate, but its partitioning behaviour is constant with composition and temperature. Our results indicate that oxygen is incorporated into FeS by substituting for sulfur. Loss of oxygen into an exolving sulfide may have resulted in a net reduction of the remaining silicate liquid, however the effect is likely to have been small.

We were able to successfully meaure hydrogen in a crystalline sulfide quenched from a liquid. It remains unclear if some hydrogen was lost from the sulfide during quenching, however no bubbles were obsersved in the texture of the sulfide. We were also unable to determine the speciation of the hydrogen, leaving open the question if the hydrogen resulted from a disproportionation of H_2O or if it was incorporated as water. Nevertheless, the effect of an exolving sulfide on the oxidation state of the mantle appears to have been small or negligible.

These results may, however, have interesting implications for diamond formation. Sulfide inclusions are common in diamonds, and have likely formed at conditions that include similar water contents to our samples. This study considered sulfide compositions that vary only in Fe. Sulfide composition is, however, known to affect the partitioning of other elements (e.g., Kiseeva and Wood, 2015). Future work could expand on these results by considering the effects of varying amounts of nickel and/or copper in the sulfide. In addition, any possible effects of pressure were not explored within this study. The results of Clesi et al. (2018) indicate that hydrogen may become more siderophile with increasing pressure. The study of Rubie et al. (2016) indicated that the likely pressure of sulfide-silicte equilibrium was $\sim 0.44 \times P_{\mathrm{CMB}}$, where P_{CMB} is the pressure of the core-mantle boundary. Therefore, the effect of pressure on the partitioning behaviour may be an important consideration.

6 Summary and major conclusions

The process(es) that established the redox state of the Earth's mantle during and after accretion are fundamentally important for understanding the distribution of volatile elements (e.g., C, O, H) in the Earth's interior, as well as the composition of the earliest atmosphere. During accretion, the most important process governing the composition of the Earth's mantle was core/mantle differentiation. The resulting depletion of siderophile elements (which partition strongly into the metallic phase) from the mantle is clear evidence that during differentiation, core-forming metallic iron must have been in equilibrium with mantle-forming silicates (e.g., Walter, 2000).

At low pressures, silicates that are in equilibrium with metallic iron establish a relatively low oxygen fugacity, with a negligible proportion of ferric iron. Such a reduced state would be expected for the mantle as a result of core mantle equilibration. From oxybarometry of mantle xenoliths and mid-ocean ridge basalts, however, it has long been known that the oxygen fugacity of the upper mantle is approximately 4-5 orders of magnitude more oxidised than the level imposed by metallic iron (e.g., Frost and McCammon, 2008). Furthermore, studies of redox-sensitive elements (Cr, V) in ancient rocks imply that this more oxidised state was established by at least 3.9 Ga, so the entire mantle appears to have oxidised very rapidly after core formation ceased (Delano, 2001; Trail et al., 2011). The oxidation state of the mantle controls the composition of degassing volatiles, and so would have had a large effect on whether the earliest atmosphere comprised reduced (CO, CH_4) or oxidised (H_2O, CO_2) species (Hirschmann, 2012). Understanding the process that oxidised the mantle would allow for better constraints on the origin of Earth's volatiles and their distribution within the Earth.

This study is an attempt to place constraints on mechanisms that may have operated to oxidise the early Earth's mantle. In chapter 3, new measurements of the volumes of Ru and RuO_2 phases at high pressure and temperature are presented and thermal equations of state and phase relations of RuO_2 phases are derived. These are then used to calibrate the metal-oxide pair Ru and RuO_2 for use as an oxygen fugacity buffer within experimental capsules to pressure and temperature conditions compatible with those at the top of the upper mantle. In chapter 4, clear evidence is presented for the increasing stabilisation of the ferric iron component in silicate melts with pressure, a similar effect to that reported for silicate minerals (e.g., Frost et al., 2004; Rohrbach et al., 2007). This effect could have enabled a magma ocean to essentially self-oxidise and establish the oxygen fugacity profile of the modern mantle. In chapter 5, the effect of a "Hadean matte", i.e., a sulfide liquid that exsolved from the magma ocean and sank to the core, on the oxidation state of the residual silicate liquid is found to have likely been relatively small.

6.1 Ru-RuO$_2$ oxygen fugactiy buffer

Oxygen fugacity (fO$_2$) is an important variable in geologic systems that controls phase relations and the partitioning behaviour of multivalent elements between reservoirs. The oxygen fugacity prevailing during the differentiation of the Earth, for example, controlled the distribution of many elements between the core and the mantle and strongly influenced the nature of the light element(s) in the core (e.g., Wade and Wood, 2005; Mann et al., 2009). In addition, throughout Earth's history, the fO$_2$ of the mantle has regulated the speciation of volatile elements, determining the redox state of gasses released to the atmosphere and where diamonds nucleate from mobile fluids or melts (e.g., Hirschmann, 2012). Oxygen fugacity also influences the composition of mantle minerals by setting the ratio of Fe^{3+}/Fe^{2+} and the amount of OH, which in turn has an effect on transport properties such as diffusion and creep.

Experimental studies of transition zone and lower mantle minerals have implied that ferric iron components may be increasingly stabilized with depth in

the mantle. To fully characterize the thermodynamic stability of such components, however, it is crucial to be able to measure their concentration at a known oxygen fugacity. One technique to impose an oxygen fugacity on an experimental charge is to add pure buffer phases, such as Ni+NiO or Fe+FeO directly into the capsule (e.g., Campbell et al., 2009). Significant uncertainties can arise, however, if the buffer phases react extensively with the sample. In addition, for an accurate determination of the oxygen fugacity imposed by the buffer, thermal equation of state properties of both phases must be known at high pressures.

The metal-oxide pair Ru+RuO$_2$ is ideal as an internal oxygen fugacity buffer. Both phases remain solid to high temperatures and react minimally with silicates, only exchanging oxygen. Additionally, the imposed fO$_2$ is relatively high, such that Fe loss into Pt capsules is minimal and ferric iron is present in sufficient concentrations to be accurately measured (e.g., O'Neill et al., 2006). Previous studies have examined the thermal expansion of both phases at ambient pressure, as well as compressivity at room temperature, however, no previous studies have investigated both simultaneously (Clendenen and Drickamer, 1964; Rao and Iyengar, 1969; Schroeder et al., 1972; Hazen and Finger, 1981). In addition, RuO$_2$ has been observed to undergo a series of phase transformations. At ambient conditions, RuO$_2$ has a tetragonal, rutile-type structure. At room temperature, it first undergoes a second-order ferroelastic phase transformation to an orthorhombic CaCl$_2$-type structure (Haines and Léger, 1993; Rosenblum et al., 1997; Ono and Mibe, 2011), and at higher pressures transforms to a cubic pyrite-type structure (Haines and Léger, 1993).

We have collected synchrotron X-ray diffraction data on the Ru+RuO$_2$ system to 19.4 GPa and 1473 K, with which we determined phase relations of RuO$_2$ and derived thermal equation of state parameters for both Ru and RuO$_2$. Further, we have derived a continuous Gibbs free energy expression for the tetragonal and orthorhombic phases of RuO2, using a model based on Landau theory combined with the modified Tait EoS (Holland and Powell, 1998; 2011), by fitting the second-order phase transition boundary and P-V-T data for both phases. The transition between the orthorhombic and cubic phases was then used along with EoS data for both phases to determine a Gibbs free energy

expression for the cubic phase. We were then able to calculate the oxygen fugacity of the equilibrium of reaction $Ru + O_2 = RuO_2$, which we have parameterised as a single polynomial across the stability fields of all three phases of RuO_2. Using the resulting expression, the fO_2 of the buffer can be determined up to 25 GPa and 2500K, with an estimated uncertainty of 0.2 log units.

6.2 Self-oxidation within a magma ocean

The early Earth is considered to have undergone at least one major collisional accretion event that would have resulted in a global magma ocean (e.g., Tonks and Melosh, 1993), and most accretion models favor final assembly of the larger terrestrial planets from a series of collisions involving Mars-sized planetary embryos (e.g., Chambers and Wetherill, 1998). At upper mantle pressures, the $Fe^{3+}/\sum Fe$ ratio of silicate liquids is strongly correlated with oxygen fugacity (Jayasuriya et al., 2004) and is near zero when in equilibrium with iron metal. However, the ratio of ferric to ferrous iron in a magma ocean was most likely set at depth, either through contact of the molten silicate with metal "ponds" that accumulated at the top of a solidified mantle, or as droplets of iron from the cores of accreting planetesimals rained through the magma column (Stevenson, 1990; Rubie et al., 2003). Iron descending through the magma ocean would impose metal saturation at all depths, however, vigourous convection (Solomatov, 2000) would have ensured that the magma was well mixed. As long as metal rained out relatively efficiently (Ichikawa et al., 2010), the ferric/ferrous ratio would ultimately reflect the average depth of equilibration.

Our experiments demonstrate a clear increase in the ratio of ferric iron to total iron in silicate melts as a function of pressure at a constant oxygen fugacity. This is possibly due to ferric iron being incorporated into a higher-coordination environment more readily than ferrous iron (Stixrude and Karki, 2005). The pressure-induced stabilisation of the ferric iron component in silicate melts therefore mirrors analogous changes that have been reported for mantle minerals over similar pressure intervals (Frost et al., 2004; Rohrbach

et al., 2007; Shim et al., 2017). The results of these studies imply that the equilibrium $3\text{FeO} = \text{Fe}_2\text{O}_3 + \text{Fe}^0$, involving the ferric and ferrous iron components of minerals, will shift to the right with increasing pressure. This will force the precipitation of metallic iron in systems that are initially poor in Fe_2O_3, such as that of the Earth's mantle during or immediately after core formation. Our experiments indicate that a similar effect will occur in silicate melts at high pressures. Removal of some of the precipitated iron metal to the core would raise the relative oxygen content of the magma ocean, resulting in a net oxidation.

Our results therefore imply that a deep magma ocean extending to lower mantle conditions would contain significant levels of ferric iron even in equilibrium with iron metal. At lower pressures near the surface, the relatively high ferric iron content would result in a relatively high oxygen fugacity. A deep magma ocean in equilibrium with iron metal at its base would therefore establish a depth-dependent redox gradient (figure 4.16), similar to the mantle oxygen fugacity gradient of the Earth today (Frost and McCammon, 2008). Such a redox gradient could explain the high C/H ratio in the modern Earth's mantle (Hirschmann, 2012). A downwelling magma with even a very small amount of dissolved CO_2 will eventually hit carbon saturation as the oxyen fugacity drops, and exsolve diamond or graphite, which would have been neutrally buoyant (Ohtani and Maeda, 2001) and remained in the mantle as the magma ocean crystallised.

This mechanism for mantle oxidation can also explain why the mantles of the moon, Mars, and Vesta are more reduced than the Earth's, despite Mars and Vesta being further out from the sun and therefore presumably deriving for more oxidised, volatile-rich material. Our results indicate the pressures of a magma ocean must be ~ 20 GPa to for ferric iron and iron metal to be in equilibrium. Magma oceans on the smaller terrestrial planets and planetesimals, where core-mantle boundary pressures (and therefore the maximum possible pressure for a global magma ocean) are ≤ 20 GPa, could, therefore, not have attained the depths necessary to stabilise ferric iron and thereby raise the oxidation state of the mantle.

6.3 Gradual oxidation through water delivery

The oxidation state of the mantle may have increased simply by the addition of more oxidised material late in accretion. The addition of oxidised material whilst metallic iron was still present in the mantle would, however, have simply led to the oxidation of the metallic iron and production of FeO. Raising the redox state of the upper mantle to the modern level, i.e., approximately the quartz-fayalite-magnetite oxygen fugacity buffer (QFM), required ferric iron to accumulate, which, at low pressures, precludes the coexistence of metallic iron.

There is significant evidence, however, that late in the Earth's accretionary history, as a global magma ocean cooled towards crystallisation, it exsolved liquid FeS sulfide, termed the Hadean matte, which sank to the core (O'Neill, 1991; Rubie et al., 2016). We have examined the plausible effects that the exolution of the Hadean matte could have had on the redox state of the residual silicate magma ocean.

We have also determined partitioning behaviour of molybdenum between liquid sulfide and silicate melt, which was found to be a potentially useful proxy for the oxygen fugacity. We have therefore used our data and literature data to calibrate the partition coefficient as a function of $f\text{O}_2$, temperature, and FeO content of the silicate melt. Future experiments may be able to employ the Mo liquid sulfide/silicate melt partition coefficient to estimate the oxygen fugacity that prevailed during the experiment; this calibration is accurate for our data within 0.3 log units.

Our results indicate that oxygen substitutes for sulfur in the FeS structure, rather than being incorporated as FeO. The loss of oxygen into an exolving sulfide, therefore, may have resulted in a net reduction of the residual magma ocean. The effect, however, is likely to have been small. We successfully measured hydrogen in a crystalline sulfide which was quenched from a liquid. However, it remains unclear if the sulfide was able to capture the entire complement of hydrogen that had dissolved in the liquid, or if some was lost during quenching. No bubbles were observed in the texture of the sulfide, however. We were also unable to determine the speciation of the hydrogen in the sul-

fide; it is therefore unclear if the hydrogen resulted from a disproportionation of H_2O to H, or if it was incorporated into the sulfide as water. Nevertheless, by examining the a maximum possible hydrogen content proposed by an in situ X-ray diffraction study, the potential effect of hydrogen loss into an exsolved sulfide can be estimated, and appears to have been even smaller than the possible effect from the loss of oxygen. Therefore, an exolving sulfide likely would have had a either a very small or negligible effect on the redox state of the residual magma ocean. The production of ferric iron in a deep magma ocean is therefore likely a much more effective mechanism for increasing the redox state of mantles of Earth-sized planetary bodies.

6.4 Outlook

There remains the opportunity for future work to address some of the issues raised here. In chapter 4, we demonstrate that the ferric iron component of silicate melts is stabilised with pressure, due to a higher compressibility of $FeO_{1.5}$ over that of FeO. Our model, however, hinted that this may ultimately change with still higher pressures, and that the trend may again reverse. Future work could investigate the equation of state parameters of $FeO_{1.5}$ and FeO to higher pressures, and explore the consequences on magma oceans that extend to greater depths. Experimental challenges, in particular that above 23 GPa the melting point of our andesitic composition was higher than that of the Pt capsule prevented experiments at higher pressure for this work, but perhaps a different setup can be envisaged. Additionally, figure 4.7 hints at a small, but nonzero effect of compositional interactions. A set of experiments designed to investigate the effect of pressure on the activity-composition relations of silicate melts could yeild interesting results. Although, as descibed in section 4.7, similar challenges regarding capsule choice and liquidus temperatures would have to be overcome.

As detailed in chapter 5, we were able to measure hydrogen in a quenched sulfide melt. There remains, however, significant doubt that the entire complement of dissolved H was captured by the crystallising melt. Further exper-

iments, with a lower H content, would be needed to test if the possible trend in figure 5.14 would show a plateau in the value of the sulfide/silicate partition coefficient with decreasing water content, indicating that true partitioning behaviour had been recorded. A potential problem arises from the detection limits of the ERDA technique, which is not much below our reported values. It would first be necessary to understand the detection limits with good accuracy; this could be accomplished by taking data from a sample known to be anhydrous. Provided these challenges could be overcome, however, it would be interesting to examine the effect of pressure on partitioning behaviour, as the results of Clesi et al. (2018) suggest that hydrogen may become more siderophile with increasing pressure. Given that the average depth of equilibration was likely fairly high, if partitioning behaviour changed with depth, our low-pressure results may not be relevant for core formation. Finally, we have demonstrated that Mo sulfide liquid/silicate melt partitioning could be useful as a proxy for oxygen fugacity. Our results indicate, however, that the effects of silicate melt composition are not fully addressed by the model presented here. A further series of experiments could potentially yeild useful results that could make Mo partitioning a robust indicator of oxygen fugacity.

References

Abe, Y. and Matsui, T., 1985. The formation of an impact-generated H_2O atmosphere and its implications for the early thermal history of the Earth. *Journal of Geophysical Research*, 90(S02): C545.

Agnor, C. B., Canup, R. M., and Levison, H. F., 1999. On the Character and Consequences of Large Impacts in the Late Stage of Terrestrial Planet Formation. *Icarus*, 142(1): 219–237.

Ahuja, R., Rekhi, S., Saxena, S. K., and Johansson, B., 2001. High-pressure structural phase transitions in RuO_2 and its geophysical implications. *The Journal of Physics and Chemistry of Solids*, 62(11): 2035–2037.

Akins, J. A. and Ahrens, T. J., 2002. Dynamic compression of SiO_2: A new interpretation. *Geophysical Research Letters*, 29(10).

Allègre, C. J., Poirier, J.-P., Humler, E., and Hofmann, A. W., 1995. The chemical composition of the Earth. *Earth and Planetary Science Letters*, 134: 515–526.

Anders, E. and Grevesse, N., 1989. Abundances of the elements: Meteoritic and solar. *Geochimica et Cosmochimica Acta*, 53(1): 197–214.

Andrault, D., Fiquet, G., Guyot, F., and Hanfland, M., 1998. Pressure-induced landau-type transition in stishovite. *Science*, 282(5389): 720–724.

Andrault, D., Muñoz, M., Pesce, G., Cerantola, V., Chumakov, A., Kantor, I., Pascarelli, S., Rüffer, R., and Hennet, L., 2018. Large oxygen excess in the primitive mantle could be the source of the Great Oxygenation Event. *Geochemical Perspectives Letters*, 6: 5–10.

Angel, R. J., Alvaro, M., and Gonzalez-Platas, J., 2014. EosFit7c and a Fortran module (library) for equation of state calculations. *Zeitschrift für Kristallographie - Crystalline Materials*, 229(5).

Angel, R. J., Alvaro, M., Miletich, R., and Nestola, F., 2017. A simple and generalised P–T–V EoS for continuous phase transitions, implemented in EosFit and applied to quartz. *Contributions to Mineralogy and Petrology*, 172(5): 29.

Ardia, P., Hirschmann, M. M., Withers, A. C., and Stanley, B. D., 2013. Solubility of CH_4 in a synthetic basaltic melt, with applications to atmosphere–magma ocean–core partitioning of volatiles and to the evolution of the Martian atmosphere. *Geochimica et Cosmochimica Acta*, 114: 52–71.

References

Ballhaus, C., 1995. Is the upper mantle metal-saturated? *Earth and Planetary Science Letters*, 132(1–4): 75–86.

Ballhaus, C., Berry, R. F., and Green, D. H., 1991. High pressure experimental calibration of the olivine-orthopyroxene-spinel oxygen geobarometer: implications for the oxidation state of the upper mantle. *Contributions to Mineralogy and Petrology*, 107(1): 27–40.

Bancroft, G. M., Maddock, A. G., and Burns, R. G., 1967. Applications of the Mössbauer effect to silicate mineralogy—I. Iron silicates of known crystal structure. *Geochimica et Cosmochimica Acta*, 31(11): 2219–2246.

Barbour, J. C. and Doyle, B. L., 1995. Elastic recoil detection: ERD (or forward recoil spectrometry FRES). In Tesmer, J. R. and Nastasi, M. A., editors, *Handbook of Modern Ion Beam Analysis*, pages 83–138. Materials Research Society.

Berry, A. J. and St. C. O'Neill, H., 2004. A XANES determination of the oxidation state of chromium in silicate glasses. *The American Mineralogist*, 89(5-6): 790–798.

Bézos, A. and Humler, E., 2005. The $Fe^{3+}/\Sigma Fe$ ratios of MORB glasses and their implications for mantle melting. *Geochimica et Cosmochimica Acta*, 69(3): 711–725.

Birner, S. K., Cottrell, E., Warren, J. M., Kelley, K. A., and Davis, F. A., 2018. Peridotites and basalts reveal broad congruence between two independent records of mantle fO_2 despite local redox heterogeneity. *Earth and Planetary Science Letters*, 494: 172–189.

Borisov, A. and Nachtweyh, K., 1998. Ru Solubility in Silicate Melts: Experimental Results in Oxidizing Region. In *29th Lunar and Planetary Science Conference*, page 1320.

Brearley, A. J. and Jones, R. H., 1998. Chondritic meteorites. *Reviews in Mineralogy and Geochemistry*, 36(1): 3.1–3.398.

Brearly, M., 1990. Ferric iron in silicate melts in the system Na_2O-Fe_2O_3-SiO_2 at high pressure. *Journal of Geophysical Research*, 95(B10): 15703.

Buono, A. S. and Walker, D., 2015. H, not O or pressure, causes eutectic T depression in the Fe-FeS System to 8 GPa. *Meteoritics and Planetary Science*, 50(4): 547–554.

Bureau, H., Raepsaet, C., Khodja, H., Carraro, A., and Aubaud, C., 2009. Determination of hydrogen content in geological samples using elastic recoil detection analysis (ERDA). *Geochimica et Cosmochimica Acta*, 73(11): 3311–3322.

Campbell, A. J., Danielson, L., Righter, K., Seagle, C. T., Wang, Y., and Prakapenka, V. B., 2009. High pressure effects on the iron–iron oxide and nickel–nickel oxide oxygen fugacity buffers. *Earth and Planetary Science Letters*, 286(3): 556–564.

Canil, D., 1997. Vanadium partitioning and the oxidation state of Archaean komatiite magmas. *Nature*, 389(6653): 842–845.

Canil, D. and O'Neill, H. S. T. C., 1996. Distribution of Ferric Iron in some Upper-Mantle Assemblages. *Journal of Petrology*, 37(3): 609–635.

References

Canil, D., O'Neill, H. S. C., Pearson, D. G., Rudnick, R. L., McDonough, W. F., and Carswell, D. A., 1994. Ferric iron in peridotites and mantle oxidation states. *Earth and Planetary Science Letters*, 123(1): 205–220.

Carpenter, M. A., Hemley, R. J., and Mao, H.-K., 2000. High-pressure elasticity of stishovite and the P4$_2$ / mnm = Pnnm phase transition. *Journal of Geophysical Research*, 105(B5): 10807–10816.

Cemič, L., 2005. *Thermodynamics in Mineral Sciences*. Springer.

Chabot, N. L., Draper, D. S., and Agee, C. B., 2005. Conditions of core formation in the earth: Constraints from Nickel and Cobalt partitioning. *Geochimica et Cosmochimica Acta*, 69(8): 2141–2151.

Chambers, J. E., 2001. Making More Terrestrial Planets. *Icarus*, 152(2): 205–224.

Chambers, J. E. and Wetherill, G. W., 1998. Making the Terrestrial Planets: N-Body Integrations of Planetary Embryos in Three Dimensions. *Icarus*, 136: 304–327.

Chantel, J., Frost, D. J., McCammon, C. A., Jing, Z., and Wang, Y., 2012. Acoustic velocities of pure and iron-bearing magnesium silicate perovskite measured to 25 GPa and 1200 K. *Geophysical Research Letters*, 39(19): L19307.

Christie, D. M., Carmichael, I. S. E., and Langmuir, C. H., 1986. Oxidation states of mid-ocean ridge basalt glasses. *Earth and Planetary Science Letters*, 79(3): 397–411.

Clendenen, R. L. and Drickamer, H. G., 1964. The effect of pressure on the volume and lattice parameters of ruthenium and iron. *The Journal of Physics and Chemistry of Solids*, 25(8): 865–868.

Clesi, V., Bouhifd, M. A., Bolfan-Casanova, N., Manthilake, G., Schiavi, F., Raepsaet, C., Bureau, H., Khodja, H., and Andrault, D., 2018. Low hydrogen contents in the cores of terrestrial planets. *Science Advances*, 4(3): e1701876.

Cottrell, E. and Kelley, K. A., 2011. The oxidation state of Fe in MORB glasses and the oxygen fugacity of the upper mantle. *Earth and Planetary Science Letters*, 305(3): 270–282.

Cullity, B. D., 1978. *Elements of X-ray Diffraction*. Addison-Wesley Publishing Company.

Daudin, L., Khodja, H., and Gallien, J.-P., 2003. Development of "position–charge–time" tagged spectrometry for ion beam microanalysis. *Nuclear Instruments and Methods in Physics Research. Section B: Beam Interactions with Materials and Atoms*, 210: 153–158.

Davis, F. A. and Cottrell, E., 2018. Experimental investigation of basalt and peridotite oxybarometers: Implications for spinel thermodynamic models and Fe^{3+} compatibility during generation of upper mantle melts. *The American Mineralogist*, 103(7): 1056–1067.

Davis, F. A., Cottrell, E., Birner, S. K., Warren, J. M., and Lopez, O. G., 2017. Revisiting the electron microprobe method of spinel-olivine-orthopyroxene oxybarometry applied to spinel peridotites. *The American Mineralogist*, 102(2): 421–435.

References

Day, J. M. D., Brandon, A. D., and Walker, R. J., 2016. Highly Siderophile Elements in Earth, Mars, the Moon, and Asteroids. *Reviews in Mineralogy and Geochemistry*, 81(1): 161–238.

Delano, J. W., 2001. Redox History of the Earth's Interior since 3900 Ma: Implications for Prebiotic Molecules. *Origins of life and Evolution of the Biosphere: The Journal of the International Society for the Study of the Origin of Life*, 31(4-5): 311–341.

Dewaele, A., Fiquet, G., Andrault, D., and Hausermann, D., 2000. P-V-T equation of state of periclase from synchrotron radiation measurements. *Journal of Geophysical Research*, 105(B2): 2869–2877.

Duncan, M. S., Dasgupta, R., and Tsuno, K., 2017. Experimental determination of CO_2 content at graphite saturation along a natural basalt-peridotite melt join: Implications for the fate of carbon in terrestrial magma oceans. *Earth and Planetary Science Letters*, 466: 115–128.

Dyar, M. D., Agresti, D. G., Schaefer, M. W., Grant, C. A., and Sklute, E. C., 2006. Mössbauer spectroscopy of Earth and planetary materials. *Annual Review of Earth and Planetary Sciences*, 34(1): 83–125.

Elkins-Tanton, L. T., 2012. Magma Oceans in the Inner Solar System. *Annual Review of Earth and Planetary Sciences*, 40(1): 113–139.

Eugster, H. P., 1957. Heterogeneous Reactions Involving Oxidation and Reduction at High Pressures and Temperatures. *The Journal of Chemical Physics*, 26(6): 1760–1761.

Fischer, R. A., Campbell, A. J., Chidester, B. A., Reaman, D. M., Thompson, E. C., Pigott, J. S., Prakapenka, V. B., and Smith, J. S., 2018. Equations of state and phase boundary for stishovite and $CaCl_2$-type SiO_2. *The American Mineralogist*, 103(5): 792–802.

Fischer-Gödde, M. and Kleine, T., 2017. Ruthenium isotopic evidence for an inner Solar System origin of the late veneer. *Nature*, 541(7638): 525–527.

Fonseca, R. O. C., Campbell, I. H., O'Neill, H. S. C., and Fitzgerald, J. D., 2008. Oxygen solubility and speciation in sulphide-rich mattes. *Geochimica et Cosmochimica Acta*, 72(11): 2619–2635.

Franke, P. and Neuschütz, D., 2006. *Thermodynamic Properties of Inorganic Materials: Binary Systems. Part 4: Binary Systems from Mn-Mo to Y-Zr.* Landolt-Börnstein - Group IV Physical Chemistry 19B4. SpringerMaterials.

Frost, D. J., 2003. Fe^{2+}-Mg partitioning between garnet, magnesiowüstite, and (Mg,Fe)2SiO4 phases of the transition zone. *The American Mineralogist*, 88(2-3): 387–397.

Frost, D. J. and Langenhorst, F., 2002. The effect of Al_2O_3 on Fe–Mg partitioning between magnesiowüstite and magnesium silicate perovskite. *Earth and Planetary Science Letters*, 199(1–2): 227–241.

Frost, D. J. and McCammon, C. A., 2008. The Redox State of Earth's Mantle. *Annual Review of Earth and Planetary Sciences*, 36(1): 389–420.

References

Frost, D. J., Liebske, C., Langenhorst, F., McCammon, C. A., Trønnes, R. G., and Rubie, D. C., 2004a. Experimental evidence for the existence of iron-rich metal in the Earth's lower mantle. *Nature*, 428(6981): 409–412.

Frost, D. J., Poe, B. T., Trønnes, R. G., Liebske, C., Duba, A., and Rubie, D. C., 2004b. A new large-volume multianvil system. *Physics of the Earth and Planetary Interiors*, 143-144: 507–514.

Frost, D. J., Mann, U., Asahara, Y., and Rubie, D. C., 2008. The redox state of the mantle during and just after core formation. *Philosophical Transactions of the Royal Society A: Mathematical, Physical, and Engineering sciences*, 366(1883): 4315–4337.

Frost, R. B., 1991. Introduction to oxygen fugacity and its petrologic importance. *Reviews in Mineralogy and Geochemistry*, 25(1): 1–9.

Fukai, Y. and Suzuki, T., 1986. Iron-water reaction under high pressure and its implication in the evolution of the Earth. *Journal of Geophysical Research*, 91(B9): 9222.

Gaillard, F., Scaillet, B., Pichavant, M., and Iacono-Marziano, G., 2015. The redox geodynamics linking basalts and their mantle sources through space and time. *Chemical Geology*, 418: 217–233.

Gale, A., Dalton, C. A., Langmuir, C. H., Su, Y., and Schilling, J.-G., 2013. The mean composition of ocean ridge basalts. *Geochemistry, Geophysics, Geosystems*, 14(3): 489–518.

Ghiorso, M. S., 2004. An equation of state for silicate melts. III. Analysis of stoichiometric liquids at elevated pressure: shock compression data, molecular dynamics simulations and mineral fusion curves. *American Journal of Science*, 304(8-9): 752–810.

Greenwood, R. C., Barrat, J.-A., Miller, M. F., Anand, M., Dauphas, N., Franchi, I. A., Sillard, P., and Starkey, N. A., 2018. Oxygen isotopic evidence for accretion of Earth's water before a high-energy Moon-forming giant impact. *Science Advances*, 4(3): eaao5928.

Gudmundsson, G. and Wood, B. J., 1995. Experimental tests of garnet peridotite oxygen barometry. *Contributions to Mineralogy and Petrology*, 119(1): 56–67.

Gupta, S. D. and Jha, P. K., 2014. Vibrational and elastic properties as a pointer to stishovite to $CaCl_2$ ferroelastic phase transition in RuO_2. *Earth and Planetary Science Letters*, 401: 31–39.

Haines, J. and Léger, J. M., 1993. Phase transitions in ruthenium dioxide up to 40 GPa: Mechanism for the rutile-to-fluorite phase transformation and a model for the high-pressure behavior of stishovite SiO_2. *Physical Review B: Condensed Matter*, 48(18): 13344–13350.

Haines, J., Léger, J. M., and Schulte, O., 1996. Pa3 Modified Fluorite-Type Structures in Metal Dioxides at High Pressure. *Science*, 271(5249): 629–631.

Haines, J., Leger, J. M., Schulte, O., and Hull, S., 1997. Neutron Diffraction Study of the Ambient-Pressure, Rutile-Type and the High-Pressure, $CaCl_2$-Type Phases of Ruthenium Dioxide. *Acta Crystallographica*, 53(6): 880–884.

References

Haines, J., Leger, J. M., Schmidt, M. W., Petitet, J. P., Pereire, A. S., Da Jornada, J. A. H., and Hull, S., 1998. Structural characterisation of the Pa$_3$ -type, high-pressure phase of ruthenium dioxide. *Journal of Physics and Chemistry of Solids*, 59(2): 239–243.

Hall, H. T., 1958. Some High-Pressure, High-Temperature Apparatus Design Considerations: Equipment for use at 100,000 atmospheres and 3000 Â°C. *The Review of Scientific Instruments*, 29(4): 267–275.

Hazen, R. M. and Finger, L. W., 1981. Bulk moduli and high-pressure crystal structures of rutile-type compounds. *The Journal of Physics and Chemistry of Solids*, 42(3): 143–151.

Herd, C. D. K., Borg, L. E., Jones, J. H., and Papike, J. J., 2002. Oxygen fugacity and geochemical variations in the martian basalts: implications for martian basalt petrogenesis and the oxidation state of the upper mantle of Mars. *Geochimica et Cosmochimica Acta*, 66(11): 2025–2036.

Hirschmann, M. M., 2012. Magma ocean influence on early atmosphere mass and composition. *Earth and Planetary Science Letters*, 341–344(0): 48–57.

Hirschmann, M. M., Withers, A. C., Ardia, P., and Foley, N. T., 2012. Solubility of molecular hydrogen in silicate melts and consequences for volatile evolution of terrestrial planets. *Earth and Planetary Science Letters*, 345-348: 38–48.

Hisao Ito, Kaoru Kawada, and Syun-iti Akimoto, 1974. Thermal expansion of stishovite. *Physics of the Earth and Planetary Interiors*, 8(3): 277–281.

Holland, T. J. B. and Powell, R., 1998. An internally consistent thermodynamic data set for phases of petrological interest. *Journal of Metamorphic Geology*, 16(3): 309–343.

Holland, T. J. B. and Powell, R., 2011. An improved and extended internally consistent thermodynamic dataset for phases of petrological interest, involving a new equation of state for solids. *Journal of Metamorphic Geology*, 29(3): 333–383.

Huang, Y. K. and Chow, C. Y., 2002. The generalized compressibility equation of Tait for dense matter. *Journal of Physics D: Applied Physics*, 7(15): 2021.

Huss, G. R., Rubin, A. E., and Grossman, J. N., 2006. Thermal metamorphism in chondrites. In Lauretta, D. S. and Mcsween, H. Y., Jr, editors, *Meteorites and the Early Solar System II*, pages 567–586. University of Arizona Press.

Ichikawa, H., Labrosse, S., and Kurita, K., 2010. Direct numerical simulation of an iron rain in the magma ocean. *Journal of Geophysical Research*, 115(B1): 1127.

Iizuka-Oku, R., Yagi, T., Gotou, H., Okuchi, T., Hattori, T., and Sano-Furukawa, A., 2017. Hydrogenation of iron in the early stage of Earth's evolution. *Nature Communications*, 8: 14096.

Ingalls, R., 1964. Electric-Field Gradient Tensor in Ferrous Compounds. *Physics Review*, 133(3A): A787–A795.

References

Ishii, T., Shi, L., Huang, R., Tsujino, N., Druzhbin, D., Myhill, R., Li, Y., Wang, L., Yamamoto, T., Miyajima, N., Kawazoe, T., Nishiyama, N., Higo, Y., Tange, Y., and Katsura, T., 2016. Generation of pressures over 40 GPa using Kawai-type multi-anvil press with tungsten carbide anvils. *The Review of Scientific Instruments*, 87(2): 024501.

Jayasuriya, K. D., OÊŒNeill, H. S. T. C., Berry, Ü. A. J., and Campbell, S. J., 2004. A Mössbauer study of the oxidation state of Fe in silicate melts. *The American Mineralogist*, 89: 1597–1609.

Kasting, J. F., Eggler, D. H., and Raeburn, S. P., 1993. Mantle redox evolution and the oxidation state of the Archean atmosphere. *The Journal of Geology*, 101(2): 245–257.

Kawai, N. and Endo, S., 1970. The Generation of Ultrahigh Hydrostatic Pressures by a Split Sphere Apparatus. *The Review of Scientific Instruments*, 41(8): 1178–1181.

Keefner, J. W., Mackwell, S. J., Kohlstedt, D. L., and Heidelbach, F., 2011. Dependence of dislocation creep of dunite on oxygen fugacity: Implications for viscosity variations in Earth's mantle. *Journal of Geophysical Research*, 116(B5): 1.

Keppler, H. and Frost, D. J., 2005. Introduction to minerals under extreme conditions. In Miletich, R., editor, *Mineral Behaviour at Extreme Conditions, European Mineralogical Union Lecture Notes in Mineralogy, Vol. 7*, pages 1–30. Mineralogical Society of Great Britain and Ireland.

Khodja, H., Berthoumieux, E., Daudin, L., and Gallien, J.-P., 2001. The Pierre Süe Laboratory nuclear microprobe as a multi-disciplinary analysis tool. *Nuclear Instruments and Methods in Physics Research. Section B: Beam Interactions with Materials and Atoms*, 181: 83–86.

Kiseeva, E. S. and Wood, B. J., 2015. The effects of composition and temperature on chalcophile and lithophile element partitioning into magmatic sulphides. *Earth and Planetary Science Letters*, 424: 280–294.

Kiseeva, E. S., Vasiukov, D. M., Wood, B. J., McCammon, C., Stachel, T., Bykov, M., Bykova, E., Chumakov, A., Cerantola, V., Harris, J. W., and Dubrovinsky, L., 2018. Oxidized iron in garnets from the mantle transition zone. *Nature Geoscience*, 11(2): 144–147.

Kleine, T. and Walker, R. J., 2017. Tungsten Isotopes in Planets. *Annual Review of Earth and Planetary Sciences*, 45(1): 389–417.

Kleine, T., Münker, C., Mezger, K., and Palme, H., 2002. Rapid accretion and early core formation on asteroids and the terrestrial planets from Hf-W chronometry. *Nature*, 418(6901): 952–955.

Kowalski, M. and Spencer, P. J., 1995. Thermodynamic reevaluation of the C-O, Fe-O and Ni-O systems: Remodelling of the liquid, BCC and FCC phases. *CALPHAD: Computer Coupling of Phase Diagrams and Thermochemistry*, 19(3): 229–243.

References

Kress, V. C. and Carmichael, I. S. E., 1991. The compressibility of silicate liquids containing Fe_2O_3 and the effect of composition, temperature, oxygen fugacity and pressure on their redox states. *Contributions to Mineralogy and Petrology*, 108(1-2): 82–92.

Kump, L. R., Kasting, J. F., and Barley, M. E., 2001. Rise of atmospheric oxygen and the "upside-down" Archean mantle. *Geochemistry, Geophysics, Geosystems*, 2: 1025–1010.

Kuwayama, Y., Hirose, K., Sata, N., and Ohishi, Y., 2005. The pyrite-type high-pressure form of silica. *Science*, 309(5736): 923–925.

Lange, R. A. and Carmichael, I. S. E., 1987. Densities of Na_2O-K_2O-CaO-MgO-FeO-Fe_2O_3-Al_2O_3-TiO_2-SiO_2 liquids: New measurements and derived partial molar properties. *Geochimica et Cosmochimica Acta*, 51(11): 2931–2946.

Lange, R. A. and Carmichael, I. S. E., 1990. Thermodynamic properties of silicate liquids with emphasis on density, thermal expansion and compressibility. In Nicholls, J. and Russell, J. K., editors, *Modern Methods of Igneous Petrology: Understanding Magmatic Processes*, pages 25–64. Reviews in Mineralogy, Mineralogical Society of America.

Larson, A. C. and Von Dreele, R. B., 2004. General Structure Analysis System (GSAS). Technical Report LAUR 86-748, Los Alamos National Laboratory.

Laurenz, V., Rubie, D. C., Frost, D. J., and Vogel, A. K., 2016. The importance of sulfur for the behavior of highly-siderophile elements during Earth's differentiation. *Geochimica et Cosmochimica Acta*, 194: 123–138.

Lauterbach, S., McCammon, C. A., van Aken, P., Langenhorst, F., and Seifert, F., 2000. Mössbauer and ELNES spectroscopy of $(Mg,Fe)(Si,Al)O_3$ perovskite: a highly oxidised component of the lower mantle. *Contributions to Mineralogy and Petrology*, 138(1): 17–26.

Lee, C.-T. A., Brandon, A. D., and Norman, M., 2003. Vanadium in peridotites as a proxy for paleo-fO$_2$ during partial melting: prospects, limitations, and implications. *Geochimica et Cosmochimica Acta*, 67(16): 3045–3064.

Li, C., Naldrett, A. J., Coats, C. J. A., and Johannessen, P., 1992. Platinum, palladium, gold, copper-rich stringers at the Strathcona Mine, Sudbury; their enrichment by fractionation of a sulfide liquid. *Economic Geology and the Bulletin of the Society of Economic Geologists*, 87(6): 1584–1598.

Li, J. and Agee, C. B., 1996. Geochemistry of mantle–core differentiation at high pressure. *Nature*, 381(6584): 686–689.

Li, Y., 2014. Chalcophile element partitioning between sulfide phases and hydrous mantle melt: Applications to mantle melting and the formation of ore deposits. *Journal of Asian Earth Sciences*, 94: 77–93.

Li, Y. and Audétat, A., 2012. Partitioning of V, Mn, Co, Ni, Cu, Zn, As, Mo, Ag, Sn, Sb, W, Au, Pb, and Bi between sulfide phases and hydrous basanite melt at upper mantle conditions. *Earth and Planetary Science Letters*, 355-356: 327–340.

References

Li, Y. and Audétat, A., 2015. Effects of temperature, silicate melt composition, and oxygen fugacity on the partitioning of V, Mn, Co, Ni, Cu, Zn, As, Mo, Ag, Sn, Sb, W, Au, Pb, and Bi between sulfide phases and silicate melt. *Geochimica et Cosmochimica Acta*, 162: 25–45.

Li, Z.-X. A. and Lee, C.-T. A., 2004. The constancy of upper mantle fO_2 through time inferred from V/Sc ratios in basalts. *Earth and Planetary Science Letters*, 228(3–4): 483–493.

Liebermann, R. C., 2011. Multi-anvil, high pressure apparatus: a half-century of development and progress. *High Pressure Research*, 31(4): 493–532.

Liu, Q. and Lange, R. A., 2006. The partial molar volume of Fe_2O_3 in alkali silicate melts: Evidence for an average Fe^{3+} coordination number near five. *The American Mineralogist*, 91(2-3): 385–393.

Lodders, K. and Palme, H., 1991. On the chalcophile character of molybdenum: determination of sulfide/silicate partition coefficients of Mo and W. *Earth and Planetary Science Letters*, 103(1): 311–324.

Long, G.L., Cranshaw, T.E. and Longworth, G., 1983. The ideal Mössbauer effect absorber thickness. *Mössbauer Effect Reference Data Journal*, 6: 42–49.

Lugovskoy, A. V., Belov, M. P., Krasilnikov, O. M., and Vekilov, Y. K., 2014. Stability of the hcp Ruthenium at high pressures from first principles. *Journal of Applied Physics*, 116(10): 103507.

Lundin, U., Fast, L., Nordström, L., Johansson, B., Wills, J. M., and Eriksson, O., 1998. Transition-metal dioxides with a bulk modulus comparable to diamond. *Physical Review B: Condensed Matter*, 57(9): 4979–4982.

Maier, W. D., Barnes, S. J., Campbell, I. H., Fiorentini, M. L., Peltonen, P., Barnes, S.-J., and Hugh Smithies, R., 2009. Progressive mixing of meteoritic veneer into the early Earth's deep mantle. *Nature*, 460(7255): 620–623.

Mallmann, G. and O'Neill, H. S. C., 2009. The Crystal/Melt Partitioning of V during Mantle Melting as a Function of Oxygen Fugacity Compared with some other Elements (Al, P, Ca, Sc, Ti, Cr, Fe, Ga, Y, Zr and Nb). *Journal of Petrology*, 50(9): 1765–1794.

Mann, U., Frost, D. J., and Rubie, D. C., 2009. Evidence for high-pressure core-mantle differentiation from the metal–silicate partitioning of lithophile and weakly-siderophile elements. *Geochimica et Cosmochimica Acta*, 73(24): 7360–7386.

Mann, U., Frost, D. J., Rubie, D. C., Becker, H., and Audétat, A., 2012. Partitioning of Ru, Rh, Pd, Re, Ir and Pt between liquid metal and silicate at high pressures and high temperatures - Implications for the origin of highly siderophile element concentrations in the Earth's mantle. *Geochimica et Cosmochimica Acta*, 84: 593–613.

Marty, B., 2012. The origins and concentrations of water, carbon, nitrogen and noble gases on Earth. *Earth and Planetary Science Letters*, 313-314: 56–66.

References

Matjuschkin, V., Brooker, R. A., Tattitch, B., Blundy, J. D., and Stamper, C. C., 2015. Control and monitoring of oxygen fugacity in piston cylinder experiments. *Contributions to Mineralogy and Petrology*, 169(1): 9.

Mavrogenes, J. A. and O'Neill, H. S. C., 1999. The relative effects of pressure, temperature and oxygen fugacity on the solubility of sulfide in mafic magmas. *Geochimica et Cosmochimica Acta*, 63(7): 1173–1180.

Mayer, M., 1999. SIMNRA, a simulation program for the analysis of NRA, RBS and ERDA. *AIP Conference Proceedings*, 475(1): 541–544.

McCammon, C., 1997. Perovskite as a possible sink for ferric iron in the lower mantle. *Nature*, 387(6634): 694–696.

McCammon, C. A., 2004. Mössbauer Spectroscopy: Applications. In Beran, A. and Libowitzky, E., editors, *Spectroscopic Methods in Mineralogy*. European Mineralogical Union.

McDonough, W. F. and Sun, S.-S., 1995. The composition of the Earth. *Chemical Geology*, 120(3): 223–253.

Miller, G. H., Stolper, E. M., and Ahrens, T. J., 1991. The equation of state of a molten komatiite: 2. Application to komatiite petrogenesis and the Hadean Mantle. *Journal of Geophysical Research*, 96(B7): 11849.

Ming, L. C. and Manghnani, M. H., 1982. High-Pressure Phase Transformations in Rutile-Structured Dioxides. In Akimoto, S. and Manghnani, M. H., editors, *High-Pressure Research in Geophysics*, pages 329–360. Center for Academic Publications, Tokyo.

Morbidelli, A., Chambers, J., Lunine, J. I., Petit, J. M., Robert, F., Valsecchi, G. B., and Cyr, K. E., 2000. Source regions and timescales for the delivery of water to the Earth. *Meteoritics and Planetary Science*, 35(6): 1309–1320.

Mysen, B. O. and Virgo, D., 1985. Iron-bearing silicate melts: Relations between pressure and redox equilibria. *Physics and Chemistry of Minerals*, 12(4): 191–200.

Nakajima, Y., Frost, D. J., and Rubie, D. C., 2012. Ferrous iron partitioning between magnesium silicate perovskite and ferropericlase and the composition of perovskite in the Earth's lower mantle. *Journal of Geophysical Research*, 117(B8): B08201.

Ohtani, E. and Maeda, M., 2001. Density of basaltic melt at high pressure and stability of the melt at the base of the lower mantle. *Earth and Planetary Science Letters*, 193(1): 69–75.

Okuchi, T., 1997. Hydrogen partitioning into molten iron at high pressure: implications for Earth's core. *Science*, 278(5344): 1781–1784.

O'Neill, H. S. C., 1991. The origin of the moon and the early history of the earth—A chemical model. Part 2: The earth. *Geochimica et Cosmochimica Acta*, 55(4): 1159–1172.

O'Neill, H. S. C. and Eggins, S. M., 2002. The effect of melt composition on trace element partitioning: an experimental investigation of the activity coefficients of FeO, NiO, CoO, MoO_2 and MoO_3 in silicate melts. *Chemical Geology*, 186(1): 151–181.

References

O'Neill, H. S. C. and Nell, J., 1997. Gibbs free energies of formation of RuO_2, IrO_2, and OsO_2: A high-temperature electrochemical and calorimetric study. *Geochimica et Cosmochimica Acta*, 61(24): 5279–5293.

O'Neill, H. S. C. and Wall, V. J., 1987. The Olivine-Orthopyroxene-Spinel Oxygen Geobarometer, the Nickel Precipitation Curve, and the Oxygen Fugacity of the Earth's Upper Mantle. *Journal of Petrology*, 28: 1169–1191.

O'Neill, H. S. C., McCammon, C. A., Canil, D., Rubie, D. C., Ross, C. R., and Seifert, F., 1993a. Mossbauer spectroscopy of mantle transition zone phases and determination of minimum Fe_{3+} content. *The American Mineralogist*, 78(3-4): 456–460.

O'Neill, H. S. C., Rubie, D. C., Canil, D., Geiger, C. A., Ross, C. R., Seifert, F., and Woodland, A. B., 1993b. Ferric Iron in the Upper Mantle and In Transition Zone Assemblages: Implications for Relative Oxygen Fugacities in the Mantle. In Takahashi, E., Jeanloz, R., and Rubie, D., editors, *Evolution of the Earth and Planets*, pages 73–88. American Geophysical Union.

O'Neill, H. S. C., Berry, A. J., McCammon, C. C., Jayasuriya, K. D., Campbell, S. J., and Foran, G., 2006. An experimental determination of the effect of pressure on the $Fe_{3+}/\sum Fe$ ratio of an anhydrous silicate melt to 3.0 GPa. *The American Mineralogist*, 91(2-3): 404–412.

Ono, S. and Mibe, K., 2011. Determination of the phase boundary of the ferroelastic rutile to $CaCl_2$ transition in RuO_2 using in situ high-pressure and high-temperature Raman spectroscopy. *Physical Review B: Condensed Matter*, 84(5): 054114.

Palme, H. and O'Neill, H. S. C., 2003. Cosmochemical Estimates of Mantle Composition. *Treatise on Geochemistry*, 2: 568.

Pearson, D. G., Shirey, S. B., Harris, J. W., and Carlson, R. W., 1998. Sulphide inclusions in diamonds from the Koffiefontein kimberlite, S Africa: constraints on diamond ages and mantle Re–Os systematics. *Earth and Planetary Science Letters*, 160(3): 311–326.

Phillips, B. and Muan, A., 1960. Stability relations of iron oxides: Phase equilibria in the system Fe_3O_4-Fe_2O_3 at oxygen pressures up to 45 atmospheres. *The Journal of Physical Chemistry*, 64: 1451–1453.

Poirier, J.-P., 1991. *Introduction to the physics of the Earth's Interior*. Cambridge University Press.

Pommier, A., Gaillard, F., and Pichavant, M., 2010. Time-dependent changes of the electrical conductivity of basaltic melts with redox state. *Geochimica et Cosmochimica Acta*, 74(5): 1653–1671.

Prescher, C., McCammon, C., and Dubrovinsky, L., 2012. MossA: a program for analyzing energy-domain Mössbauer spectra from conventional and synchrotron sources. *Journal of Applied Crystallography*, 45(2): 329–331.

References

Pringle, E. A., Savage, P. S., Badro, J., Barrat, J.-A., and Moynier, F., 2013. Redox state during core formation on asteroid 4-Vesta. *Earth and Planetary Science Letters*, 373: 75–82.

Raepsaet, C., Bureau, H., Khodja, H., Aubaud, C., and Carraro, A., 2008. μ-Erda developments in order to improve the water content determination in hydrous and nominally anhydrous mantle phases. *Nuclear Instruments and Methods in Physics Research Section B: Beam Interactions with Materials and Atoms*, 266: 1333–1337.

Rancourt, D. G. and Ping, J. Y., 1991. Voigt-based methods for arbitrary-shape static hyperfine parameter distributions in Mössbauer spectroscopy. *Nuclear Instruments and Methods in Physics Research Section B: Beam Interactions with Materials and Atoms*, 58(1): 85–97.

Rao, K. V. K. and Iyengar, L., 1969. X-ray studies on the thermal expansion of ruthenium dioxide. *Acta Crystallographica Section A: Foundations of Crystallography*, 25(2): 302–303.

Raymond, S. N., Quinn, T., and Lunine, J. I., 2004. Making other earths: dynamical simulations of terrestrial planet formation and water delivery. *Icarus*, 168(1): 1–17.

Reed, S. J. B., 2005. *Electron Microprobe Analysis and Scanning Electron Microscopy in Geology*. Cambridge University Press.

Righter, K., Campbell, A. J., Humayun, M., and Hervig, R. L., 2004. Partitioning of Ru, Rh, Pd, Re, Ir, and Au between Cr-bearing spinel, olivine, pyroxene and silicate melts. *Geochimica et Cosmochimica Acta*, 68(4): 867–880.

Rinaldi, R. and Llovet, X., 2015. Electron Probe Microanalysis: A Review of the Past, Present, and Future. *Microscopy and Microanalysis*, 21(5): 1053–1069.

Ringwood, A. E., 1966. Chemical evolution of the terrestrial planets. *Geochimica et Cosmochimica Acta*, 30(1): 41–104.

Ringwood, A. E., 1979. *Composition and Origin of the Earth*. Academic Press, New York.

Robie, R. A. and Hemingway, B. S., 1995. Thermodynamic properties or minerals and related substances at 298.15 K and 1 bar pressure and at higher temperatures. Technical Report 2131, U.S. Geological Survey.

Rohrbach, A., Ballhaus, C., Golla-Schindler, U., Ulmer, P., Kamenetsky, V. S., and Kuzmin, D. V., 2007. Metal saturation in the upper mantle. *Nature*, 449(7161): 456–458.

Rosenblum, S. S., Weber, W. H., and Chamberland, B. L., 1997. Raman-scattering observation of the rutile-to-$CaCl_2$ phase transition in RuO_2. *Physical Review B: Condensed Matter and Materials Physics*, 56(2): 529–533.

Rubie, D. C., 1999. Characterising the sample environment in multianvil high-pressure experiments. *Phase Transitions*, 68(3): 431–451.

Rubie, D. C., Melosh, H. J., Reid, J. E., Liebske, C., and Righter, K., 2003. Mechanisms of metal–silicate equilibration in the terrestrial magma ocean. *Earth and Planetary Science Letters*, 205(3–4): 239–255.

References

Rubie, D. C., Frost, D. J., Mann, U., Asahara, Y., Nimmo, F., Tsuno, K., Kegler, P., Holzheid, A., and Palme, H., 2011. Heterogeneous accretion, composition and core–mantle differentiation of the Earth. *Earth and Planetary Science Letters*, 301(1): 31–42.

Rubie, D. C., Jacobson, S. A., Morbidelli, A., O'Brien, D. P., Young, E. D., de Vries, J., Nimmo, F., Palme, H., and Frost, D. J., 2015. Accretion and differentiation of the terrestrial planets with implications for the compositions of early-formed Solar System bodies and accretion of water. *Icarus*, 248(0): 89–108.

Rubie, D. C., Laurenz, V., Jacobson, S. A., Morbidelli, A., Palme, H., Vogel, A. K., and Frost, D. J., 2016. Highly siderophile elements were stripped from Earth's mantle by iron sulfide segregation. *Science*, 353(6304): 1141–1144.

Rubin, A. E., 2011. Origin of the differences in refractory-lithophile-element abundances among chondrite groups. *Icarus*, 213(2): 547–558.

Sack, R. O., Carmichael, I. S. E., Rivers, M., and Ghiorso, M. S., 1980. Ferric-ferrous equilibria in natural silicate liquids at 1 bar. *Contributions to Mineralogy and Petrology*, 75(4): 369–376.

Schroeder, R. H., Schmitz-Pranghe, N., and Kohlhaas, R., 1972. Experimentelle Bestimmung der Gitterparameter der Platinmetalle im Temperaturbereich von -190 bis 1709Â°C. *Zeitschrift Metallkunde*, 63: 12–16.

Sharp, Z. D., McCubbin, F. M., and Shearer, C. K., 2013. A hydrogen-based oxidation mechanism relevant to planetary formation. *Earth and Planetary Science Letters*, 380: 88–97.

Shibazaki, Y., Ohtani, E., Terasaki, H., Tateyama, R., Sakamaki, T., Tsuchiya, T., and Funakoshi, K.-I., 2011. Effect of hydrogen on the melting temperature of FeS at high pressure: Implications for the core of Ganymede. *Earth and Planetary Science Letters*, 301(1): 153–158.

Shim, S.-H., Grocholski, B., Ye, Y., Alp, E. E., Xu, S., Morgan, D., Meng, Y., and Prakapenka, V. B., 2017. Stability of ferrous-iron-rich bridgmanite under reducing midmantle conditions. *Proceedings of the National Academy of Sciences of the United States of America*, 114(25): 6468–6473.

Siebert, J., Badro, J., Antonangeli, D., and Ryerson, F. J., 2013. Terrestrial accretion under oxidizing conditions. *Science*, 339(6124): 1194–1197.

Smith, E. M., Shirey, S. B., Nestola, F., Bullock, E. S., Wang, J., Richardson, S. H., and Wang, W., 2016. Large gem diamonds from metallic liquid in Earth's deep mantle. *Science*, 354(6318): 1403–1405.

Smyth, J. R., Bolfan-Casanova, N., Avignant, D., El-Ghozzi, M., and Hirner, S. M., 2014. Tetrahedral ferric iron in oxidized hydrous wadsleyite. *The American Mineralogist*, 99(2-3): 458–466.

References

Solomatov, Y. S., 2000. Fluid Dynamics of Terrestrial Magma Ocean. In Canup, R. and Righter, K., editors, *Origin of the Earth and Moon*, pages 323–338.

Sorbadere, F., Laurenz, V., Frost, D. J., Wenz, M., Rosenthal, A., McCammon, C., and Rivard, C., 2018. The behaviour of ferric iron during partial melting of peridotite. *Geochimica et Cosmochimica Acta*, 239: 235–254.

Stagno, V. and Frost, D. J., 2010. Carbon speciation in the asthenosphere: Experimental measurements of the redox conditions at which carbonate-bearing melts coexist with graphite or diamond in peridotite assemblages. *Earth and Planetary Science Letters*, 300(1): 72–84.

Stagno, V., Tange, Y., Miyajima, N., McCammon, C. A., Irifune, T., and Frost, D. J., 2011. The stability of magnesite in the transition zone and the lower mantle as function of oxygen fugacity. *Geophysical Research Letters*, 38(19).

Stevenson, D. J., 1990. Fluid dynamics of core formation. In Newsom, H. E. and Jones, J. H., editors, *Origin of the Earth*, pages 231–249. New York: Oxford University Press.

Stixrude, L. and Karki, B., 2005. Structure and freezing of $MgSiO_3$ liquid in Earth's lower mantle. *Science*, 310(5746): 297–299.

Stolper, E., 1982. Water in silicate glasses: An infrared spectroscopic study. *Contributions to Mineralogy and Petrology*, 81(1): 1–17.

Sundman, B., 1991. An assessment of the Fe-O system. *Journal of Phase Equilibria and Diffusion*, 12(2): 127–140.

Tao, R., Fei, Y., Bullock, E. S., Xu, C., and Zhang, L., 2018. Experimental investigation of Fe^{3+}-rich majoritic garnet and its effect on majorite geobarometer. *Geochimica et Cosmochimica Acta*, 225: 1–16.

Toby, B. H., 2001. EXPGUI a graphical user interface for GSAS. *Journal of Applied Crystallography*, 34(2): 210–213.

Tonks, W. B. and Melosh, H. J., 1993. Magma ocean formation due to giant impacts. *Journal of Geophysical Research*, 98(E3): 5319–5333.

Trail, D., Watson, E. B., and Tailby, N. D., 2011. The oxidation state of Hadean magmas and implications for early Earth's atmosphere. *Nature*, 480(7375): 79–82.

Tse, J. S., Klug, D. D., Uehara, K., Li, Z. Q., Haines, J., and Léger, J. M., 2000. Elastic properties of potential superhard phases of RuO_2. *Physical Review B: Condensed Matter*, 61(15): 10029–10034.

Tsuchiya, T., 2003. First-principles prediction of the P-V-T equation of state of gold and the 660-km discontinuity in Earth's mantle. *Journal of Geophysical Research*, 108(B10): 2462.

Tsuchiya, T., Caracas, R., and Tsuchiya, J., 2004. First principles determination of the phase boundaries of high-pressure polymorphs of silica. *Geophysical Research Letters*, 31(11).

References

Vandenberghe, R. E., De Grave, E., and de Bakker, P. M. A., 1994. On the methodology of the analysis of Mössbauer spectra. *Hyperfine Interactions*, 83(1): 29–49.

Wade, J. and Wood, B. J., 2005. Core formation and the oxidation state of the Earth. *Earth and Planetary Science Letters*, 236(1–2): 78–95.

Wadhwa, M., 2008. Redox Conditions on Small Bodies, the Moon and Mars. *Reviews in Mineralogy and Geochemistry*, 68(1): 493–510.

Walker, D., 1991. Lubrication, gasketing, and precision in multianvil experiments. *The American Mineralogist*, 76: 1092–1100.

Walker, D., Carpenter, M. A., and Hitch, C. M., 1990. Some simplifications to multianvil devices for high pressure experiments. *The American Mineralogist*, 75(9-10): 1020–1028.

Walter, M. J., 2000. Partitioning and Implications for Core Formation. In Canup, R. and Righter, K., editors, *Origin of the Earth and Moon.*

Wang, Y., Rivers, M., Sutton, S., Nishiyama, N., Uchida, T., and Sanehira, T., 2009. The large-volume high-pressure facility at GSECARS: A "Swiss-army-knife" approach to synchrotron-based experimental studies. *Physics of the Earth and Planetary Interiors*, 174(1): 270–281.

Wänke, H., 1981. Constitution of terrestrial planets. *Philosophical Transactions of the Royal Society of London Series A: Mathematical and Physical Sciences*, 303(1477): 287–302.

Wänke, H., Dreibus, G., and Jagoutz, E., 1984. Mantle Chemistry and Accretion History of the Earth. In *Archaean Geochemistry*, pages 1–24. Springer Berlin Heidelberg.

Weisberg, M. K., McCoy, T. J., and Krot, A. N., 2006. Systematics and evaluation of meteorite classification. In Lauretta, D. S. and McSween, H. Y., Jr., editors, *Meteorites and the Early Solar System II*. University of Arizona Press.

Weiss, B. P. and Elkins-Tanton, L. T., 2013. Differentiated Planetesimals and the Parent Bodies of Chondrites. *Annual Review of Earth and Planetary Sciences*, 41(1): 529–560.

Wendlandt, R. F., 1982. Sulfide saturation of basalt and andesite melts at high pressures and temperatures. *The American Mineralogist*, 67(9-10): 877–885.

Withers, A. C., Bureau, H., Raepsaet, C., and Hirschmann, M. M., 2012. Calibration of infrared spectroscopy by elastic recoil detection analysis of H in synthetic olivine. *Chemical Geology*, 334: 92–98.

Wood, B. J., Walter, M. J., and Wade, J., 2006. Accretion of the Earth and segregation of its core. *Nature*, 441(7095): 825–833.

Wood, B. J., Kiseeva, E. S., and Matzen, A. K., 2013. Garnet in the Earth's Mantle. *Elements*, 9(6): 421–426.

Wood, J. A., 1988. Chondritic meteorites and the solar nebula. *Annual Review of Earth and Planetary Sciences.*

References

Woodland, A. B. and O'Neill, H. S. C., 1997. Thermodynamic data for Fe-bearing phases obtained using noble metal alloys as redox sensors. *Geochimica et Cosmochimica Acta*, 61(20): 4359–4366.

Woodland, A. B., Kornprobst, J., and Tabit, A., 2006. Ferric iron in orogenic lherzolite massifs and controls of oxygen fugacity in the upper mantle. *Lithos*, 89(1): 222–241.

Wriedt, H. A., 1991. The Fe-O (iron-oxygen) system. *Journal of Phase Equilibria and Diffusion*, 12: 170–200.

Wykes, J. L. and Mavrogenes, J. A., 2005. Hydrous sulfide melting: experimental evidence for the solubility of H_2O in sulfide melts. *Economic Geology and the Bulletin of the Society of Economic Geologists*, 100(1): 157–164.

Yoshino, T. and Katsura, T., 2013. Electrical Conductivity of Mantle Minerals: Role of Water in Conductivity Anomalies. *Annual Review of Earth and Planetary Sciences*, 41(1): 605–628.

Zhang, H. L., Hirschmann, M. M., Cottrell, E., and Withers, A. C., 2017. Effect of pressure on $Fe^{3+}/\Sigma Fe$ ratio in a mafic magma and consequences for magma ocean redox gradients. *Geochimica et Cosmochimica Acta*, 204: 83–103.

Zhang, H. L., Cottrell, E., Solheid, P. A., Kelley, K. A., and Hirschmann, M. M., 2018. Determination of $Fe^{3+}/\Sigma Fe$ of XANES basaltic glass standards by Mössbauer spectroscopy and its application to the oxidation state of iron in MORB. *Chemical Geology*, 479: 166–175.

Acknowledgements

First and foremost, I must graciously thank my supervisor, Dan Frost, for his depths of patience and good humor. I was granted a wide berth of freedom to explore and try many things, not all of which were successful. I was never afraid to ask questions, and am truly grateful for the generous support and kindness throughout the years. I thank all the technical and support staff of BGI for their assistance, without which not nearly as much could have been accomplished. In particular, the multianvil experiments that were the foundation of this work would not have been nearly as successful without Heinz Fischer and Stefan Übelhack crafting extremely high-quality assemblies and anvils. The excellent sample preparation from Hubert Schulze, Raphael Njul, and Alexander Rother ensured that the maximum amount of information could be obtained from every experiment. Detlef Krausse and Anke Potzel are gratefully thanked for assistance with the electron microprobe, and Doro Wiesner and Ulrike Trenz for aid with the chemical laboratory.

I very warmly thank Catherine McCammon for assissting me with Mössbauer spectroscopy and for good advice. I also thank Tiziana Boffa-Ballaran for helping me with X-ray diffraction, at BGI and especially at APS, which wouldn't have worked out nearly as well without her help. I gratefully acknowledge Hélène Bureau for help in organising the work at the nuclear microprobe and teaching me the ERDA technique and data processing. I am in debt to Gerd Steinle-Neumann for assistance with the German-language translation of the abstract. Many thanks to Nicki Siersch, Pierre Condamine, and Sumith Abeykoon for also travelling to the APS and CEA facilities for this project. I also thank all my other former and current BGI colleagues for creating an engaging and positive work environment, and for their camraderie and companionship.

Finally, I thank my parents, Monika and Wade Hassler, and Sam Armstrong, for their constant and unwavering support through all my many years of schooling. This would not have been possible without them. And, most of all, I thank my partner, main supporter, and proofreader Will Davis, whom I wouldn't even have met if not for my time at BGI. Thank you for the unconditional support and patience over the last nearly two years, and your unfailing kindness.

(Eidesstattliche) Versicherungen und Erklärungen

(§9 Satz 2 Nr. 3 PromO BayNAT)

Hiermit versichere ich eidesstattlich, dass ich die Arbeit selbstständig verfasst und keine anderen als die von mir angegebenen Quellen und Hilfsmittel benutzt habe (vgl. Art. 64 Abs. 1 Satz 6 BayHSchG).

(§9 Satz 2 Nr. 3 PromO BayNAT)

Hiermit erkläre ich, dass ich die Dissertation nicht bereits zur Erlangung eines akademischen Grades eingereicht habe und dass ich nicht bereits diese oder eine gleichartige Doktorprüfung endgültig nicht bestanden habe.

(§9 Satz 2 Nr. 4 PromO BayNAT)

Hiermit erkläre ich, dass ich Hilfe von gewerblichen Promotionsberatern bzw. -vermittlern oder ähnlichen Dienstleistern weder bisher in Anspruch genommen habe noch künftig in Anspruch nehmen werde.

(§9 Satz 2 Nr. 7 PromO BayNAT)

Hiermit erkläre ich mein Einverständnis, dass die elektronische Fassung meiner Dissertation unter Wahrung meiner Urheberrechte und des Datenschutzes einer gesonderten Überprüfung unterzogen werden kann.

(§9 Satz 2 Nr. 8 PromO BayNAT)

Hiermit erkläre ich mein Einverständnis, dass bei Verdacht wissenschaftlichen Fehlverhaltens Ermittlungen durch universitätsinterne Organe der wissenschaftlichen Selbstkontrolle stattfinden können.

_____

Ort, Datum, Unterschrift